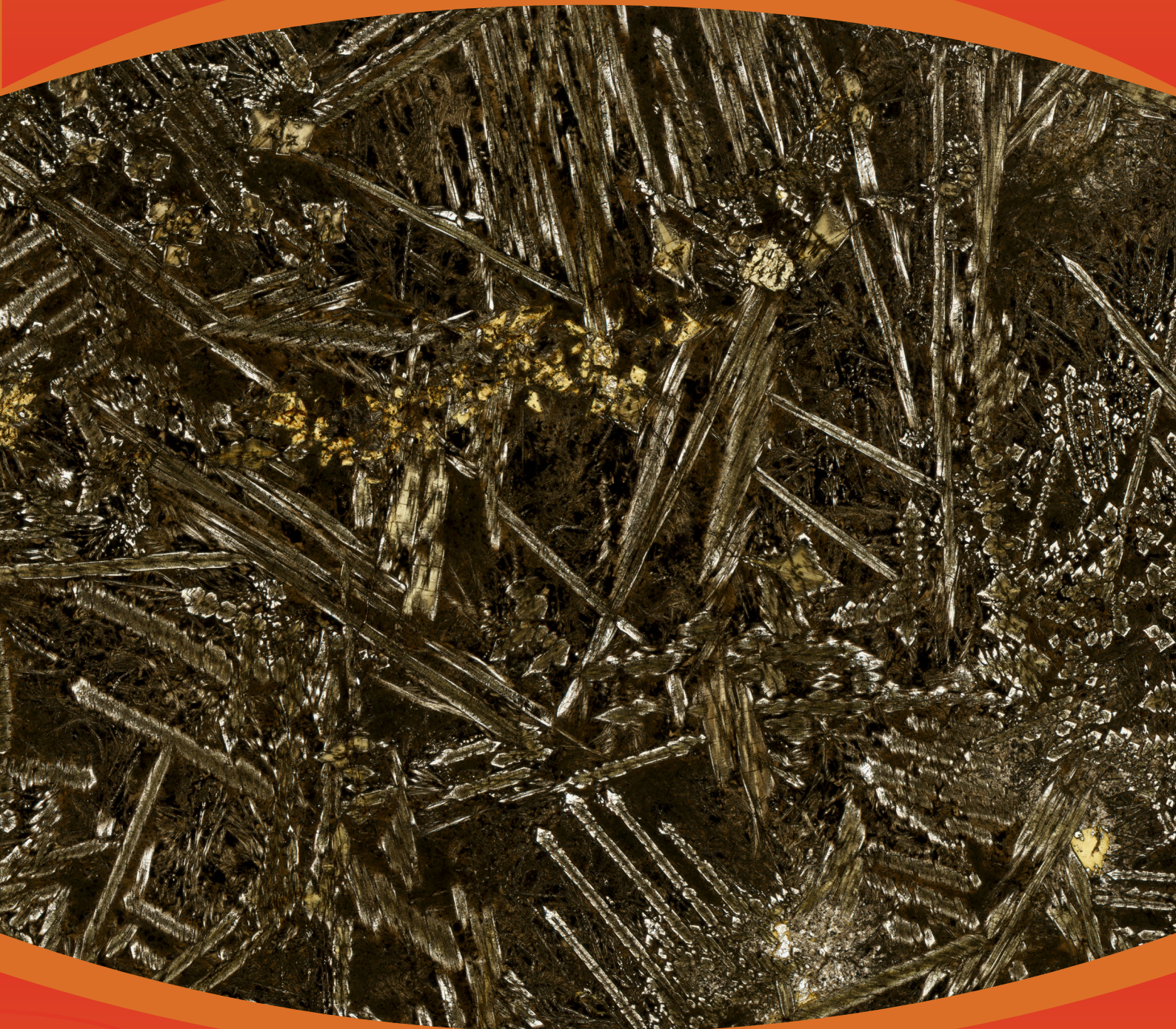


REPORT 259



PETROGENESIS OF C. 2820–2738 MA MAGMATISM IN THE NORTHWESTERN YUANMI TERRANE, YILGARN CRATON

JR LOWREY



Department of **Energy, Mines,
Industry Regulation and Safety**

RECORD 2025/5

PETROGENESIS OF C. 2820–2738 MA MAGMATISM IN THE NORTHWESTERN YUANMI TERRANE, YILGARN CRATON

JR Lowrey

PERTH 2025



**Geological Survey of
Western Australia**

MINISTER FOR MINES AND PETROLEUM
Hon David Robert Michael MLA

DIRECTOR GENERAL, DEPARTMENT OF ENERGY, MINES, INDUSTRY REGULATION AND SAFETY
Jai Thomas

EXECUTIVE DIRECTOR, GEOLOGICAL SURVEY AND RESOURCE STRATEGY
Michele Spencer

REFERENCE

The recommended reference for this publication is:

Lowrey, JR 2025, Petrogenesis of c. 2820–2738 Ma magmatism in the northwestern Youanmi Terrane, Yilgarn Craton: Geological Survey of Western Australia, Report 259, 269p.

ISBN 978-1-76148-066-9

ISSN 2204-4345

Grid references in this publication refer to the Geocentric Datum of Australia 1994 (GDA94). Locations mentioned in the text are referenced using Map Grid Australia (MGA) coordinates, Zone 50. All locations are quoted to at least the nearest 100 m.

About this publication

This Report is a thesis written by Jack Lowrey in December 2021, in fulfilment of the requirements for the degree of Doctor of Philosophy at The University of Sydney. The work undertaken was a collaborative research project between The University of Sydney and the Geological Survey of Western Australia (GSWA), funded by Australian Research Council Grant LP130100722 and the Government of Western Australia's Exploration Incentive Scheme. Jack was supervised during his Doctor of Philosophy candidature by Associate Professor Derek Wyman of the University of Sydney and Dr Tim Ivanic and Dr Hugh Smithies of GSWA. The thesis contains pre-copyedited, author-produced versions of two articles previously published in the Journal of Petrology and one article that was later published in Precambrian Research, all of which were peer reviewed by persons appointed by the relevant publishers. The collective works contained in the thesis were additionally examined by Associate Professor Robert Lodge at the University of Wisconsin Eau Claire and Associate Professor Marco Fiorentini at The University of Western Australia. The scientific content of the Report, and the drafting of figures, was the responsibility of the author, however, as the published materials reflect contributions from several co-authors, a detailed statement of authorship attributions is included in the acknowledgement section of the thesis (pages v-vi).

Pre-copyedited, author produced material in Chapter 2 has been previously published in 'Platy Pyroxene: New Insights into Spinifex Texture' by Jack R Lowrey, Tim J Ivanic, Derek A Wyman and Malcolm P Roberts in Journal of Petrology, volume 58, Issue 9 2017 <<https://doi.org/10.1093/petrology/egx069>>. This material is used with permission of Oxford University Press; permission conveyed through Copyright Clearance Center Inc.

Pre-copyedited, author produced material in Chapter 3 has been previously published in 'Archean Boninite-like Rocks of the Northwestern Youanmi Terrane, Yilgarn Craton: Geochemistry and Genesis' by Jack R Lowrey, Derek A Wyman, Tim J Ivanic, R Hugh Smithies, and Roland Maas in Journal of Petrology, volume 60, Issue 11, 2019 <<https://doi.org/10.1093/petrology/egaa002>>. This material is used with permission of Oxford University Press; permission conveyed through Copyright Clearance Center Inc.

Pre-copyedited, author produced material in Chapters 4 and 5 has since been published under an Open Access Creative Commons license in 'Reappraising the petrogenesis of 2820–2738 Ma magmas of the western Youanmi Terrane, Western Australia' by Jack R Lowrey, Derek A Wyman, Tim J Ivanic, R Hugh Smithies, and Roland Maas in Precambrian Research, volume 410, Issue 15, 2024 <<https://doi.org/10.1016/j.precamres.2024.107456>>.

Disclaimer

This product uses information from various sources. The Department of Energy, Mines, Industry Regulation and Safety (DEMIRS) and the State cannot guarantee the accuracy, currency or completeness of the information. Neither the department nor the State of Western Australia nor any employee or agent of the department shall be responsible or liable for any loss, damage or injury arising from the use of or reliance on any information, data or advice (including incomplete, out of date, incorrect, inaccurate or misleading information, data or advice) expressed or implied in, or coming from, this publication or incorporated into it by reference, by any person whatsoever.

Acknowledgement of Country

The Department of Energy, Mines, Industry Regulation and Safety (DEMIRS) respectfully acknowledges Aboriginal peoples as being the traditional custodians of Western Australia. We acknowledge the enduring connection Aboriginal people continue to share with the land, sea and sky through both their ancestral ties and custodianship to Country. We pay our respect to Elders both past and present, and acknowledge the value brought to our department through the collective contribution of Aboriginal and Torres Strait Islander peoples across Western Australia.

Published 2025 by the Geological Survey of Western Australia

This Record is published in digital format (PDF) and is available online at <www.demirs.wa.gov.au/GSWApublications>.



© State of Western Australia (Department of Energy, Mines, Industry Regulation and Safety) 2025

With the exception of the Western Australian Coat of Arms and other logos, and where otherwise noted, these data are provided under a Creative Commons Attribution 4.0 International Licence. (<https://creativecommons.org/licenses/by/4.0/legalcode>).

Further details of geoscience products are available from:

First Floor Counter
Department of Energy, Mines, Industry Regulation and Safety
100 Plain Street EAST PERTH WESTERN AUSTRALIA 6004
Telephone: +61 8 9222 3459 Email: publications@demirs.wa.gov.au
www.demirs.wa.gov.au/GSWApublications

Cover image Platy pyroxene spinifex textured basalt from the Polelle Syncline, immediately east of Meekatharra. Photomicrograph taken using plain-polarized light

**Petrogenesis of c. 2820–2738 Ma magmatism in the northwestern
Youanmi Terrane, Yilgarn Craton.**

Jack Ryland Lowrey

B.Sc (Hons), University of Adelaide

A thesis submitted in fulfilment of the requirements for the degree of Doctor of Philosophy

School of Geosciences

University of Sydney

December 2021

Supervisors: Dr Derek A. Wyman

Dr Tim J. Ivanic

Dr R. Hugh Smithies

Declaration

I declare that I am responsible for all portions of this thesis. To the best of my knowledge, the intellectual content is my own work and all the assistance received in preparing this thesis and sources have been acknowledged. I have not presented any material included in this thesis for the award of a degree at this or any other university. No ethical approval was required during the course of this study.

Jack Ryland Lowrey

22nd December 2020

Abstract

The Yilgarn Craton is one of the largest remaining fragments of Earth's Archean crust and is therefore critical to our understanding of geodynamic processes operating on early Earth.

Several lines of evidence call for a geodynamic reappraisal of *c.* 2820–2738 Ma magmatism in the northwestern Youanmi Terrane (or 'Murchison Domain') of the Yilgarn Craton. (1) The distribution of komatiites reported in previous studies is grossly overstated, and the necessity for anomalously high mantle temperatures of a mantle plume is therefore questionable. (2) The volcanic stratigraphy comprises mafic volcanic rocks with boninite-like compositions and mineralogy, MORB-like tholeiitic basalts, siliceous high-Mg basalts and high-Mg calc-alkaline intermediate–felsic rocks, locally with shoshonitic compositions; these lithologies could collectively be considered diagnostic of subduction setting, if documented in the modern geologic record. (3) Th/Yb–Nb/Yb systematics for volcanic rocks define several distinct trends, parallel to the modern mantle-array, that overlap with trends from modern subduction settings. The trends do not indicate crustal contamination of plume magmas and it is interpreted that LILE±LREE enrichment typical of *c.* 2820–2738 Ma magmatic rocks was a characteristic of their mantle sources, which evolved in composition over time. (4) Coeval mafic–ultramafic sills and granitic rocks that intrude the greenstone sequence contain locally abundant hornblende and indicate widespread hydrous metasomatised mantle sources throughout the northwestern Youanmi Terrane from *c.* 2810 Ma.

Using new geochemical data and existing geochronological data, this study defines a chemostratigraphic framework with 16 units that can be correlated between structurally separated greenstone belts and, on a regional scale, define discontinuous, broadly NNE trends that extend ≤ 350 km long and ≤ 50 km wide. Although the structural history has likely modified the paleogeographic distribution of these chemostratigraphic units, in general, they young and become more enriched in incompatible elements (e.g. Ba, Cs, Th) from east to west. Neodymium isotope and trace element systematics of magmatic rocks implicate increasing degrees of mantle metasomatism from *c.* 2820 to

2738 Ma and variable recycling of a ≥ 3050 –2920 Ma crustal component, which also increases from east to west and upwards through the stratigraphic sequence. The mantle sources of mafic rocks in the Singleton Formation and Meekatharra Formation are interpreted to have been metasomatised by fluids derived from hydrated mafic crust whereas the mantle sources to *c.* 2754 Ma shoshonitic rocks (hornblende-biotite rich lamprophyres and granitic plutons) are interpreted to have mixed with and been metasomatised by ancient sedimentary components.

Based on the temporal and spatial constraints resulting from this study, a preliminary geodynamic framework is proposed: (1) Integration of the available geochemical, geochronological and isotopic data implicates two consecutive magmatic events involving lithospheric thinning and upwelling asthenosphere, as well as depletion and metasomatism of mafic magma sources at *c.* 2820 and *c.* 2793 Ma, which cannot be achieved by sagduction or crustal drip models. Conversely, two subduction events with associated rifting, *c.* 25 Ma apart, may be attributed to subduction step-back or plate arrangements. (2) Following a *c.* 20 Ma hiatus, a second magmatic episode from *c.* 2761–2738 Ma that included crustal-derived transitional TTGs and mantle-derived shoshonitic and sanukitoid (and sanukitoid-like) rocks is interpreted to represent a post-orogenic event related to delamination of arc-crust or slab breakoff.

Acknowledgements

This project would not have been possible without the ongoing support and guidance of my supervisors Derek Wyman, Tim Ivanic and Hugh Smithies. As an external student, Derek and I communicated mainly by email and video calls, but I always felt like my research was a priority for Derek and he was always enthusiastic to assist in any way he could. Without Derek's passion for Archean geodynamics and his work to establish this investigation in the first place, I may not have followed a path into research.

Throughout my candidature I was kindly hosted and supported by the Geological Survey of Western Australia – they provided significant in-kind support, including field support and additional analytical expenses, but most importantly, they provided me with an environment where I could work surrounded by steady-handed, experienced geoscientists who mentored me in how to manage a scientific study. In particular, my supervisors Tim Ivanic and Hugh Smithies were very welcoming, always generous with their time and supported me in any way they could. Their intimate knowledge of my study area and passion for unravelling the geodynamic history of the Yilgarn Craton were critical for the success of this project. Conversations with Yongjun Lu, Paul Morris, Steve Wyche, Ivan Zibra and Sandra Romano were also very helpful and sincerely appreciated. Over the years, I have been blown away by the kindness and support that the GSWA, especially Hugh Smithies, have shown towards me and other research students and it is a huge honour to now be part of GSWA's Archean geoscience team and to be in a position to support future research students in their studies of WA's unique geology.

To my wife Liz and children Hazel, Max, Zoe and Yvette – thank you for your patience! Your love and support has motivated me to persevere with this project and helped me to re-focus during challenging times – especially over the last few months! Completing this thesis has truly been a team effort and I could never have done it without Liz helping me to balance raising our kids, working and studying – even squeezing in extra study on weekends and evenings. I would also like to thank my parents, Karen and Ed, and my brother Dylan for their unwavering support throughout my entire life, and especially for their encouragement over the last few years.

FUNDING

This work was funded by the Australian Research Council Grant LP130100722 as well as by the Geological Survey of Western Australia and Government of Western Australia's Exploration Incentive Scheme.

ORGANISATION OF THE THESIS

The University of Sydney regulations regarding the thesis and examination of higher degrees by research allow students to include published papers that are reformatted as long as it is clear that the text in the thesis is identical to that in the published paper. The PhD candidate of this study is listed as the first author of both published sections presented here for examination, and the authorship listing is ordered by the author's contributions to each section. Dr Derek A. Wyman is the project supervisor and was listed as the corresponding author for each of the published sections in this thesis (Chapters 2 and 3), and as such, gives permission for the inclusion of these published works for examination.

AUTHORSHIP ATTRIBUTION STATEMENT

Chapter 2 of this thesis is published as Lowrey, JR, Ivanic, TJ, Wyman, DA, and Roberts, MP, 2017, 'Platy Pyroxene: New Insights into Spinifex Texture', *Journal of Petrology*, vol. 58, no. 9, pp. 1671–1700. The authorship list is ordered by the contribution made by each author. As principal investigator of the Australian Research Council Grant LP130100722 and primary supervisor to this project, Derek Wyman is listed as the corresponding author. I designed the study, conducted fieldwork, collected samples, analysed the data and wrote the manuscript. My supervisors Derek Wyman and Tim Ivanic assisted me with designing the study and conducting fieldwork and provided comments and minor editing that improved the manuscript. Malcolm Roberts, Jeremy Shaw, Andrew Mehnert and Stefano Caruso of the Centre for Microscopy, Characterisation and Analysis, University of Western Australia assisted with setting up analytical equipment for analysis of mineral compositions and X-ray computed tomography. Commercial laboratories ALS Global, Intertek Genalysis and Bureau Veritas determined whole rock compositions.

Chapter 3 of this thesis is published as Lowrey, JR, Wyman, DA, Ivanic, TJ, Smithies, RH, and Maas, R, 2020, 'Archean Boninite-like Rocks of the Northwestern Youanmi Terrane, Yilgarn Craton: Geochemistry and Genesis', Journal of Petrology. Like Chapter 1, the authorship list is ordered by the contribution made by each author and Derek Wyman is again listed as corresponding author. I designed the study, conducted fieldwork, collected samples, analysed data and wrote the manuscript. My supervisors Derek Wyman and Tim Ivanic assisted me with designing the study and conducting fieldwork and provided comments and minor editing that improved the manuscript. Hugh Smithies provided comments and minor editing that improved the manuscript. Roland Maas determined the neodymium isotopic compositions reported in this chapter and provided comments and minor editing that improved the manuscript relating to isotopic systematics. Commercial laboratories ALS Global, Intertek Genalysis and Bureau Veritas determined whole rock compositions.

The remaining chapters of this thesis have not been published. In each of these sections, I have designed the study, analysed data and written the content. My supervisors Derek Wyman, Tim Ivanic and Hugh Smithies have assisted me with designing the study and conducting fieldwork as well as providing comments and minor editing that improved the content of this thesis.

As supervisor for the candidature upon which this thesis is based, and corresponding author on published and submitted papers, I can confirm that the authorship attribution statements above are correct.

Derek Wyman,

December 20, 2021

During the course of this project, the PhD candidate first authored or co-authored two conference abstracts and four peer reviewed scientific studies. The author placement in the citations below are in order of the contributions made by each author:

Lowrey, J.R. and Ivanic, T.J. (2018). Platy pyroxene spinifex: re-evaluating the distribution of komatiite across Western Australia's Archean cratons, *Australian Journal of Mineralogy* 19 (2) p39–42.

Smithies, R. H., Ivanic, T. J., Lowrey, J. R., Morris, P. A., Barnes, S. J., Wyche, S. and Lu, Y.-J. (2018). Two distinct origins for Archean greenstone belts. *Earth and Planetary Science Letters* 487, 106–116.

Smithies, R.H., Lu, Y-J., Gessner, K., Ivanic, T.J., Wyche, S., Lowrey, J.R., Morris, P.A. and Champion, D.C. (2018). New approaches in understanding the Yilgarn Craton, *in* GSWA 2018 extended abstracts: Geological Survey of Western Australia, Record 2018/2, p. 1–3

Lowrey, J.R. (2020). A subduction origin for 2820–2735 Ma magmatism in the western Youanmi Terrane, Yilgarn Craton *in* GSWA 2020 extended abstracts: advancing the prospectivity of Western Australia: Geological Survey of Western Australia, Record 2020/2, p. 29.

Barnes, S.J., Williams, M., Smithies, R.H., Hanski, E., and Lowrey, J.R. (2021). Trace Element Contents of Mantle-Derived Magmas through time. *Journal of Petrology*, 62, doi: 10.1093/petrology/egab024.

Smithies, R.H., Lowrey, J.R., Sapkota, J., De Paoli, M., Hayman, P., Masurel, Q., Thébaud, N. and Grech L.L. (in review). Geochemical characterisation of the magmatic stratigraphy of the Kalgoorlie and Black Flag Groups - Ora Banda to Kambalda region. Geological Survey of Western Australia, Report.

Table of Contents

DECLARATION.....	I
ABSTRACT.....	II
ACKNOWLEDGEMENTS	IV
Funding.....	v
Organisation of the thesis.....	v
Authorship attribution statement	v
TABLE OF CONTENTS	VIII
CHAPTER 1: INTRODUCTION.....	1
1.1 Regional Geology Background	3
1.2. Sample Selection and Analytical Procedures	14
1.2.1. Whole rock major, minor and trace element concentrations	14
1.2.2. Sm-Nd isotope analytical methodology.....	16
CHAPTER 2: PLATY PYROXENE – NEW INSIGHTS INTO SPINIFEX TEXTURE.....	17
2.1. Introduction	17
2.2. Geological background.....	21
2.3. Sample selection and analytical procedures.....	23
2.3.1. <i>X-RAY computed tomography</i>	25
2.3.2. <i>Electron probe microanalysis and element mapping</i>	26
2.3.3. <i>Whole-rock major and trace element compositions</i>	30
2.4. Field relations of the Bundle Volcanic Member	31
2.4.1. <i>Differentiated flow sequence</i>	32
2.4.2. <i>Platy pyroxene spinifex textured flows</i>	33
2.4.3. <i>Acicular pyroxene habits</i>	47
2.4.4. <i>Dendritic pyroxene habits</i>	50
2.5. X-ray computed tomography.....	52
2.6. Mineral chemistry.....	56
2.6.1. <i>Electron Probe Microanalysis (EPMA)</i>	56
2.7. Whole rock chemistry.....	60
2.8. Spinifex textures	64
2.9. Comparison with other pyroxene spinifex textured sequences	64
2.9.1. <i>Development of platy pyroxene</i>	67
2.10. Petrogenesis.....	70

2.10.1. Melt composition	70
2.10.2. Dry liquidus and mantle potential temperature.....	71
2.10.3. Geodynamic implications	71
2.11. Future work.....	73
2.12. Conclusions.....	73
CHAPTER 3: ARCHEAN BONINITE-LIKE ROCKS OF THE NORTHWEST YOUANMI TERRANE, YILGARN CRATON – GEOCHEMISTRY AND GENESIS.....	75
3.1. Introduction	75
3.2. Geological Background	77
3.2.1. Norie Group.....	80
3.2.2. Polelle Group.....	82
3.3. Sample Selection and Analytical Procedures	83
3.3.1. Whole rock major, minor and trace element concentrations.....	83
3.3.2. Sm-Nd isotope analytical methodology.....	88
3.4. Results.....	90
3.4.1. Petrography and mineral chemistry.....	90
3.4.2. Whole-rock geochemistry and Sm-Nd isotopes	102
3.5. Discussion	114
3.5.1. Comparison of Archean boninite-like rocks with Cenozoic boninites	114
3.5.2. Classification and source characteristics of northwestern Youanmi Terrane mafic-ultramafic volcanic rocks	118
3.5.3. Mode of mantle-crust interaction	123
3.5.4. Significance of textural observations from northwestern Youanmi Terrane mafic-ultramafic ultramafic rocks.	132
3.5.5. Geodynamic Synthesis.....	134
3.6. Conclusions.....	135
CHAPTER 4: CHEMOSTRATIGRAPHY OF THE NORTHWESTERN YOUANMI TERRANE	138
4.1. Sample screening	138
4.2. Stratigraphic correlation by chemical similarities	139
4.3. Age, distribution, petrography and chemical characteristics of stratigraphic units ...	140
4.3.1. Magmatic Episode 1	144
4.3.2. Magmatic Episode 2	172
4.4. Required Stratigraphic Changes.....	196
4.5. Geospatial organisation.....	198
4.6. Conclusions.....	198

CHAPTER 5: PETROGENETIC IMPLICATIONS AND GEODYNAMIC SYNTHESIS..	200
5.1. Spatiotemporal assessment of Sm-Nd data	200
<i>5.1.1. Mantle source components.....</i>	<i>201</i>
5.2. Petrogenetic implications of intermediate to felsic magmatic rocks	207
<i>5.2.1. Tholeiitic and transitional-tholeiitic rocks</i>	<i>207</i>
<i>5.2.2. Sanukitoids and sanukitoid-like rocks.....</i>	<i>211</i>
<i>5.2.3. Transitional TTGs and Shoshonites</i>	<i>212</i>
5.3. Geodynamic setting	215
<i>5.3.1. Non-subduction models for crust-mantle interaction</i>	<i>215</i>
<i>5.3.2. Towards an arc accretion model.....</i>	<i>218</i>
5.4. Further work.....	222
<i>5.4.1. Earlier crust building episodes in the western Yilgarn</i>	<i>222</i>
<i>5.4.2. Subduction zone metamorphism.....</i>	<i>223</i>
CHAPTER 6: CONCLUSIONS	225
REFERENCES.....	229

Chapter 1: Introduction

This research project primarily uses whole rock geochemical and isotopic datasets to better understand the magmatic components and the geodynamic history of the Youanmi Terrane, in the western part of the Yilgarn Craton. The Yilgarn Craton is one of the largest remaining fragments of Earth's Archean crust and is therefore critical to our understanding of geodynamic processes operating on early Earth. It is also one of the most metallogenically endowed regions in the world, hosting world class gold, nickel sulfide and volcanogenic massive sulfide (VMS) base metal deposits, and a better understanding of its geodynamic history has the potential to aid in the discovery of further resources.

The most extensive greenstone geochemical dataset relating this study area, prior to this work, included approximately 1400 samples collected during regional mapping by the Geological Survey of Western Australia and analysed for major elements and a limited range of trace elements (Watkins and Hickman, 1990). These data were used in the construction of stratigraphic frameworks supporting the interpretation that greenstone belts in the west Yilgarn were emplaced within ensialic basins (intracratonic rifts) overlying the voluminous granites that dominate the Craton (Gee, 1979; Gee *et al.*, 1981; Groves and Batt, 1984; Watkins and Hickman, 1990; Hammond and Nisbet, 1992; Swager, 1997). Subsequent studies at various scales yielded crucial geochronological context to the stratigraphic framework (Wang *et al.* 1993, 1995; Wiedenbeck and Watkins, 1993; Schiøtte and Campbell, 1996; Mueller *et al.* 1996; Yeats *et al.* 1996; Hallberg, 2000; Pidgeon and Hallberg, 2000; GSWA, 2021), and significantly improved understanding of the ages and compositions of granitic rocks (Cassidy *et al.*, 2002). Concurrent to many of these studies, arc accretion models for the western Yilgarn were also suggested (Myers 1990, 1995; Nutman *et al.* 1991; Wilde *et al.* 1996) and Champion and Cassidy (2002) concluded that the compositions of high-Mg diorites in the Meekatharra area “suggest subduction and slab melting occurred at or before ca. 2755 Ma” which they considered consistent with the presence of similarly aged High-HFSE granites that reflect at least local extension.

Renewed detailed geological mapping in the late 2000s led to the largest revision of western Yilgarn stratigraphy since the work of Watkins and Hickman (1990), including a series of studies advocating a plume-driven vertical dynamic model for *c.* 2820 to 2710 Ma magmatism in the western Yilgarn (Ivanic *et al.*, 2010; Ivanic *et al.*, 2012; Van Kranendonk *et al.*, 2013), with strong synergies to the Campbell and Hill (1988) model for the eastern Yilgarn. Van Kranendonk *et al.*, (2013), in particular, considered the fact that the northwestern Youanmi Terrane shares a large amount of common history with the rest of the craton, including *c.* 2720 Ma (ultra)mafic volcanism, widespread *c.* 2690–2600 Ma crustally derived granitic rocks, *c.* 2660–2630 Ma ductile shearing and gold mineralization, to be at odds with arc magmatism or terrane accretion models and proposed that one or more significant mantle plume event(s) led to “ribbon-style rifting of a previously coherent craton”. Details of Van Kranendonk *et al.*’s (2013) model included: (1) the rise of deep (>250 km) mantle-derived melts at *c.* 2820 Ma yielded (purported) Al-depleted komatiites at the base of the Murchison Supergroup; (2) shallower mantle-derived basaltic melts were yielded at *c.* 2800 Ma as the plume rose; (3) conductive heating from 2785 to 2760 Ma resulted in widespread partial melting of older crust and produced granitic magmas, and; (4) mingling of crustally-derived felsic magmas and mantle-derived magmas at *c.* 2760–2740 Ma produced high-Mg intermediate to felsic magmas with arc-like trace element characteristics.

The discovery of a boninite–low-Ti basalt association in the Polelle Group (Wyman and Kerrich, 2012), however, raised significant questions about aspects of the plume-related models. This discovery resulted in a coordinated investigation between the University of Sydney and the Geological Survey of Western Australia into the significance of the boninite-like rocks, on a local and regional scale, and whether they could be reconciled of the prevailing tectono-stratigraphic model of Van Kranendonk *et al.*, 2013.

The first main chapter of this study (Chapter 2) was written and published (Lowrey *et al.*, 2017) early in the project. It demonstrated that purported komatiites, which are intercalated with boninite-like rocks and were earlier cited as evidence for a *c.* 2820 Ma mantle plume by Van Kranendonk *et al.* (2013), are actually a new class of high-Mg basalts characterised by a variety of platy pyroxene

spinifex texture. It was shown that these rocks do not necessitate anomalously hot mantle potential temperatures. The second published section of this thesis (Chapter 3; Lowrey *et al.*, 2019) provides additional context to the initial discovery of a boninitic-low-Ti association by Wyman and Kerrich (2012) and concludes that the broader *c.* 2820–2790 Ma stratigraphy in the west Youanmi Terrane, which also includes tholeiitic basalt, high-Mg basalt-andesite-dacite, sanukitoids and hornblende-rich gabbros, is indeed consistent with a primitive arc setting. At around the time that Chapter 3 was written and published, a concurrent PhD project in the Yalgoo–Singleton greenstone belt was abandoned. The study area of the abandoned PhD project included a selection of lithologies, including shoshonitic series rocks, that are critical to understanding the geodynamic history of the Youanmi Terrane, thereby triggering an expansion in the scope of this research project to include all of the *c.* 2820 to 2738 Ma magmatism within the ‘Murchison Domain’ in the west Youanmi Terrane (Fig 1.1). Chapter 4 gives a detailed account of the ages, petrographic, chemical and isotopic characteristics of stratigraphic units from this revised, broader study area and documents a total of 16 chemostratigraphic units, all of which are interpreted to be compatible with widely hydrated and metasomatised mantle sources and subduction-related magmatism. Finally, Chapter 5 investigates several important magmatic suites present in the broader study area, including sanukitoids, shoshonites and transitional tholeiitic rocks that necessitate ancient evolved crustal components to be recycled into the mantle at or prior to *c.* 2760 Ma.

1.1 Regional Geology Background

The Youanmi Terrane is located on the western side of the Archean Yilgarn Craton in Western Australia. It is bounded to the southwest by the South West Terrane, to the northwest by the Narryer Terrane and to the east by the Eastern Goldfields Superterrane (Fig 1.1). The Youanmi Terrane consists of two structural domains; the western Youanmi Terrane (previously Murchison Domain) and the eastern Youanmi Terrane (previously Southern Cross Domain), which are separated by the Youanmi Fault. Recent geological mapping in the northwestern Youanmi Terrane has led to a relatively well-constrained chronostratigraphic and magmatic framework (Van Kranendonk and Ivanic, 2009; Van Kranendonk *et al.*, 2013; Quentin de Gromard *et al.*, 2021) that incorporates

findings from previous chronostratigraphic studies (Watkins and Hickman, 1990; Pidgeon and Wilde, 1990; Mueller *et al.*, 1996; Schiøtte and Campbell, 1996; Wang, 1998; Wang *et al.*, 1993, 1995; Pidgeon and Hallberg, 2000) and more recent, high-precision U-Pb in zircon ages, many of which directly date the volcanic rocks described here (GSWA, 2021, see also Table 1.1).

Supracrustal rocks are divided into the Southern Cross (3050–2920 Ma) and Murchison (2820–2720 Ma) Supergroups, while coeval intrusive rocks are divided into the Thundelarra (3000–2920 Ma) and Annean (2820–2730 Ma) Supersuites (Van Kranendonk *et al.*, 2013; Quentin de Gromard *et al.*, 2021). The Southern Cross Supergroup and Thundelarra Supersuite are distributed along the western boundary of the study area (e.g., Pidgeon and Wilde, 1990; Yeats *et al.*, 1996; Wang, 1998; Pidgeon and Hallberg, 2000; Van Kranendonk *et al.*, 2013), and include the Gossan Hill Formation of locally hydrothermally altered *c.* 2960–2930 Ma intermediate to felsic volcanic rocks that hosts world class Cu-Zn-Au rich massive sulfide deposits of Golden Grove mining district (Sharpe and Gemmell, 2002). Slightly older, but of similar lithological range, is the Madoonga Formation in the Weld Range (Guilliamse, 2014). The chemistry and petrogenetic evolution of this earlier magmatic period remain poorly understood but are the subject of ongoing work by the Geological Survey of Western Australia.

Unconformably overlying the Southern Cross Supergroup is the Murchison Supergroup, which includes the second, long-lived period of magmatism in the Youanmi Terrane, erupted after a 100 Ma magmatic hiatus. The Murchison Supergroup is mainly preserved in greenstone belts between Meekatharra to Mount Magnet, and Yalgoo to Mount Singleton (Fig. 1.1). Major peaks in zircon age populations (Fig 1.2) reflect episodes of felsic magmatism, and constrain the existing stratigraphic framework (Van Kranendonk *et al.*, 2013). These felsic episodes include: (1) the *c.* 2818 to 2799 Ma Yaloginda Formation volcanic rocks and coeval Mount Kenneth Suite intrusions; (2) the *c.* 2793 to 2782 Ma Meekatharra Formation and coeval Nannine Tonalite; and (3) the 2761 to *c.* 2738 Ma Greensleeves Formation volcanic rocks and coeval Eelya (*c.* 2760 Ma), Rothsay (*c.* 2763 to 2742 Ma) and Cullculli (2761–2746 Ma, excluding the afore mentioned Nannine Tonalite) Suites (Fig 1.3). Although they cannot be directly dated precisely, the ages and stratigraphic positions of mafic

volcanic rocks and coeval intrusive rocks are constrained by association with the felsic units (Figs 1.2, 1.3).

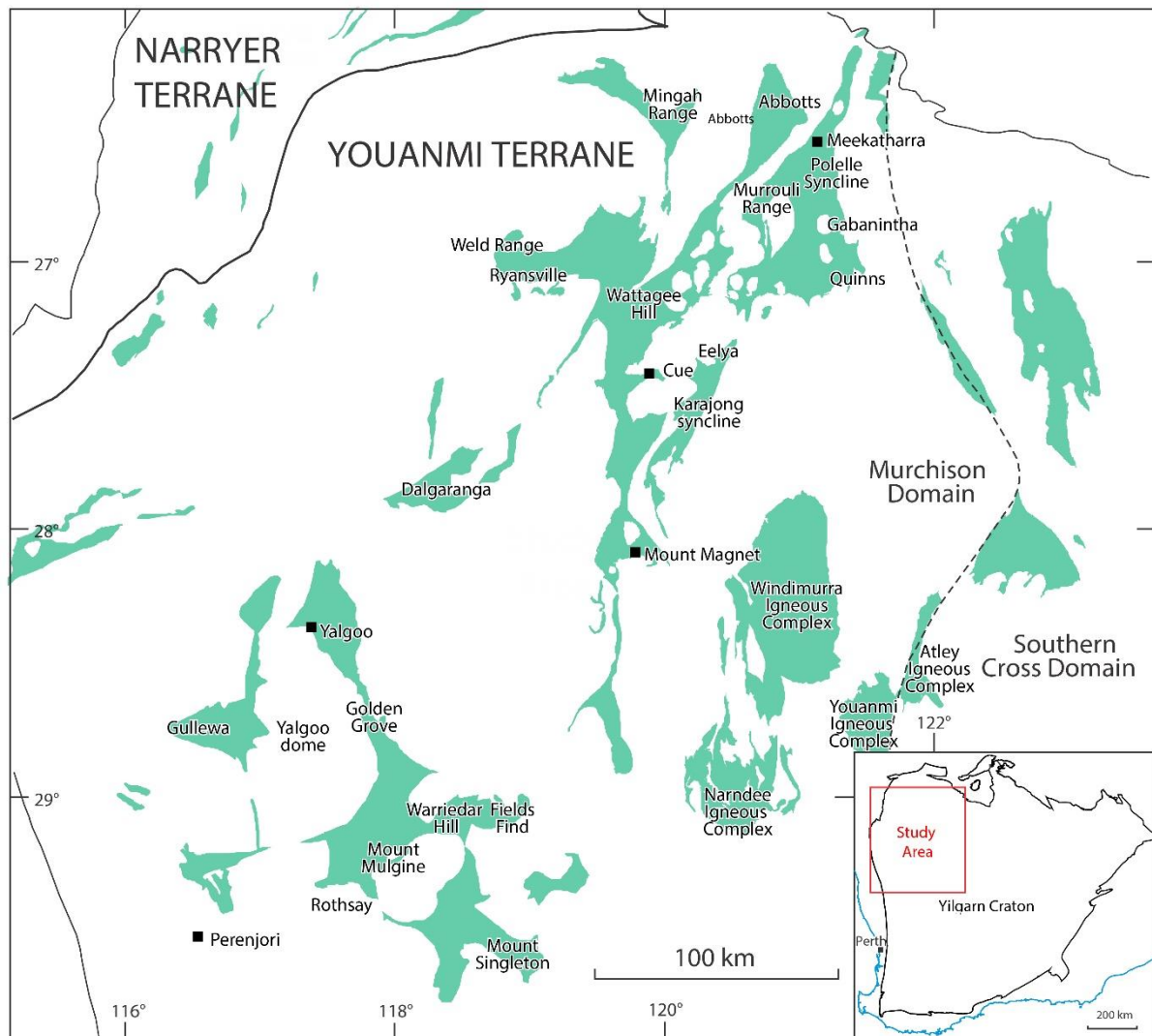


Figure 1.1. Map of this study area with greenstones shaded in green (inset: location of the study area relative to the rest of the Study area and Perth).

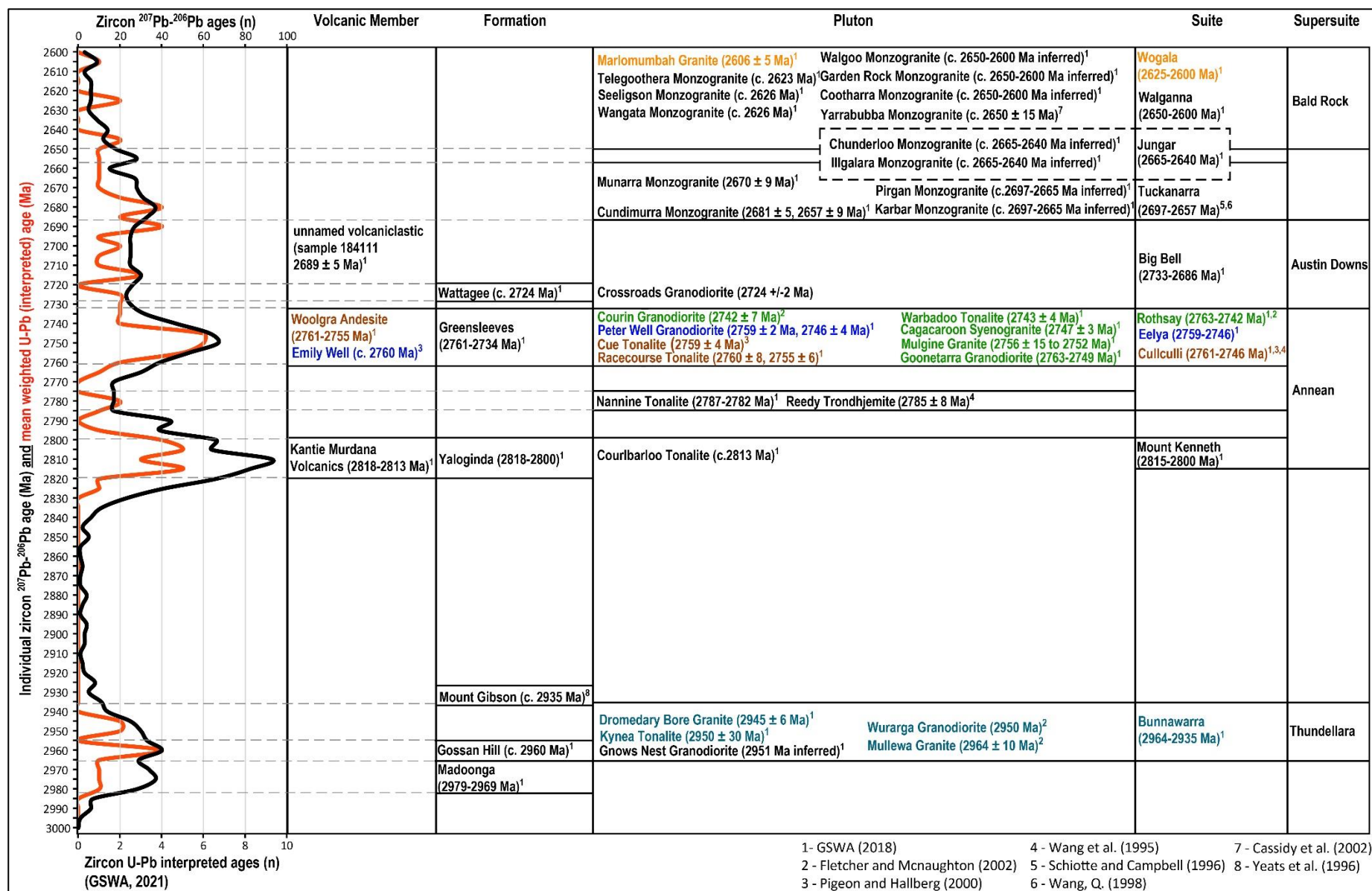


Figure 1.2. SHRIMP zircon ages for Youanmi Terrane samples correlated with major volcanic and plutonic stratigraphic units. Pb-Pb axis shows individual zircon Pb-Pb ages for crystals interpreted to be magmatic, xenocrystic or detrital. U-Pb axis shows weighted mean ages for populations of magmatic zircons only (interpreted crystallization age for sample). Data from GSWA geochronological compilation (GSWA, 2021).

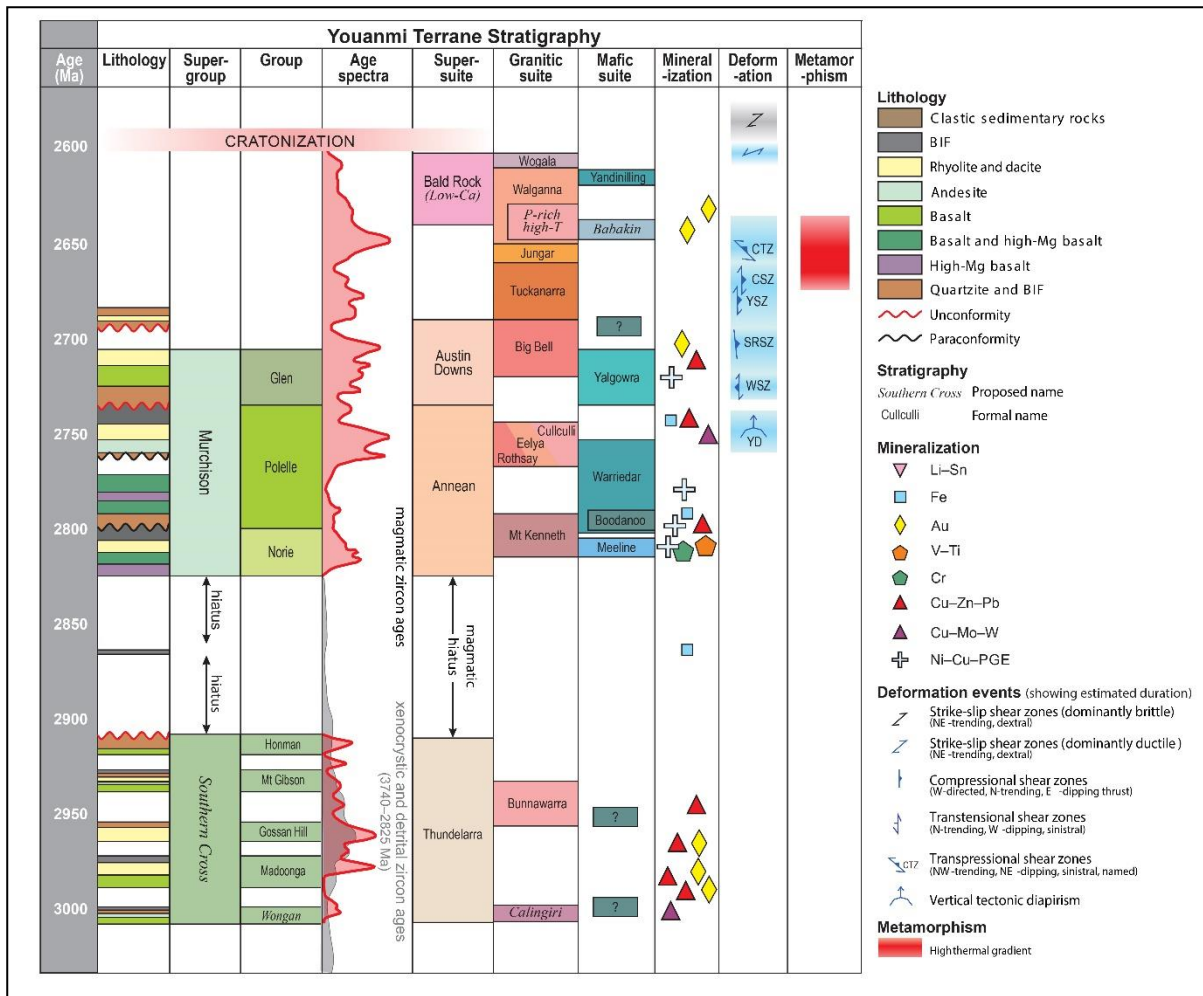


Figure 1.3. Tectonostratigraphic framework for the Youanmi Terrane (modified after De Gromard *et al.*, 2021)

Table 1.1. compilation of publically available geochronology										
Sample ID	Lithology	Latitude	Longitude	Locality	Age (95% conf)	Age type	Inherited/ detrital age component	Chemical Unit	Stratigraphic unit	Reference
194751	Metadolerite	-28.75	118.68	Youanmi Igneous Complex; c. 115km SE of Mount Magnet	2825 ± 7	igneous crystallization (max)		Unclassified	Youanmi Igneous Complex	GSWA, 2021
96-631	Gabbro	-26.93	118.63	Meekatharra-Karajong belt; c. 40km SW of Meekatharra	2821 ± 5	igneous crystallization		Unclassified	Lady Alma Igneous Complex; Meeline Suite	Wang, 1998
7-22.1	Pyroxene-gabbro	-28.63	118.80	Youanmi Igneous Complex	2819 ± 10	igneous crystallization		Unclassified	Youanmi Igneous Complex	Gill, 2011
193979	Meta-andesite	-28.98	118.08	Narndee Igneous Complex; c. 115km SE of Mount Magnet	2818 ± 3	igneous crystallization		Unclassified	Yaloginda Formation	GSWA, 2021
185998	Quartz-chlorite-muscovite schist	-27.14	118.51	Meekatharra-Karajong belt; c. 60km S of Meekatharra	2817 ± 3	max. depositional age		Unit 1	Yaloginda Formation	GSWA, 2021
198296	Sandstone	-29.11	117.09	Yalgoo-Singleton belt; c. 110km SE of Yalgoo	2817 ± 3	max. depositional age		Unclassified	Mougooderra Formation	GSWA, 2021
155522	Monzogranitic gneiss	-28.46	117.72	Cue-Mount Magnet belt; c. 45km S of Mount Magnet	2816 ± 6	igneous crystallization		Unclassified	Mount Kenneth Suite	GSWA, 2021
93-976	Andesite	-26.90	118.55	Meekatharra-Karajong belt; c. 35km SW of Meekatharra	2815 ± 7	igneous crystallization		Unit 4	Yaloginda Formation	Wang, 1998
169067	Quartz-chlorite schist	-28.72	118.79	Youanmi Igneous Complex; c. 115km SE of Mount Magnet	2814 ± 14	igneous crystallization	c. 2853, 2840 Ma	Unit 1	Yaloginda Formation	GSWA, 2021
183953	Felsic meta-volcaniclastic rock	-26.53	118.54	Meekatharra-Karajong belt; c. 8km NE of Meekatharra	2814 ± 2	max. depositional age		Unit 4	Yaloginda Formation	GSWA, 2021
169003	Rhyolite	-28.16	118.44	Windimurra Igneous Complex; 50km East of Mount Magnet	2813 ± 3	igneous crystallization		Unit 1	Yaloginda Formation	GSWA, 2021
194747	Metagabbro	-28.29	118.55	Windimurra Igneous Complex; 50km East of Mount Magnet	2813 ± 3	igneous crystallization		Unclassified	Meeline Suite	GSWA, 2021
198209	Quartz-feldspar schist	-28.42	118.23	Windimurra Igneous Complex; 50km East of Mount Magnet	2813 ± 5	igneous crystallization		Unit 1	Yaloginda Formation	GSWA, 2021
198298	Metadacite	-28.32	116.83	Yalgoo-Singleton belt; c. 15km SE of Yalgoo	2813 ± 3	igneous crystallization		Unit 4	Yaloginda Formation	GSWA, 2021
9896 8104	Hornblende tonalite	-28.57	118.89	Atley Igneous Complex; c. 115km SE of Mount Magnet	2813 ± 5	igneous crystallization		Unit 4	Courbarloo Tonalite; Mount Kenneth Suite	Fletcher and McNaughton, 2002
96-128	Felsic volcaniclastic rock	-26.64	118.52	Meekatharra-Karajong belt; c. 5km SW of Meekatharra	2812 ± 7	igneous crystallization/ max. depositional age		Unit 4	Yaloginda Formation	Wang, 1998
193967	Hornblende-biotite granodiorite	-28.97	118.25	Narndee Igneous Complex; c. 115km SE of Mount Magnet	2811 ± 7	igneous crystallization		Unit 4	Mount Kenneth Suite	GSWA, 2021
205750	Felsic metavolcanic rock	-27.51	118.14	Meekatharra-Karajong belt; c. 25km SE of Cue	2810 ± 4	igneous crystallization		Unit 4	Yaloginda Formation	GSWA, 2021
93-975	Andesite	-26.90	118.55	Meekatharra-Karajong belt; c. 35km SW of Meekatharra	2810 ± 5	igneous crystallization		Unit 4	Yaloginda Formation	Wang, 1998
198210	Meta-monzogranite	-28.42	118.23	Windimurra Igneous Complex; 50km East of Mount Magnet	2809 ± 2	igneous crystallization		Unit 4	Mount Kenneth Suite	GSWA, 2021

Table 1.1. continued										
178142	Metarhyolite	-27.03	118.38	Meekatharra-Karajong belt; c. 50km S of Meekatharra	2806 ± 4	igneous crystallization		Unit 4	Yaloginda Formation	GSWA, 2021
185995	Metagranite	-29.05	118.15	Narndee Igneous Complex; c. 115km SE of Mount Magnet	2806 ± 3	igneous crystallization	2828 ± 6	Unit 4	Mount Kenneth Suite	GSWA, 2021
207580	Metavolcanic rock	-26.67	118.52	Meekatharra-Karajong belt; c. 9km SE of Meekatharra	2806 ± 6	igneous crystallization		Unit 4	Yaloginda Formation	GSWA, 2021
194757	Metadolerite	-26.98	117.59	Mingah-Ryansville belt; c. 60km NW of Cue	2805 ± 19	igneous crystallization (max)		Unclassified	Gnanagooragoo Igneous Complex	GSWA, 2021
198228	Volcaniclastic metasandstone	-29.45	117.31	Yalgoo-Singleton belt; c. 150km SE of Yalgoo	2805 ± 5	max. depositional age (detrital zircons)	single c. 2832 Ma zircon	Unclassified	Yaloginda Formation	GSWA, 2021
185996	Metagranite	-29.05	118.15	Narndee Igneous Complex; c. 115km SE of Mount Magnet	2803 ± 4	igneous crystallization		Unit 4	Mount Kenneth Suite	GSWA, 2021
194749	Metagabbroonorite	-28.20	118.30	Windimurra Igneous Complex; 50km East of Mount Magnet	2802 ± 19	igneous crystallization		Unclassified	Windimurra Igneous Complex; Meeline Suite	GSWA, 2021
198294	Meta-quartz diorite	-29.10	117.00	Yalgoo-Singleton belt; c. 105km SE of Yalgoo	2801 ± 6	igneous crystallization		Unclassified	Warriedar Suite	GSWA, 2021
198295	Metadacite	-29.10	117.10	Yalgoo-Singleton belt; c. 110km SE of Yalgoo	2801 ± 5	igneous crystallization (max)	c. 2801, 2935-2957 and 3259 Ma pops. interp. as xenocrystic by authors	Unclassified	Mougooderra Formation	GSWA, 2021
25600	Aplite	-28.63	118.80	Youanmi Igneous Complex	2800 ± 11	igneous crystallization		Unclassified	Mount Kenneth Suite?	Gill, 2011
183921	Felsic volcaniclastic rock	-26.82	118.51	Meekatharra-Karajong belt; c. 25 km S of Meekatharra	2799 ± 2	max. depositional age		Unclassified	Yaloginda Formation?	GSWA, 2021
191056	Gabbroonorite	-29.02	118.16	Narndee Igneous Complex; c. 115km SE of Mount Magnet	2799 ± 7	igneous crystallization		Unit 5	Boodanoo Suite	GSWA, 2021
93-1009	Chert	-28.05	117.83	Mount Magnet	2794 ± 14	max. depositional age		Unclassified	Yaloginda Formation?	Wang, 1998
198299	Metatonalite	-28.29	116.82	Yalgoo-Singleton belt; c. 15km SE of Yalgoo	2793 ± 4	igneous crystallization		Unclassified	Olive Queen Gabbro; Warriedar Suite	GSWA, 2021
207579	Mudstone	-26.78	118.54	Meekatharra-Karajong belt; c. 20km SW of Meekatharra	2793 ± 5	igneous crystallization		Unclassified	Meekatharra Formation	GSWA, 2021
242683	Rhyolite	-28.65	116.39	Gullewa belt; c. 65km SW of Yalgoo	2793 ± 8	igneous crystallization	2947 ± 5	Unit 7	Meekatharra Formation	GSWA, 2021
207686	Volcaniclastic metasandstone	-28.22	116.71	Yalgoo-Singleton belt; c. 5km SW of Yalgoo	2793 ± 8	max. depositional age	c. 3094, 3025, 3005, 2975, 2950 and 2882 Ma detrital pops.	Unclassified	Meekatharra Formation	GSWA, 2021
155568	Tuffaceous metasilstone	-26.98	117.59	Mingah-Ryansville belt; c. 60km NW of Cue	2792 ± 9	max. depositional age	c. 2882, and 2793 Ma	Unclassified	Gnanagooragoo Igneous Complex	GSWA, 2021
96-125	Metadolerite	-26.81	118.35	Meekatharra-Karajong belt; c. 25km SW of Meekatharra	2792 ± 5	igneous crystallization		Unclassified	Warriedar or Boodanoo Suite?	Wang, 1998
93-974	Shale	-26.73	118.57	Meekatharra-Karajong belt; c. 15km SE of Meekatharra	2788 ± 30	max. depositional age		Unclassified	Yaloginda Formation?	Wang, 1998
178102	Biotite-hornblende tonalite	-26.75	118.30	Meekatharra-Karajong belt; c. 30km SW of Meekatharra	2787 ± 3	igneous crystallization		Unit 8	Nannine Tonalite; Annean Supersuite	GSWA, 2021

Table 1.1. continued										
178104	Biotite granodiorite	-26.79	118.29	Meekatharra-Karajong belt; c. 30km SW of Meekatharra	2782 ± 7	igneous crystallization		Unit 8	Nannine Tonalite; Annean Supersuite	GSWA, 2021
207576	Metavolcanic rock	-26.81	118.29	Meekatharra-Karajong belt; c. 30km SW of Meekatharra	2782 ± 5	igneous crystallization		Unit 8	Polelle Group	GSWA, 2021
93-977	Andesite	-26.90	118.55	Meekatharra-Karajong belt; c. 35km SW of Meekatharra	2780 ± 11	igneous crystallization		Unit 4	Yaloginda Formation. Age conflicts with other ages for this locality	Wang, 1998
155875	Biotite meta-granodiorite	-28.96	116.84	Yalgoo Dome; c. 85km S of Yalgoo	2766 ± 4	igneous crystallization	Single 2787 ± 6 Ma zircon	Unit 11	Goonetarra Granodiorite; Rothsay Suite	GSWA, 2021
214101	Monzogranite gneiss	-28.47	116.75	Yalgoo Dome; c. 30km S of Yalgoo	2763 ± 6	igneous crystallization		Unit 11	Goonetarra Granodiorite; Rothsay Suite	GSWA, 2021
185957	Intermediate metavolcanic rock	-26.77	118.46	Meekatharra-Karajong belt; c. 20km S of Meekatharra	2761 ± 6	igneous crystallization		Unit 10	Greensleeves Formation	GSWA, 2021
W372 / W373	Felsic tuff	-27.34	117.85	Abbotts-Cuddingwarra belt; c. 10km NW of Cue	2761 ± 1	igneous crystallization		Unit 9	Greensleeves Formation	Pidgeon and Hallberg, 2000
13HODD 004-162	Rhyodacite	-27.36	118.22	Meekatharra-Karajong belt; c. 30km NE of Cue	2760 ± 1	igneous crystallization		Unit 9	Eelya Suite	Hayman <i>et al.</i> , 2015
185933	Biotite granodiorite	-27.35	118.16	Meekatharra-Karajong belt; c. 30km NE of Cue	2759 ± 2	igneous crystallization		Unit 9	Eelya Suite	GSWA, 2021
96-129	Granite	-26.91	118.62	Meekatharra-Karajong belt; c. 40km SW of Meekatharra	2759 ± 7	igneous crystallization		Unclassified	Annean Supersuite - affinity unknown	Wang, 1998
W378	Tonalite	-27.40	117.92	Cue	2759 ± 4	igneous crystallization		Unit 9	Cue Tonalite; Eelya Suite?	Pidgeon and Hallberg, 2000
211101	Volcaniclastic mudstone	-28.31	116.79	Yalgoo-Singleton belt; c. 15km SE of Yalgoo	2758 ± 4	max. depositional age	c. 2950, 2929, and 2762 Ma detrital pops.	Unclassified	Mougooderra Formation	GSWA, 2021
185921	K-feldspar-quartz monzogranite	-27.15	117.59	Mingah-Ryansville belt; c. 40km NW of Cue	2757 ± 4	igneous crystallization	single zircon 2960 ± 12 Ma	Unit 11	Rothsay Suite	GSWA, 2021
205751	Felsic meta-volcanic rock	-27.44	118.10	Meekatharra-Karajong belt; c. 20km E of Cue	2757 ± 6	igneous crystallization		Unit 9	Greensleeves Formation	GSWA, 2021
9996 4016C	Biotite syenogranite	-29.19	116.98	Mount Mulgine	2756 ± 20	igneous crystallization		Unit 11	Mulgine Granite; Rothsay Suite	Fletcher and McNaughton, 2002
178105	Andesite	-26.88	118.49	Meekatharra-Karajong belt; c. 30km S of Meekatharra	2755 ± 5	igneous crystallization		Unit 10	Greensleeves Formation	GSWA, 2021
185958	Microgranite	-26.77	118.46	Meekatharra-Karajong belt; c. 20km S of Meekatharra	2755 ± 6	igneous crystallization		Unit 10	Cullculi Suite	GSWA, 2021
185959	Intermediate metavolcanic rock	-26.77	118.46	Meekatharra-Karajong belt; c. 20km S of Meekatharra	2755 ± 5	igneous crystallization		Unit 10	Greensleeves Formation	GSWA, 2021
242695	Hornblende diorite	-28.65	116.35	Gullewa belt; c. 65km SW of Yalgoo	2754 ± 4	igneous crystallization		Unit 12	Cagacaroon Syenogranite; Rothsay Suite	GSWA, 2021
155858	Monzogranite	-28.79	116.81	Yalgoo Dome; c. 70km S of Yalgoo	2752 ± 13	igneous crystallization		Unit 11	Goonetarra Granodiorite; Rothsay Suite	GSWA, 2021
207628	Muscovite-quartz schist	-29.18	116.98	Yalgoo-Singleton belt; c. 115km SE of Yalgoo	2752 ± 8	igneous crystallization	c. 2965–2800 Ma ages from 5 zircons	Unit 11	Mulgine Granite; Rothsay Suite	GSWA, 2021

Table 1.1. continued										
93-989	Meta-monzogranite	-27.30	118.17	Meekatharra-Karajong belt; c. 30km NE of Cue	2752 ± 4	igneous crystallization		Unit 14	Eelya Suite	Wang, 1998
96-120	Felsic tuff	-26.98	117.59	Mingah-Ryansville belt; c. 60km NW of Cue	2752 ± 9	igneous crystallization/ max. dep. age	2927 ± 9 Ma, 3263 ± 9 Ma	Unclassified	Gnanagooragoo Igneous Complex	Wang, 1998
92-283	Felsic porphyry	-28.05	117.82	Mount Magnet	2752 ± 5	igneous crystallization	2931 ± 9 Ma	Unclassified	Annean Supersuite - affinity unknown	Schiøtte and Campbell, 1996
96-119	Cherty felsic volcanic rock	-26.81	118.32	Meekatharra-Karajong belt; c. 30km SW of Meekatharra	2750 ± 5	igneous crystallization		Unclassified	Greensleeves Formation	Wang, 1998
96-623	Felsic tuff	-26.54	118.37	Abbotts-Cuddingwarra belt; c. 13km NW of Meekatharra	2750 ± 9	max. depositional /igneous crystallization		Unit 15	Greensleeves Formation	Wang, 1998
155822	Monzogranite gneiss	-28.61	116.85	Yalgoo Dome; c. 50km S of Yalgoo	2749 ± 4	igneous crystallization	single 2920 ± 8 Ma zircon	Unit 11	Goonetarra Granodiorite; Rothsay Suite	GSWA, 2021
93-990	Meta-monzogranite	-27.32	118.17	Meekatharra-Karajong belt; c. 30km NE of Cue	2749 ± 6	igneous crystallization		Unit 14	Eelya Suite	Wang, 1998
W308	Felsic tuff	-27.75	117.20	Dalgaranga belt; c. 70km SW of Cue	2749 ± 2	igneous crystallization		Unit 14	Greensleeves Formation	Pidgeon and Hallberg, 2000
178196	Biotite granodiorite	-27.12	117.59	Mingah-Ryansville belt; c. 40km NW of Cue	2748 ± 3	igneous crystallization	Two zircons with c. 2925 and c. 2908 Ma ages	Unit 11	Rothsay Suite	GSWA, 2021
185920	Biotite-hornblende meta-monzogranite	-27.07	117.73	Mingah-Ryansville belt; c. 40km NW of Cue	2748 ± 5	igneous crystallization	Single Zircon 2950 ± 6 Ma	Unit 12	Rothsay Suite	GSWA, 2021
205717	Felsic schist	-28.07	117.75	Cue-Mount Magnet belt; c. 10km W of Mount Magnet	2748 ± 11	igneous crystallization		Unclassified	Wilgie Mia Formation	GSWA, 2021
224210	Metagranitic rock	-29.17	116.96	Yalgoo-Singleton belt; c. 115km SE of Yalgoo	2748 ± 4	igneous crystallization	2950–2778 Ma ages from 7 zircons	Unit 11	Mulgine Granite; Rothsay Suite	GSWA, 2021
155572	Volcaniclastic metasandstone	-27.03	117.47	Mingah-Ryansville belt; c. 60km NW of Cue	2747 ± 4	max. depositional age		Unclassified	Wilgie Mia Formation	GSWA, 2021
183338	Metadacite	-26.51	117.99	Mingah-Ryansville belt; c. 50km NW of Meekatharra	2747 ± 5	igneous crystallization	Three zircons; 3028 ± 12 Ma	Unit 15	Greensleeves Formation	GSWA, 2021
9996 9142	Biotite-hornblende quartz monzonite	-28.65	116.35	Gullewa belt; c. 65km SW of Yalgoo	2747 ± 3	igneous crystallization		Unit 12	Cagaroon Syenogranite; Rothsay Suite	Fletcher and McNaughton, 2002
93-991	Granodiorite	-27.35	118.17	Meekatharra-Karajong belt; c. 30km NE of Cue	2747 ± 6	igneous crystallization		Unit 14	Eelya Suite	Wang, 1998
155874	Biotite-muscovite meta-monzogranite	-28.93	116.89	Yalgoo Dome; c. 85km S of Yalgoo	2746 ± 4	igneous crystallization	two zircon cores c. 2956 2844 Ma	Unit 11	Goonetarra Granodiorite; Rothsay Suite	GSWA, 2021
178141	Quartz diorite	-27.09	118.30	Meekatharra-Karajong belt; c. 60km SW of Meekatharra	2746 ± 5	igneous crystallization		Unit 10	Cullculli Suite	GSWA, 2021
185932	Metarhyolite	-27.34	118.18	Meekatharra-Karajong belt; c. 30km NE of Cue	2746 ± 4	igneous crystallization	c. 2844 Ma	Unit 14	Greensleeves Formation	GSWA, 2021
185939	Felsic metavolcanic rock	-26.31	117.82	Mingah-Ryansville belt; c. 75km NW of Meekatharra	2746 ± 3	igneous crystallization	Single 3423 ± 18 Ma zircon	Unit 14	Greensleeves Formation	GSWA, 2021

Table 1.1. continued										
W297 and W298	Felsic tuff	-27.70	117.25	Dalgaranga belt; c. 70km SW of Cue	2746 ± 8	igneous crystallization	Eight zircons with 3034 ± 8 Ma age, single c. 3940 Ma zircon	Unit 14	Greensleeves Formation	Pidgeon and Hallberg, 2000
W296	Felsic tuff	-27.72	117.23	Dalgaranga belt; 70km SW of Cue	2745 ± 4	igneous crystallization		Unit 14	Greensleeves Formation	Pidgeon and Hallberg, 2000
178106	Basaltic andesite	-26.39	118.38	Abbotts-Cuddingwarra belt; c. 25km NW of Meekatharra	2744 ± 4	igneous crystallization	c. 2766, 2761	Unit 15	Greensleeves Formation	GSWA, 2021
178194	Granite gneiss	-27.23	117.67	Mingah-Ryansville belt; c. 30km NW of Cue	2744 ± 3	igneous crystallization	Single zircon 2958 ± 5 Ma	Unit 11	Rothsay Suite	GSWA, 2021
93-970	Felsic tuff	-26.53	118.37	Abbotts-Cuddingwarra belt; c. 13km NW of Meekatharra	2744 ± 8	igneous crystallization	3499 ± 32 Ma	Unit 15	Greensleeves Formation	Wang, 1998
9996 4100	Biotite monzogranite	-28.15	116.74	Yalgoo-Singleton belt; c. 4km N of Yalgoo	2743 ± 4	igneous crystallization		Unit 11	Warbadoo Tonalite; Rothsay Suite	Fletcher and McNaughton, 2002
W310	Felsic tuff	-27.80	117.16	Dalgaranga belt; c. 70km SW of Cue	2743 ± 4	igneous crystallization		Unit 14	Greensleeves Formation	Pidgeon and Hallberg, 2000
9996 9164A	Biotite monzogranite	-28.21	116.43	Gullewa belt; c. 30km W of Yalgoo	2742 ± 7	igneous crystallization		Unit 11	Courin Granodiorite; Rothsay Suite	Fletcher and McNaughton, 2002
93-986	Felsic tuff	-27.22	117.87	Abbotts-Cuddingwarra belt; c. 25km NW of Cue	2742 ± 7	max depositional age/igneous crystallization		Unit 15	Greensleeves Formation	Wang, 1998
93-987	Felsic tuff	-27.22	117.87	Abbotts-Cuddingwarra belt; c. 25km NW of Cue	2742 ± 4	max. depositional age		Unit 15	Greensleeves Formation	Wang, 1998
185926	Porphyritic microgranite	-26.84	117.89	Mingah-Ryansville belt; c. 60km NW of Cue	2741 ± 7	igneous crystallization		Unit 11	Rothsay Suite	GSWA, 2021
185925	Andalusite-rich quartzite	-26.94	117.90	Mingah-Ryansville belt c. 70km SW of Meekatharra	2740 ± 4	max. depositional age		Unclassified	Ryansville Formation	GSWA, 2021
185138	Felsic volcanic rock	-26.38	118.36	Abbotts-Cuddingwarra belt; c. 25km NW of Meekatharra	2739 ± 10	igneous crystallization		Unit 15	Greensleeves Formation	GSWA, 2021
92-269	Rhyolite	-28.05	117.83	Mount Magnet	2739 ± 11	igneous crystallization		Unclassified	Wattagee Formation? (high uncertainty)	Schiøtte and Campbell, 1996
96-139	Felsic tuff	-26.54	118.37	Abbotts-Cuddingwarra belt; c. 13km NW of Meekatharra	2738 ± 19	igneous crystallization		Unit 15	Greensleeves Formation	Wang, 1998
96-632	Felsic volcanic rock	-27.22	117.87	Abbotts-Cuddingwarra belt; c. 25km NW of Cue	2738 ± 4	igneous crystallization		Unit 15	Greensleeves Formation	Wang, 1998
185922	Leucogabbro	-27.35	117.83	Abbotts-Cuddingwarra belt; c. 10km NW of Cue	2735 ± 5	igneous crystallization		Unclassified	Yalgowra Suite	GSWA, 2021
97-124	Porphyritic microgranite	-28.01	117.79	Mount Magnet	2735 ± 8	igneous crystallization		Unclassified	Big Bell Suite or Annean Supersuite? High uncertainty	Wang, 1998
93-971	Felsic tuff	-26.53	118.37	Abbotts-Cuddingwarra belt; c. 13km NW of Meekatharra	2734 ± 5	igneous crystallization		Unit 15?	Greensleeves Formation. Age is an outlier from rest of the unit.	Wang, 1998
185928	Biotite-hornblende metatonalite	-26.72	117.97	Mingah-Ryansville belt; c. 55km SW of Meekatharra	2733 ± 6	igneous crystallization		Unclassified	Big Bell Suite	GSWA, 2021

Table 1.1. continued

96-641	Granite/diorite	-27.77	117.34	Dalgaranga belt; c. 70km SW of Cue	2733 ± 7	igneous crystallization		Unclassified	Keygo monzogranite; age much younger than Fletcher and McNaughton in same body	Wang, 1998
155507	Monzogranite	-27.87	117.83	Cue-Mount Magnet belt; c. 20km N of Mount Magnet	2732 ± 4	igneous crystallization		Unclassified	Big Bell Suite	GSWA, 2021
155511	Granodiorite gneiss	-27.53	118.15	Meekatharra-Karajong belt; c. 25km SE of Cue	2728 ± 9	igneous crystallization	c. 2916–2751 Ma	Unclassified	Big Bell Suite	GSWA, 2021
197420	Metasandstone	-27.02	117.52	Mingah-Ryansville belt; c. 60km NW of Cue	2728 ± 11	max. depositional age		Unclassified	Ryansville Formation	GSWA, 2021
94-117	Rhyolite	-28.05	117.83	Mount Magnet	2727 ± 6	igneous crystallization		Unclassified	Wattagee Formation? (large uncertainty)	Schiøtte and Campbell, 1996
183975	Quartz-sericite schist (metarhyolite)	-27.15	117.86	Abbotts-Cuddingwarra belt; c. 30km NW of Cue	2725 ± 4	igneous crystallization		Unclassified	Wattagee Formation? or intrusive?	GSWA, 2021
185923	Biotite-hornblende tonalite gneiss	-27.41	117.70	Mingah-Ryansville belt; c. 20km W of Cue	2724 ± 2	igneous crystallization		Unclassified	Big Bell Suite	GSWA, 2021
199699	Biotite monzogranite	-28.04	117.75	Cue-Mount Magnet belt; c. 10km W of Mount Magnet	2720 ± 6	igneous crystallization		Unclassified	Big Bell Suite	GSWA, 2021

1.2. SAMPLE SELECTION AND ANALYTICAL PROCEDURES

The following section describing sample selection and analytical methodology follows from Lowrey *et al.* (2019). Most of the samples in this data compilation were collected by, and analysed for, the Geological Survey of Western Australia or the University of Sydney and are supplemented by analyses of granitic rocks collected and reported by Geoscience Australia (Champion and Cassidy, 2002; see Electronic Appendix 1.1). The samples selected for this study represent those with the least weathering, alteration, veining or metamorphic- or deformation-related recrystallization. Metamorphic grade varies from sub-greenschist to greenschist facies.

1.2.1. Whole rock major, minor and trace element concentrations

Whole rock geochemical data were acquired at several commercial laboratories in Western Australia: Australian Laboratory Services (ALS); Bureau Veritas (BV) Minerals Pty Ltd and Intertek Genalysis Laboratory Services Pty Ltd (Genalysis). All newly collected samples were crushed in a jaw crusher and milled in a low-Cr steel mill (>85% passing through 75 µm sieve). Reanalyses of GSWA powders included some samples that were milled in tungsten carbide mills, in these instances W and Co are not reported.

For samples analysed at ALS, major and minor elements (Si, Ti, Al, Cr, Fe, Mn, Mg, Ca, Sr, Ba, Na, K, and P) were determined by X-ray fluorescence spectrometer (XRF; ALS method ME-XRF26). For this purpose, fused discs were prepared by fusing a 1:10 sample-flux mix (0.66g of sample powder, 5.9g LiBO₂, LiB₄O₇ and LiNO₃ flux) at 1025°C. Loss on ignition (LOI) was determined by thermogravimetric analysis (their ME-GRA05). Lithophile trace element concentrations (Cr, Sn, W, V, Ga, Cs, Rb, Ba, Sr, Th, U, Nb, Ta, Zr, Hf, Y, La, Ce, Pr, Nd, Sm, Eu, Gd, Tb, Dy, Ho, Er, Tm, Yb and Lu) were determined by solution-mode ICP-MS, after digestion of the sample powder with lithium borate flux followed by dissolution of the fluxed material in acid (ALS method ME-MS81). Concentrations for base metals (Ag, Cd, Co, Cu, Li, Mo, Ni, Pb, Sc and Zn) were determined by ICP-AES after digestion of sample powder with 4-acid procedure (HClO₄, HNO₃, HF and HCl; ALS method 4ACD81).

Samples analysed at Intertek Genalysis Laboratory Services Pty Ltd (Genalysis) in Western Australia, used procedures for major elements and LOI (Genalysis methods FB1, XRF and TGA) that were very similar to those used at ALS. The procedures used to measure trace elements (Genalysis methods FB6/4A, MS/OE) were also similar except for analysis of Cu, Cr, Ni, V, Sc and Zn which were determined by ICP-OES.

For samples analysed at BV, major and minor elements and LOI were determined by similar methods to ALS and Genanalysis, but trace elements (Ag, As, Ba, Be, Bi, Cd, Ce, Co, Cr, Cs, Cu, Dy, Er, Eu, Ga, Gd, Ge, Hf, Ho, In, La, Lu, Mo, Nb, Nd, Ni, Pb, Pr, Rb, Re, Sb, Sc, Se, Sm, Sn, Sr, Ta, Tb, Te, Th, Tl, Tm, U, V, W, Y, Yb, Zn, Zr) were determined by laser ablation ICP-MS (LA-ICP-MS) on a fragment of the fused glass disc that were prepared for and analysed by the XRF method. Precious metals (Au, Pd and Pt) were analyzed on a separate pulp aliquot by Pb collection fire assay and ICP-MS

Data quality at the three laboratories is broadly comparable. Total uncertainties for major elements are $\leq 1.5\%$, those for minor elements are $<2.5\%$ (at concentrations >0.1 wt. %) and those for trace elements are $\leq 10\%$ (Lu $\pm 20\%$). Major elements are reported on an anhydrous basis. Primitive mantle abundances quoted throughout this study are those of McDonough *et al.*, (1992) unless otherwise stated. The elemental compositions of all samples discussed here, including those compiled from publicly available sources, are presented in Electronic Appendix 1.1.

Samples with compositions that are clearly altered, such as those with LOI that far exceeds results typical of the unit, were excluded from this dataset. Rocks with $\text{SiO}_2 > 57$ wt% were excluded from the dataset if their aluminium saturation index (ASI; $\text{Al}_2\text{O}_3 / (\text{CaO} + \text{Na}_2\text{O} + \text{K}_2\text{O})$ on a molar basis) exceeded 1.1 (i.e., the sample was peraluminous). Rocks with SiO_2 exceeding 77.5 wt% were also excluded from the dataset and samples containing >70 wt% SiO_2 are treated with caution because saturation in accessory phases potentially adds additional and less-predictable influences on compositional trends.

1.2.2. Sm-Nd isotope analytical methodology

Sm-Nd isotopic compositions for 43 samples were acquired at the University of Melbourne, following Maas *et al.* (2015). Powders (ca. 0.1 g) were weighed into Krogh-type PTFE vessels and mixed with a ^{149}Sm - ^{150}Nd tracer calibrated against the Caltech Sm-Nd mixed normal solution (Wasserburg *et al.*, 1981). Samples were dissolved at high pressure (2.5 ml 3:1 HF-HNO₃, 48 h, 160 °C; 2x dry-down with conc. HNO₃; 2.5 ml 6M HCl, 24 h, 160 °C); clear solutions were obtained in all cases. Sm and Nd were extracted using Eichrom TRU- and LN-resin (Pin and Santos Zalduegui, 1997). Total blanks (0.1 ng Nd, 0.016 ng Sm) were negligible compared to sample sizes and no blank corrections were applied. All isotopic data were acquired on a Nu Plasma multi-collector ICPMS, with sample introduction via a Glass Expansion low-uptake PFA nebulizer and Cetac Aridus desolvator. Instrumental mass bias for data collected in static mode was corrected by internal normalisation to $^{146}\text{Nd}/^{145}\text{Nd}=2.0719425$ (equivalent to the more familiar $^{146}\text{Nd}/^{144}\text{Nd}=0.7219$; Vance and Thirlwall, 2002) and $^{152}\text{Sm}/^{147}\text{Sm} = 1.78307$, respectively, using the exponential law as part of an online iterative spike subtraction/internal normalisation procedure. $^{143}\text{Nd}/^{144}\text{Nd}$ in unknowns and quality controls was adjusted to a nominal $^{143}\text{Nd}/^{144}\text{Nd} = 0.511860$ for the La Jolla Nd standard, which was analyzed every fourth run and yielded measured (mass bias-corrected) ratios in the ranges 0.511848-0.511871, 0.511862-0.511884 and 0.511919-0.511969 in the three analytical sessions, respectively. After adjustment, the JNd-1 Nd standard averaged 0.512120 ± 14 (2sd, n=6) while the USGS basalt BCR-2 yielded $^{147}\text{Sm}/^{144}\text{Nd}=0.1382 \pm 2$ (2sd, n=4) and $^{143}\text{Nd}/^{144}\text{Nd}=0.512625 \pm 17$ (2sd, n=6); these results are consistent with long-term averages and with TIMS/MC-ICPMS reference numbers. External precisions for $^{147}\text{Sm}/^{144}\text{Nd}$ and $^{143}\text{Nd}/^{144}\text{Nd}$ are $\pm 0.2\%$ and $\pm 0.004\%$ (2sd), respectively. ϵ_{Nd} values were calculated using the CHUR parameters of Bouvier *et al.* (2008): $^{147}\text{Sm}/^{144}\text{Nd}=0.1960$, $^{143}\text{Nd}/^{144}\text{Nd}=0.512632^*$, (*adjusted to the La Jolla value used here). $^{147}\text{Sm}/^{144}\text{Nd}$ and $^{143}\text{Nd}/^{144}\text{Nd}$ in modern depleted mantle (DM) are 0.2136 and 0.513163, respectively, and are based on a linear evolution from $\epsilon_{\text{Nd}}=0$ at 4.56 Ga to $\epsilon_{\text{Nd}}=+10$ at present (modified from Goldstein *et al.*, 1984). The ^{147}Sm decay constant is $6.54 \times 10^{-12}/\text{y}$. Age corrections (ϵ_{NdT}) Age corrections (ϵ_{NdT}) are based on U-Pb zircon ages where available (Electronic Appendix 1.2), otherwise generic ages for the stratigraphic unit are used.

Chapter 2: Platy pyroxene – new insights into spinifex texture

2.1. INTRODUCTION

Spinifex textures are a striking feature of ultramafic to mafic rocks that are interpreted to form in lavas or high-level intrusions when crystals cool in the presence of a thermal gradient (Faure *et al.*, 2006, Arndt *et al.*, 2008). Individual crystals are typically olivine or pyroxene, which have plate or acicular aspect ratios, and grow *in situ* in tightly clustered aggregates. When viewed in cross section the texture has a superficially similar appearance to spinifex grasses (*Triodia* sp.) for which the texture was named (Nesbitt 1971). Spinifex textures are largely restricted to Archean komatiites and komatiitic basalts but they have also been identified in non-komatiitic suites, such as Cretaceous boninites (Wood 1980), and in Proterozoic komatiitic basalts that are not always associated with komatiite *sensu-stricto* (e.g., Arndt 1982, Baragar and Scoates 1987, Puchtel *et al.*, 1996, Zhou *et al.*, 2000).

The mineralogy of spinifex textured rocks is rarely preserved in Archean terranes because their delicate skeletal features have typically been overprinted by repeated episodes of regional metamorphism, hydrothermal alteration and surface weathering. More commonly the primary minerals are replaced by secondary minerals such as chlorite, serpentine, amphiboles and talc. Many geologists who specialise in Archean granite-greenstone terrains use the heuristic rule that platy pseudomorphs indicate olivine precursors whereas acicular pseudomorphs indicate pyroxene. A logical extension of this rule is to use platy spinifex textures to infer komatiitic affinity, because the bulk chemistry of an olivine spinifex rock is typically more than 18 wt% MgO, and if it is assumed to be representative of the initial melt composition then the unit would be designated as komatiitic.

Here we define an important exemption to these rules; in the Murchison Domain of the Youanmi Terrane, Yilgarn Craton, there are areas where the low-grade regional metamorphic regime (prehnite-pumpellyite to greenschist) has allowed for preservation of textures such as random acicular pyroxene spinifex, oriented acicular pyroxene spinifex ('string-beef'), and platy pyroxene spinifex. Table 2.1 also includes a summary of spinifex or spinifex-like terminology that we have encountered in the

literature, including at the crystal and crystal group scales. Platy pyroxene spinifex textured rocks were initially described and mapped as ‘komatiitic’ because of their resemblance to platy olivine spinifex (Watkins and Hickman 1990, Hallberg 2000, Wyche *et al.*, 2007, Van Kranendonk *et al.*, 2013), but we show that non-cumulate rocks have compositions that range from ~11-16 wt% MgO and 51-57 wt% SiO₂. These compositions are far less magnesian and more siliceous than typical olivine spinifex textured rocks, and given the remarkable preservation of primary igneous textures, they were targeted for detailed investigation into their unusual geochemistry. Platy pyroxene spinifex textured rocks are abundant in our study area, and we suggest that they are a product of unusually high-Si and moderately high-Mg parental melts.

Considering these findings, several localities worldwide probably require re-examination. We view our results as a first step towards clarification of moderate- to high-MgO volcanic rock classifications, particularly relevant to Archean and Proterozoic greenstone terranes.

Table 2.1. Summary of spinifex-related nomenclature

Textural term/grouping	Dominant phase(s) identified	Description	Aspect ratio	Natural example reference
<i>Micro-scale texture</i>				
Acicular/needly	Ca-Cpx or low-Ca Px, Crystals are elongate along the c-axis. Sections normal to c-axis are commonly chemically zoned	Crystals are elongate along the c-axis. Sections normal to c-axis are typically rhombic to euhedral. Characteristic of pyroxene in rapidly cooled high-Mg volcanics (e.g. komatiitic basalt, boninite).	$L \gg W \approx T$	Canada (Arndt 1977); South Africa (Kareem and Bryerly 2003); Zimbabwe (Shimizu <i>et al.</i> , 2005); Japan (Natland 1982); this study
Chain/lattice (Donaldson 1976) or swallowtail (Faure <i>et al.</i> , 2003)	Olivine or pyroxene	Chain/lattice is used to describe dendritic forms with bladed or thinly tabular aspect ratios. The texture is named for their comprising numerous linked crystal units, which are typically H-shaped (in sections parallel to either [001] or [100]), and units are locally connected to one another by "tongues". Chains may grow in random or parallel orientation, (Donaldson, 1976).	$L \approx W \gg T$ or $L > W \gg T$	Zimbabwe (olivine and augite; Renner <i>et al.</i> , 1994).
Plate/blade/tabular (collectively sheaves, plate sets)	Olivine or pyroxene (typically clinopyroxene)	Individual crystals may internally be solid, dendritic or skeletal.	$L \approx W \gg T$ or $L > W \gg T$	South Africa (Viljoen and Viljoen 1969); Australia (Nesbitt 1971); Canada (Arndt 1977); Zimbabwe; (Nisbet <i>et al.</i> , 1987)
Plate, locally with acicular protruding terminations	Pyroxene (typically clinopyroxene)	Individual crystals may be solid or skeletal. Plates are typically discrete however, in some instances plates may develop acicular shaped protrusions at the crystal margins, which are elongate in the orientation of the crystallographic <i>c</i> -axis.	$L \approx W \gg T$	This study.
Dendritic (AKA arborescent)	Olivine, pyroxene, oxides	Branching crystals that are each made of several units in contrast to euhedral or skeletal crystals which are made of only one unit (Welsch <i>et al.</i> , 2013). They form fractal or "hierarchical" (Fowler <i>et al.</i> , 2002) crystal geometries. Many examples in volcanic and hydrothermal rocks. Associated with undercooling, and hence association with spherulites/varioles.	N/A	Canada (Fowler <i>et al.</i> , 2002). Australia (Hallberg 2000); this study

Table 2.1 Continued

Textural term/grouping	Dominant phase(s) identified	Description	Natural example reference
<i>Macro-scale texture</i>			
Harrisite	Olivine	Distinctive radiating bunches of >20 cm crystals, develops in layers within intrusive and some extrusive rocks, associated with olivine cumulates. The term 'harristitic texture' is typically used for a radiating, spinifex-like texture in intrusive rocks and is also applied to minerals other than olivine.	Scotland (Emeleus 1987 after Harker, 1908)
String-beef (AKA oriented pyroxene spinifex)	Pyroxene (typically clinopyroxene)	A special case of pyroxene spinifex texture where coarse, parallel to sub-parallel acicular pyroxene crystals form $\geq 60\%$ of the rock. Further work may confirm that platy pyroxenes are a ubiquitous component, hence it would be a descriptor for rocks with crystal populations transitional to platy and acicular textures (see above).	Canada (Arndt 1977, Barnes 1985, Arndt <i>et al.</i> , 2004); South Africa (Wilson and Versfeld 1994); this study
Random spinifex	Olivine, pyroxene, amphibole	Randomly oriented plates within a matrix of acicular or platy pyroxene and devitrified glass.	South Africa (Viljoen and Viljoen 1969); Canada (Arndt 1977); this study
Plate spinifex	Olivine, pyroxene, amphibole, calcite	criss-crossing sets of numerous, closely spaced and parallel, blade- or plate-like crystals which form $\geq 50\%$ of the rock. This texture typically develops within volcanic or sub-volcanic units, adjacent to random spinifex (see above), away from the chilled margin.	Canada (Pyke <i>et al.</i> , 1973); this study.

2.2. GEOLOGICAL BACKGROUND

The chronostratigraphic and magmatic framework of the Murchison Domain has most recently been documented by Van Kranendonk *et al.* (2013), who divide supracrustal rocks of this area into three main stratigraphic groups: the Norie Group (2820–2800 Ma), Polelle Group (2800–2735 Ma) and Glen Group (2735–2710 Ma). The study area extends from approximately 10 km SE of Meekatharra to approximately 25 km SSE of Meekatharra within the Polelle Syncline structure (Fig. 2.1). All volcanic rocks that we describe from our study area belong to the Meekatharra Formation of the Polelle Group, which is dominated by high-Mg basalts, and associated olivine-pyroxene cumulates, and tholeiitic basalts.

In the Polelle Syncline (Locality 2; Fig 2.1), the Lordy Basalt Member and Bassets Volcanic Member are both predominantly fine grained, vitrophyric, trachytic or porphyritic textured high-Mg basalts that typically contain abundant acicular pyroxene phenocrysts. Most flows are massive and undifferentiated, but some flows around the base of the Formation have differentiated into lower, olivine-pyroxene cumulate layers, and upper spinifex textured flow tops. Watkins and Hickman (1990) and Hallberg (2000) described the Lordy Basalt Member as high-Mg basalt, whereas Van Kranendonk *et al.* (2013) described it as komatiitic basalt, with local komatiite horizons. The Bassetts Volcanic Member has recently been differentiated in the stratigraphy (from within the Lordy Basalt Member), on the basis of textural differences, and boninite-like chemistry (Wyman and Kerrich 2012). Overlying these high-Mg units is the Stockyard Basalt Member, which consists of fine grained, massive or pillowed, tholeiitic basalt.

In the centre of the Polelle Syncline, at Locality 1 (Figs 2.1, 2.2), the volcanic stratigraphy is dominated by high Mg basalts of the Bundle Volcanic Member (overlying the Stockyard Basalt Member). Based on field textures that resemble platy olivine spinifex, these lavas were described as komatiite (Hallberg 2000, Wyche *et al.*, 2007, Van Kranendonk *et al.*, 2013) and high-Mg basalt (Watkins and Hickman, 1990). Locality 1 is the best-preserved sequence of spinifex textured flows, which are described in greater detail in the ‘Spinifex Textures’ section.

Regional metamorphism, shearing deformation, granitic intrusion, and dolerite dykes have affected portions of this sequence. Apart from a few distal granitic intrusions, all these are late in the geological history of the study area, i.e., post 2730 Ma (e.g., Van Kranendonk *et al.*, 2013) and the study area is located away from any pervasive overprinting events.

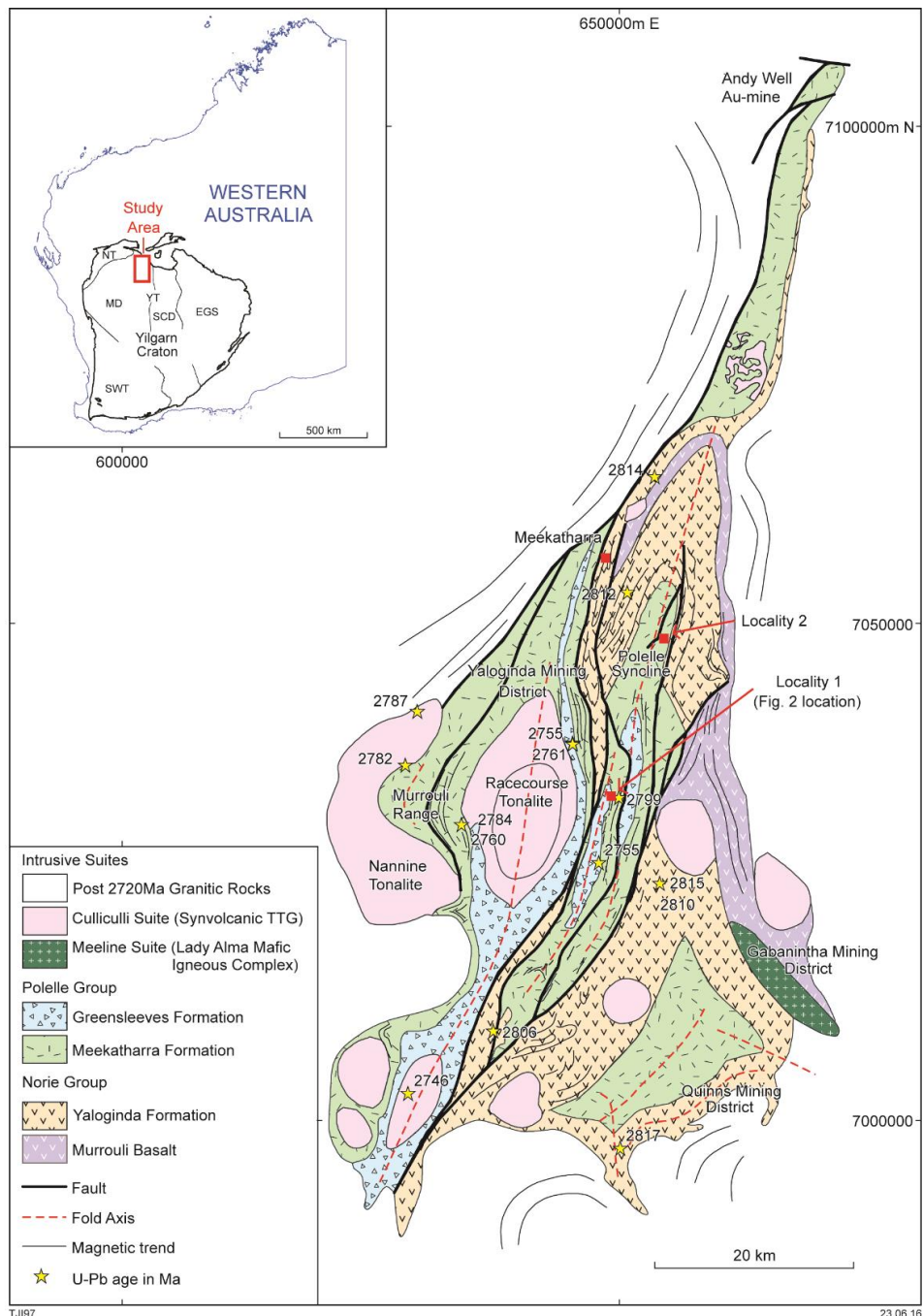


Figure 2.1 Interpreted bedrock geology map of the northern Murchison Domain, Yilgarn Craton. This map shows the distribution of supracrustal groups and co-genetic intrusive suites, available geochronological data, major structural features and significant localities. Interpretation is based on 1:100,000 mapping by the Geological Survey of Western Australia (GSWA), and supplemented by our interpretation of aeromagnetic and Landsat multispectral images. Coordinates are relative to GDA94/MGA Z50. Inset abbreviations: MD = Murchison Domain, SCD = Southern Cross Domain, YT = Youanmi Terrane, NT = Narryer Terrane, SWT = South West Terrane, EGS = Eastern Goldfields Superterrane.

2.3. SAMPLE SELECTION AND ANALYTICAL PROCEDURES

Nineteen rock samples were collected from outcrops at Locality 1. The samples are representative of a continuous stratigraphic sequence, rich in high-Mg volcanic rocks. Most samples were collected from one transect that crosses the best exposed basal section of the sequence, and three samples were collected along strike, at a slightly higher stratigraphic level (Fig. 2.2). Several samples were also collected from Locality 2, but those are described for petrography only, to compare textures and crystal habits with samples from Locality 1. A comprehensive study of geochemistry from samples from Locality 2, and the enveloping stratigraphy is in preparation. All rock samples were selected for low amounts of metamorphism, alteration and veining as well as their preservation of igneous textures. Effort was made to sample a broad range of bulk compositions.

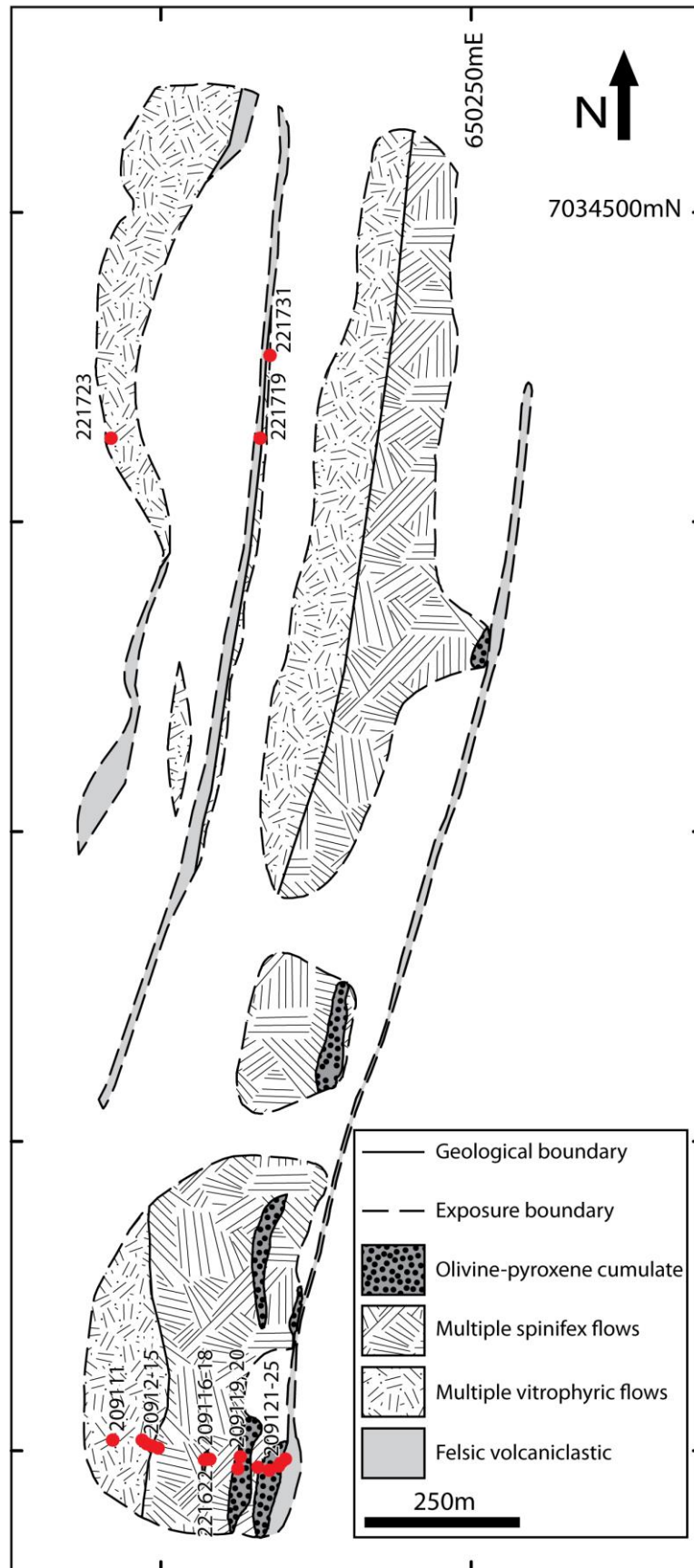


Figure. 2.2. Interpreted bedrock map of Locality 1 (see Fig 2.1 for location). Outcrop is locally covered by saprolite; however, the dashed lines indicate areas with the most continuous outcrop. Note: spinifex textured basalt and vitrophyric textured basalt map units both comprise many individual flows.

2.3.1. X-RAY computed tomography

A core of 7.5mm diameter was drilled from a thin section billet of an A₂ Zone platy pyroxene spinifex sample (209114). The core was scanned at 80 kV and 87 μ A using an X-ray microscope (XRM) (Versa XRM520, Zeiss) running Scout and Scan software (v10.6.2005.12038, Zeiss). A total of 3201 projections were collected over 360°, each with a 5 second exposure. 2x binning and source filter LE5 was used to achieve a suitable signal to noise ratio and 0.4x optical magnification was used to achieve an isotropic voxel resolution of 7.4 μ m. Raw data were reconstructed using XMReconstructor software (v10.7.3679.13921, Zeiss) following a standard centre shift and beam hardening correction procedure. The standard 0.7 kernel size recon filter setting was also used. The visualization and analysis of data generated from XRM scans was performed using Avizo® software (v8.1.1, FEI).

The output of the scan is a map of the variation of the attenuation of X-rays as they are transmitted through the sample. The attenuation coefficient is linear and depends upon the average atomic number and density of the material through which the X-ray is transmitted. Where phases in a sample have contrasting density, or mean atomic number, they can typically be delineated and segmented using thresholding values of X-ray attenuation. In this instance the attenuation coefficients from altered crystal cores overlap with those of altered matrix, and it was impossible to distinguish between these phases using automatic segmentation methods. Instead, a selection of crystals were segmented manually by selecting voxels belonging to an individual crystal using the Avizo® segmentation editor.

In several instances the sample volume was less than the dimensions of larger crystals, and in these cases, our measurements reflect their minimum dimensions. In other instances, where the entire crystal was contained within the volume, the measurements reflect their full dimensions. Table 2.2 records crystal dimension measurements. Video images of X-ray computed tomography are included in Electronic Appendix 2.1.

Table 2.2. X-ray computed tomography 3D measurements of representative pyroxene crystals.

Measurement number	Length μm (maximum dimension)	Width μm (max, 90° to length)	Thickness μm (mean, mode)	Rim thickness μm	Aspect ratio	Comment	
<i>First-order plates</i>							
1	1815	1115	120	15-20	$L \approx W \gg T$ or $L > W \gg T$	Plate intersects other first-order plates	
2	>6965	2430	95	24		Plate's width is truncated by two other plates	
3	>1845	>1750	100	20-25			
<i>First-order acicular crystals (associated with first-order plates)</i>							
4	1330	160	140	20	$L \gg W \approx T$		
5	1240	245	190	20-25			
6	>1710	140	120	20			
<i>Second-order plates (occur interstitial to first-order plate sets)</i>							
7	1460	710	45	N/A	$L \approx W > T$ or $L > W > T$		
8	770	480	55	N/A			
9	275	230	50	N/A			
10	240	165	70	N/A			
11	192	101	30	N/A			
<i>Second-order acicular crystals</i>							
12	150	55	50	N/A	$L > W \approx T$	Appear randomly oriented between oblique first-order plate sets; limited by resolution of data	
13	430	50	50	N/A			
14	730	50	50	N/A			

Note: For length and width measurements, > denotes a measurement where the crystal extrudes beyond the scanned volume in that dimension, and is therefore a minimum measurement.

2.3.2. Electron probe microanalysis and element mapping

Electron probe microanalysis (EPMA) was conducted on points within relict olivine, poikilitic pyroxene, and Cr-spinel in B₂ Zone cumulate sample 209122 as well as traverses across platy pyroxene crystals, dendritic pyroxene and Cr-spinel from A₂ zone sample 209114. Average compositions are presented in Table 2.3 and individual point analyses are included in Electronic Appendix 2.2.

Polished thin sections (30 μm thickness) were analysed over the course of three analytical sessions using a JEOL 8530F electron microprobe equipped with five tuneable wavelength dispersive (WD) spectrometers at the Centre for Microscopy, Characterization and Analysis (CMCA) at the University of Western Australia. Elements were acquired using the following crystals: TAP for SiK α ,

AlK α , NaK α and MgK α ; PETJ for CaK α and KK α , LIF for FeK α , NiK α , ZnK α and LIFH for TiK α , CrK α , MnK α and VK α , which were analysed over 2-4 passes. Primary calibration of the electron microprobe was performed on well characterised, homogenous standards.

Operating conditions for point analyses were 40° take-off angle, accelerating voltage of 15 kV and beam intensity of 20 nA with a fully focused beam. Elemental maps were acquired under the same conditions but with a beam intensity of 50 nA, pixel dwell time of 20 ms, a fully focused beam, and a 1 x 1 μ m pixel dimension. For point analyses, on-peak count times during session one for all elements (SiK α , TiK α , AlK α , CrK α , FeK α , NiK α , MnK α , MgK α , CaK α , NaK α , KK α) were 20s; during session two on-peak count times were 40 s for eleven elements (SiK α , TiK α , ZnK α , AlK α , VK α , CrK α , FeK α , NiK α , MnK α , MgK α , CaK α , and 20 s for two elements (NaK α , KK α). For the element mapping session on peak times for all 10 elements (SiK α , TiK α , AlK α , CrK α , FeK α , NiK α , MgK α , CaK α , NaK α , KK α) were 20 s.

EPMA point analyses were collected and post processing was carried out using Probe for EPMA®. Elemental maps were acquired using a combination of Probe for EPMA® and Probe Image® with post acquisition processing using CalcImage® and output to Surfer® for further treatment. Unknown and standard intensities were corrected for deadtime. Matrix correction was by the Armstrong/Love Scott $\phi(\rho z)$ method (Armstrong 1988). Mean Atomic Number background corrections were used throughout (Donovan and Tingle 1996). On peak interference corrections were applied as appropriate (Donovan *et al.*, 1993). Oxygen was calculated by cation stoichiometry. Results are presented in Table 2.3.

Table 2.3. Average mineral chemical compositions from EPMA point analyses.

	1st order plate and needle cores (altered)*		1st order Plate cores (altered)		Plate rims (augite)		Acicular rims (augite)		Dendritic augite		Poikilitic augite		Poikilitic Opx		Olivine (Relict material)		Cr-spinel		Cr-spinel	
Sample	209114 (A ₂)		209114 (A ₂)		209114 (A ₂)		209114 (A ₂)		209114 (A ₂)		209122 (B ₂)		209122 (B ₂)		209122 (B ₂)		209114 (A ₂)		209122 (B ₂)	
	Calc. from Map Session		Session 1		Session 1		Session 1		Session 1		Session 2		Session 2		Session 2		Session 1		Session 2	
Point count	n=49555 pixels		n=55		n=18		n=28		n=7		n=12		n=19		n=10		n=35		n=10	
	Avg	SD	Avg	SD	Avg	SD	Avg	SD	Avg	SD	Avg	SD	Avg	SD	Avg	SD	Avg	SD	Avg	SD
SiO ₂	55.00	20.12	59.33	15.7	48.93	1.37	47.9	1.64	47.1	0.74	51.8	1.19	55.9	0.57	41.4	0.20	0.12	0.03	0.20	0.02
TiO ₂	0.20	0.76	0.13	0.29	0.84	0.18	0.93	0.22	1.06	0.20	0.47	0.13	0.11	0.02	0.02	0.01	0.40	0.04	0.38	0.01
Al ₂ O ₃	8.10	4.60	5.92	4.41	7.37	2.46	7.53	1.55	8.67	0.59	3.39	1.07	0.99	0.25	0.06	0.01	9.48	0.36	8.80	0.24
Cr ₂ O ₃	0.40	0.43	0.32	0.21	0.03	0.03	0.03	0.03	0.01	0.01	0.36	0.18	0.56	0.08	0.14	0.04	56.4	0.83	55.6	0.50
Fe ₂ O ₃	-	-	-	-	0.31	1.31	0.60	2.15	0.00	0.77	1.19	0.96	0.00	0.59	0.00	-	5.79	0.39	6.01	0.25
FeO	9.80	4.84	9.43	3.96	10.77	0.39	11.1	0.49	13.9	0.35	4.90	0.62	7.39	0.63	10.5	0.49	13.8	1.40	17.4	2.02
NiO	0.20	0.29	0.03	0.04	0.02	0.02	0.02	0.02	0.01	0.01	0.10	0.01	0.15	0.01	0.39	0.01	0.13	0.02	0.16	0.01
MnO	Not analysed		0.16	0.07	0.23	0.05	0.23	0.08	0.27	0.04	0.18	0.02	0.19	0.01	0.18	0.01	0.18	0.06	0.27	0.01
MgO	14.30	6.24	14.41	5.22	13.68	2.11	13.3	1.58	12.0	0.91	18.4	1.36	32.7	0.34	48.2	0.31	12.3	0.98	9.62	1.34
CaO	2.50	2.96	5.33	4.64	16.49	1.98	16.9	1.74	15.1	1.23	18.2	1.44	1.53	0.21	0.18	0.01	0.07	0.03	0.06	0.02
Na ₂ O	0.20	0.50	0.09	0.12	0.55	1.25	0.25	0.13	0.48	0.57	0.19	0.03	0.03	0.01	0.01	0.01	0.02	0.04	0.19	0.08
K ₂ O	0.10	0.13	0.02	0.02	0.02	0.02	0.02	0.04	0.04	0.06	0.01	0.01	0.01	0.01	0.01	0.00	0.03	0.04	0.08	0.01
V ₂ O ₃	Not analysed		Not analysed		Not analysed		Not analysed		Not analysed		0.07	0.01	0.03	0.00	0.02	0.00	Not analysed		0.16	0.01
ZnO	Not analysed		Not analysed		Not analysed		Not analysed		Not analysed		0.05	0.01	0.03	0.01	0.04	0.01	Not analysed		0.35	0.05
Total	90.80	9.75	95.17	4.40	99.22	0.60	99.0	0.54	98.8	0.37	99.4	0.45	99.7	0.57	101.20	0.27	98.8	0.53	99.3	0.42
Cation units	Cations per 6 oxygens															Cations per 4 oxygens				
Si	-	-	-	-	1.83	0.04	1.81	0.04	1.79	0.02	1.90	0.03	1.96	0.01	1.01	0.00	0.00	0.00	0.01	0.00
Ti	-	-	-	-	0.02	0.01	0.03	0.01	0.03	0.01	0.01	0.00	0.00	0.00	0.00	0.00	0.01	0.00	0.01	0.00
Al	-	-	-	-	0.32	0.10	0.34	0.07	0.39	0.03	0.15	0.05	0.04	0.01	0.00	0.00	0.37	0.01	0.35	0.01
Cr	-	-	-	-	0.00	0.00	0.00	0.00	0.00	0.00	0.01	0.01	0.02	0.00	0.00	0.00	1.47	0.02	1.48	0.01
Fe ³⁺	-	-	-	-	0.34	0.04	0.02	0.07	0.01	0.02	0.03	0.03	0.04	0.02	0.00	-	0.14	0.01	0.15	0.01
Fe ²⁺	-	-	-	-	0.01	0.01	0.35	0.01	0.43	0.01	0.15	0.02	0.18	0.02	0.21	0.01	0.38	0.04	0.49	0.06
Ni	-	-	-	-	0.00	0.00	0.00	0.00	0.00	0.00	0.00	0.00	0.00	0.00	0.01	0.00	0.00	0.00	0.00	0.00
Mn	-	-	-	-	0.01	0.00	0.01	0.00	0.01	0.00	0.01	0.00	0.01	0.00	0.00	0.00	0.01	0.00	0.01	0.00
Mg	-	-	-	-	0.76	0.12	0.75	0.08	0.68	0.05	1.01	0.07	1.71	0.02	1.75	0.01	0.61	0.04	0.48	0.06
Ca	-	-	-	-	0.66	0.08	0.69	0.07	0.62	0.05	0.72	0.06	0.06	0.01	0.00	0.00	0.00	0.00	0.00	0.00
Na	-	-	-	-	0.04	0.09	0.02	0.01	0.04	0.04	0.01	0.00	0.00	0.00	0.00	0.00	0.00	0.00	0.00	0.00
K	-	-	-	-	0.00	0.00	0.00	0.00	0.00	0.00	0.00	0.00	0.00	0.00	0.00	0.00	0.00	0.00	0.00	0.00
V	-	-	-	-	Not analysed		Not analysed		Not analysed		0.00	0.00	0.00	0.00	0.00	0.00	Not analysed		0.00	0.00
Zn	-	-	-	-	Not analysed		Not analysed		Not analysed		0.00	0.00	0.00	0.00	0.00	0.00	Not analysed		0.01	0.00
Total cation units	-	-	-	-	4.00	0.00	4.00	0.01	4.00	0.00	4.01	0.01	4.01	0.01	2.99	0.00	3.00	0.00	3.00	0.00
Wollastonite (Wo)	-	-	-	-	37.30	2.73	38.0	3.71	35.3	1.94	37.7	3.37	2.90	0.39	-	-	-	-	-	-
Ferrosilite (Fs)	-	-	-	-	19.70	2.87	20.6	4.56	25.5	1.74	9.60	0.86	10.9	0.28	-	-	-	-	-	-
Enstatite (En)	-	-	-	-	43.00	3.92	41.4	3.71	39.2	1.53	52.7	3.11	86.2	0.66	-	-	-	-	-	-
Fosterite (Fo)	-	-	-	-	-	-	-	-	-	-	-	-	-	-	89.1	0.01	-	-	-	-
Fayalite (Fa)	-	-	-	-	-	-	-	-	-	-	-	-	-	-	10.9	0.01	-	-	-	-
Fe ²⁺ /(Mg ²⁺ +Fe ²⁺)	-	-	-	-	-	-	-	-	-	-	-	-	-	-	-	-	0.59	0.04	0.70	0.05
Fe ³⁺ /(Fe ³⁺ +Cr ³⁺)	-	-	-	-	-	-	-	-	-	-	-	-	-	-	-	-	0.08	0.01	0.09	0.00
Cr/(Cr+Al)	-	-	-	-	-	-	-	-	-	-	-	-	-	-	-	-	0.89	0.00	0.89	0.00
Mg/(Mg+Fe ²⁺)	-	-	-	-	0.69	0.05	0.68	0.06	0.61	0.02	0.87	0.01	0.91	0.00	0.89	0.00	0.41	0.04	0.30	0.05

* Average composition of pixels from all 1st order plate and needle cores in mapped area.

Table 2.4. Selected major, minor and trace element chemical analyses.																			
Sample ID	209111	209112	209113	209115	221731	221719	221723	209118	221722	209114	209117	209121	209116	209120	209122	209123	209124	209119	209125
Laboratory	ALS	Genalysis	ALS	ALS	Genalysis	Genalysis	Genalysis	Genalysis	Genalysis	ALS	ALS	ALS	ALS	ALS	ALS	ALS	ALS	ALS	ALS
Easting	649676	649727	649730	649748	649923	649908	649667	649828	649825	649739	649828	649906	649825	649878	649924	649938	649944	649874	649950
Northing	7032521	7032518	7032515	7032508	7034269	7034129	7034134	7032490	7032489	7032512	7032490	7032477	7032490	7032494	7032472	7032480	7032486	7032475	7032491
Field Description	Random acicular pyroxene spinifex SHMB				String-beef SHMB	Variolitic SHMB	Vitrophyric SHMB		A ₁ Zone Chilled Margin		A ₂ Zone platy spinifex			B ₂ Zone orthocumulate					Footwall sediment
SiO ₂ _pct	53.28	57.54	54.56	52.43	54.52	61.25	53.62	49.29	50.79	55.86	51.54	52.1	44.5	44.43	43.85	43.98	43.82	43.79	75.07
TiO ₂ _pct	0.69	0.69	0.75	0.62	0.84	0.99	0.67	0.6	0.6	0.64	0.62	0.65	0.27	0.3	0.28	0.32	0.29	0.28	0.31
Al ₂ O ₃ _pct	12.11	10.5	12.38	9.57	10.66	10.82	10.92	8.75	8.74	10.32	10.2	9.74	4.96	4.89	4.64	4.74	4.92	4.61	12.9
Cr ₂ O ₃ _pct	0.07	0.11	0.08	0.19	0.1	0.11	0.11	0.2	0.2	0.2	0.18	0.16	0.76	0.46	0.4	0.47	0.48	0.54	0.01
Fe ₂ O ₃ T_pct	12.05	8.7	9.9	10.64	12.28	9.22	10.36	11.04	11.18	10.29	10.66	10.14	9.93	10.39	9.86	10.48	10.54	10.53	1.75
MnO_pct	0.16	0.14	0.18	0.14	0.16	0.12	0.16	0.19	0.18	0.15	0.16	0.15	0.15	0.15	0.14	0.15	0.15	0.15	0.02
MgO_pct	9.28	8.5	8.5	14.15	9.75	5.64	11.33	15.35	13.99	11.05	13.9	14.3	29.8	29.4	30.1	29.2	29.2	30	0.78
CaO_pct	6.94	6.64	6.78	7.29	6.38	6.15	8.55	9.84	9.39	6.55	7.41	6.85	3.17	3.95	3.89	4.45	4.28	3.9	0.56
Na ₂ O_pct	2.09	1.82	2.25	1.88	2.72	3.78	1.38	1.34	1.88	2.36	2.14	2.1	0.26	0.21	0.21	0.15	0.16	0.18	5.38
K ₂ O_pct	0.23	0.73	1.02	0.09	0.49	0.14	0.46	0.2	0.48	0.2	0.36	0.34	0.06	0.06	0.07	0.08	0.07	0.06	2.34
P ₂ O ₅ _pct	0.07	0.102	0.08	0.06	0.068	0.068	0.067	0.057	0.059	0.06	0.06	0.07	0.03	0.03	0.03	0.04	0.03	0.03	0.09
LOI_pct	3.3	4.38	3.39	3.46	2.48	1.59	2.96	3.2	2.8	2.56	3.18	3.8	6.9	7.05	7.11	6.8	6.85	6.98	0.6
Total	100.33	99.89	99.93	100.54	100.47	99.88	100.60	100.07	100.309	100.26	100.45	100.44	100.8	101.33	100.59	100.87	100.8	101.06	99.88
Cr ppm	580	816	620	1290	691	746	756	1417	1393	1470	1380	1210	5480	3370	3010	3540	3690	3970	50
Ni ppm	135	175	160	362	171.7	203.7	178.6	318.1	346.3	230	243	237	1430	1380	1490	1290	1310	1380	18
Al ₂ O ₃ /TiO ₂	17.55	15.22	16.51	15.44	12.69	10.93	16.30	14.58	14.57	16.13	16.45	14.98	18.37	16.30	16.57	14.81	16.97	16.46	41.61
Mg-number	60.29	65.83	62.87	72.39	61.02	54.67	68.32	73.27	71.16	67.92	72.00	73.55	85.54	84.80	85.75	84.60	84.53	84.89	46.78

2.3.3. Whole-rock major and trace element compositions

Nineteen rock samples were sent to two laboratories for determination of major and trace elements and Loss on Ignition. Well characterised reference materials prepared by the Geological Survey of Western Australia, including a komatiitic olivine-cumulate (MW1), and a basalt (BB1) were submitted together with unknown samples. The major elements for both laboratories have a total uncertainty of $\pm 1.5\%$. Total uncertainty for trace elements is $\pm 10\%$ in flow rocks and $\pm 20\%$ for olivine-pyroxene-Cr-spinel-orthocumulates.

2.3.3.1. Australian Laboratory Services

Thirteen samples were submitted to Australian Laboratory Services (ALS) in Wangara, Western Australia. A subsample of 200-1000 g was crushed by a jaw crusher to $>70\%$ passing 6 mm mesh and subsequently ground in a tungsten carbide ring mill to $>85\%$ passing 75 μm mesh.

Major and minor elements (Si, Ti, Al, Cr, Fe, Mn, Mg, Ca, Na, K, P) were analysed by mixing a 0.66 g aliquot of sample with lithium borate flux (LiBO_2 , LiB_4O_7 and LiNO_3) in $\sim 1:10$ ratio, and then fusing the mixture at 1025°C which was then poured into a platinum mould. The resulting disc was analysed by an X-ray fluorescence spectrometer (XRF; their method ME-XRF26). Loss on ignition (LOI) was determined by thermogravimetric analysis (their ME-GRA05). For resistive trace elements (Cr, V, Cs, Rb, Ba, Sr, Th, U, Nb, Zr, Hf, Y, La, Ce, Pr, Nd, Sm, Eu, Gd, Tb, Dy, Ho, Er, Tm, Yb and Lu), an aliquot of the sample was mixed with lithium borate and fused, then digested in acid and then analysed by inductively coupled plasma mass spectroscopy (ICP-MS; their method ME-MS81). For base metals (Co, Cu, Ni, Sc and Zn) an aliquot of the sample was digested by a mixture of four acids (HClO_4 , HNO_3 , HF and HCl) and then analysed by inductively coupled plasma atomic emission spectroscopy (ICP-AES; their ME-4ACD81).

2.3.3.2. Intertek Genalysis

Six samples were submitted to Intertek Genalysis Laboratory Services Pty Ltd in Maddington, Western Australia. The methods were identical to those of ALS for sample preparation, analysis of major elements and LOI (their methods FB1, XRF and TGA). The methods were also the same for most trace elements (their methods FB6/4A, MS/OE) with the following exceptions. Firstly, Cu, Cr,

Ni, V and Zn were read by inductively coupled plasma optical emission spectroscopy (ICP-OES) rather than by ICP-MS. Secondly, Sc was digested by the fusion/mixed acid digest method, rather than the four-acid digest method, and was read by ICP-OES rather than ICP-MS.

Results for a subset of major and trace elements are presented in Table 2.4, these are re-calculated to 100% on an anhydrous basis, while the complete set of elements are included in Electronic Appendix 2.3.

2.4. FIELD RELATIONS OF THE BUNDLE VOLCANIC MEMBER

The best-preserved spinifex textured flows in the Polelle Syncline are at its centre, at Locality 1 (Figs 2.1, 2.2; see also Locality 17 in Wyche *et al.*, 2007); they outcrop along a ridge comprised of several low hills that extend along strike for approximately 2500 m towards 010° from grid north (GDA94-MGA Z50). The width of the outcrop varies from 270 m at the southern limit to 700 m at the northern limit.

Surface exposure is better than in most of the Yilgarn Craton, estimated at 20–30%, but this still means that most of the sequence is interrupted by laterite. Contacts are obscured by saprolite and erosional debris in many places and we note that erosionally recessive lithofacies may not be well represented by the exposed outcrop.

Sedimentary layering in the footwall rocks to the east of the (ultra-)mafic volcanic sequence dips at approximately 60° towards west, and sporadic exposures of inter-flow sedimentary horizons in the western part of the ultramafic sequence also dip towards the west. Based on an approximate dip of 60° the volcanic sequence has an inferred true thickness \approx 230 m. Footwall sedimentary rocks have been dated using the sensitive high-resolution ion microprobe (SHRIMP) U-Pb in zircon method which yielded an age 2799 ± 2 Ma, which is interpreted to be maximum age of deposition for the sedimentary footwall rocks and therefore also the maximum age for the overlying volcanic rocks in the study area (Wingate *et al.*, 2008). The background sedimentary input is felsic/siliceous in composition and sediments were deposited as very fine grained sandstones, locally turbiditic, which form the footwall and hangingwall, and occur sporadically as thin interflow horizons between the

upper basalt flows. We interpret this to indicate a proximal to continental setting, or subaqueous intracontinental setting. The sedimentary rocks preserve rip-up marks and ripples, as well as graded bedding (Figs. 2.3a,b), which give a consistent younging direction towards the west (see also Wyche *et al.*, 2007). This younging direction is corroborated independently by differentiated volcanic flow facies and geochemical trends (see below).

The eastern-most (footwall) contact of the (ultra-)mafic sequence is abrupt and juxtaposes fine grained olivine–pyroxene–Cr-spinel–orthocumulate against fine grained siliceous volcanic-derived sediments. At Locality 1 this appears to be a conformable igneous contact (e.g., Fig. 2.3c), but the precise relationship (i.e., nature of thermal erosion, intermixing etc.) cannot be further substantiated due to talus material covering most of the contact.

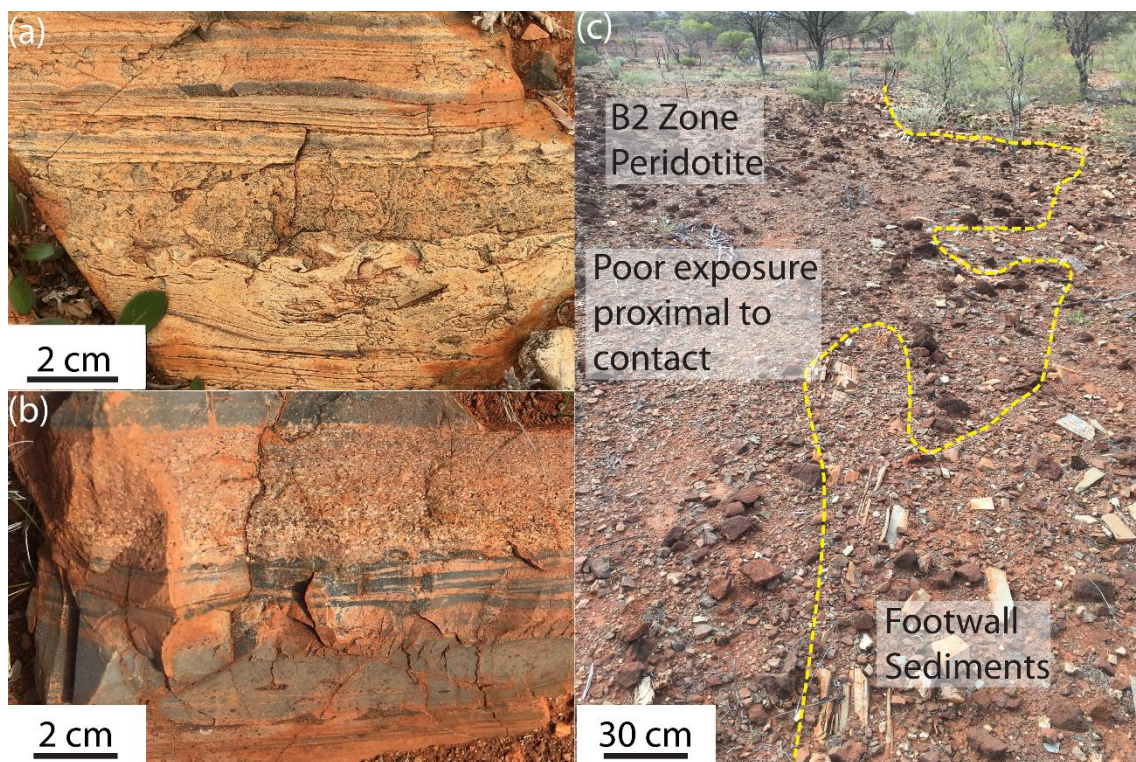


Figure. 2.3. Field photographs at Locality 1. (a). scour marks/ rip up textures in footwall sediments indicate way up towards west (650204mE, 7034537mN GDA94/MGA Z50); (b) graded bedding in interflow sediments indicate way up towards west (649940mE, 7034548mN GDA94/MGA Z50). (c) Footwall contact between peridotitic flow base and underlying sedimentary unit: the contact undulates along strike, but the exact nature of the contact is typically obscured by erosion and deposition of talus (649938mE, 7032480mN GDA94/MGA Z50).

2.4.1. Differentiated flow sequence

Our outcrop mapping (Fig. 2.2) indicates that the hills at Locality 1 comprise many individual lava flows, broadly comparable to komatiite sheet flow facies (e.g., Arndt *et al.*, 2008), indicating a

similar volcanic emplacement. The south east part of the mapped area is dominated by two ~30 m thick lenses of fine to medium grained serpentized olivine–orthopyroxene–clinopyroxene–(Cr-spinel) orthocumulates. The two orthocumulates are both overlain by ~5 m of pyroxene spinifex textured rocks, which are interpreted to be flow tops, but there are local breaks in the exposed outcrop. The extremities of the orthocumulates are largely obscured by *in situ* saprolite and so their boundaries are locally inferred on the outcrop map from *in situ* erosional lag and the positions of footwall or spinifex textured rocks, which are less prone to erosion. Orthocumulate zones outcrop less consistently along strike, but always as discrete lens or lozenge shaped bodies, with similar orientations, and consistently overlain by spinifex textured rocks.

Above the two thicker flows, there is a ~120m sequence of thin (0.5 – 10 m) platy pyroxene spinifex and string-beef textured flows. We have identified only one thin (0.5 – 5 m) basal cumulate zone amongst these flows, which has been mostly eroded (Fig 2.2); cumulate zones are either poorly developed in the case of thinner flows, or else they do not outcrop. Individual flows can be traced for several 10s of metres along strike, but due to the many breaks in exposure we have mapped these flows collectively as a single unit (Fig. 2.2).

Above the uppermost spinifex textured flows, the textures change to vitrophyric or trachytic, with randomly oriented acicular phenocrysts of zoned pyroxene varying in length from <1-5 cm, that are contained in a fine grained or glassy matrix.

2.4.2. Platy pyroxene spinifex textured flows

Platy pyroxene spinifex occurs in all high-Mg Members of the Meekatharra Formation, but it is found in increasing abundance in order of Bassets Volcanic Member < Lordy Basalt Member < Bundle Volcanic Member. In Figure 2.4 we show an ideal section through a typical platy pyroxene spinifex textured flow from the Bundle Volcanic Member at Locality 1. Like platy olivine spinifex textured flows (e.g., Munro Township), these flows are vertically differentiated into a spinifex textured upper part and a cumulate textured lower part. They also exhibit similar vertical gradation of crystal morphology, size, and orientation. We use the classic komatiite nomenclature of Pyke *et al.*, (1973) to describe their characteristics, from a basal cumulate B₂ Zone up through four non-cumulate

zones, including locally, a lower acicular pyroxene A₄ Zone, spinifex-textured A₂₋₃ Zones and an upper chilled margin A₁ Zone. The following descriptions are mainly derived from thin section observations, but also from hand specimen examinations, SEM imagery and 3D X-ray computed tomography (CT) imagery.

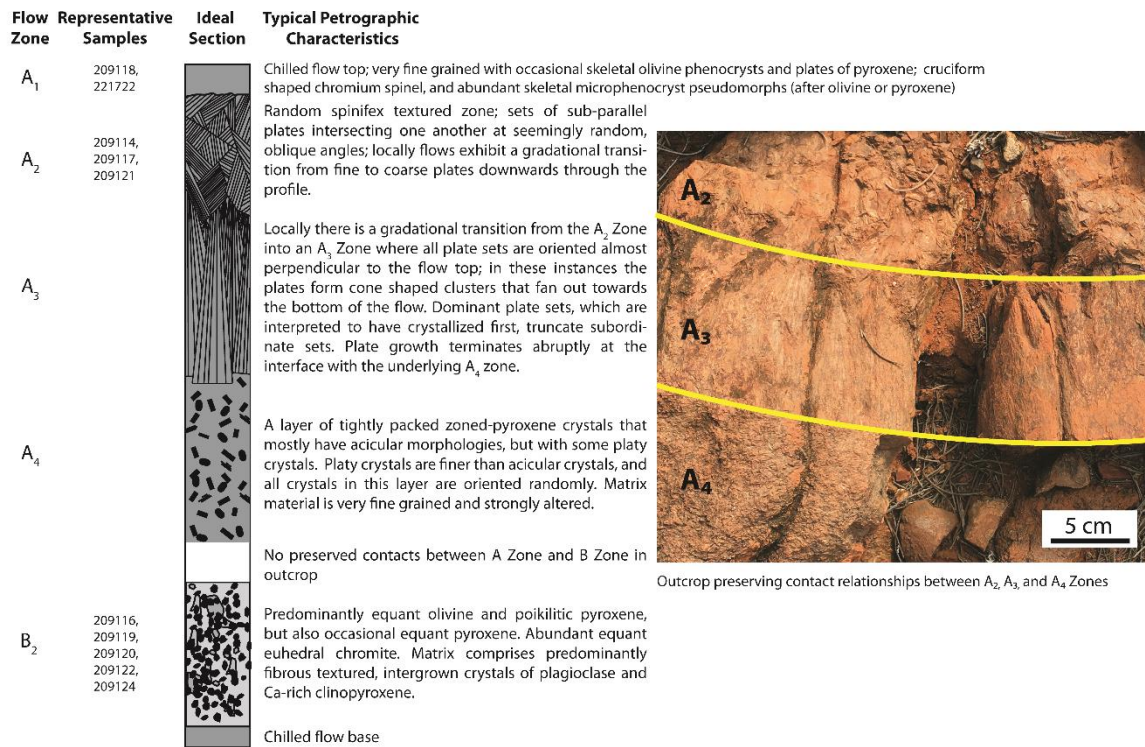


Figure. 2.4. Spinifex zone terminology applied to a generalised flow sequence from Locality 1 with petrographic notes. Inset is a platy spinifex horizon with preserved contacts between A₂, A₃ and A₄ Zones (649896mE, 7032746mN GDA94/MGA Z50). Vertical scale is variable but approximately 0.5–2m. Sample IDs are indicative of relative position within their respective flows only. They were collected from several different flows and their locations are shown on Fig. 2.2.

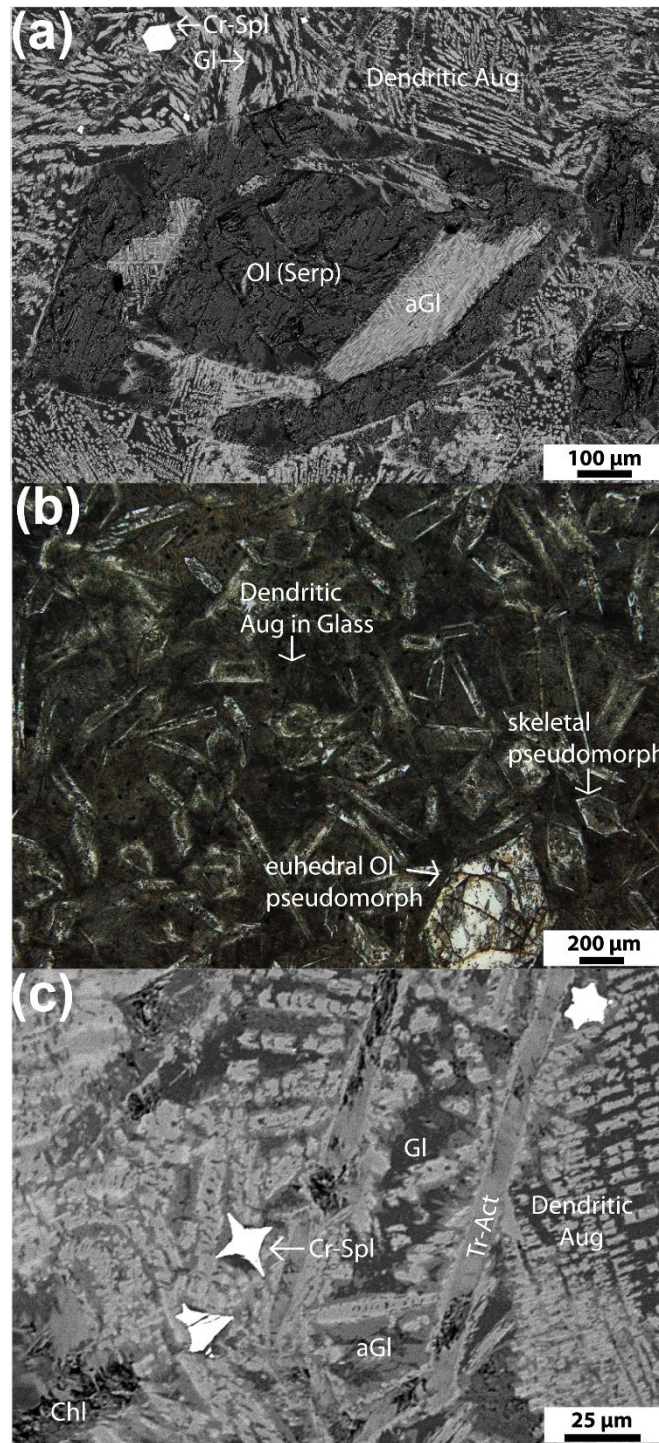


Figure. 2.5. Images of A1 Zone Chilled flow top (sample 209118): (a) backscatter electron (BSE) image showing large skeletal serpentized olivine pseudomorph (Ol-Srp) in dendritic augite (Aug) and devitrified glass (Gl) matrix, which is locally altered (aGl), note the open and enclosed embayments filled with matrix material; (b) photomicrograph in plane polarised light (PPL) showing tremolite pseudomorphing skeletal olivine or pyroxene and euhedral olivine pseudomorph in glassy matrix.; (c) BSE image skeletal cruciform shaped Cr-spinel (Cr-Spl) crystals (white) in matrix of dendritic pyroxene and locally altered glass (aGl) matrix. Silicate phenocrysts have altered largely to tremolite-actinolite (Tr-Act) and chlorite (Chl).



Figure. 2.6. Field photograph of A₂ Zone platy pyroxene spinifex at Locality 2 (655631mE, 7051848mN GDA94/MGA Z50; see Fig 2.1). Note coarse obliquely intersecting plate sets, hence the descriptor ‘random’ spinifex. Individual plates measure up to 1.5 cm.

2.4.2.1. A₁ Zone - chilled flow top

The A₁ Zone has been observed in one outcrop (649828mE, 7032490mN GDA94/MGA Z-50) where it is interpreted to be the uppermost part of the flow, but due to its fractured nature it is poorly preserved. In this example there is a thin (5-10 cm) break in exposure between the A₁ and A₂ Zones. This Zone is predominantly composed of devitrified glass, dendritic augite, and olivine phenocrysts with skeletal morphologies. Serpentinized skeletal olivine pseudomorphs form $\lesssim 5\%$ of the rock, and typically have embayments containing matrix material (e.g., Fig. 2.5a). Most of the rock consists of

fine grained dendritic forms of augite and skeletal microphenocrysts that were probably olivine or pyroxene but are now entirely pseudomorphed by tremolite (e.g., Fig. 2.5b); these dendritic and skeletal crystals occur in a matrix of variably altered, devitrified glass. Locally within the A₁ Zone, Cr-spinel crystals also have skeletal forms (e.g., Fig. 2.5c.), which are not observed in the platy spinifex or cumulate zones, and indicates that they crystallized more rapidly. We interpret these samples to be from chilled margins, and representative of the liquid composition. Locally, the A₁ Zone contains sparse platy pyroxene crystals that are like those found in the A₂ Zone, but in the A₁ Zone they are not observed to be in contact with each other and they comprise $\lesssim 2\%$ of the rock.

2.4.2.2. A₂₋₃ Zone – *platy pyroxene spinifex*

The A₂ ‘random’ platy pyroxene horizon consists of thin plates of pyroxene that are typically arranged in sets of several crystals with similar orientations (Fig 2.6). Plate sets intersect one another obliquely (e.g., Figs. 2.7a, b and Fig. 2.8.), giving the impression of an overall random orientation. In the upper parts of platy textured spinifex zones, individual crystals range up to 15 mm in length and width, and 30-120 μm thick (see Table 2.2). Larger plates feature lozenge shaped internal skeletal features (Figs. 2.7c, 2.8a), and smaller plates have skeletal embayments along their margins (Fig. 2.8b), similar to those documented for diopside dendrites (e.g., Zhao *et al.*, 2011). A third, finer dendritic form of pyroxene accommodates much of the interstice volume between plates (e.g., Fig 2.8c). In several flows the size of individual plates, and plate sets coarsen downwards into the flow.

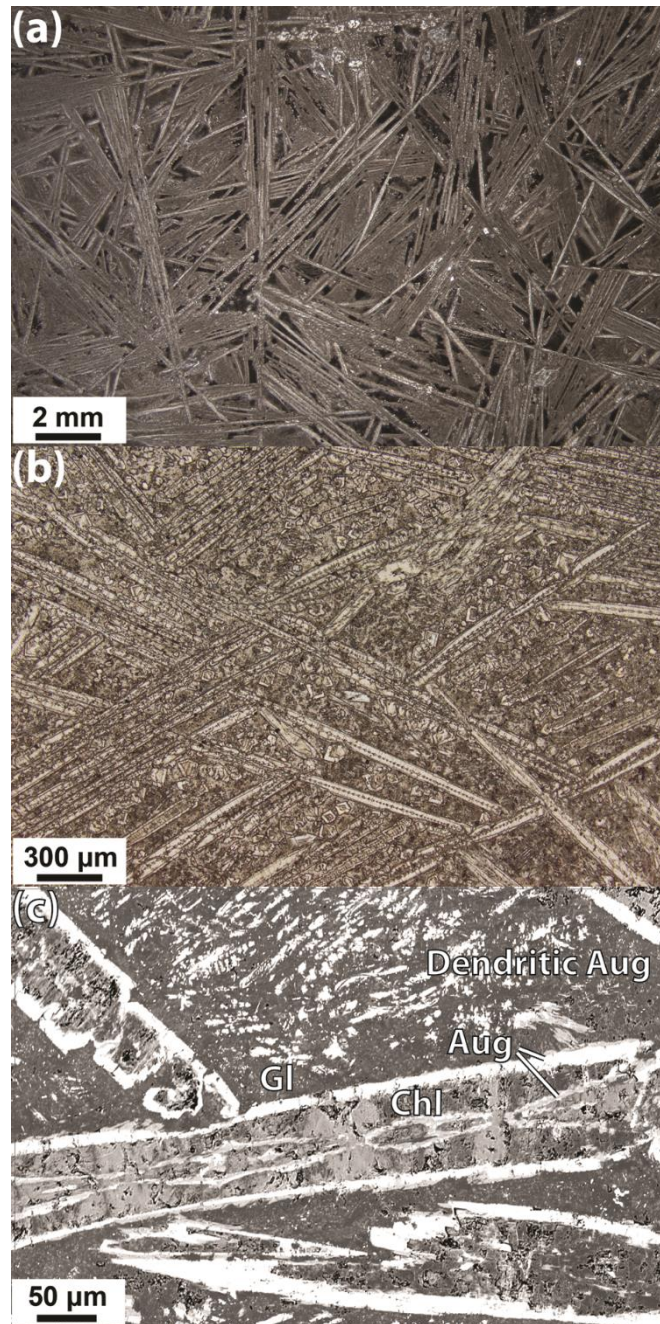


Figure. 2.7. Images of A₂ Zone random platy pyroxene spinifex (sample 209114): (a) thin section in plane polarized light (larger field of view); (b) the same thin section in plane polarized light (smaller field of view). Note the spaced internal texture in the cores of the plates; (c) BSE image of A₂ Zone pyroxene plates showing lozenge-shaped internal structures, similar to those described for dendrites (*e.g.*, Zhao et al., 2011)

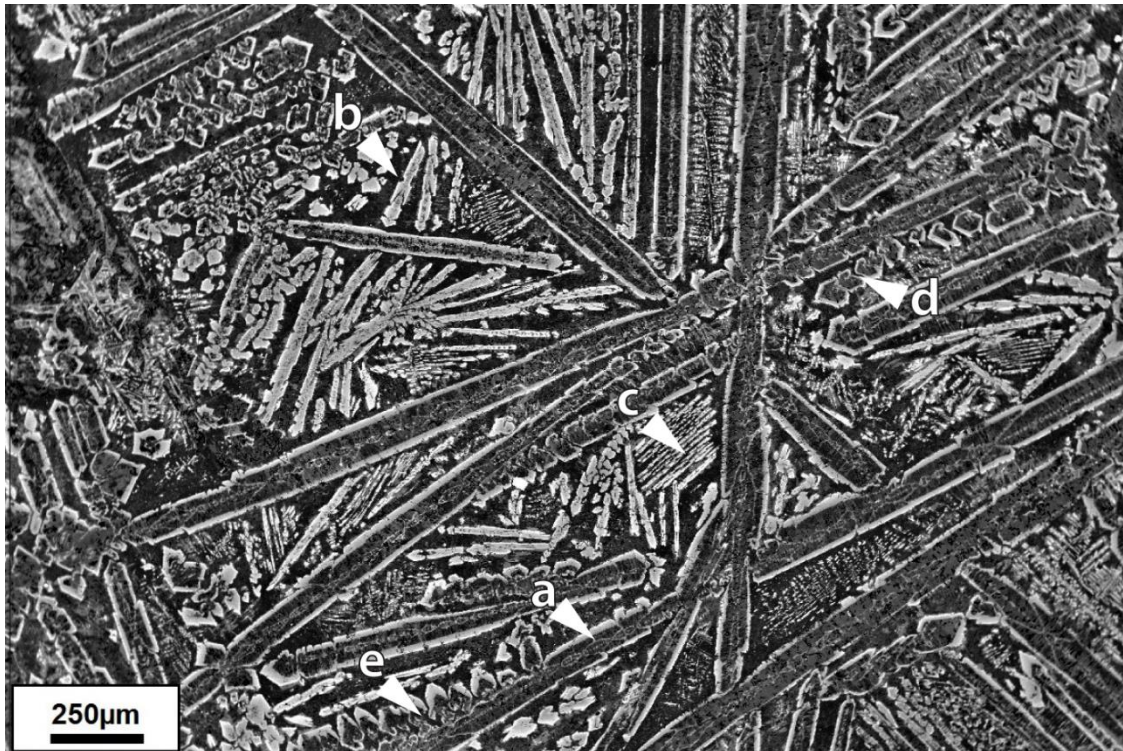


Figure. 2.8. BSE image of A₂ Zone pyroxene crystals (sample 209114) highlighting: (a) rhombus/lozenge and hourglass shaped skeletal features in 1st order plate; (b) skeletal 2nd order augite plate; (c) dendritic pyroxene accommodating interstices; (d) section through a series of acicular pyroxene crystals perpendicular to a 1st order plate set; (e) section through stacked/merged acicular crystals, transitional to plate and similar to observations for platy olivine (Faure et al., 2006; their Fig. 5).

Orthogonally cut surfaces of hand specimens show that most plates are well formed and continuous, but in thin section, the edges of plates locally have acicular protrusions, continuing in the plane of the plate. This is also observable in the X-ray CT imagery. Where thin sections intersect aligned acicular pyroxene crystals, they are in crystallographic continuity with one another, and with adjacent plates. Plates within a set are also typically in near crystallographic continuity, as observed by their similar extinctions in cross polarized light. Locally, acicular crystals that stack side-by-side appear to merge along their length to form a composite crystal (e.g., Fig. 2.8e and Fig. 2.9a); this is discussed in more detail in the ‘X-ray Computed Topography’ section. Interstitial dendritic augite also have preferred orientations and platy morphologies, similarly to the larger, zoned pyroxene plates (e.g., Fig 2.9b).

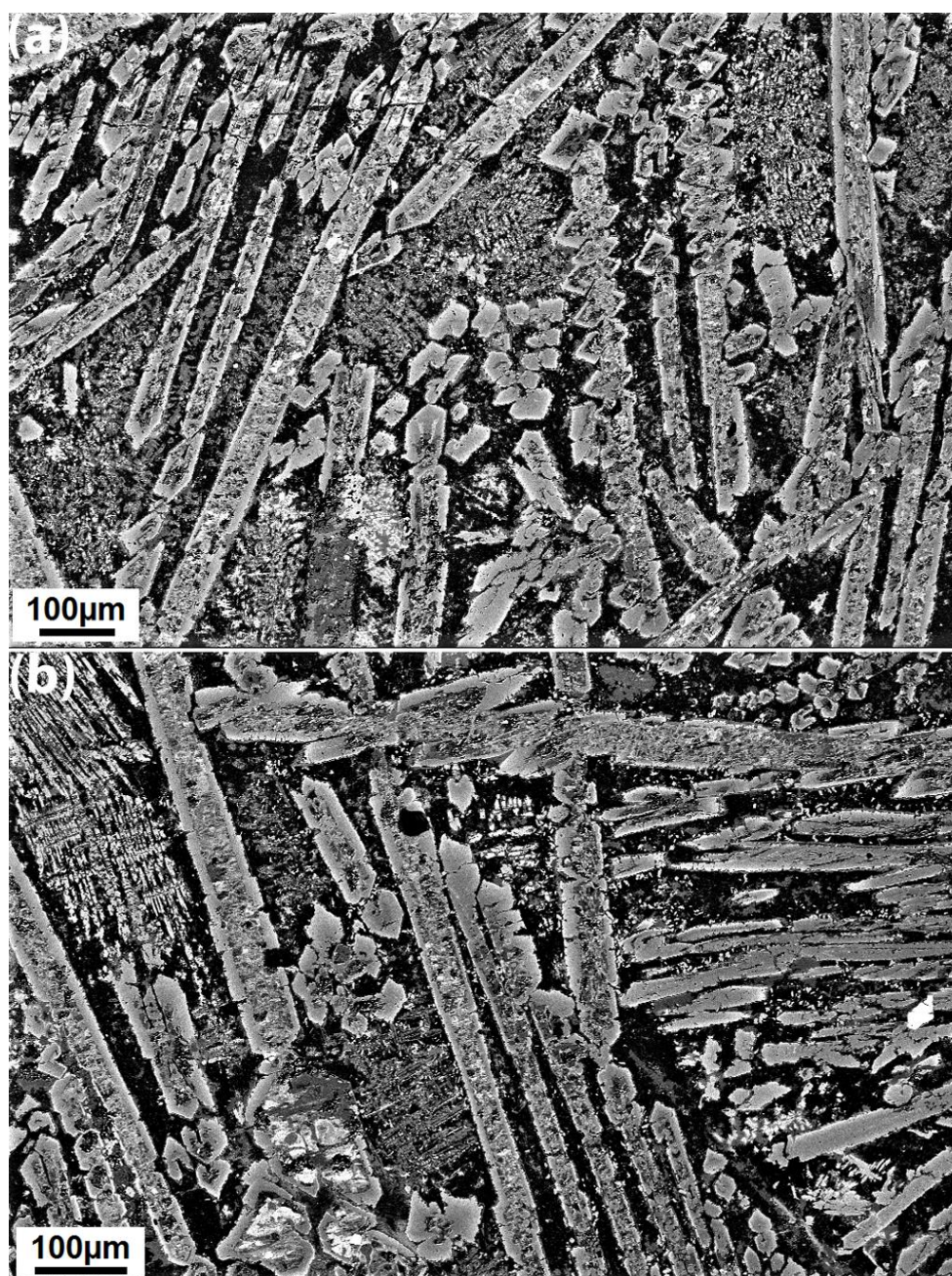


Figure. 2.9. BSE images of A₂ Zone pyroxene plates (sample 221628 from Lordy Basalt Member from Locality 2; see Fig 2.1). (a) Locally, plates transition into acicular crystals that are joined along (100) crystal faces, and outer rims of both plates and acicular crystals have a higher X-ray intensity on backscatter image; (b) weakly zoned core material near to the unaltered rims: it is possible that this is representative of all core material, or that the more heavily chloritized parts were originally more magnesian (i.e., Mg-orthopyroxene, Pigeonite or amphibole; see Mineral Chemistry), which altered to chlorite + SiO₂. In the upper left corner of the image, dendritic augite mimics the growth of adjacent plates, but on a smaller scale.

Invariably, the cores of larger plates consist of low-temperature hydrous alteration minerals, mostly chlorite, and are mantled by a 10-30 µm rim of augite (e.g., Fig. 2.7c), like zoned pyroxene phenocrysts in the random acicular pyroxene spinifex and “string beef” textured examples. In the underlying Lordy Basalt Member, acicular pyroxene phenocrysts retain variably preserved augite

cores while in the Bassetts Volcanic Member, zoned pyroxene phenocrysts have augite rims, but retain variably preserved pigeonite cores, and by analogy we suggest that plate cores were also originally augite or pigeonite (see ‘mineral chemistry’ section).

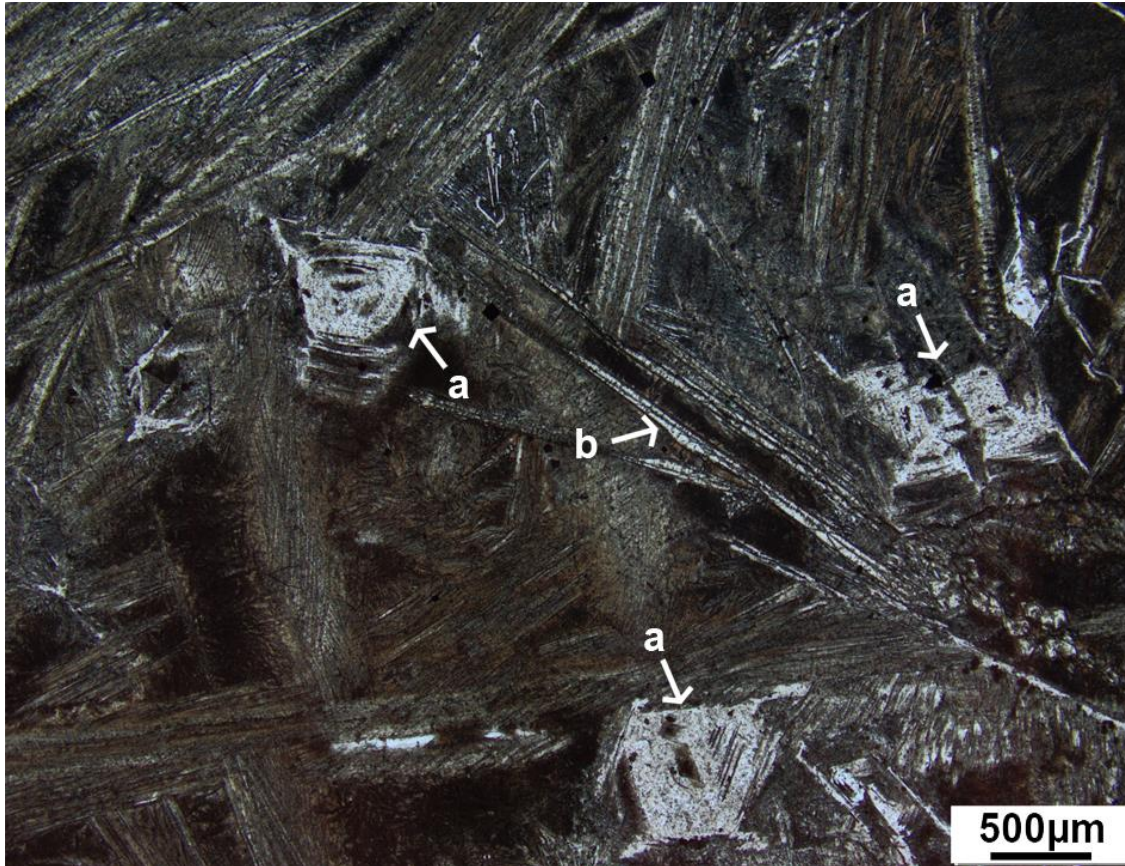


Figure. 2.10. Photomicrograph of A₂ Zone sample 209117 (PPL) highlighting (a) Skeletal olivine pseudomorphs and (b) thin plates of pyroxene forming sets in the matrix.

Although euhedral olivine is only found in the cumulate B₂ Zone, locally within the A₂ Zone there are skeletal olivine pseudomorphs (e.g., Fig. 2.10), which demonstrates that olivine was also a liquidus phase. Olivine phenocrysts that were not trapped between larger pyroxene plates probably settled downwards whilst continuing to crystalize into polyhedral forms; this is supported by similar FeO/MgO ratios in polyhedral olivine phenocrysts in B₂ Zone sample 209122, compared to the estimated liquid composition derived from A₁ Zone chilled margins (See ‘Whole rock chemistry’).

As with the olivine spinifex A₂₋₃ Zone, random platy pyroxene of the A₂ Zone grades downwards into ‘oriented’ platy pyroxene of A₃ Zone. The A₃ oriented platy pyroxene horizon was observed in two outcrops (649896mE, 7032746mN and 649754mE, 7032527mN, GDA94/MGA Z-50). In a

profile section through (i.e., X-Z or Y-Z section) both flows there is a gradational change from plate sets with a random orientation (i.e., A₂ Zone), down into sets where individual plates are all consistently oriented near-vertical (i.e., A₃ Zone). These sub-vertical plate sets spread out towards the bottom of the flow (Fig. 2.11a), yielding an overall steep-sided conical- or pyramid-like structure. In a section through the A₃ Zone, perpendicular to the vertical profile (i.e., X-Y section), plate sets intersect one another at oblique angles relative to adjacent plate sets (Fig. 2.11b) similarly to plate sets in a section at any angle through the A₂ Zone 'random' platy spinifex.

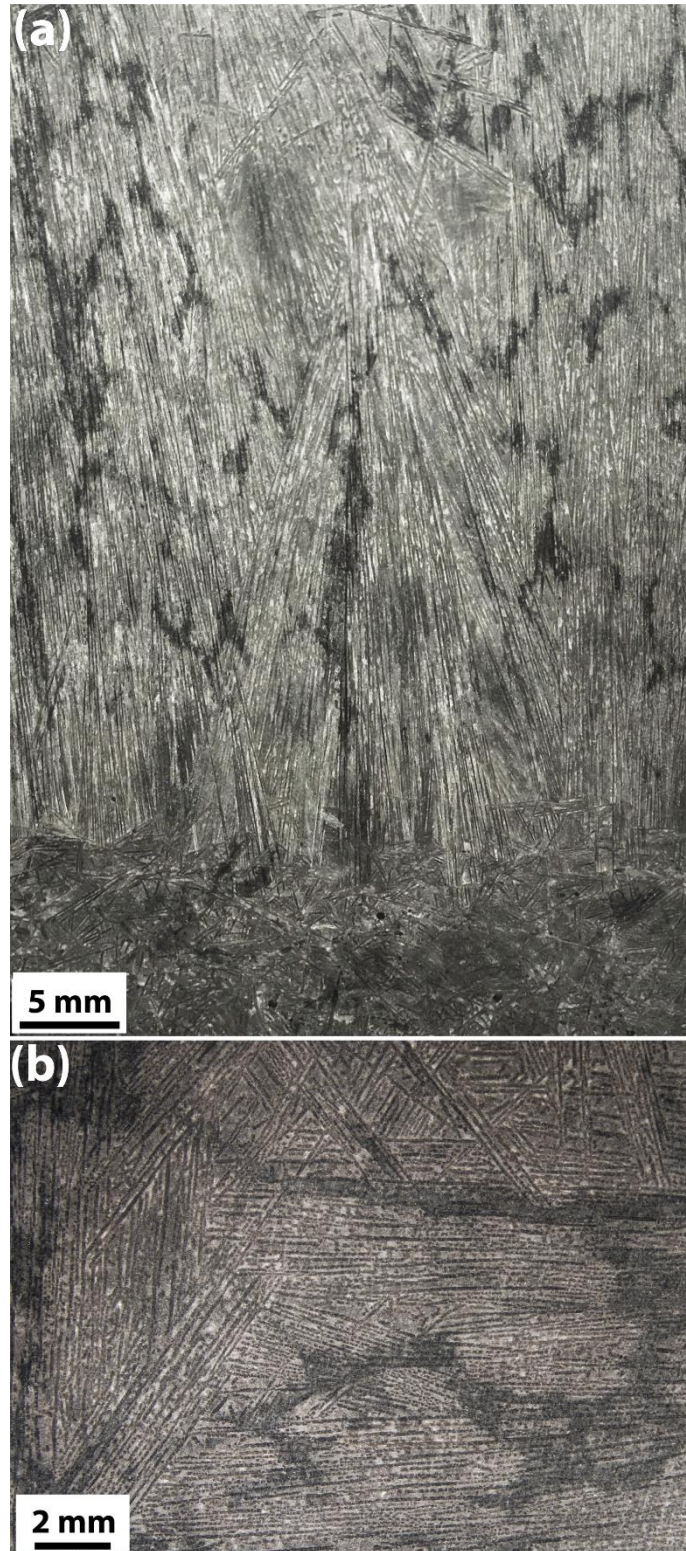


Figure. 2.11. Photographs of orthogonal sections through A₃ Zone oriented platy pyroxene spinifex from type section at Locality 1 (Fig 2.4; 649896mE, 7032746mN GDA94/MGA Z50): (a). interface between A₃ Zone oriented platy spinifex and A₄ Zone acicular pyroxene (section cut parallel to profile- i.e., X-Z or Y-Z); (b) oriented platy spinifex cut perpendicular to profile (i.e., X-Y section) showing obliquely oriented plate sets.

2.4.2.3. A₄ Zone – randomly oriented acicular pyroxene

The A₄ Zone has been identified at one outcrop at Locality 1. In this instance, it is composed predominantly of acicular pyroxene phenocrysts and sparse randomly oriented, fine grained platy pyroxene pseudomorphs like those in the A₂₋₃ Zones (Fig. 2.12). This zone is similar to the zone of acicular pyroxene phenocrysts reported by Arndt *et al.*, (2008) in a position below the A₃ Zone at the Proterozoic komatiitic basalt locality of Gilmour Island in Canada (their Fig. 2.23d. p43).

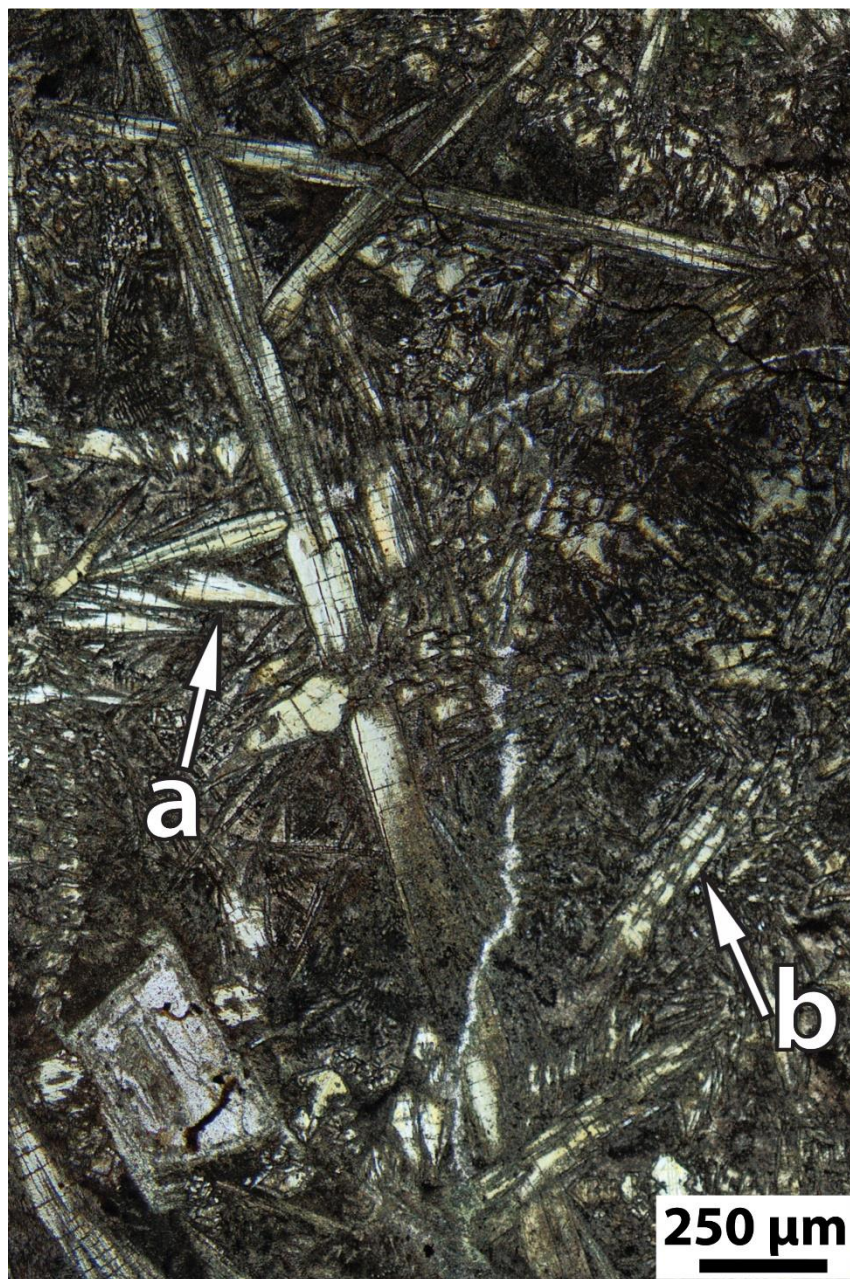


Figure. 2.12. Photomicrograph (PPL) of A₄ Zone at Locality 1 (649896mE, 7032746mN GDA94/MGA Z50) composed predominantly of (a) acicular zoned clinopyroxene phenocrysts in fine grained matrix, and locally (b) skeletal zoned pyroxene phenocrysts that resemble plates from A₂₋₃ Zone.

2.4.2.4. *B₂ Zone - orthocumulate*

A commonly documented feature in platy olivine spinifex textured flows is the occurrence of horizontally aligned skeletal olivine between the A₃ Zone and the B₂ Zone (e.g., Arndt 1986, Renner *et al.*, 1994, Kerr *et al.*, 1996) where it is typically referred to as B₁ Zone; we do not observe any occurrences of this horizon in the study area. However, in keeping with the terminology used widely for spinifex textured flows, we use the term 'B₂ Zone' for all cumulate facies rocks in the mapped area (Fig. 2.2). All examples of cumulate facies rocks that we observed in outcrop were similar in terms of their grain size and mineralogy, and all samples were homogeneous in their petrography and chemistry. The B₂ Zone is the most continuous and best preserved horizon within the sequence. Olivine is a cumulus phase, and forms polyhedral equant phenocrysts that are now mostly serpentinized but local unaltered relics remain (e.g., Fig. 2.13a). Olivine crystals frequently contain inclusions of euhedral, equant Cr-spinel, and vesicles of melt (Fig. 2.13b, c). Cr-spinel also occurs as a cumulus phenocrysts, in the interstices between olivine phenocrysts. Orthopyroxene and augite typically form large oikocrysts, which partially or fully overgrow smaller olivine and Cr-spinel chadacrysts, and these pyroxenes remain mostly unaltered. Orthopyroxene is also locally present as a cumulus phenocryst phase, but these are typically serpentinized. Locally, orthopyroxene and augite form coarsely branching textures (Fig. 2.13d), loosely resembling but coarser than typical plate dimensions at Locality 1. Similar crystal morphologies have been recognized in fractionated gabbroic layers below A₂₋₃ Zones in komatiite flows in the Archean Abitibi Greenstone Belt (Arndt 1977). Plagioclase and augite have crystallized as fibrous intergrowths in domains of residual liquid. Based on these observations, the crystallization sequence within the B₂ Zone was: Cr-spinel→Olivine→Orthopyroxene→Orthopyroxene+Augite→Augite+Plagioclase.

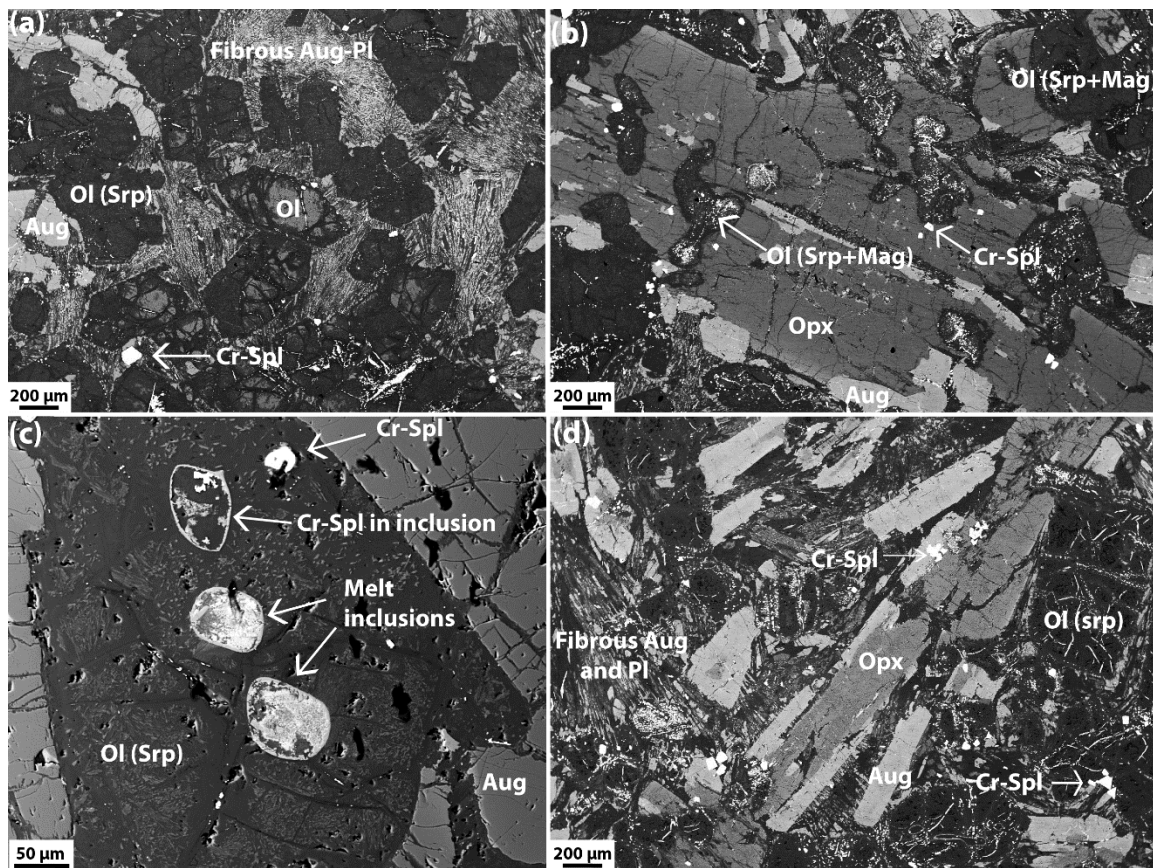


Figure. 2.13 BSE images of B₂ Zone cumulate: (a) Relict olivine in serpentinized polyhedral phenocrysts. Matrix is fibrous dendrites of plagioclase and augite. White euheral phenocrysts are Cr-spinel, lighter oikocrysts surrounding olivine (top left) are augite (sample 209122); (b) Poikilitic orthopyroxene (Opx) and augite, and serpentine after olivine, some relict olivine. Poikilitic habit pyroxene only encloses sub-hedral olivine, suggesting it came before olivine formed euheral crystal habits. Olivine locally encloses euheral Cr-spinel, and hence must have crystallized after Cr-spinel (sample 209122); (c) Olivine locally contains melt inclusions that are typically strongly altered. The inclusions in turn locally contain fine, euheral Cr-spinel microphenocrysts (sample 209122); (d) Coarsely branching pyroxene (compared to A₂₋₃ Zone) (sample 209116). In images (a, b and d) the cumulate crystals are set in a matrix with a distinctly fibrous texture. The darker regions of this fibrous matrix are plagioclase whereas lighter regions are augite.

2.4.3. Acicular pyroxene habits

2.4.3.1. *Random acicular pyroxene spinifex*

At Localities 1 and 2 (Fig. 2.1) there are excellent examples of basaltic flows that contain abundant acicular pyroxene phenocrysts (Table 2.1, see also ‘vitrophyric basalts’ in Fig. 2.2). Their micro- to macro-scale features are comparable to many komatiitic basalt sequences in the Archean and Proterozoic (e.g., Arndt *et al.*, 1977, Shimizu *et al.*, 2005, Arndt *et al.*, 2008), Phanerozoic boninites (e.g., Wood 1980, Natland 1982, Bloomer and Hawkins 1987, Taylor *et al.*, 1994), and even quartz-normative lunar basalts (e.g., Lofgren *et al.*, 1975). Most of these ‘needly’ textured horizons are characterized by abundant randomly oriented acicular pyroxene phenocrysts set in a fine-grained matrix of devitrified glass or intergrown fibrous or plumose augite and plagioclase. An example of this texture in a hand sample from Locality 1 is shown in Fig. 2.14a. In this example, phenocrysts range between <0.5 – 2 cm, but throughout the study area there are locally megacrysts up to 10 cm. Pyroxene phenocrysts are typically compositionally zoned with augite rims and pigeonite cores; most examples are now chlorite, but some retain unaltered pigeonite, and in these instances the rims and cores are not in crystallographic continuity. Pigeonite cores and augite rims are themselves also internally chemically zoned, becoming increasingly Fe-Al rich, and Mg poor outwards towards the crystal edge. Many of the phenocrysts exhibit simple twinning, and occasionally grow cruciform shaped phenocrysts (Fig. 2.14b, c).

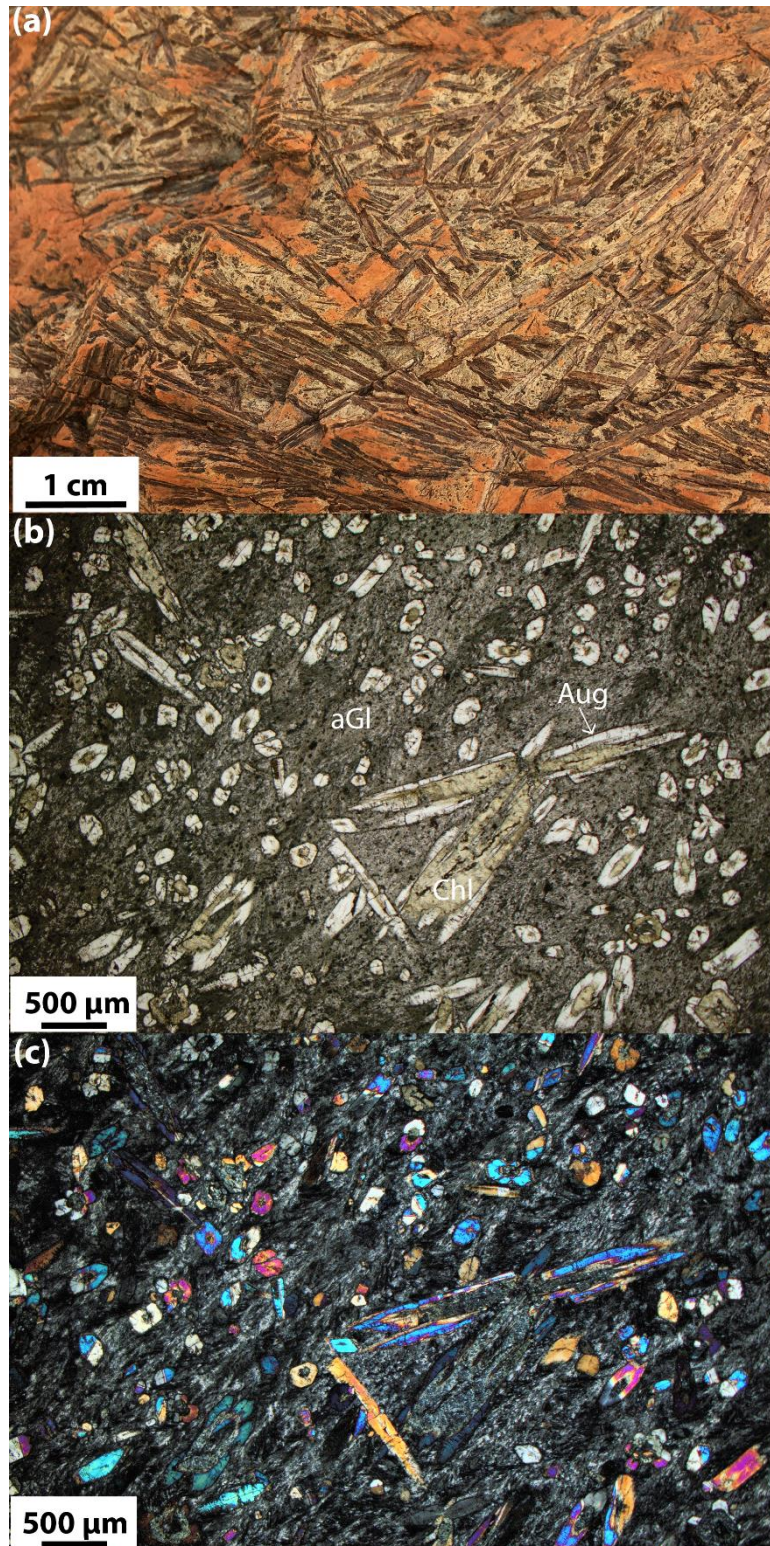


Figure. 2.14. Images showing random acicular pyroxene texture: (a) Field photograph of hand sample at Locality 1 (650091mE, 7033593mN GDA94/MGA Z50); (b, c) photomicrographs from Locality 2 (652092mE, 7049072mN, GDA94/MGA Z50). Zoned clinopyroxene phenocrysts are elongate in the direction of the crystallographic c-axis, with augite rims and chloritized cores (Chl). Note the cruciform twinned phenocryst in the centre right of the images. (b) PPL; (c) Cross polarized light (XPL).

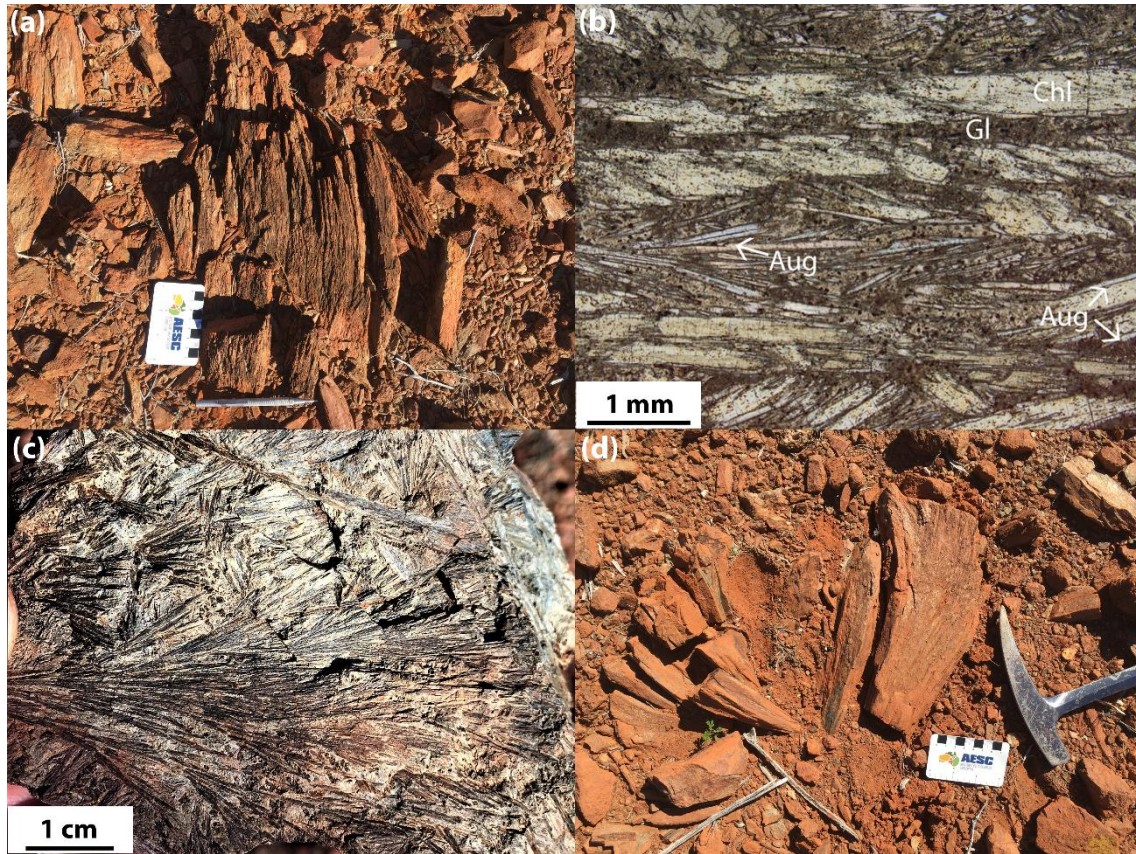


Figure. 2.15. Images of string-beef textured SHMB (sample 209115); (a) Field photograph of outcrop at Locality 1 (649744mE, 7032393mN GDA94/MGA Z50); (b) Photomicrograph (in plane polarized light) of thin section that is cut parallel to the long axis of dominant crystal orientations. Note the zonation of clinopyroxene phenocrysts, and the low volume of interstitial matrix material; (c) Coarsely branching morphology of acicular pyroxenes at Locality 1 (approx. 649885mE/7032525mN GDA94/MGA Z50); (d) String beef cone structure at Locality 1 (649811mE, 7032459mN GDA94/MGA Z50).

2.4.3.2. 'String-beef' (AKA oriented pyroxene spinifex)

A variation of acicular pyroxene spinifex is string-beef texture, documented first in Canada by Arndt *et al.* (1977), which is composed almost entirely of tight clusters of acicular shaped pyroxene phenocrysts with little or no matrix material. At Locality 1 there are well preserved, $\lesssim 5$ m thick horizons of string-beef textured basalts (e.g., Fig. 2.15a). Individual pyroxene crystals are typically $< 500 \mu\text{m}$ in diameter and $\gtrsim 5$ cm long (Fig. 2.15b). Locally, there are examples where the phenocrysts are less densely clustered, and phenocrysts branch/fan out from a central nucleus (e.g., Fig. 2.15c). On the outcrop scale this tendency to branch and fan out can form conical structures that are 10-50 cm in height (e.g., Fig. 2.15d), similar to those described for the Witkop Formation in the Nondweni Greenstone Belt (Wilson and Versfeld 1994). In that example, Wilson and Versfeld suggested that the

cone structures give a reliable way up direction; pyroxene crystals branch out and grow away from the chilled margin into the liquid below.

2.4.4. Dendritic pyroxene habits

Dendritic textures are locally preserved at Localities 1 and 2 in platy pyroxene spinifex, and vitrophyric textured basalts. In the platy pyroxene spinifex samples, dendritic pyroxene typically occupies the interstitial spaces between plate sets and it is surrounded by altered, devitrified glass. Dendritic pyroxene superficially resembles platy pyroxene crystals, but at a finer scale (e.g., Fig. 2.16a). The dendrites have similar X-ray intensities to augite plate rims, and smaller augite-only plates (see 'X-ray Computed Tomography'), and EPMA indicates they have similar compositions. In vitrophyric textured samples (221629 and 221701) dendrites are also surrounded by devitrified glass and are similarly represented by several orders of scale ($<5\text{ }\mu\text{m}$ – $30\text{ }\mu\text{m}$ wide). However, in these cases dendrites have complicated geometries that include central chains that vary between straight and curved, and bifurcations that are typically at right angles to the central chain (e.g., Fig. 2.16b). In our samples, the dendritic pyroxene appears to have crystalized in the interstices between plates and needles prior to the remaining liquid quenching to glass.

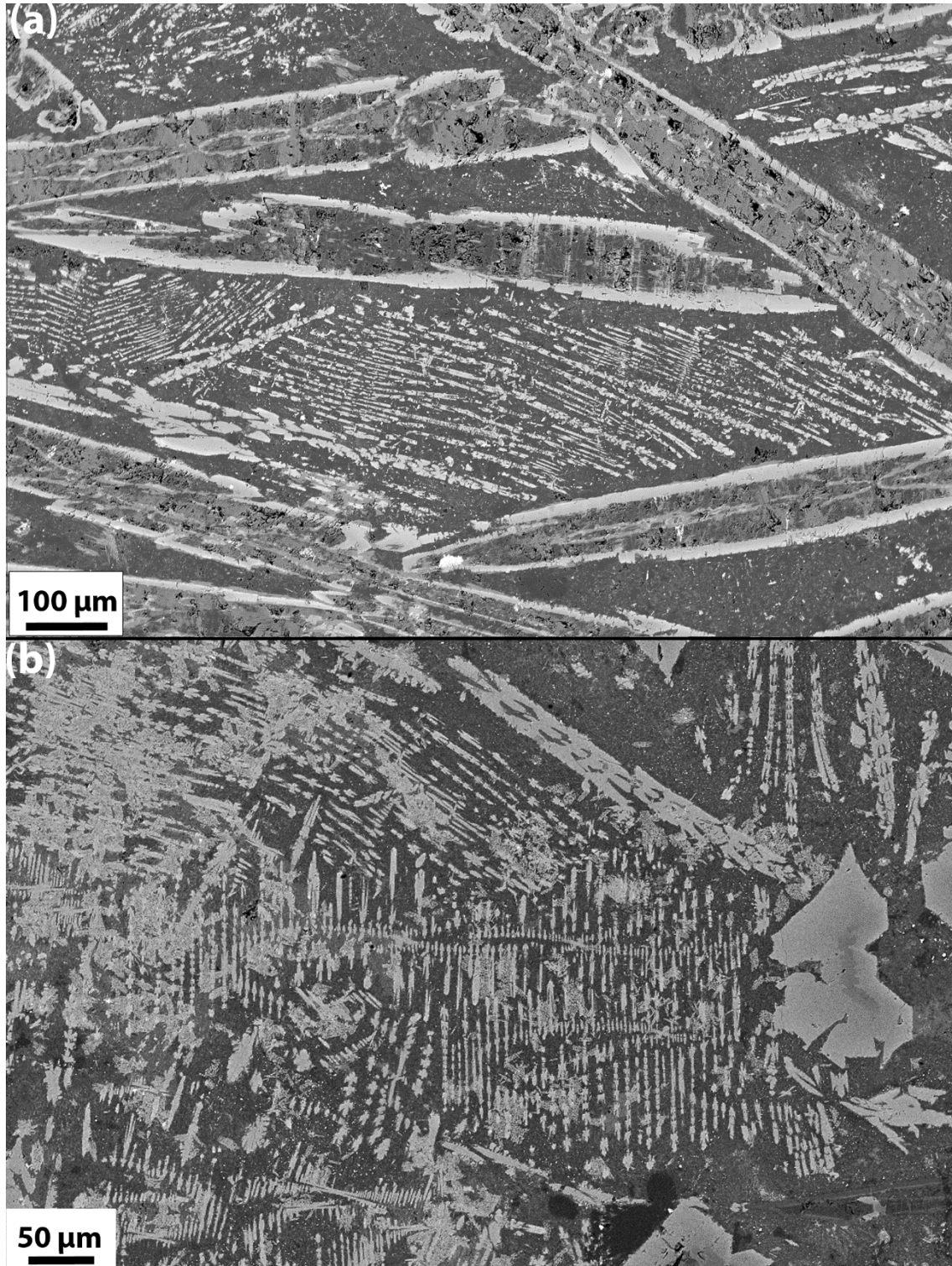


Figure. 2.16. BSE images of dendritic pyroxene forms: (a) A2 Zone sample (209114; Locality 1). Dendrites occupy the space between 1st order plates. Note that dendrites have similar x-ray intensity to plate rims, and occur in sets of parallel chains/crystals. In 3D, these chains probably also define plates, but they are smaller than the resolution of our X-ray CT data; (b) Vitrophyric example from Locality 2 (within the Bassets Volcanic Member; sample 221701). Note the similar morphology between skeletal crystals and dendrites, and the curvaceous central chains of several dendrites.

2.5. X-RAY COMPUTED TOMOGRAPHY

To address concerns over whether the pyroxenes were truly platy, rather than being aggregates of parallel-oriented acicular crystals, we performed an X-ray computed tomography (X-ray CT) scan of a small cylindrical sub-sample of sample 209114. We have included videos to enable a 3D view of the whole volume analysed (see Electronic Appendix 2.1).

Representative plates were traced within the sample using the manual segmentation tool within Avizo®: examples of these segmented plates are pictured in Fig. 2.17a and measurements are reported in Table 2.1. Cr-spinel occurs throughout the volume, easily recognized by its high linear attenuation coefficient values (high x-ray intensity values); crystals are typically euhedral and range from 15-80 μm in diameter. Material interstitial to pyroxene and spinel crystals is altered devitrified glass. Pyroxene crystals can be divided into two broad categories: those with a thickness of $\geq 95 \mu\text{m}$ which contain an altered core component (1st order), and those with a thickness $\leq 70 \mu\text{m}$ and do not contain an altered core (2nd order).

For larger (1st order) plates ($>500 \mu\text{m}$ length and/or width) sections spaced at $25 \mu\text{m}$ were digitized, and then the intervals between were interpolated and the resulting volume was inspected on each interpolated section to ensure that it honours the plate boundaries. For smaller (2nd order) plates ($<500 \mu\text{m}$ length and/or width) every section was digitized manually. 1st order plates intersect one another at oblique angles (e.g., Fig. 2.17b), but in some instances, they are only partially truncated by one another and continue beyond the intersection. The largest of the 1st order plates extend beyond the volume that was imaged, and we only report minimum lengths and/or widths for these plates ($>6610 \mu\text{m}$ and $>5850 \mu\text{m}$ respectively), although the thicknesses for these plates are well constrained and measurements vary from 95-165 μm . 1st order plates are locally limited in one or more direction by the crystal faces of other 1st order plates. In some instances, plates develop acicular protrusions on their edges, particularly where they protrude into glassier domains of the sample. Acicular protrusions from the plate margin are shown for the 3D digitized crystal in Fig. 2.17c. Parallel stacked plates (in a plate set) also locally transition to domains of similarly aligned acicular crystals (see Video 1, 2 in Electronic Appendix 2.1). Figure 2.27d shows an example of a plate to acicular crystal transition in a

1st order plate set; six acicular crystals can be observed in the same plane of the adjacent plate, and these are oriented in one direction, parallel to one another in the crystallographic *c*-axis, and in crystallographic continuity.

2nd order plates do not crosscut 1st order plates; they typically form discrete plates that are confined within the interstitial spaces between oblique 1st order plate sets (Figs. 2.17e, f). 2nd order plates are typically much smaller than 1st order plates in all dimensions, with length 190-1460 μm, width 100-710 μm, and thickness 30-70 μm. These relationships indicate that 1st order sets crystallized before 2nd order sets. 2nd order plates have the same X-ray intensities as the rims of 1st order plates and are similar in composition (see 'Mineral chemistry').

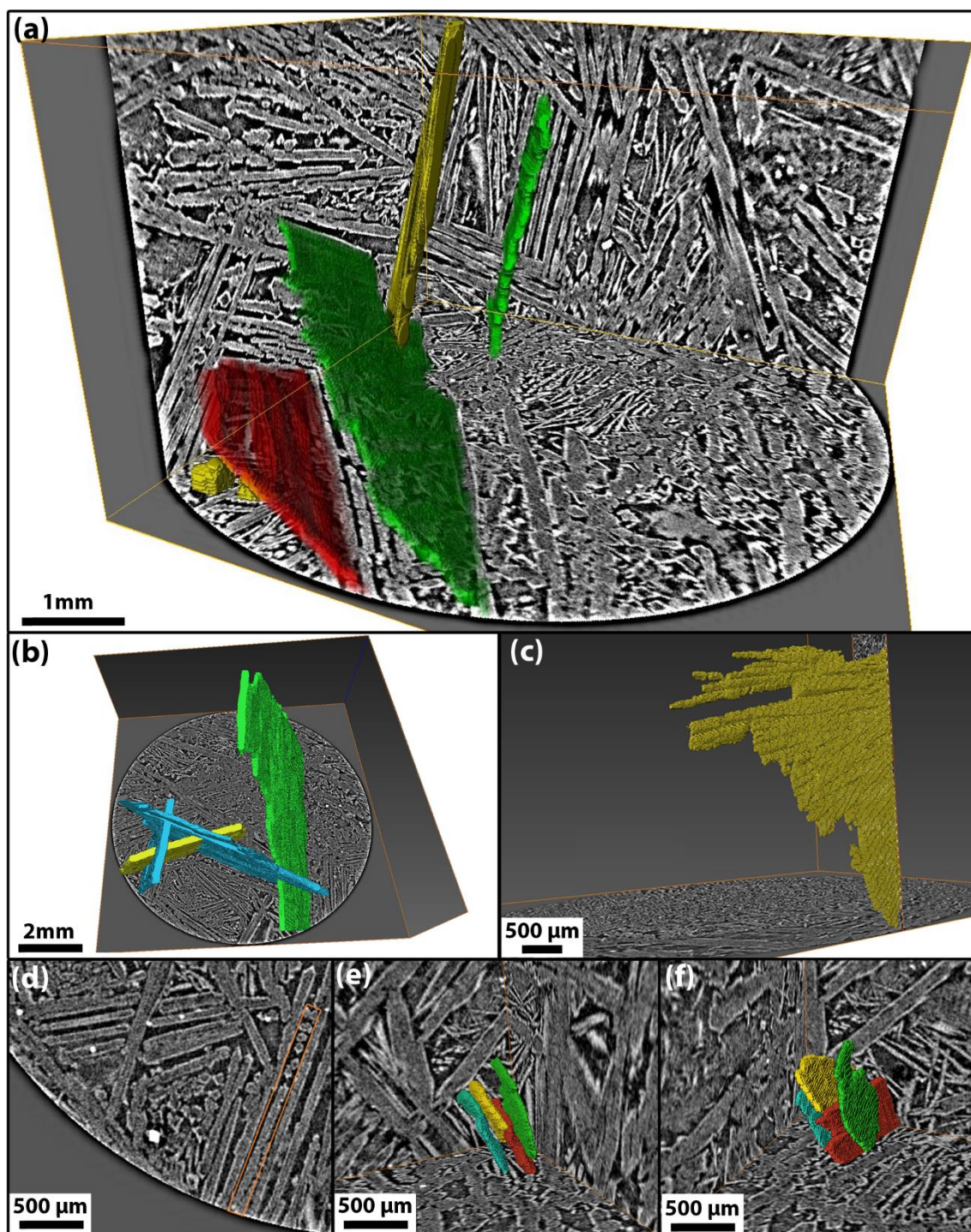


Figure. 2.17. Three-dimensional (3D) characterization of A₂ Zone sample 209114. Background images have a B-spline background detection correction applied to remove background illumination and an Unsharp Masking filter was applied to sharpen the edges of features. The pixel intensity correlates to pale grey = augite rim, mid grey = chloritized core, dark grey = devitrified glass, white = Cr-spinel. Individual images: (a) Representative 1st order pyroxene crystals with platy aspect ratios; (b) 1st order pyroxene crystals demonstrating intersecting relationships between obliquely oriented plates; (c) 1st order pyroxene plate with acicular protrusions at one margin (this plate extends beyond scanned volume); (d) acicular crystals oriented in the same plane as plate; (e) and (f) illustrate a 2nd order plate set viewed from slightly oblique views (note that plates are truncated by 1st order plates observable in the background image).

Discrete acicular pyroxene crystals occur throughout the volume, but in greater abundance in glassier domains. As with plates, acicular crystals typically terminate abruptly where they meet obliquely oriented plates. They are typically oriented sub-parallel to adjacent plate sets, and they are locally in crystallographic continuity, indicating that plates and acicular crystals grew in association with one another. There are examples of discrete acicular crystals associated with plates of both 1st and 2nd order scales. Representative 1st order acicular crystals range from 1240->1700 μm long, while 2nd order acicular crystals range from 150-730 μm long. Width and thickness (which are approximately equal) range from 120-245 μm for 1st order acicular crystals and 50-55 μm for 2nd order acicular crystals.

In 1st order sets, both plates and acicular crystals have rims of higher x-ray intensity that surround a core of lower intensity; these correlate to the augite rims, and altered cores described above and analysed by EPMA (see 'Mineral chemistry'), the rims range in thickness from 15-25 μm . Second order plates and acicular crystals are characterized by similarly high x-ray intensity values to 1st order, augite plate rims, but do not have the lower x-ray intensity, altered cores. Further interrogation of their features is limited by the resolution of this data, but BSE images of thin sections of the same sample show the 2nd order crystals to be skeletal. Representative measurements of the thickness of 2nd order crystals are approximately 30 – 70 μm , which is roughly equivalent to the average combined thickness of two rims, in the case of 1st order plates and acicular crystals.

2.6. MINERAL CHEMISTRY

2.6.1. Electron Probe Microanalysis (EPMA)

The following is a description of the chemical variation for minerals from the A₂ Zone (sample 209114), and B₂ Zone (sample 209122). Table 2.3 summarizes the average compositions obtained.

In sample 209114, plate rims have close to ideal pyroxene stoichiometry, augite compositions, and oxide totals between 98.3–99.85 wt% (Fig. 2.18, Table 2.3). They have lower Mg-numbers (47–76, avg 67) and compatible elements Cr₂O₃ and NiO (≤ 0.11 , ≤ 0.07 wt% respectively) compared to B₂ Zone augites (see below), but higher Al₂O₃ (4.0–15.5, avg 7.5 wt%) and TiO₂ (0.4–1.3, avg 0.9 wt%), and are probably due to the different crystallization rates in their respective Zones. Coish and Taylor (1979) suggest that Al-Ti content is directly related to cooling rate and that under high cooling rates, crystal growth in preferred orientations exceeds the diffusion rate of Al and Ti away from growth surfaces, and they are effectively trapped within the crystal structure. High Al-Ti in pyroxene has also been observed in other spinifex textured flows (e.g., Arndt *et al.*, 1977, Arndt and Fleet 1979, Kareem 2005, Barr *et al.*, 2009, Bouquain *et al.*, 2009), and in rapidly cooled boninites (e.g., Coish and Taylor 1979, Natland 1982, Ohnenstetter and Brown 1992).

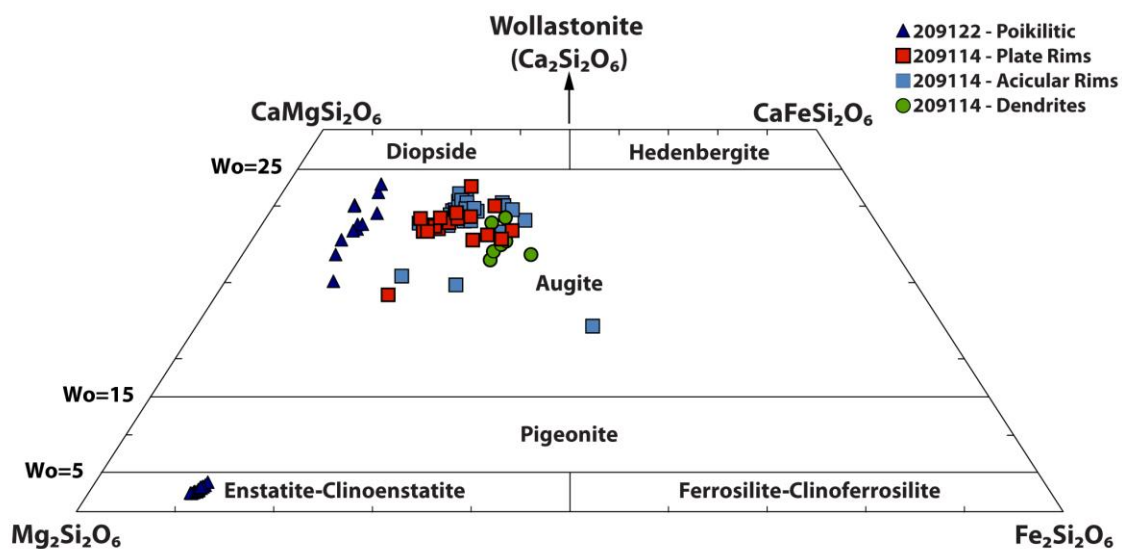


Figure. 2.18. Pyroxene Quadrilateral diagram (after Morimoto *et al.*, 1988). 209114 plate cores are all altered.

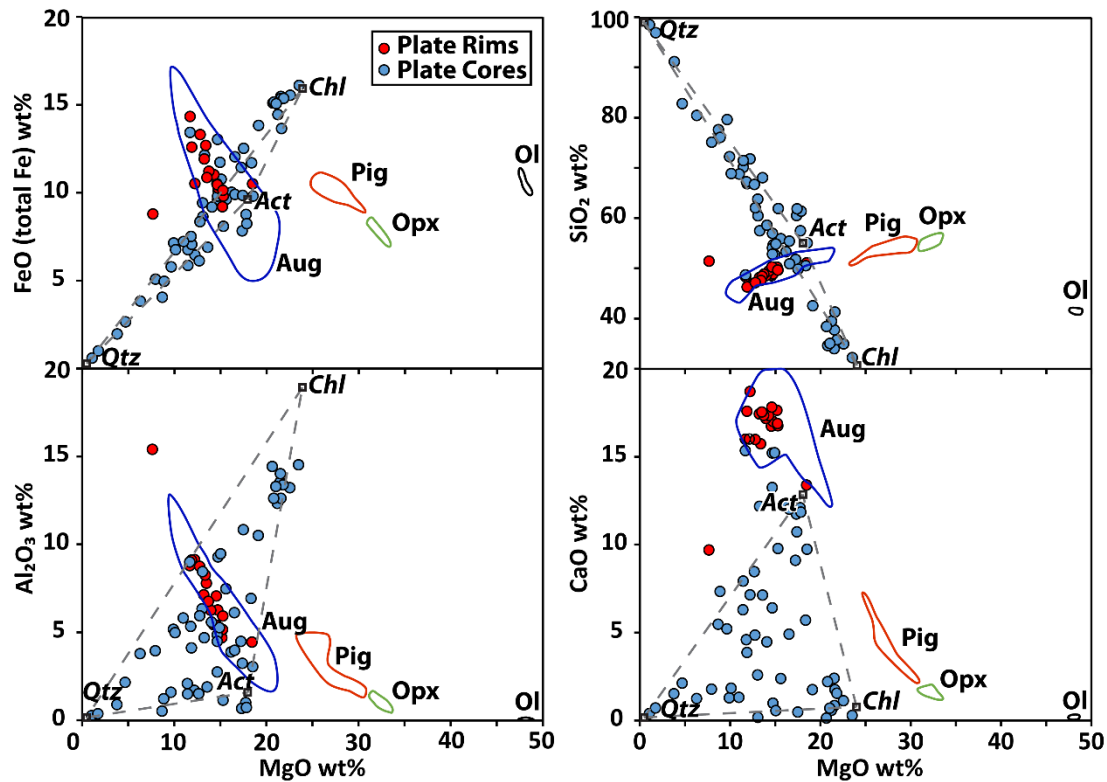


Figure 2.19. Major element variation diagrams for EPMA point analyses collected in traverses across platy crystals in sample 209114. Black squares give likely metamorphic alteration mineral compositions and grey dashed lines are tie lines between these compositions; *Chl* – Chlorite analysis 30 from Deer, Howie and Zussman (1962), their Table 25; *Act* – actinolite analysis 6 from Deer, Howie and Zussman (2013), their Table 23; *Qtz* – Quartz (100% SiO₂). Outlined fields are EPMA composition ranges for fresh pyroxene and relict olivine in Meekatharra Formation samples from the Polelle Syncline analysed using similar operating conditions and standards.

Plate core material was analysed by a combination of EPMA point analyses, and EPMA maps with mixed results (analyses are included in Electronic Appendix 2.2), probably because of the very fine grained, mixed nature of the alteration minerals. Variation diagrams of major element oxides for EPMA point analyses are plotted in Fig. 2.19, they indicate that the alteration products are mostly a mixture between chlorite and quartz, and potentially contain minor amounts of actinolite or weakly altered augite, but they do not appear to correlate to serpentine minerals, which are typically >40 wt% MgO (e.g., Deer *et al.*, 2013). The average compositions are included in Table 2.3; they have large standard deviations, due to the altered, heterogeneous nature of the mineralogy, but as an approximation they show the cores to contain high SiO₂, Al₂O₃, FeO (total Fe) and MgO, and low TiO₂, Cr₂O₃ and CaO. The plate cores have low oxide totals (90.8%), indicating that there has been a net loss of cations from the plate cores, which was presumably incurred during chloritization by the addition of H₂O, but strongly mobile elements such as K₂O and Na₂O are typically below detection

levels, and the FeO/MgO ratio is similar between the plate cores and rims (0.69 vs 0.79 respectively), so we infer that cation exchange was mostly restricted to within individual cores.

The main cations are Si, Al, Mg and Fe, in quantities that are indicative of pyroxene or amphibole chemistry. Figure 2.19 shows plate core analyses overlap with the field for augite for the main cation elements except CaO; if plate cores have experienced a moderate net loss of CaO, then augite is a plausible precursor mineral. Similarly, if plate cores have experienced a moderate net loss of MgO then pigeonite is a plausible precursor mineral. Olivine is not considered a likely precursor mineral because Si and Al are too high, and MgO and Ni are too low. The closest amphibole composition is anthophyllite, and while we do not rule it out as a possible precursor, we could find no documented volcanic examples of anthophyllite. In contrast, zoned clinopyroxene with pigeonite cores and augite rims are well documented in Archean komatiites and high-Mg basalts (e.g., Arndt *et al.*, 1977, Puchtel *et al.*, 1996, Stiegler *et al.*, 2012), and in these rock types pigeonite alters to chlorite more readily than augite (e.g., Arndt and Fleet, 1979). We have identified variably preserved pigeonite in the cores of zoned phenocrysts in the underlying Bassetts Volcanic Member. Those pigeonites had high-Al compositions (~3.6 wt% Al₂O₃; sample 209130, Electronic Appendix 2.2), and in examples where pigeonite cores were partially altered, they have altered to similar chlorite-dominated assemblages.

All B₂ Zone pyroxene analyses are from poikilitic crystals. They form a trend on the pyroxene quadrilateral diagram that is relatively straight, although discontinuous through the miscibility gap, with orthopyroxene and augite compositions (Fig 2.18, Table 2.3). Compared to A₂ Zone augites, B₂ Zone augites have higher Mg-numbers (82–86, avg 85) and higher concentrations of compatible elements Cr₂O₃, and NiO (0.09–0.11, and 0.11–0.79 wt% respectively), but lower concentrations of Al₂O₃ (1.7–4.8; avg 3.4 wt%) and TiO₂ (0.25–0.7, avg 0.45 wt%). Orthopyroxenes have high Mg-numbers (88–89) and high concentrations of compatible elements Cr₂O₃ (0.41–0.68, avg 0.56 wt%) and NiO (0.13–0.17, avg 0.15 wt%), and very low concentrations of incompatible elements Al₂O₃ (0.5–1.4, avg 1.0 wt%) and TiO₂ (0.08–0.15, avg 0.11 wt%). The average composition for

orthopyroxene is $\text{En}_{86.2}$, $\text{Fs}_{10.9}$ and $\text{Wo}_{2.9}$, classifying it as enstatite after the Morimoto *et al.*, (1988) scheme.

Olivine compositions from the B₂ Zone range from $\text{Fo}_{88.2-89.6}$ and average $\text{Fo}_{89.1}$. NiO in olivine ranges from 0.37–0.41 wt% and Cr_2O_3 ranges from 0.1–0.25 wt%. Stoichiometry for olivine is close to ideal, with a total of 2.99 cations per 4 Oxygens including 1.01 Si cation. As expected, average concentrations of incompatible elements Al_2O_3 and TiO_2 are very low, (0.06 and 0.01 wt% respectively). Olivine was not found in the A₂ Zone.

Ferric iron content of Cr-spinel has been calculated using the method of Barnes and Roeder (2001). Ratios of $\text{Fe}^{3+} / (\text{Cr} + \text{Al} + \text{Fe}^{3+})$ are exceptionally low when compared to global datasets of terrestrial spinel compositions (e.g., Barnes and Roeder 2001), averaging 0.08 and 0.09 for A₂ and B₂ Zone Cr-spinels respectively. Ratios of $\text{Cr} / (\text{Cr} + \text{Al})$ are exceptionally high, with averages of 0.89 for both A₂ and B₂ Zone Cr-spinels. Ratios of $\text{Fe}^{2+} / (\text{Fe}^{2+} + \text{Mg})$ are also relatively high at 0.41 and 0.30 for A₂ and B₂ Zone Cr-spinels respectively. Barnes and Roeder (2001) presented two diagrams for discriminating between various terrestrial volcanic settings: $\text{Cr} / (\text{Cr} + \text{Al})$ vs $\text{Fe}^{2+} / (\text{Fe}^{2+} + \text{Mg})$ and $\text{Fe}^{3+} / (\text{Cr} + \text{Al} + \text{Fe}^{3+})$ vs $\text{Fe}^{2+} / (\text{Fe}^{2+} + \text{Mg})$. Cr-spinels from Locality 1 plot in or close to the p90 contours for komatiite for both discrimination diagrams, but they also border the p90 contours for both boninite and island arc basalts, erring to lower $\text{Fe}^{2+} / (\text{Fe}^{2+} + \text{Mg})$ values among the latter two populations.

2.7. WHOLE ROCK CHEMISTRY

Geochemical variation is discussed with emphasis on elements considered immobile (e.g., major elements, Cr and Ni). Whole rock chemical analyses for 19 samples collected from Locality 1 (Fig 2.2) are reported in Table 2.4, including 18 volcanic rocks and 1 sedimentary rock from below the footwall contact. LOI values are ≤ 4.4 wt% for non-cumulate rocks (low to moderate for Archean greenstones), and approximately 7 wt% for orthocumulates, reflecting hydration in association with the serpentinization process. Variation diagrams for MgO vs. Al_2O_3 , CaO, TiO_2 , SiO_2 , Cr and Ni are presented in Fig. 2.20 and MgO vs FeO (total Fe as Fe^{2+}) is presented in Fig. 2.21.

Two samples from the A₁ Zone (209118 and 221722) are fine grained chilled flow tops that we interpret as representative of initial liquid compositions (Table 2.4). These rocks have compositions between those of the A₂ and B₂ Zone samples (Figs. 2.21, 2.22), because of olivine fractionation and accumulation in those Zones respectively. They contain 51 and 52 wt% SiO_2 , 15.8 and 14.4 wt% MgO, and their Mg-numbers are 73 and 71 respectively. They both contain 9 wt% Al_2O_3 and 0.6 wt% TiO_2 , with $\text{Al}_2\text{O}_3/\text{TiO}_2$ ratios of 14.6 (i.e., moderately Al-depleted relative to chondrite).

The string-beef sample and three A₂ Zone samples have compositions ranging from 53 – 57 wt% SiO_2 , 14.3 – 14.8 wt% MgO, and Mg-numbers range from 68 – 74. They contain abundant zoned clinopyroxene (>90% in the case of the string beef sample), and have fractionated a small amount of olivine, so they are probably enriched in SiO_2 and slightly depleted in MgO relative to the initial liquid compositions. Al_2O_3 has a narrow range from 9.9 – 10.6 wt% and TiO_2 is consistently around 0.65 wt%, with $\text{Al}_2\text{O}_3/\text{TiO}_2$ in these samples ranging from 15 – 16.5. Campbell and Arndt (1982) suggest that spinifex textured rocks such as these contain cumulus pyroxene crystals, and can be regarded as pyroxene cumulates, and therefore they do not reflect frozen liquid compositions.

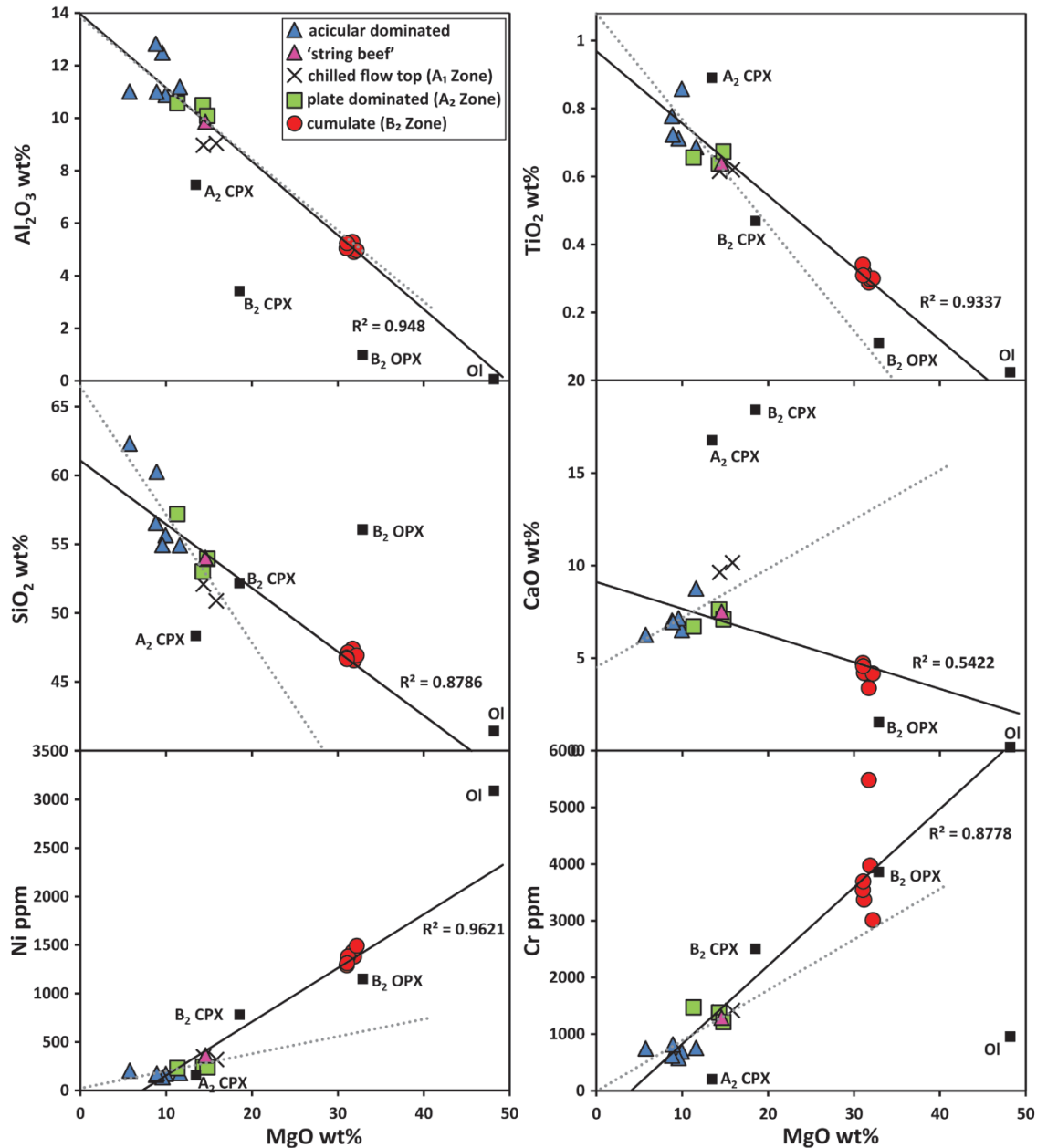


Figure 2.20. Major element (anhydrous and normalised to 100%) variation digrams for whole rock analyses of 18 volcanic samples from Locality 1. Solid line is regression line for all samples in the cogenetic SHMB suite. The dashed grey line is a regression curve for non-cumulate samples. Black squares are averages of measured compositions for A₂ Zone augite and B₂ Zone olivine, poikilitic Opx, poikilitic augite from EPMA analyses. Regression lines for MgO vs Al₂O₃, TiO₂, and Ni show strong correlations ($R^2 \geq 0.93$) and project close to the measured compositions of olivine in the B₂ Zone (sample 209122), demonstrating olivine control for these elements. Whereas MgO vs SiO₂ and Cr have only moderate correlations ($R^2 = 0.86$ and 0.88 respectively), which implies a more complicated mineralogical control; probably pyroxene and Cr-spinel respectively. CaO vs MgO has poor correlation ($R^2 = 0.54$); this may reflect post-emplacment CaO mobility, or else possibly a more complicated mineralogical control.

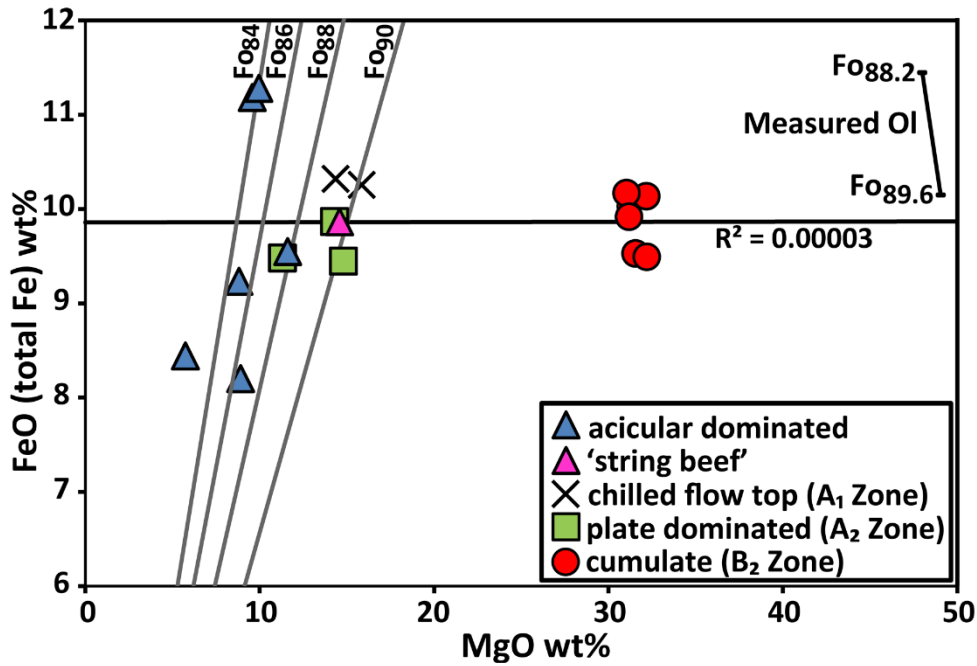


Figure. 2.21. FeO (total Fe) wt% vs MgO wt% (anhydrous and normalised to 100%) (after Barnes 2006). Symbols are the same as for Fig. 2.20, but the range of Fo values for olivine EPMA analyses (from sample 209122, B₂ Zone cumulate) are given rather than the average. Solid grey diagonal lines represent FeO/MgO ratios of liquids in equilibrium with a particular olivine Fo content, as calculated by the equation:

$K_D = \frac{FeO}{MgO} Ol \times \frac{FeO}{MgO} liquid = 0.3$ (after Roeder and Emslie 1970 at 0.1 MPa). There is good agreement between the calculated FeO/MgO ratio for melts in equilibrium with measured olivine compositions (Fo_{88.2}-Fo_{89.6}) from sample 209122, and FeO/MgO ratio for the chilled upper margin samples (in equilibrium with Fo_{90.2}).

All six B₂ Zone samples are olivine–orthopyroxene–augite–Cr–Spinel orthocumulates. They have homogeneous compositions, with SiO₂ consistently 47 wt% and MgO ranging narrowly from 31 – 32.2 wt%. Mg-number ranges from 85 – 86. Al₂O₃ ranges from 3.9 – 4.2 wt% and TiO₂ is consistently ~0.3 wt%, with Al₂O₃/TiO₂ ranging from 14.8 – 18.4. B₂ Zone samples plot distinctly lower for SiO₂ and TiO₂, and higher for Ni than would be expected by simply extrapolating along the non-cumulate regression line (dashed line in Fig. 2.20), which is probably due to a combination of fractionation/accumulation of olivine and pyroxene and mobility of MgO and other elements during alteration. Within the B₂ Zone samples, there is a large spread in Cr abundance, ranging from 3010–5480 ppm, which produces a vertical trend in this sub-population on the MgO vs Cr diagram (Fig. 2.20), indicating Cr-spinel accumulation.

The six vitrophyric basalt samples from above the spinifex textured sequence (see Fig 2.2) range from 55 – 62 wt% SiO₂ and 5.6 – 11.7 wt% MgO. They contain 10.9 – 12.8 wt% Al₂O₃ and 0.7 – 1.0

wt% TiO₂, with Al₂O₃/TiO₂ ratios of 10.9-17.5 (i.e., strongly Al-depleted to relatively Al-undepleted).

Because the samples are mostly fine grained, we do not consider them to have accumulated significant pyroxene, like the underlying spinifex textured rocks. The compositions of vitrophyric textured rocks are therefore representative of their respective liquids, which are notably more siliceous and less magnesian than the composition that we have inferred for the spinifex textured rocks from A₁ zone chilled margins.

Figure 2.22 demonstrates that chilled liquid, platy pyroxene and string-beef samples plot on or close to FeO/MgO ratios that are in equilibrium with olivine of Fo₈₈₋₉₀ compositions, which approximates the measured olivine compositions from B₂ zone sample 209122. In comparison, vitrophyric basalts have higher FeO/MgO ratios and their liquid compositions were in equilibrium with less magnesian olivine (Fo₈₄₋₈₈), indicating that their liquid compositions have fractionated olivine and pyroxene.

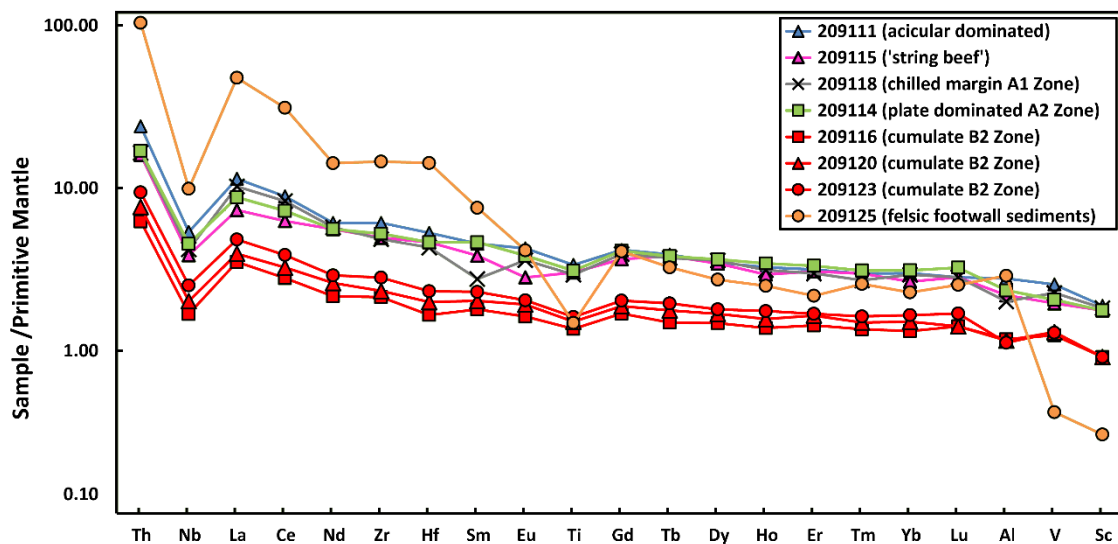


Figure. 2.22. Multi-element plot of representative samples normalised to primitive mantle (normalising values after Palme and O'Neill, 2014).

Although the samples from Locality 1 are relatively unaltered, compared with most Archean greenstones, the different sample groups show variable enrichment in the mobile incompatible elements (e.g., Cs, Rb, Ba; Fig. 2.22), which is probably alteration related. In contrast, the relatively immobile incompatible elements (e.g., Th, Nb, Zr, Hf, and REE) increase in abundance systematically

with MgO, indicating olivine control, and the different portions of the flow have identical shaped mantle normalised multi-element patterns (Fig. 2.22). The significant feature of all patterns is the light REE enrichment between La to Sm, with relatively flat middle to heavy REE between Gd to Lu. All samples have a small negative Eu-anomaly. The analysis from the footwall felsic volcanoclastic sample also has similarly elevated incompatible elements, much higher light REE, but mostly flat heavy REE, with a slight kick between Er and Lu that may be attributed to minor amphibole fractionation, or may be within analytical error of a flat HREE pattern.

2.8. SPINIFEX TEXTURES

In our study area, we observe that spinifex textures, and internal flow differentiation, can occur over a broad range of chemical compositions from komatiite through to andesite, and in a review of spinifex texture in literature, we found spinifex textures in volcanic rocks with extreme compositions. In the Musgraves Province of Western Australia, Howard *et al.*, (2011) have reported platy calcic amphibole spinifex in rhyolite (their Fig. 70), and in south western Namibia, Cooper and Reid (1991) have reported platy calcite spinifex in a carbonatite flow. In the latter example, the flow was similarly differentiated into an upper spinifex horizon and a lower dolomite cumulate layer. Unlike pyroxene spinifex, those examples are unlikely to be mistaken for being komatiite, but they demonstrate that spinifex textures occur over a broad compositional spectrum.

2.9. COMPARISON WITH OTHER PYROXENE SPINIFEX TEXTURED SEQUENCES

Pyroxene spinifex in the upper parts of differentiated flows has been well documented in Archean komatiitic sequences in Canada (Arndt *et al.*, 1977, Barnes 1985), South Africa (Wilson and Versfeld 1994, Wilson 2003, Kareem 2005, Stiegler *et al.*, 2012), and Zimbabwe (Bickle *et al.*, 1993, Orpen *et al.*, 1993, Renner *et al.*, 1994, Shimizu *et al.*, 2005). Variations of pyroxene spinifex are also common in flow tops in Archean basalt sequences that do not have an obvious komatiite (*sensu stricto*) component in the Mallina Basin of the Pilbara Craton in Western Australia (Sun *et al.*, 1989,

Arndt *et al.*, 2001) and from Proterozoic flows at Gilmour Island in Hudson Bay in Canada (Arndt 1982)) and the Lion Hills in the SE Baltic Shield in Russia (Puchtel *et al.*, 1996).

In the above examples, pyroxene is the dominant phase in spinifex zones and it has typically been reported in variations of acicular habits. However, some notable exceptions do exist:

- Viljoen and Viljoen (1969) document platy pyroxene pseudomorphs that are enclosed between large randomly oriented olivine plates (their ‘crystalline quench structures’) from the Komati Formation in the Barberton Greenstone Belt in South Africa.
- Wilson and Versfeld (1994) report platy spinifex textures from the Nondweni Greenstone Belt in South Africa, which they suggest may have been igneous amphibole.
- Renner (1994) include descriptions of ‘chain augite’ from Zimbabwe, but while they have a similar appearance in 2D sections to our platy examples, it is unclear whether those crystals are also elongate in a second dimension and therefore platy.
- Wood (1980) documents platy pigeonite pseudomorphs (now chlorite) with augite rims in a boninite from the Kopi Formation in New Zealand (their Fig 1b).

We present the first documented example of platy pyroxene from the Yilgarn Craton, but this texture is not unique to our study area. When we identified this new texture within the Youanmi Terrane, we broadened our search within Western Australia and identified similar platy pyroxene in the Loudon Volcanics from the Mallina Basin in the Pilbara Craton (Fig. 2.23a-c). Other examples may also have been misrepresented in the literature due to the entrenched heuristic of platy olivine and acicular pyroxene, and the limitations of traditional 2D petrography.

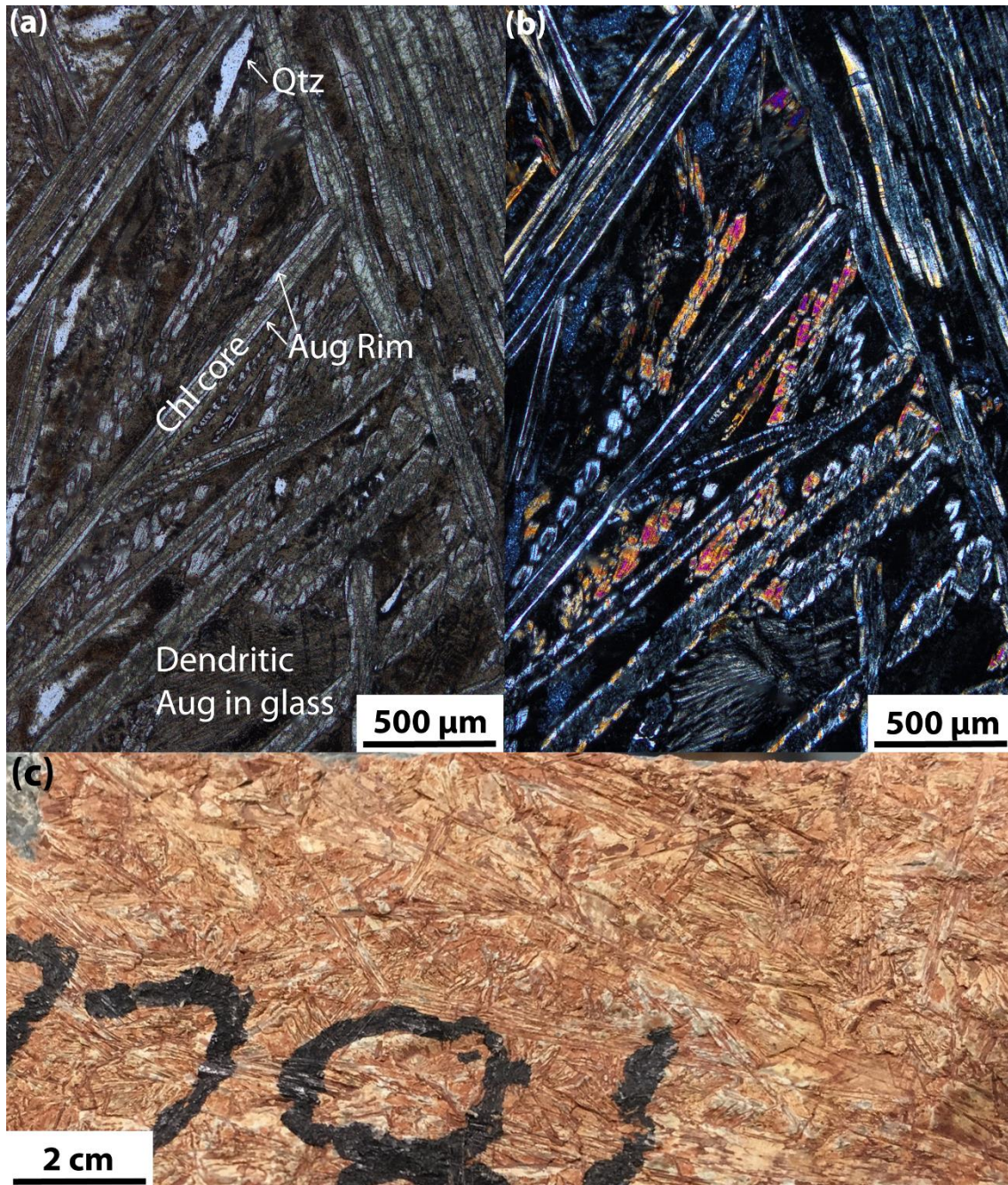


Figure. 2.23. Images of platy pyroxene spinifex texture from Pilbara Craton SHMB (sample 142281, collected by Smithies et al., 2004). (a) Photomicrograph taken in plane polarized light (dAug = dendritic augite, Qtz = Quartz); (b) Photomicrograph of same view in cross polarized light; (c) Photograph of hand sample (FOV 5 cm wide).

In high-Mg basalts near Kambalda in Western Australia, there appears to be confusion about the phase that constitutes the platy crystals; in Said and Kerrich (2010), their Fig. 3e caption refers to platy pyroxene whereas the discussion refers to it as platy olivine.

In other examples, photomicrographs show zoned clinopyroxene crystals that are all in parallel alignment, but they have been interpreted as being acicular crystals that have all been cut

perpendicular to the *c*-axis (e.g., Orpen *et al.*, 1993; their Figs 4.6p, 4.6r and 4.7a, Bouquain *et al.*, 2009; samples Ax105 and M626 on p602). Considering our study, platy spinifex rocks, especially those with high SiO₂, might benefit from a reassessment of their petrography to confirm the platy phase. Pyroxene spinifex rocks with parallel crystal growth, like the examples above, might also benefit from 3D petrography to confirm the crystal morphology.

2.9.1. Development of platy pyroxene

Because this is the first documented example of platy pyroxene, in nature or the laboratory, discussion surrounding preferential growth of plates instead of the more typical acicular forms must be speculative. To constrain this discussion, we refer to a combination of our observations from this type locality, and relate these to insights from experimental studies of similar textures.

In our study area, platy pyroxene, and string-beef texture, are only developed in samples that contain ~11–16 wt% MgO, with Mg-numbers ≥ 68 . More generally, spinifex textures are restricted to high-Mg volcanic, or sub-volcanic rocks, such as komatiites and komatiitic basalts (e.g., Arndt *et al.*, 2008) and it is intuitively reasonable to assume that moderate- to high-Mg liquid compositions are required to form these textures.

Flows with platy pyroxene are typically differentiated into an olivine-bearing cumulate basal layer and a spinifex textured upper layer. In contrast, vitrophyric, trachytic or porphyritic flows, dominated by acicular pyroxene phenocrysts, are comparatively massive. This is probably in part due to flow thickness, where differentiated flows are thicker and cool over a wider range of thermal gradients, but there could also be differences due to eruption temperature and/or the amount of pyroxene phenocrysts already contained in the liquid prior to eruption.

The skeletal nature of platy pyroxene indicates that it grew under high degrees of undercooling, and that crystal growth was rapid, similarly to dendritic crystal growth (Faure *et al.*, 2006), indeed 1st order plates have dendrite-like interiors. Crystal growth may have initially been dendritic, prior to ripening, and in that case the initial dendrite shape would influence the final crystal habit. The nucleation of 1st order plate cores, and 2nd order augite plates was probably homogenous, whereas augite overgrowths on 1st order plates was probably heterogeneous, nucleating on the existing plate

cores. In all cases, crystal growth was probably limited by the rate of diffusion between liquid and the crystal solid (see discussions in Donaldson 1979, Faure *et al.*, 2006).

In crystal growth experiments in aqueous solutions, mineral habits have been modified when grown in the presence of an ‘impurity’ (e.g., Buckley 1949, Joshi 2012). The modified platy pyroxene habit might have been influenced by the presence of an unknown habit modifier in the silicate melt, and this hypothesis could be explored in experimental studies.

2.9.1.1. Experimental study of spinifex texture

In Faure *et al.*’s (2006) experimental study of olivine spinifex, they recreated vertically oriented plates of olivine (A₃ Zone-like) under ‘low’ cooling rates (2–5 °C/hr) and ‘normal’ thermal gradients (~20 °C/cm). They were also able to accurately measure the degree of undercooling that the crystals grew in, which for olivine was 37–56°C below the equilibrium liquidus. Oblique sections through those plates demonstrate apparent juxtaposition of olivine units (their Fig. 5b), which superficially resembles the juxtaposed acicular pyroxene crystals that we show in Fig. 2.8a, b. The observations from those experiments correspond well with spinifex textures from natural examples of olivine spinifex. We assume that similar cooling rate, thermal gradient, and degree of undercooling applied to flows in our example, given the similar vertical positions of the A₂ and A₃ Zones. However, Faure *et al.* also ran cooling experiments with pyroxene-like compositions, keeping other variables similar, and the pyroxenes that crystallized appear to be long, hollow, acicular crystals, like in ‘string-beef’ texture (Table 2.1, Fig 2.15 a, b, d). Given the similarities, between their pyroxene crystals in 2D sections (their Fig. 17), and our transitional acicular-platy pyroxene examples, the transition from acicular to platy habit may be unpredictable.

Future experimental work may try to recreate platy pyroxene spinifex texture. We would suggest using starting compositions that approximate the liquid compositions from the Bundle Volcanic Member, or from the Loudon Volcanics (Table 2.5). It would also be reasonable to experiment with a composition that approximates the platy pyroxene textured samples (Table 2.4), which would be saturated in the chemical components necessary to recreate this texture. A 3D petrographic study of experimentally created textures, including examples like Faure *et al.*’s pyroxene crystals, would

further quantify the texture, especially since their unaltered nature would be well-suited to automatic segmentation methods (cf. ‘X-ray computed tomography’ in analytical methods section).

Table 2.5. Compositions of selected komatiites and other high-MgO liquids						
	Commondale, South Africa	Barberton, South Africa	Alexo, Canada	Belingwe, Zimbabwe	Louden Volcanics, Australia	Bundle Volcanic Member – this study
	High-Si komatiite	Al-depleted komatiite	Al-undepleted komatiite	Al-undepleted komatiite	SHMB	SHMB
SiO ₂ wt. %	49.9	46.8	45.9	49.4	54.2	50.9
TiO ₂ wt. %	0.11	0.38	0.35	0.41	0.42	0.62
Al ₂ O ₃ wt. %	7.6	4.43	7.1	8.66	10.54	9.03
FeO(tot) wt. %	5.4	11.45	10.92	11.6	10.87	10.26
MnO wt. %	0.12	0.18	0.17	0.1	0.19	0.2
MgO wt. %	30.8	30.28	28.21	20	13.19	15.85
CaO wt. %	5.4	5.78	6.57	8.6	8.28	10.16
Na ₂ O wt. %	0.34	0.07	0.29	0.92	2.01	1.38
K ₂ O wt. %	0.01	0.01	0.1	0.05	0.24	0.21
Volatile content	<0.5	<0.5	<0.5	<0.5	-	-
Max Fo	96.3	93.9	94.1	91.3	~88 ^a	89.6
Anhydrous liquidus °C	1616	1606	1564	1400	1290	1312-1342
Probable eruption Temperature °C	~1600	~1600	~1550	1430	~1290	~1340

Modified after Arndt (2008), including Loudon Volcanics analysis from ‘chill zone’ sample 96957 (Arndt *et al.*, 2001). Note: *a* - Fo content calculated to be in equilibrium with liquid composition.

2.10. PETROGENESIS

2.10.1. Melt composition

Interrogation of the extensive collection of Meekatharra Formation volcanic samples (n=164) in the GSWA state geochemical database shows that nearly all volcanic rocks contain ≤ 16 wt% MgO. The only exceptions are samples that contain abundant equant olivine phenocrysts, such as olivine-pyroxene cumulates, and picrites (e.g., sample 183914 ~20 wt% MgO; Van Kranendonk et al 2013). We have not identified any flows within the Meekatharra Formation to be komatiite (*sensu stricto*), either by having liquid compositions >18 wt% MgO or having platy olivine spinifex textures. Ultramafic volcanics within the underlying Norie Group have been interpreted as komatiite (e.g., Barley *et al.*, 2000), but those are separated from the Meekatharra Formation by a thick sedimentary sequence, and they are inferred to be >10 My older. Like previous studies (Watkins and Hickman 1990, Pidgeon and Hallberg 2000, Van Kranendonk *et al.*, 2013), we interpret those units to be related to an earlier magmatic event.

In Table 2.5, we compare the composition of the Bundle Volcanic Member, the most spinifex-rich Member of the Meekatharra Formation, to well-studied komatiitic associations such as those from the Abitibi (Canada), Belingwe (Zimbabwe), Comondale (South Africa) and Barberton (South Africa) greenstone belts. All those examples except for Comondale have associated komatiitic basalt flows, with 12–16 wt% MgO, like the Bundle Volcanic Member. We also include an estimated liquid composition for the Loudon Volcanics (Arndt *et al.*, 2001), which contains only komatiitic basalt compositions. If the estimated liquid compositions in Table 2.5 have not been modified significantly from their initial melt compositions (e.g., by fractional crystallization), then they vary considerably in their melting conditions; temperature, pressure, melt fraction, or a combination of these.

Compared to komatiitic basalts from most of the localities mentioned above, the Bundle Volcanic Member is enriched in SiO₂ and incompatible trace elements, such as light REEs, large-ion lithophile elements (LILEs) and high field strength elements (HFSEs). The predominance of pyroxene

in fine grained volcanic rocks of the Meekatharra Formation, and as a cumulus phase at the bases of those flows indicates that high SiO₂ at least, was a primary feature of the melt composition.

2.10.2. Dry liquidus and mantle potential temperature

Arndt et al (2008) after Nisbet (1982) assessed the results of experimental cooling experiments conducted at 1 atm pressure and determined that the relationship between MgO and dry liquidus temperature is linear, and that Liquidus temperature (T°C) = 1033 + 19.5 x MgO. Accordingly, the liquid compositions derived from chilled flow top samples 209118 (15.85 wt% MgO) and 221722 (14.35 wt% MgO) give calculated dry liquidus temperatures of 1342°C and 1312°C respectively.

Herzberg *et al.*, (2010) showed that mantle potential temperature (Tp) is also intimately related to MgO, and can be calculated using the equation $T_p (^{\circ}\text{C}) = 1463 + 12.74 \times \text{MgO} - 2974/\text{MgO}$. Using this expression, we calculate the mantle potential temperature for the Bundle Volcanic Member to be 1440–1480°C, and given all the Meekatharra Formation volcanics contain less than 18 wt% MgO (except for those with appreciable olivine accumulation), the calculated mantle potential temperature for this period of magmatism is <1530 °C, which is comparable to secular thermal Earth models for ambient mantle (e.g., Korenaga 2008).

2.10.3. Geodynamic implications

In our study area, Van Kranendonk *et al.*, (2013) have attributed the melting event that produced the Norie and Polelle Group volcanics to the impingement of a mantle plume beneath the Yilgarn Craton at c.2825-2800 Ma, and they suggest that the high-Si, and incompatible element enriched characteristics of the Meekatharra Formation to assimilation fractional crystallization (AFC) processes. Our observations are consistent with some aspects of this model; an open magmatic system in an intracontinental or near to continental setting would be prone to AFC processes, but the mantle temperatures calculated above do not necessitate, or refute a mantle plume origin, so that aspect at least remains equivocal.

Boninite-like chemistry in the lower parts of the Meekatharra Formation (Wyman and Kerrich, 2012), and primary hydrous minerals in the contemporaneous Narndee Igneous Complex in the

southern Murchison Domain further complicate the mantle plume-AFC model. Ivanic *et al.*, (2015) suggested that geochemical characteristics of the Narndee Igneous Complex, which also has relatively high-Mg content, and is SiO₂ and light REE enriched, could be related to metasomatised mantle sources, ambient crustal assimilation or subduction-related inputs. Considering these studies, a more detailed petrological study of the Meekatharra Formation, and a critical evaluation of those models is required.

2.11. FUTURE WORK

A concerted effort is encouraged to reassess high-Mg volcanic sequences for additional occurrences of platy pyroxene. We suggest targeting spinifex textured rocks with 10–18 wt% MgO and 50–55 wt% SiO₂, particularly those with platy minerals, for both chemical and 3D petrographic analysis.

Experimental petrology studies using the appropriate compositions, cooling rates and thermal gradients (e.g., Faure *et al.*, 2006), could yield similar pyroxene morphologies to those documented here. We suggest starting compositions like the compositions of A₁ and/or A₂ Zones from our Locality 1 (i.e., very close to pyroxene itself).

Further work is required to establish a strong petrogenetic argument as to the formation of these high silica and moderately LILE-enriched rocks. In addition, a chemostratigraphic assessment of the Polelle Syncline is the subject of ongoing research in the Yilgarn Craton.

2.12. CONCLUSIONS

Platy pyroxene is reported here from two Archean cratons in Western Australia: at *c.* 2800 Ma in the Yilgarn Craton and at *c.* 3100 Ma in the Pilbara Craton. It probably also occurs in other greenstone terrains, where it may have been misidentified either as platy olivine or acicular pyroxene due to heuristical assumptions. Furthermore, as Phanerozoic examples of platy pyroxene spinifex exist, the texture may be present throughout the geological record.

Careful petrographic evaluation is required to distinguish dominant mineral species from one another in spinifex textured rocks. The inference of any precursor mineralogy in altered examples should not be based upon crystal habit alone; instead we recommend using a combination of texture and whole rock chemistry (where it can be demonstrated that the composition is largely unaffected by alteration). We have highlighted reports of platy spinifex textures in rocks ranging in composition from komatiite to rhyolite, and even in carbonatite.

In our example, pigeonite or augite probably formed 1st order plate and needle cores, then augite crystallized as epitaxial rims on 1st order crystals and formed discrete 2nd order plates and needles, and

lastly, 3rd order dendritic augite formed in the interstices prior to the quenching of the remaining liquid to glass. Plate growth was clearly rapid, and indicates a high degree of undercooling. Liquid composition, eruption temperature (relative to pyroxene liquidus), cooling rate and thermal gradient are all important variables required to form platy pyroxene spinifex texture.

Chapter 3: Archean boninite-like rocks of the northwest

Youanmi Terrane, Yilgarn Craton – geochemistry and genesis

3.1. INTRODUCTION

The beginning of modern-style plate tectonics is a subject of much debate, and one of the most contested arguments is whether some Archean greenstones are analogous to modern volcanic arcs, or that their similarities are superficial (Barley, 1984, 1989; Campbell and Hill 1988; Condie 2005a,b; Smithies, 2005; Bédard 2006, 2018; Pearce 2008; Bédard, 2013; Wyman 2013). Many Archean greenstone sequences contain volcanic rocks that are chemically similar to modern arc rocks (Basalt-Andesite-Dacite-Rhyolite; BADR), yet such chemical signatures could be superimposed on non-arc melts by crustal contamination or by mixing with crustally-derived melts (Pearce, 2008; Said and Kerrich, 2010; Barnes, 2012; Barnes and Van Kranendonk 2014).

To assess whether arc-like characteristics in evolved BADR rocks were indeed derived from subduction-metasomatised mantle, it is necessary to first constrain the composition of their inferred mantle source. High-Mg mafic volcanic rocks (including boninites) are particularly useful in this respect because their compositions are relatively close to those of their primary melts. A potential disadvantage of using highly magnesian samples to trace primary magma composition are their intrinsically low concentrations of incompatible trace elements, which are easily modified by alteration and/or small amounts of crustal contamination.

The best-known examples of Phanerozoic boninites, such as those in the Cenozoic Izu- Ogasawara-Mariana arcs, or the Tonga Ridge, are exclusively found in subduction zone settings, where they are mainly associated with the embryonic stages of subduction. Boninites in ophiolites are commonly thought to be representative of oceanic crust that formed in such settings (e.g., Crawford, 1989; Pearce and Robinson, 2010; Haase, 2015). Typically regarded as products of mantle flux-melting, some authors have proposed that boninites, like komatiites, may additionally require anomalously high melting temperatures, and have suggested that upwelling hot refractory mantle plume-material is drawn into the

mantle wedge where it interacts with hydrous fluids and partial melts released from subducting crust (e.g., Taylor, 1994; Portnyagin, 1997; Macpherson and Hall 2001; Falloon, 2008; Kanayama, 2012). A similar model has also been proposed for ultra-depleted Al-enriched komatiites in the Comondale greenstone belt, South Africa (Wilson, 2003a,b), which plot as boninites in the new scheme of Pearce and Reagan (2019).

Like komatiites and komatiitic basalts, boninitic melts can have high-MgO (e.g., up to 20 wt% MgO; Walker and Cameron 1983), but incompatible lithophile elements are much higher than in komatiites. For example, Cenozoic boninites typically have very characteristic concave REE patterns, and Th/Nb ratios higher than those inferred for MORB-OIB mantle. However, similar characteristics would be expected in komatiitic melts contaminated by felsic crust, and so differentiating between boninite and contaminated komatiite can be difficult. This is particularly pertinent for Archean boninite-like and low-Ti basalt (LOTI) suites, which form a component of greenstone sequences in many cratons and have been cited as strong evidence for modern-style subduction processes in the Archean (Fan and Kerrich, 1997; Kerrich, 1998; Boily and Dion, 2002; Polat, 2002; Manikyamba, 2005; Smithies, 2002, 2004, 2005; Wyman and Kerrich, 2012; Angerer, 2013; Turner, 2014). In many Archean greenstone terranes, it is unclear whether volcanism occurred in an oceanic or continental setting, because pre-existing crust cannot be identified. Under such circumstances, tectonic models must rely heavily on inferences from sedimentary provenance, inherited zircon geochronology and isotopic compositions, and whole rock geochemistry with potentially ambiguous results and conflicting interpretations (e.g., Arndt, 2001 vs Smithies, 2004).

Here we present new whole-rock chemical and Sm-Nd isotopic data and investigate the petrogenesis of high-Mg mafic volcanic rocks from a 2820-2735 Ma volcano-sedimentary sequence near Meekatharra, in the Youanmi Terrane of the Yilgarn Craton, Western Australia. Previous work identified a volcanic unit with boninite-like compositions within this sequence (Wyman and Kerrich, 2012) and this study confirms that boninite-like rocks are both laterally extensive and more representative of the Meekatharra Formation than previously appreciated. In addition, we describe a newly identified occurrence of boninite-like rocks formed during the early stages of magmatism at c.

2820 Ma. Unlike most Archean boninite-like rocks described to date, the examples in the northwestern Youanmi Terrane are remarkably well-preserved (low grade, greenschist facies metamorphism in some) and retain much of their primary igneous mineralogy. This allows the rocks to be placed within a chemostratigraphic framework that can be used for comparisons with modern volcanic settings. The new results, combined with existing chemical and isotopic data from the northwestern Youanmi Terrane, are used to further assess the petrogenesis of these magmas against the competing crustally contaminated komatiite and embryonic subduction models.

3.2. GEOLOGICAL BACKGROUND

The chronostratigraphic and magmatic framework of the northwestern Youanmi Terrane (northern Murchison Domain) was recently revised by Van Kranendonk (2013). Archean supracrustal rocks are defined as the Murchison Supergroup, which is divided into three main stratigraphic successions: (1) mostly felsic volcanic and sedimentary rocks from 2980-2920 Ma; (2) voluminous (ultra)mafic to felsic volcanics and (volcano-) sedimentary rocks (Norie Group, *c.* 2820-2800 Ma; Polelle Group, 2800-2735 Ma), and (3) siliciclastic and mafic volcanic rocks (Glen Group, *c.* 2735-2710 Ma), which unconformably overlies the Polelle Group. Two main geodynamic models are proposed for volcanism between *c.* 2820 and 2735 Ma, including rifting and mantle upwelling, leading to autochthonous crustal growth (Watkins and Hickman, 1990; Ivanic, 2012; Van Kranendonk, 2013), and hydrous melting in a subduction zone environment (Wyman, 2019) or a combination of the two (Champion and Cassidy, 2002; Wyman and Kerrich, 2012). The stratigraphic relationships of the Murchison Supergroup are summarised in Fig 3.1.

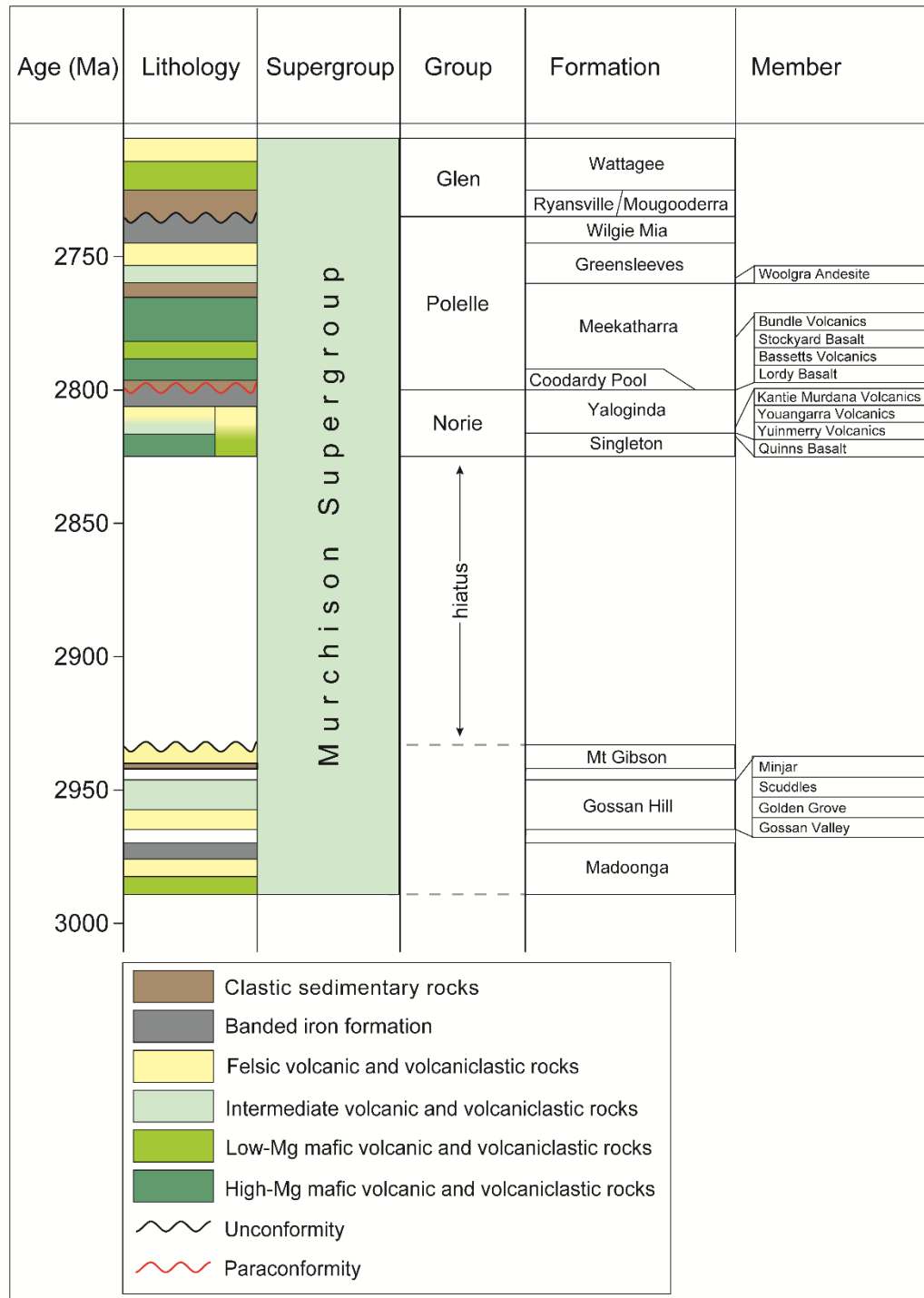


Figure 3.1. Stratigraphic relationships of the Murchison Supergroup (modified after Ivanic, 2016; see also Romano, 2018).

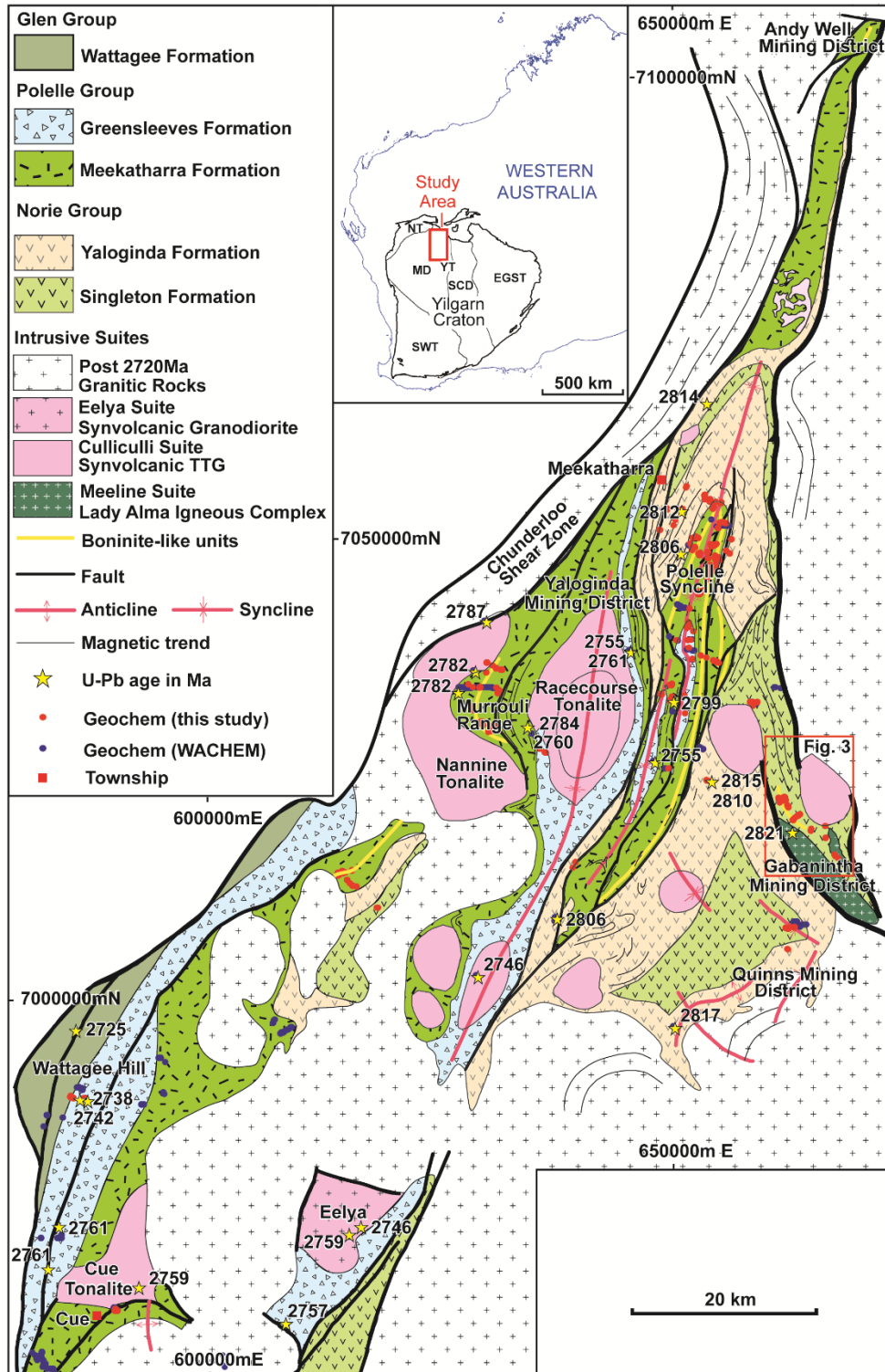


Figure 3.2. Interpreted bedrock geology map of the northwest Youanmi Terrane (i.e., north Murchison Domain), Yilgarn Craton (modified after Lowrey *et al.*, 2017). This map shows the distribution of supracrustal groups and co-genetic intrusive suites, available geochronological data, major structural features and significant localities. Interpretation is based on 1:100,000 mapping by the Geological Survey of Western Australia (GSWA), and supplemented by our interpretation of aeromagnetic and Landsat multispectral images. Coordinates are relative to GDA94/MGA Z50. Geochronology sample sources (Wang, 1998, Pidgeon and Hallberg, 2000, Geological Survey of Western Australia 2018). Inset abbreviations: MD = Murchison Domain, SCD = Southern Cross Domain, YT = Youanmi Terrane, NT = Narryer Terrane, SWT = South West Terrane, EGS = Eastern Goldfields Superterrane.

The field area for this work lies between the towns of Cue and Meekatharra, where several geological mapping and geochronological studies (Watkins and Hickman, 1990; Wang, 1998; Hallberg, 2000; Pidgeon and Hallberg, 2000; Romano, 2018) have established the ages of geological units (Fig 3.2). Two areas with well-exposed stratigraphic intervals were studied in detail:

1. Outcrops in the Gabanintha Mining District (approximately 40 km SE of Meekatharra; Figs 3.2, 3.3) expose the transition between two chemically distinct suites of mafic-ultramafic volcanic rocks in the Singleton Formation. Most rocks are metamorphosed to greenschist facies, but preserve primary characteristics such as vesicles and relict igneous crystal boundaries.

2. Outcrops in the Polelle Syncline (approximately 10km SE of Meekatharra; Fig 3.2) expose the upper Norie Group (Yaloginda Formation) to upper Polelle Group (Greensleeves Formation). The rocks in this area experienced only low-grade metamorphic overprinting (prehnite-pumpellyite to lower greenschist facies) and are generally well-preserved, retaining both igneous textures and in many cases primary mineralogy.

3.2.1. Norie Group

The Norie Group in the study area (Fig 3.2) consists of a basal sequence of mafic-ultramafic volcanics assigned to the Singleton Formation, overlain by a sequence of intermediate volcanics and sedimentary units, including jaspilitic banded iron formation, cherts, and shales, all assigned to the Yaloginda Formation.

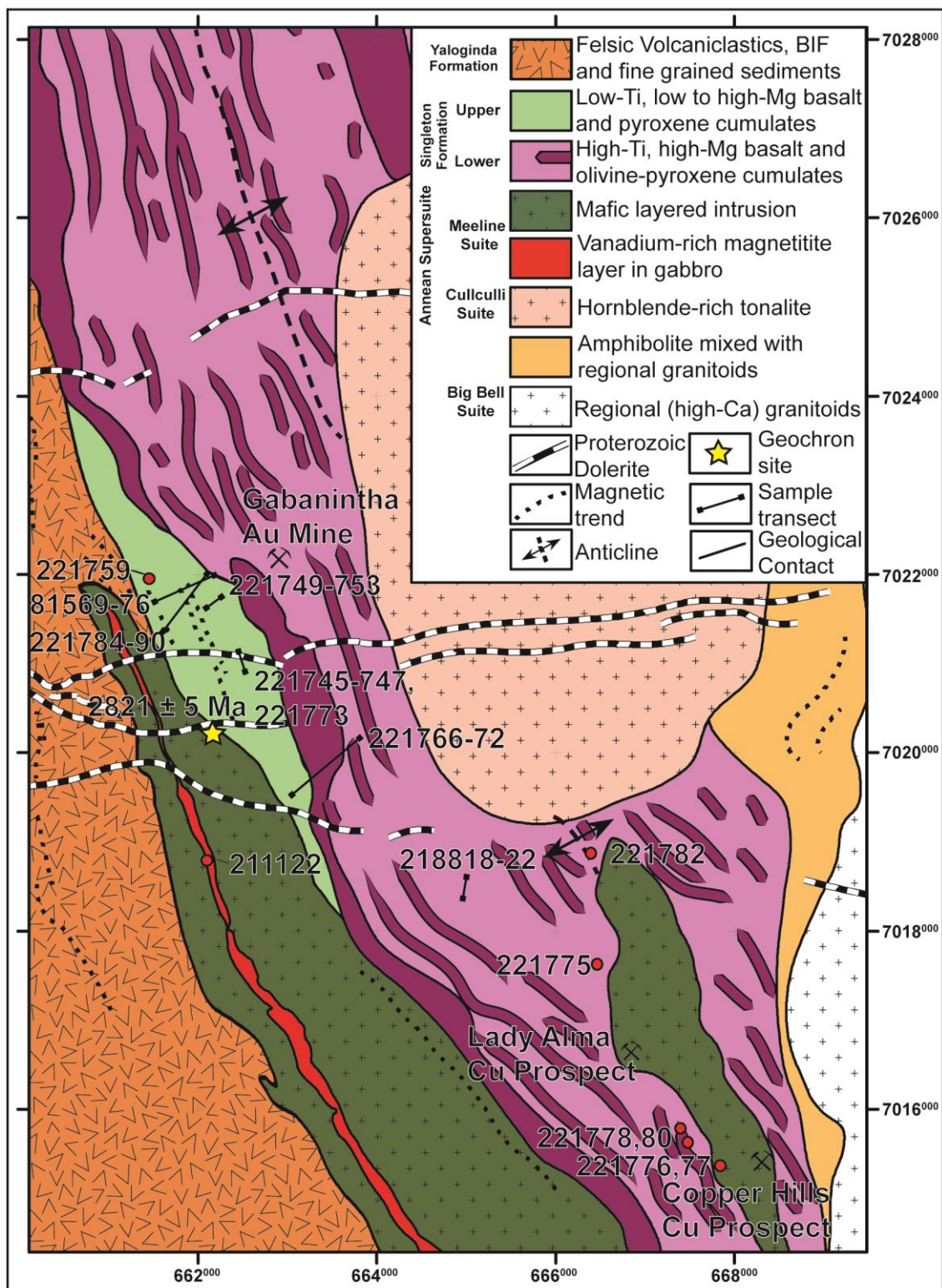


Figure 3.3. Interpreted bedrock geology map of Gabanintha Mining District (see Fig 3.2 for regional context). This map shows the distribution of geochemical samples discussed in this section.

The mafic-ultramafic metavolcanics of the Singleton Formation (now mostly talc-chlorite-tremolite-serpentine schists) have been interpreted by most previous studies to have a komatiitic

association (Jackson, 1990; Reudavey, 1990; Watkins and Hickman, 1990; Barley, 2000; Hallberg, 2000; Pidgeon and Hallberg, 2000; Van Kranendonk, 2013). Barley (2000) invoked mantle plume ascent beneath subduction-modified lithosphere to account for their trace element signatures and high volatile content, as reflected by pyroclastic occurrences. Wyman (2019), however, argued that the rocks were similar to picrites from Phanerozoic ophiolites and that pyroclastic occurrences were the product of magma mixing with wet crustal melts.

Mafic intrusions of the 2820-2815 Ma Meeline Suite, including the Lady Alma Igneous Complex in the Gabanintha region (Figs 3.2-3.3) and the voluminous Windimurra and Youanmi Igneous Complexes (approximately 100km south of the study area; Ivanic, 2017), are broadly coeval with the Singleton Formation.

The Singleton Formation is overlain by a c. 2 km thick sequence of intermediate to felsic volcanics assigned to the Yaloginda Formation. U-Pb zircon dating of these volcanics in the study area yielded ages ranging from c. 2815 ± 7 to 2806 ± 4 Ma (Wang, 1998; Wingate, 2011). In this area, the Yaloginda Formation consists of porphyritic basaltic andesites near its base, overlain by porphyritic and volcanoclastic (medium-coarse grained breccia) andesite to dacite and fine-grained rhyolitic tuffs.

Numerous fine-grained interflow sediments (prominent ridges of jaspilitic banded iron formation, cherts, shales and siltstones) are locally intruded by mafic-ultramafic sills. A c. 1500 m thick unit of these sediments marks the boundary between the Yaloginda Formation and the overlying Polelle Group. The abundance of thick ridges of finely laminated banded iron formation, shale and chert indicates an extended period (at least locally) of volcanic quiescence between the Norie and Polelle Groups.

3.2.2. Polelle Group

The Polelle Group in the study area consists of the basal Meekatharra Formation and the overlying Greensleeves Formation (Fig 3.1). The Polelle Group is exposed throughout much of the northwestern Youanmi Terrane, but is best preserved in the Polelle Syncline (Fig 3.2). In this locality the Meekatharra Formation comprises four discrete units (Fig 3.1). The basal unit is the Lordy Basalt

Member, which is dominated by high-Mg basalt with coarse acicular pyroxene phenocrysts and, locally, pyroxene spinifex textures. This is overlain by the Bassetts Volcanic Member, a high-Mg mafic volcanic unit with boninite-like chemical compositions and textural characteristics (see also Wyman and Kerrich, 2012) that typically contains abundant fine acicular pyroxene phenocrysts and, locally, orthopyroxene-rich cumulate layers. The Bassetts Volcanic Member is overlain by the Stockyard Basalt Member, which is dominated by lower-Mg tholeiitic basalt that is typically massive, but locally contains pillow structures and vesicles. The youngest member of the Meekatharra Formation is the Bundle Volcanic Member, which is a high-Mg basalt to basaltic andesite unit that consists of a sequence of several flows, internally zoned into platy pyroxene spinifex textured flow tops and olivine-rich cumulate bases (Lowrey *et al.*, 2017).

The 2799 ± 7 Ma Narndee Igneous Complex, 100km south of the study area, is intruded immediately prior to or coincident with the Meekatharra Formation and hosts similar volumes of high-Mg lithologies (Ivanic, 2015). Importantly, Narndee gabbros contain abundant igneous hornblende, with mantle-like H-O isotopic ratios, reflecting the presence of (locally) hydrated mantle at the time of the Meekatharra Formation high-Mg magmatic activity.

The basal unit of the Greensleeves Formation, the Woolgra Andesite Member, consists of interbedded volcanic flows, fragmental units, and volcanogenic sedimentary units, ranging in composition from basaltic andesite to dacite. Flows and volcanic fragmental rocks are locally amygdular and typically porphyritic, with euhedral plagioclase, clinopyroxene and, locally, hornblende phenocrysts, which commonly form glomerocrysts (Hallberg, 1976). U-Pb in zircon ages (2761-2734 Ma; Van Kranendonk, 2013) indicate a *c.* 20 Ma period of apparently continuous felsic volcanism. Numerous hornblende-rich tonalite plutons assigned to the Cullculli Suite (dominantly 2760-2740 Ma; Van Kranendonk, 2013) intrude the greenstone stratigraphy and are broadly coeval with this period of volcanism.

3.3. SAMPLE SELECTION AND ANALYTICAL PROCEDURES

3.3.1. Whole rock major, minor and trace element concentrations

Our study is based on a large set of whole rock chemical analyses for 445 samples of volcanic rocks from the Norie and Polelle Groups within the Meekatharra-Mt Magnet greenstone belt (Fig 3.2). Most samples were collected from outcrops during this study (301 samples) with care taken to avoid weathered, altered, veined or highly metamorphosed rocks. The Polelle Group samples (sub-greenschist to greenschist) are better preserved than those from the Norie Group (greenschist to locally granulite facies).

The samples were crushed by jaw crusher, milled by low-Cr steel mill and then analysed at three Western Australian laboratories; Australian Laboratory Services (ALS), Intertek Genalysis Laboratory Services Pty Ltd (Genalysis), and Bureau Veritas (BV). In addition to the samples collected during this study, we also report compositions for an additional 144 samples collected by GSWA during a previous mapping campaign (Watkins and Hickman, 1990) that were crushed in a plate jaw crusher, milled in a tungsten-carbide mill and analysed together with our samples by ALS and Genalysis.

Major and minor elements (Si, Ti, Al, Cr, Fe, Mn, Mg, Ca, Sr, Ba, Na, K, and P) were determined by X-ray fluorescence spectrometry (ALS method ME-XRF26, Genalysis method FB1/XRF; BV method XRF202). For this purpose, fused discs were prepared by fusing a 1:10 sample-flux mix (LiBO_2 , LiB_4O_7 and LiNO_3 flux) at 1025-1100°C (depending on lab). Loss on ignition was determined by thermogravimetric analysis (ALS method ME-GRA05, Genalysis method TGA, BV method LOI-1000). ALS and Genalysis determined lithophile trace element concentrations by fusing the sample with a flux mix (LiBO_2 , LiB_4O_7) then dissolving in acid and analysis by ICP-MS (for Cs, Rb, Ba, Sr, Th, U, Nb, Ta, Zr, Hf, Y, La, Ce, Pr, Nd, Sm, Eu, Gd, Tb, Dy, Ho, Er, Tm, Yb and Lu at both labs, and Cr, V at ALS only; ALS method ME-MS81, Genalysis method FB6/MS), or ICP-OES (Cr, V, Sc at Genalysis only, method FB6/OE). ALS and Genalysis determined base metal concentrations by dissolving samples with a 4-acid mixture (HClO_4 , HNO_3 , HF and HCl) followed by analysis via ICP-AES (Co, Cu, Ni, Pb, Sc and Zn; ALS method 4ACD81), ICP-OES (Cu, Ni, and Zn; Genalysis method 4A/OE) or ICP-MS (Co and Pb; Genalysis method 4A/MS). BV determined

lithophile element and base metal concentrations by laser ablation on the fused discs prepared for XRF (BV method LA101).

Data reproducibility at the three laboratories is broadly comparable. Total uncertainties for major elements are $\leq 1.5\%$, those for minor elements are $< 2.5\%$ (at concentrations > 0.1 wt%) and those for trace elements are $\leq 10\%$ (Lu $\pm 20\%$). Major elements are re-calculated to anhydrous concentrations. Primitive mantle abundances are those of (Sun and McDonough, 1989). The elemental compositions of selected samples are presented in Table 3.1, while the complete set of results, including sample locations, are included in Electronic Appendix 3.1.

Table 3.1. Major, Minor and selected trace-element data for representative samples of Norie and Polelle Group volcanic rocks.																
	Norie Group															
Geological unit:	lower Singleton Formation						upper Singleton Formation					Quinns Basalt	Yaloginda Formation	Yaloginda Formation		
Lithology:	basalt		picrite to Ol orthocumulate				dolerite/gabbro to Px cumulate		basalt (LOTI-boninite-like)		High HFSE basalt to rhyolite		High-Mg basaltic andesite to andesite			
Sample ID:	21881	221772	218820	221769	221770	221759	221754	221755	221758	221746	221752	217739	217748	227208	217765	217768
% (anhydrous)																
Al ₂ O ₃	10.37	8.40	4.66	6.29	4.07	10.68	14.63	10.75	10.98	15.66	12.60	14.26	14.34	11.88	15.07	14.23
CaO	10.27	9.71	4.87	8.46	4.78	10.69	5.73	5.97	7.24	10.97	10.60	8.90	0.05	6.76	5.15	5.95
Fe ₂ O ₃ (Total Fe)	12.46	12.87	13.76	13.17	12.64	11.32	9.52	10.47	10.68	10.89	12.17	10.20	3.85	11.07	8.31	3.93
K ₂ O	0.29	0.04	0.03	0.04	0.02	0.54	1.50	0.31	0.07	0.31	0.27	0.25	0.68	0.62	2.01	0.12
MgO	10.32	16.00	28.78	23.49	31.62	14.01	13.85	19.06	17.87	7.54	10.51	6.40	4.14	11.73	6.72	5.40
MnO	0.20	0.19	0.15	0.16	0.20	0.18	0.18	0.18	0.19	0.16	0.21	0.14	0.01	0.14	0.12	0.07
Na ₂ O	2.21	1.62	0.21	0.77	0.16	0.92	1.86	0.87	0.87	2.03	1.55	2.36	0.51	1.78	3.72	7.34
P ₂ O ₅	0.08	0.07	0.04	0.06	0.04	0.03	0.02	0.02	0.02	0.09	0.05	0.24	0.02	0.14	0.16	0.13
SiO ₂	52.68	50.24	46.92	46.83	45.95	51.32	52.63	52.28	51.91	51.63	51.48	56.02	76.10	55.09	58.02	62.17
TiO ₂	1.11	0.86	0.59	0.74	0.51	0.32	0.10	0.11	0.16	0.72	0.54	1.20	0.29	0.79	0.68	0.64
LOI	1.12	2.6	7.01	3.34	7.87	1.43	3.56	2.41	1.55	1.75	1.53	100.22	99.7	100.03	2.52	0.93
ppm																
Cs	0.14	0.2	0.1	0.2	0.2	0.2	0.68	0.48	0.06	0.1	0.2	0.1	0.15	0.1	0.57	0.18
Rb	9.4	0.5	1.8	0.8	1	16.6	37.6	5.9	1.7	7	6.8	5.5	18.4	11.4	46.1	2.9
Ba	70.8	93.7	67	5.8	11.7	58.7	335	14.5	32.5	86.9	68.3	130.5	146.5	251.7	670	31.2
Th	0.75	0.3	0.21	0.2	0.1	0.4	bdl	0.07	0.39	1	0.8	1.99	8.1	2.2	3.23	5.43
U	0.17	-0.1	0.1	-0.1	-0.1	0.1	bdl	0.02	0.14	0.2	0.2	0.44	2.12	0.4	0.81	0.92
Nb	3.6	2.5	1.8	1.6	0.9	1.1	0.21	0.38	0.7	2.8	1.5	7.8	22.9	3.2	5.6	6.6
Sr	120	44.3	37.8	38.4	18.7	36.7	68	36.8	55.9	128.1	63.6	115	25.9	293.7	212	31.1
Pb	bdl	0.9	3	-0.5	0.8	bdl	bdl	bdl	bdl	1.8	1.3	bdl	6	6.4	3	3
Hf	2	1.3	0.8	1	0.6	0.7	0.18	0.22	0.52	1.6	1.1	4.3	15.3	1.7	2.6	3.5
Zr	72	44	32	35	23	22	5	7.5	17	60	42	162	512	60	108	137
Y	19.6	12.8	8.7	9.9	6.4	11.1	4.44	4.08	5.6	18.7	17.1	46.2	117.5	15.6	15.7	19
Ta	0.1	0.2	bdl	0.3	0.4	0.3	bdl	0.02	0.04	0.6	0.4	0.4	1.4	0.2	0.3	0.4
La	5.1	4.1	3.1	2.5	1.6	2.1	0.27	0.54	1.91	6	4.1	12	37.9	10.3	16.5	17
Ce	12.8	9.5	6	5.3	3.1	4.1	0.46	1.22	4.68	12.2	7.6	26.5	92	21.6	30	33.8
Pr	1.91	1.3	0.97	0.9	0.6	0.7	0.07	0.19	0.62	1.5	1	3.92	11.7	2.9	3.43	4.02
Nd	9.4	7.3	4.6	4.8	3.1	3.6	0.33	0.86	2.52	7.4	5.8	17.6	52.4	12.2	12.6	15
Sm	2.85	1.9	1.37	1.8	1	0.8	0.09	0.24	0.5	1.8	1.4	4.85	14.95	2.9	2.64	3.35
Eu	1.01	0.6	0.46	0.6	0.4	0.3	0.07	0.1	0.21	0.6	0.5	1.56	4.16	0.6	0.81	0.9
Gd	3.28	2.6	1.53	2	1.3	1.4	0.24	0.34	0.7	2.4	2.1	6.75	16.75	3	2.74	3.06
Tb	0.56	0.4	0.2	0.3	0.2	0.2	0.06	0.07	0.1	0.4	0.4	1.18	2.86	0.5	0.38	0.41
Dy	3.41	2.3	1.48	2.2	1.1	1.9	0.5	0.59	0.8	2.9	2.8	8.01	18.25	2.6	2.48	2.63
Ho	0.66	0.5	0.29	0.4	0.3	0.4	0.16	0.16	0.19	0.6	0.7	1.74	4.1	0.6	0.49	0.57
Er	1.97	1.3	0.82	1.2	0.9	1.1	0.54	0.46	0.73	2	1.8	5.37	13.15	1.8	1.58	1.8
Tm	0.27	0.2	0.12	0.2	0.1	0.2	0.1	0.08	0.11	0.3	0.3	0.8	2.01	0.3	0.22	0.25
Yb	1.76	1	0.75	1	0.6	1.3	0.86	0.66	0.87	2.3	1.8	4.92	13.65	1.9	1.43	1.86
Lu	0.25	0.2	0.11	0.2	0.1	0.3	0.15	0.12	0.14	0.4	0.3	0.8	2.33	0.3	0.23	0.27
Ni	243	637	1680	1167	1652	675	366	684	802	145	313	87	2	268	120	154
Cr	810	2020	2710	2002	1945	2881	884	3170	2670	317	853	120	10	820	260	190
V	282	249	115	190	122	189	126	131	117	220	210	248	bdl	219	150	115
Co	61	74	161	74	108	69	61	80	76	44	57	34	bdl	48	31	13
Cu	14	101	10	20	8	9	bdl	4	bdl	148	10	55	3	78	1	6
Sc	40	35	24	23	15	31	35	31	30	32	34	32	3	24	19	15
Zn	70	96	94	57	93	63	35	50	45	64	84	74	53	80	58	18

Table 3.1. Continued.													
Geological unit:	Polelle Group												
	Meekatharra Formation, Lordy Basalt Member				Meekatharra Formation, Bassetts Volcanic Member					Meekatharra Formation, Stockyard Basalt Member			
Lithology:	basalt to basaltic andesite (siliceous high-Mg basalt)		Ol cumulate		basalt to basaltic andesite (siliceous high-Mg basalt)			Ol-Px cumulate	Opx cumulate	Tholeiitic basalt to basaltic andesite (population 1)		Tholeiitic basalt to basaltic andesite (population 2)	
Sample ID	217712	217771	221627	217714	221693	209130	217798	209176	209198	217755	217757	217788	217791
% (anhydrous)													
Al ₂ O ₃	10.81	13.36	9.54	6.28	13.96	12.27	11.49	6.09	8.53	14.44	14.78	13.97	14.83
CaO	8.20	6.55	7.85	4.95	10.52	9.76	8.25	5.01	6.34	11.93	11.70	10.00	10.35
Fe ₂ O ₃ (Total Fe)	12.73	10.94	12.39	12.88	9.56	10.19	10.28	10.91	9.93	10.11	10.71	14.34	11.25
K ₂ O	0.06	0.12	0.04	0.15	0.07	0.08	0.12	0.05	0.37	0.11	0.15	0.38	0.35
MgO	16.43	9.81	19.34	27.44	9.55	12.00	14.35	29.70	19.37	7.56	6.16	6.29	5.49
MnO	0.17	0.13	0.18	0.17	0.16	0.18	0.17	0.17	0.18	0.18	0.20	0.20	0.23
Na ₂ O	1.15	3.63	0.38	0.52	1.40	1.15	1.25	0.14	0.69	2.08	1.87	2.05	2.51
P ₂ O ₅	0.06	0.07	0.05	0.03	0.06	0.05	0.04	0.02	0.04	0.06	0.07	0.13	0.14
SiO ₂	49.54	54.56	49.32	46.78	54.12	53.69	53.41	47.20	53.94	52.74	53.48	51.25	53.50
TiO ₂	0.63	0.76	0.58	0.35	0.55	0.46	0.46	0.23	0.35	0.75	0.85	1.39	1.34
LOI	4.42	2.79	4.95	6.97	1.98	3.13	2.63	6.01	3.37	0.93	0.8	99.93	99.06
ppm													
Cs	0.1	0.1	0.12	0.78	0.18	1.3	0.25	0.53	4	0.06	0.06	0.09	0.1
Rb	1.4	3.6	2	5	1.7	2.5	3.6	3.7	24.3	1.4	2.2	12	11.4
Ba	32	49.8	28.1	29	30.6	22.3	194.5	22.4	27.7	49.6	97.1	79.9	77.2
Th	0.82	1.38	0.8	0.43	0.68	0.69	0.65	0.24	0.5	0.22	0.28	0.46	0.44
U	0.22	0.36	0.28	0.08	0.22	0.19	0.17	0.05	0.1	bdl	0.07	0.12	0.09
Nb	1.8	2.2	1.6	0.9	1	1.1	0.6	0.3	0.5	1.7	1.9	3	3.2
Sr	57.1	46.7	9.6	17	32.1	37.5	32.9	5.8	26.3	89.7	131.5	126	101.5
Pb	bdl	bdl	bdl	bdl	5	4	bdl	4	0.5	bdl	bdl	bdl	bdl
Hf	1.3	1.7	1.2	0.7	1.2	1	0.9	0.4	0.8	1.1	1.6	2.3	2.4
Zr	44	65	45	23	44	38	36	15	21	44	57	89	88
Y	15.5	17.6	13.7	7.8	14.8	15.2	13.5	6	9.5	16.8	19.4	29.5	27
Ta	bdl	0.1	0.1	bdl	0.1	bdl	bdl	bdl	bdl	bdl	0.1	0.1	0.1
La	3.9	4.9	3.2	1.9	2.7	2.7	2.4	1.1	1.4	2.3	2.8	4.3	4.3
Ce	8.5	11.2	7.8	4.1	5.6	5.5	4.9	2.1	3.3	6.2	7.9	12.1	11.8
Pr	1.09	1.48	1.01	0.58	0.73	0.7	0.61	0.3	0.4	1.01	1.3	1.91	1.94
Nd	5.3	6.6	4.8	2.5	3.5	3.3	2.9	1.3	1.8	5.1	6.4	9.8	10.1
Sm	1.48	2.03	1.42	0.74	1.19	1.11	0.97	0.38	0.7	1.56	2.14	3.29	3.24
Eu	0.55	0.57	0.54	0.27	0.47	0.42	0.46	0.16	0.3	0.68	0.82	1.15	1.37
Gd	1.99	2.59	1.86	1	2.17	1.89	1.65	0.75	1.4	2.54	2.99	4.43	4.35
Tb	0.39	0.47	0.35	0.18	0.4	0.36	0.36	0.14	0.2	0.41	0.51	0.8	0.75
Dy	2.56	3.27	2.51	1.28	2.57	2.5	2.35	0.95	1.4	2.86	3.38	5.5	5.03
Ho	0.54	0.67	0.5	0.26	0.55	0.58	0.55	0.21	0.3	0.63	0.76	1.13	1.05
Er	1.67	2	1.54	0.8	1.88	1.68	1.49	0.79	1.1	2.03	2.1	3.4	3.12
Tm	0.22	0.3	0.23	0.13	0.29	0.26	0.25	0.11	0.2	0.28	0.34	0.57	0.47
Yb	1.53	1.93	1.34	0.77	1.73	1.73	1.5	0.71	1.3	1.86	2.01	3.36	3.09
Lu	0.23	0.3	0.23	0.13	0.25	0.26	0.24	0.13	0.2	0.26	0.34	0.5	0.45
Ni	521	106	761	1200	175	280	360	1010	357	106	118	120	102
Cr	1310	420	2450	2640	420	1150	1340	3200	1798	250	210	110	110
V	217	263	217	86	303	235	230	120	181	285	306	368	355
Co	72	42	78	119	44	48	53	87	55	35	41	54	42
Cu	98	89	21	43	53	47	43	23	29	21	9	191	193
Sc	31	40	29	20	36	33	33	19	33	38	38	39	37
Zn	79	78	94	79	65	61	68	63	58	58	67	106	109

3.3.2. Sm-Nd isotope analytical methodology

Sm-Nd isotopic compositions for 16 samples were acquired at the University of Melbourne, following Maas (2015) and Mole (2018). Powders (c. 0.1 g) were weighed into Krogh-type PTFE vessels and mixed with a ^{149}Sm - ^{150}Nd tracer calibrated against the Caltech Sm-Nd mixed normal solution (Wasserburg, 1981). Samples were dissolved at high pressure (2.5 ml 3:1 HF-HNO₃, 48 h, 160 °C; 2x dry-down with conc. HNO₃; 2.5 ml 6M HCl, 24 h, 160 °C); clear solutions were obtained in all cases. Sm and Nd were extracted using Eichrom TRU- and LN-resin (Pin and Santos Zalduegui, 1997). Total blanks (0.1 ng Nd, 0.016 ng Sm) were negligible compared to sample sizes and no blank corrections were applied. All isotopic data were acquired on a Nu Plasma multi-collector ICPMS, with sample introduction via a Glass Expansion low-uptake PFA nebulizer and Cetac Aridus desolvator. Instrumental mass bias for data collected in static mode was corrected by internal normalisation to $^{146}\text{Nd}/^{145}\text{Nd}=2.0719425$ (equivalent to the more familiar $^{146}\text{Nd}/^{144}\text{Nd}=0.7219$; Vance and Thirlwall, 2002) and $^{152}\text{Sm}/^{147}\text{Sm} = 1.78307$, respectively, using the exponential law as part of an online iterative spike subtraction/internal normalisation procedure. $^{143}\text{Nd}/^{144}\text{Nd}$ in unknowns and quality controls was adjusted to a nominal $^{143}\text{Nd}/^{144}\text{Nd} = 0.511860$ for the La Jolla Nd standard, which was analyzed every fourth run and yielded measured (mass bias-corrected) ratios in the ranges 0.511848-0.511871, 0.511862-0.511884 and 0.511919-0.511969 in the three analytical sessions, respectively. After adjustment, the JNd-1 Nd standard averaged 0.512120 ± 14 (2sd, n=6) while the USGS basalt BCR-2 yielded $^{147}\text{Sm}/^{144}\text{Nd}=0.1382 \pm 2$ (2sd, n=4) and $^{143}\text{Nd}/^{144}\text{Nd}=0.512625 \pm 17$ (2sd, n=6); these results are consistent with long-term averages and with TIMS/MC-ICPMS reference numbers. External precisions for $^{147}\text{Sm}/^{144}\text{Nd}$ and $^{143}\text{Nd}/^{144}\text{Nd}$ are $\pm 0.2\%$ and $\pm 0.004\%$ (2sd), respectively. ϵNd values were calculated using the CHUR parameters of Bouvier (2008): $^{147}\text{Sm}/^{144}\text{Nd}=0.1960$, $^{143}\text{Nd}/^{144}\text{Nd}=0.512632^*$ (*adjusted to the La Jolla value used here). $^{147}\text{Sm}/^{144}\text{Nd}$ and $^{143}\text{Nd}/^{144}\text{Nd}$ in modern depleted mantle (DM) are 0.2136 and 0.513163, respectively, and are based on a linear evolution from $\epsilon\text{Nd} = 0$ at 4560 Ma to $\epsilon\text{Nd} = +10$ at present (modified from Goldstein, 1984). The ^{147}Sm decay constant is $6.54 \times 10^{-12} \text{ yr}^{-1}$. Age corrections (ϵNd_T) are based on U-Pb zircon ages where available (see Table 3.2); otherwise, generic ages of 2820 Ma are used for

Singleton Formation samples, 2815 Ma for Yaloginda Formation samples and 2800 Ma for Meekatharra Formation samples.

Results are presented in Table 3.2 and are included in digital format in Electronic Appendix 3.2 (together with data published by the Geological Survey of Western Australia, 2019). Nd isotopic data for 12 samples from similar aged geologic units in the Yalgoo-Singleton belt were obtained by identical methods and are compared to our data in the discussion section ('Sm-Nd isotopic variation'). These will be tabulated in Chapter 3 where they are presented in their geological context.

Table 3.2. Isotopic data for Norie and Polelle Group volcanic rocks.

Sample ID	Group	Formation	Member	Age (T)	Sm (ppm)	Nd (ppm)	¹⁴³ Nd/ ¹⁴⁴ Nd (standard corrected)	error (2se)	¹⁴⁷ Sm/ ¹⁴⁴ Nd	εNd _T	T ₂ DM (Ga)
221772	Norie	Singleton	lower	2820	2.1	7.3	0.512233	0.000014	0.171125	1.2	3.03
221754	Norie	Singleton	upper	2820	0.1	0.4	0.512848	0.000046	0.201898	2.0	2.96
221755	Norie	Singleton	upper	2820	0.2	0.8	0.512332	0.000016	0.179153	0.2	3.10
221768	Norie	Singleton	upper	2820	1.3	4.1	0.512410	0.000011	0.182926	0.3	3.09
221757	Norie	Singleton	upper	2820	0.9	3.0	0.512324	0.000008	0.177419	0.6	3.06
221797	Norie	Singleton	upper	2820	1.7	6.2	0.512131	0.000010	0.168017	0.3	3.09
221747	Norie	Singleton	upper	2820	2.0	7.8	0.511905	0.000009	0.154109	0.9	3.04
217768	Norie	Yaloginda		2820	3.2	16.5	0.511174	0.000012	0.116769	0.2	3.09
227204	Norie	Yaloginda		2800	2.0	8.0	0.511741	0.000008	0.148014	-0.1	3.11
209130	Polelle	Meekatharra	Bassetts	2800	1.1	3.1	0.512756	0.000013	0.203760	-0.5	3.13
217797	Polelle	Meekatharra	Bassetts	2800	1.0	2.9	0.512825	0.000012	0.207501	-0.5	3.13
209114	Polelle	Meekatharra	Bundle	2800	2.0	7.6	0.511995	0.000010	0.160856	0.1	3.08
217712	Polelle	Meekatharra	Lordy	2800	1.7	5.6	0.512338	0.000013	0.179573	0.1	3.09
217771	Polelle	Meekatharra	Lordy	2800	2.0	6.7	0.512264	0.000012	0.176330	-0.2	3.11
217788	Polelle	Meekatharra	Stockyard	2800	2.8	8.6	0.512715	0.000010	0.196856	1.2	3.00
217790	Polelle	Meekatharra	Stockyard	2800	4.2	13.5	0.512537	0.000010	0.188383	0.8	3.04

3.4. RESULTS

3.4.1. Petrography and mineral chemistry

The following section describes the key petrographic features of mafic volcanic suites, which are the focus of the discussion sections below, as well as chemical variations in pyroxenes and Cr-spinels from the Meekatharra Formation. Electron probe micro analysis (EPMA) methods are identical to those described in Lowrey *et al.*, 2017) and compositions are tabulated in Electronic Appendix 3.3.

3.4.1.1. Singleton Formation

Lower Singleton Formation samples vary between fine-grained mafic volcanics (locally amygdular; Fig 3.4a, b) and olivine-pyroxene cumulates with varying olivine abundance (Fig 3.4c-f). Igneous minerals have typically been replaced by greenschist-amphibolite metamorphic assemblages: olivine is typically altered to serpentine; pyroxene is typically altered to actinolite and chlorite; and plagioclase is typically saussuritized. Locally, textures are well preserved, including skeletal crystal features (Fig 3.4d).

Higher in the Formation, textural preservation is quite variable, due to locally amphibolite-hornfels facies metamorphism, but where textures are preserved (at greenschist facies), volcanic rocks

vary from aphyric to intensely plagioclase-pyroxene phyric or glomerophyric (Fig 3.5a,b).

Outcropping together with the volcanic rocks are fine-grained sub-volcanic units, typically with sub-ophitic textures dominated by stubby to acicular zoned pyroxene pseudomorphs and albitized feldspar \pm Cr-spinel (Fig 3.5c,d) Both volcanic and sub-volcanic rocks locally contain segregated amorphous domains of leucocratic material with cusped margins (now altered to actinolite-tremolite-chlorite) within relatively homogenous mafic groundmass, which may reflect mixing between two melts or partially resorbed material that crystallized earlier in shallow-level magma chambers (Fig 3.5e,f).

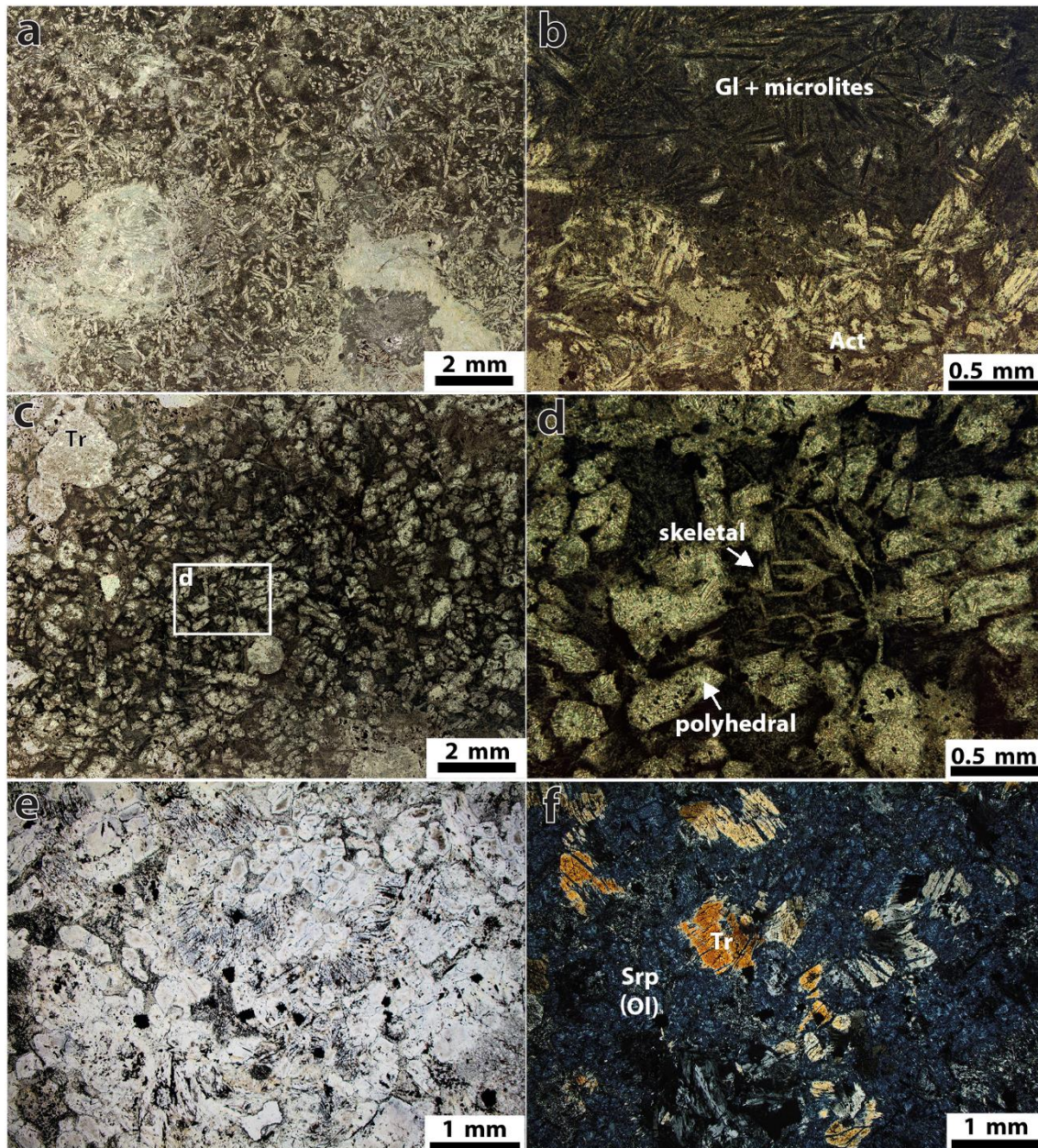


Figure 3.4. Lower Singleton Formation photomicrographs showing a variety of cooling histories, mineralogy and textures. a) Fine-grained high-Mg basalt containing abundant pseudomorphed acicular pyroxene phenocrysts in a groundmass of devitrified, altered glass (221772 - 16 wt% MgO); b) microlite pseudomorphs (probably plagioclase originally) in devitrified, altered glass (221772); c) picrite containing abundant pseudomorphed olivine phenocrysts in a glassy groundmass, with coarser phenocryst now pseudomorphed by tremolite (sample 9344 of Hallberg 2000; 24 wt% MgO) d) olivine crystal morphologies in sample 9344 include discrete phenocrysts or glomerocrysts and locally skeletal forms; e) and f) PPL and XPL images, respectively, of orthocumulate with polyhedral olivine and poikilitic pyroxene pseudomorphs, now altered to serpentine and tremolite (218822 - 28 wt% MgO).

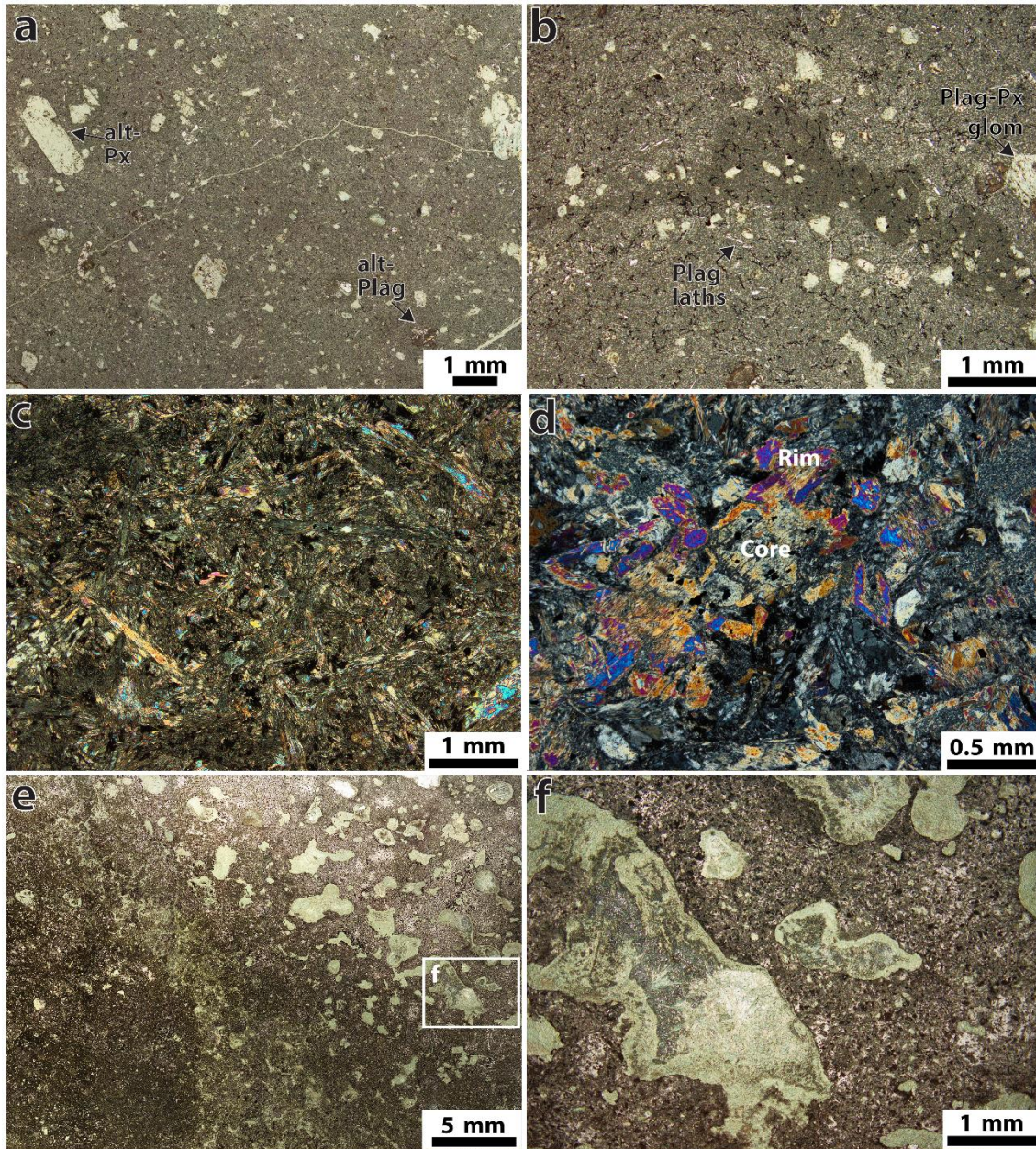


Figure 3.5. Upper Singleton Formation photomicrographs. a) porphyritic basaltic andesite with plagioclase and pyroxene phenocrysts in fine-grained groundmass (221799 - 8 wt% MgO); b) pyroxene-plagioclase glomerocryst set in a fine-grained groundmass containing abundant plagioclase microphenocrysts (221799); c) pyroxene-rich basalt with acicular phenocryst pseudomorphs set in a possibly trachytic textured groundmass (221754 - 14 wt% MgO); d) compositional zoning in pyroxene pseudomorph (81573, 16 wt% MgO); e) and f) amorphous mafic globules within a discrete zone of leucocratic groundmass adjacent to more mafic groundmass (221793, 6 wt% MgO).

3.4.1.2. Meekatharra Formation

The Lordy Basalt Member is characterized by coarse (1–10 cm), randomly oriented, acicular zoned clinopyroxene (augite) phenocrysts within a pyroxene microphenocryst-rich, or glassy groundmass (Fig 3.6a-d). Locally, flows have developed spectacular platy pyroxene spinifex textured tops (Fig 3.6e; see also Lowrey *et al.*, 2017), and olivine-pyroxene cumulate bases (Fig 3.6f). Olivine

is typically serpentinized, while orthopyroxene and augite are variably preserved. Vitrophyric flows locally contain globular ‘varioles’ of devitrified glass and variably altered acicular pyroxene microphenocrysts (Fig 3.7).

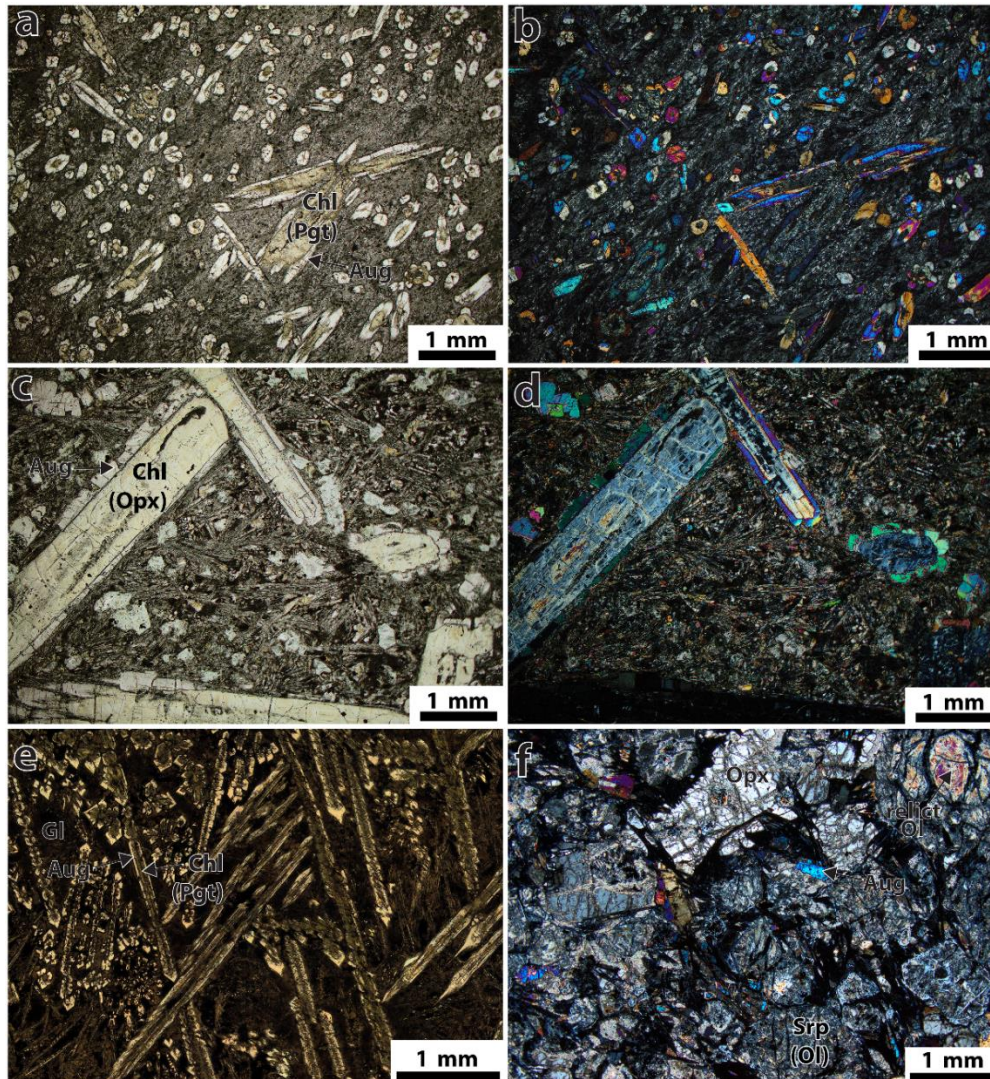


Figure 3.6. Lordy Basalt Member photomicrographs. a) PPL and b) XPL images of zoned acicular pyroxene phenocrysts with augite rims and pigeonite cores (pseudomorphed by chlorite) in a fine, altered groundmass (sample 217771 - 10 wt% MgO); c) PPL and d) XPL images of coarse acicular zoned pyroxene phenocrysts with augite rims and orthopyroxene cores (now altered to chlorite-serpentine) in a trachytic textured groundmass of plagioclase and pyroxene microlites (sample 217796 - 17 wt% MgO); e) platy pyroxene spinifex textured flow top (sample 217703 – no compositional data) and f) XPL image of orthocumulate with relicts of olivine (mostly serpentinized) and poikilitic orthopyroxene and augite (sample 217714 - 27 wt% MgO).

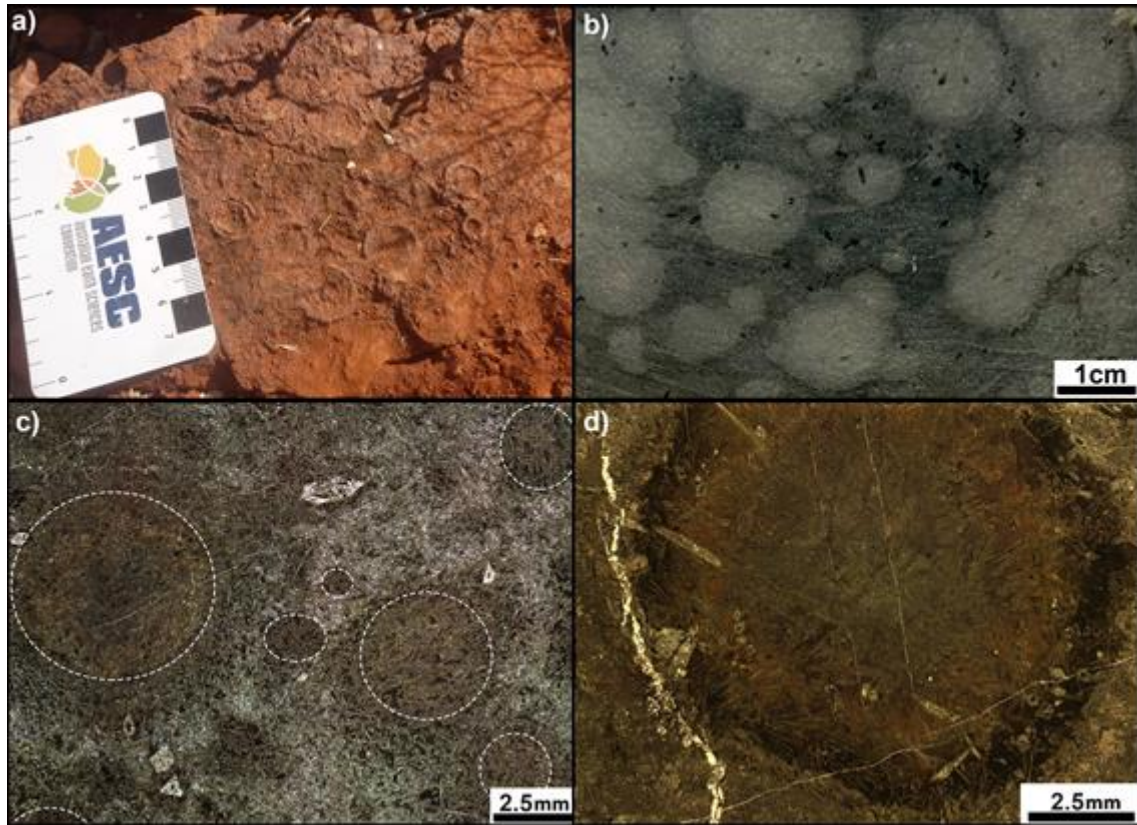


Figure 3.7. Variolitic textured mafic volcanic rocks of the Meekatharra Formation: a) varioles in siliceous high-Mg basalt (near sample 217771); b) varioles coalescing in hand sample (221664); c) varioles in thin section (PPL) of vitrophyric boninite-like rock (sample 221630), several varioles highlighted by white dashed outlines; d) large variole in thin section (PPL) of high-Mg andesite west of Cue (sample 217784).

Samples from the Bassetts Volcanic Member are typically fine-grained mafic volcanic rocks, with glassy (vitrophyric) or microlitic groundmass (Fig 3.8a-f), reflecting high cooling rates and/or magma undercooling linked to rapid fluid loss from water-saturated magmas during ascent (Crabtree and Lange, 2011). Vitrophyric rocks commonly contain globular varioles (≤ 2 cm; Fig 3.7), composed of acicular pyroxene microphenocrysts and devitrified glass that locally merge together to form discrete domains of leucocratic groundmass (≤ 10 cm; e.g., Fig 3.7b).

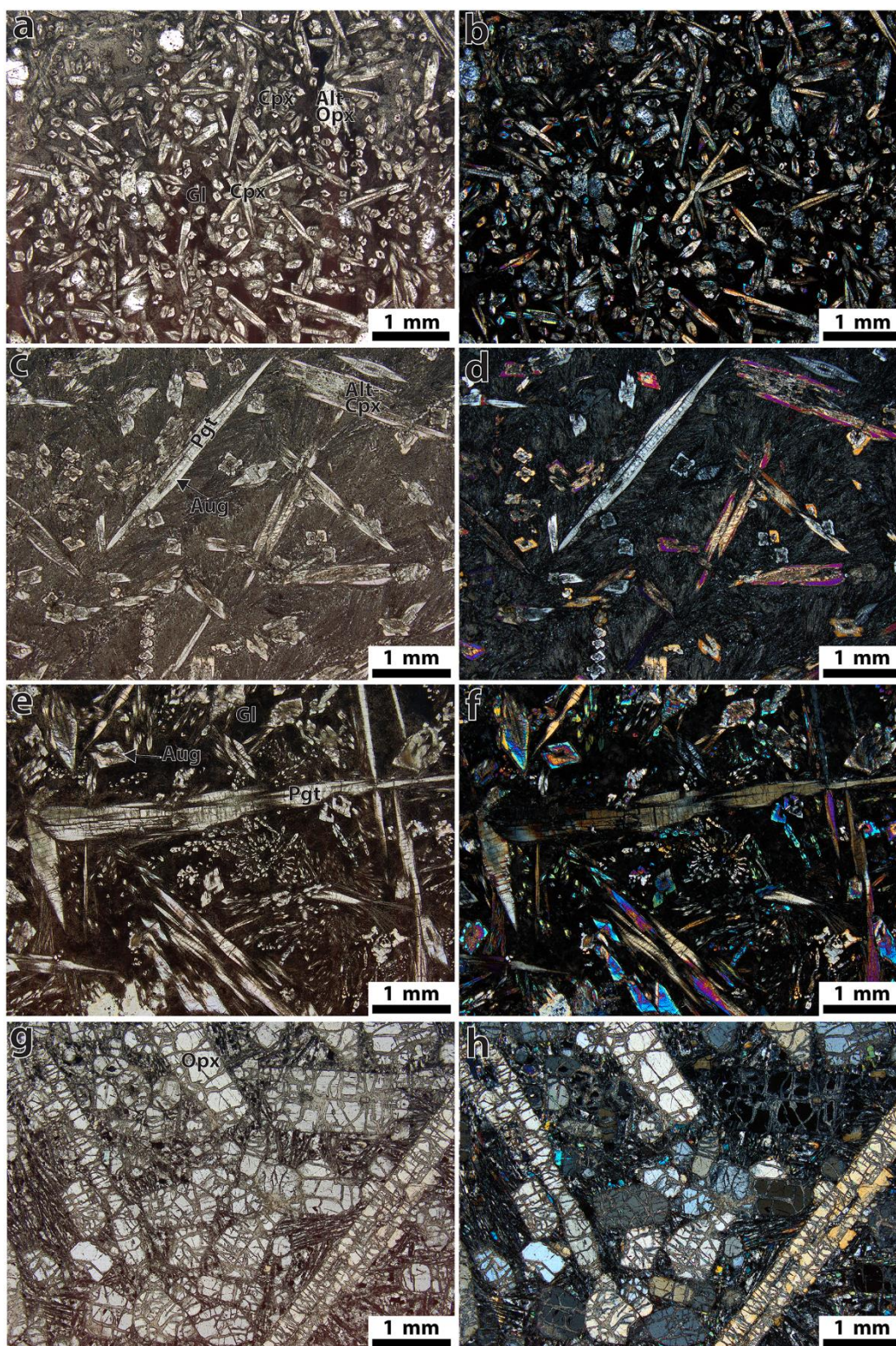


Figure 3.8. Bassett's Volcanic Member photomicrographs with PPL images on left and XPL images on right. a) and b) fine acicular pyroxene microphenocrysts with augite rims and pigeonite cores and euhedral orthopyroxene phenocrysts set in a glassy groundmass (sample 221621 - 13 wt% MgO); c) and d) acicular zoned pyroxene phenocrysts with augite rims and pigeonite cores (variably altered) within a felted groundmass of plagioclase and pyroxene microlites (sample 221693 - 10 wt% MgO) ; e) and f) acicular zoned pyroxene phenocrysts with augite rims and pigeonite cores within a groundmass of dendritic pyroxene and glass (sample 221699 - 12 wt% MgO); g) and h) orthopyroxene cumulate with interstices filled by microlitic plagioclase, augite and opaque minerals (sample 81515 - 20.6 wt% MgO).

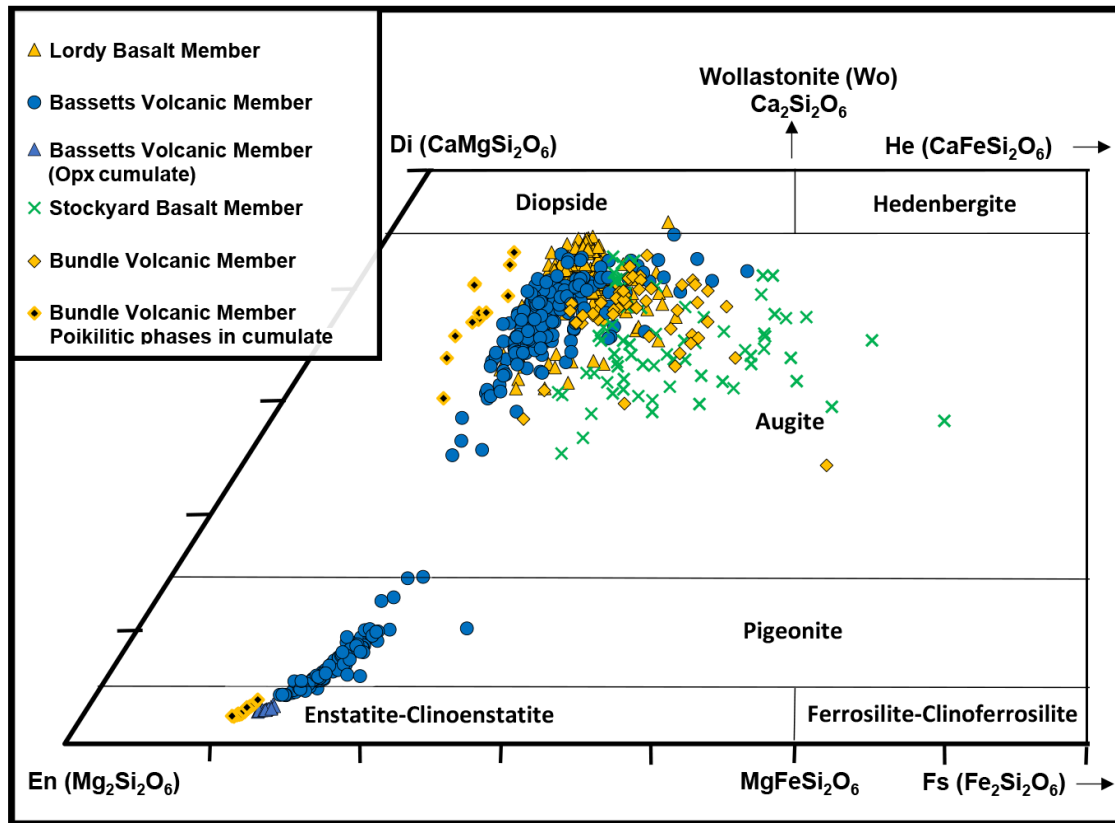


Figure 3.9. Pyroxene compositions from Bassetts Volcanic Member samples projected onto the Mg-rich region of the pyroxene quadrilateral, after Morimoto *et al.*, (1988).

Clinopyroxene microphenocrysts in the Bassetts Volcanic Member are randomly oriented and compositionally zoned and where fresh core material is retained it has compositions mostly within the pigeonite field, however the most magnesian analyses encroach slightly into the clinoenstatite field; from core to rim these range from $Wo_4En_{83}Fs_{13}$ to $Wo_{15}En_{68}Fs_{17}$ (Fig 3.9). Clinoenstatite is rare in terrestrial rocks, having only been reported from Phanerozoic boninites (e.g., Shiraki *et al.*, 1980, Ohnenstetter and Brown 1992, Taylor *et al.*, 1994). In those instances, CaO and Al_2O_3 were lower in clinoenstatite than for coexisting orthopyroxene and always $\leq Wo_3$, whereas in our study area the lowest Ca clinopyroxene compositions are notably richer in CaO and Al_2O_3 relative to coexisting orthopyroxene (see compositional break on Fig 3.9) and are always $> Wo_4$, close to the pigeonite compositional boundary. Hence, we suggest that Low-Ca clinopyroxenes from the Bassetts Volcanic Member are sub-calcic pigeonite, rather than discrete clinoenstatite phases. Incompatible elements Al_2O_3 and TiO_2 increase from the core towards the rim, 1.2–3.5 wt% and 0.1–0.2 wt% respectively, whereas Cr_2O_3 decreases from 0.7–0.1 wt% towards the rim.

In this study area, augite has crystallized around a pigeonite core with an abrupt compositional boundary between the two phases (Fig 3.10) that is most obvious in FeO, MgO, and CaO (Fig 3.11). Similar chemical zoning patterns occur in pyroxene in lunar mare basalts, and were re-created during dynamic crystallization experiments (e.g., Lofgren *et al.*, 1974, Grove and Bence 1977). Those studies suggested that the chemical zonation as the product of high cooling rates whereby the area immediately surrounding the pyroxene is enriched or depleted in certain cations depending on their distribution coefficients between the mineral and the surrounding liquid. In Bassets Volcanic Member samples the surrounding liquid has become enriched in CaO, Al₂O₃ and TiO₂, which promotes the epitaxial growth of augite with an abundance of those cations. Conversely, Cr₂O₃ is strongly partitioned into the pigeonite and is depleted in the augite rims.

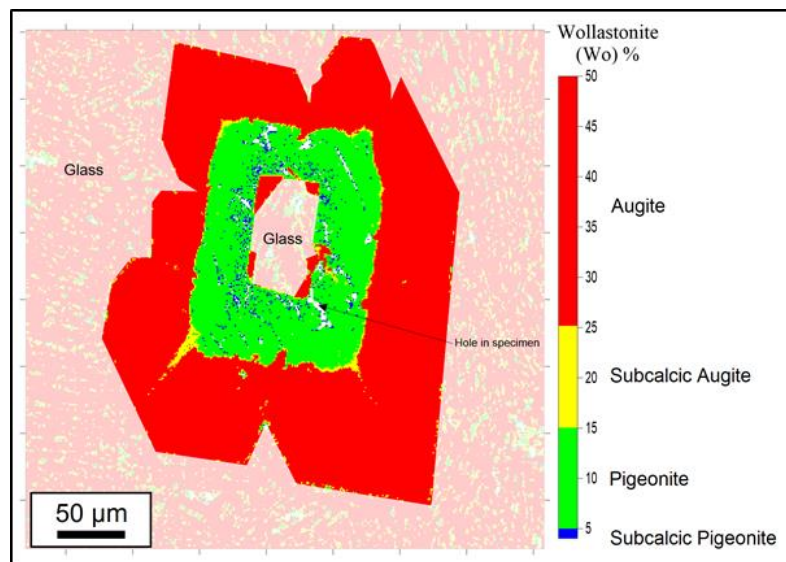


Figure 3.10. Pyroxene composition map coloured by Wollastonite component (Wo %). Phenocryst is from sample 209130 from the Polelle Syncline (Fig 3.2). The core comprises predominantly pigeonite compositions (Wo₅ to Wo₁₅) while the outer and inner rims comprise predominantly augite compositions.

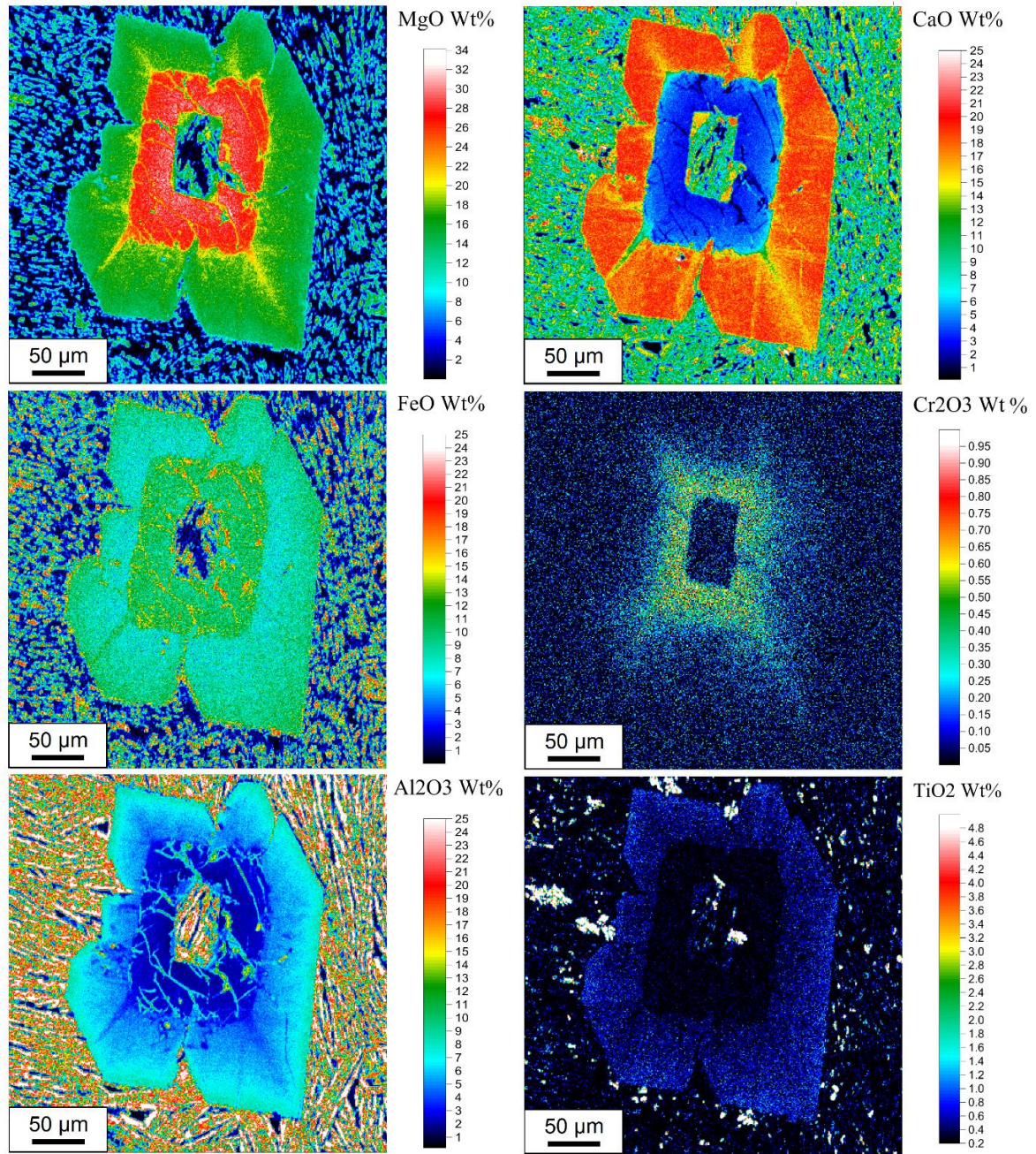


Figure 3.11. Pyroxene element maps obtained by EPMA from a representative phenocryst from sample 209130 in the Polelle Syncline a. MgO; b. CaO; c. FeO; d. Cr₂O₃; e. Al₂O₃; f. TiO₂ (after Lowrey *et al.*, 2017).

Augite rim compositions range from $\text{Wo}_{25}\text{En}_{61}\text{Fs}_{14}$ to $\text{Wo}_{44}\text{En}_{36}\text{Fs}_{20}$. Al_2O_3 and TiO_2 rise to extreme values at the augite rim (≤ 12 wt% and ≤ 1 wt% respectively; Electronic Appendix 3.3), and Cr_2O_3 falls to below detection limit (< 0.02 wt%). Groundmass crystals are augite with dendritic morphologies and have similar compositions to the edges of augite rims.

Orthopyroxene is present as a phenocryst phase in fine grained samples and is typically altered to chlorite \pm serpentine minerals. Orthopyroxene phenocrysts ($\text{Wo}_3\text{En}_{85}\text{Fs}_{12}$ to $\text{Wo}_3\text{En}_{84}\text{Fs}_{13}$; Electronic Appendix 3.3) in orthocumulate zones, however, are typically fresh, coarse, and elongate or columnar ($\leq 5 \times 1 \text{ mm}$). Representative orthopyroxene analyses from cumulate samples have a narrow compositional range from $\text{Wo}_3\text{En}_{85}\text{Fs}_{12}$ to $\text{Wo}_3\text{En}_{84}\text{Fs}_{13}$ (Electronic Appendix 3.3 and Fig 3.9) and do not show compositionally zoning but locally have thin reaction rims where they contact the surrounding matrix. Olivine phenocrysts in orthocumulate zones are fine and equant (150-500 μm), polyhedral or sub-angular and typically serpentinized (not shown).

Cr-spinel is present as a minor phase ($< 5\%$), typically in clusters of fine (10-50 μm) euhedral phenocrysts with an irregular distribution. Cr-spinels contain high Cr_2O_3 (47.2–53.7 wt%), high $\text{Cr}/(\text{Cr} + \text{Al})$ (0.82–0.85), low $\text{Fe}^{3+}/(\text{Fe}^{3+} + \text{Cr} + \text{Al})$ (0.09–0.11), high $\text{Fe}^{2+}/(\text{Mg} + \text{Fe}^{2+})$ (0.58–0.87) and low TiO_2 (0.2–0.3 wt%), plotting entirely within the 90th percentile (and mostly within the 50th percentile) contours for both boninite and komatiite on Barnes and Roeder's (2001) trivalent ion ternary plot. Plagioclase is absent from vitrophyric samples, but is present in slower cooled examples as lath shaped microlites (locally fan shaped spherulites) in a fine groundmass (Fig 3.8c, d). Olivine has not been observed in any fine-grained examples, however, several flows include 5-10 m thick orthocumulate layers containing cumulus orthopyroxene \pm olivine with fibrous intergrowths of augite, plagioclase, and opaque minerals in the interstices between orthopyroxene phenocrysts (Fig 3.8g, f).

Samples from the Stockyard Basalt Member are typically aphyric and fine-grained, with groundmass comprising predominantly augite, plagioclase and opaque minerals (magnetite, titanomagnetite etc.) (Fig 3.12a, b). Compositions of augites are more iron-rich than in the other Member units of the Meekatharra Formation (Fig 3.9 in Electronic Appendix 3.3).

Samples from the Bundle Volcanic Member samples are typically pyroxene spinifex textured, or olivine-pyroxene orthocumulates. The chilled margins of flows are rarely preserved, but those that outcrop are aphyric, with skeletal olivine microphenocrysts and dendritic clinopyroxene. The petrography of the Bundle Volcanic Member is described in detail in Lowrey *et al.* (2017).

Basalts from the Cue area (Fig 3.2) typically have microlitic to sub-ophitic textures and have been subjected to upper greenschist – lower amphibolite facies metamorphism. The microlitic textured rocks have pseudomorphed microphenocrysts of plagioclase (saussuritized) and/or pyroxene (now typically actinolite-tremolite) characteristic of rapid cooling. The groundmass typically comprises lath-shaped plagioclase microlites with clinopyroxene pseudomorphs filling the spaces between laths (Fig 3.12c, d). Locally they contain larger euhedral pyroxene \pm plagioclase glomerocryst pseudomorphs that have been entirely replaced by ultrafine-grained alteration minerals. Locally, microlitic textures grade into coarser, almost subophitic textures, with coarse laths of plagioclase (saussuritized), acicular pyroxene pseudomorphs (now actinolite-tremolite) and almost no fine-grained groundmass, reflecting variable cooling histories.

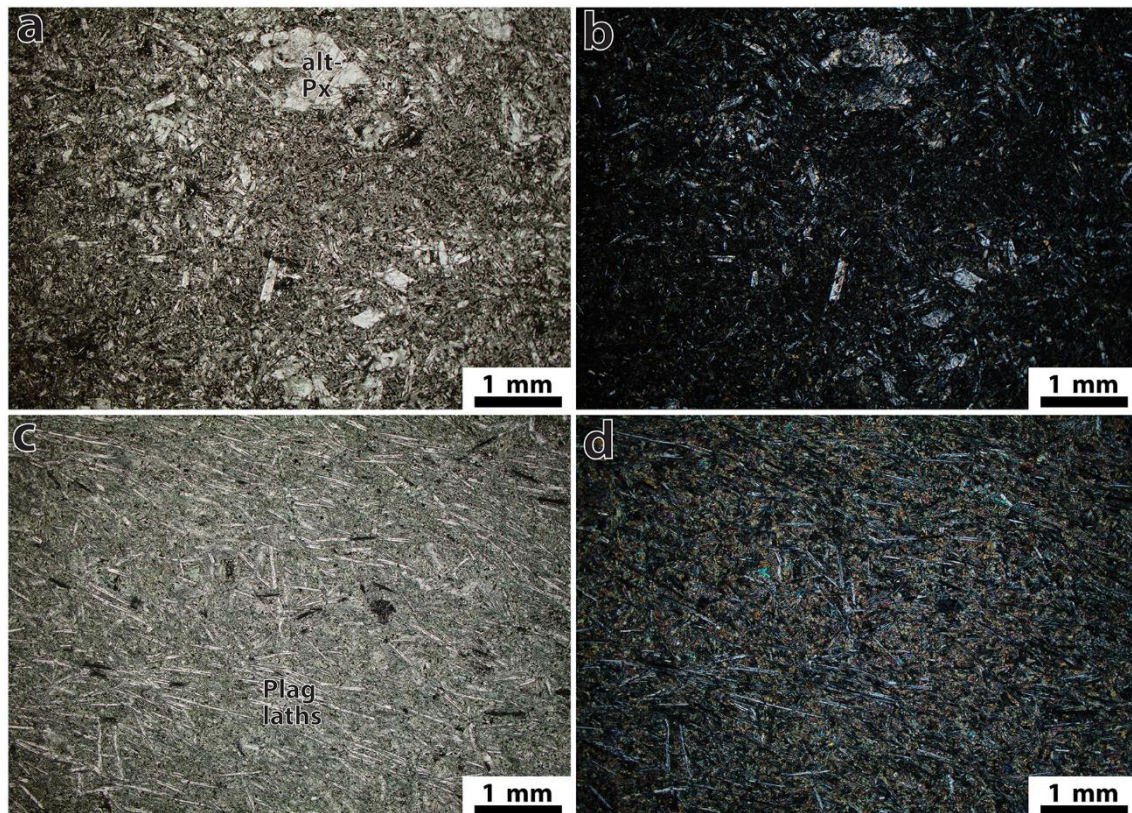


Figure 3.12. Meekatharra Formation Tholeiitic basalts with PPL images on left and XPL images on right: a) and b) Stockyard Basalt Member (sample 217790); c) and d) Cue basalt (sample 217800).

3.4.2. Whole-rock geochemistry and Sm-Nd isotopes

Whilst every effort was taken to sample the freshest material available, we nevertheless concentrate our discussion on elements considered immobile (e.g., major elements, high-field strength elements (HFSEs), rare earth elements (REEs), Cr, Ni). X-Y variation diagrams for many of these elements are provided in Fig 3.13a-h. We describe the chemical and isotopic variation within successive stratigraphic intervals of the Norie and Polelle Groups below and compare key chemical attributes to well-known examples of boninite and komatiite in Fig 3.14a-f. We also present a summary of chemical variation within stratigraphic units of the Norie and Polelle Groups in Table 3.3.

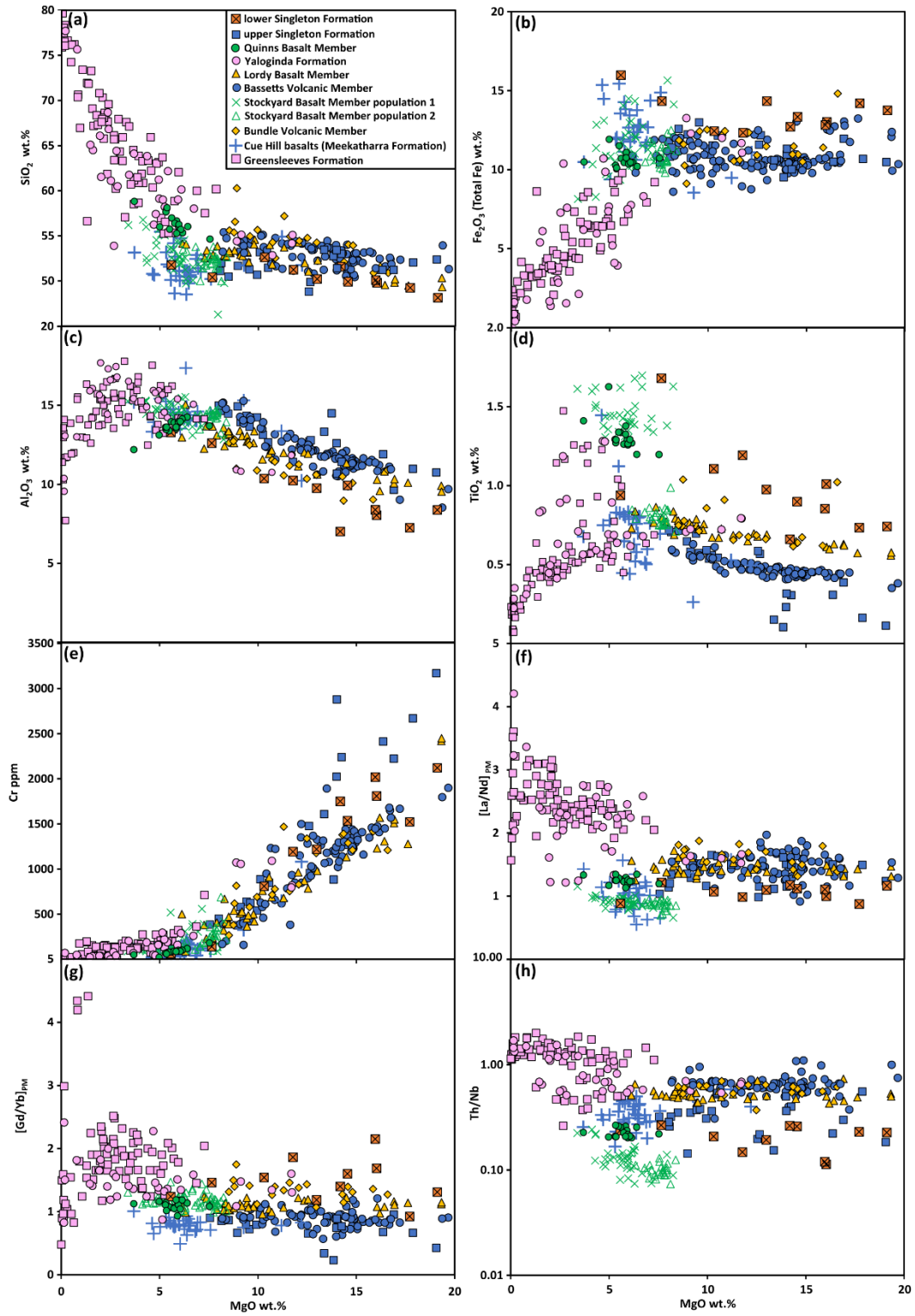


Figure 3.13. Major and trace element variation diagrams for Norie and Polelle Group samples: a) SiO₂ vs MgO; b) Fe₂O₃ (total Fe as Fe³⁺) vs MgO; c) Al₂O₃ vs MgO; d) TiO₂ vs MgO; e) CaO vs MgO; f) Cr vs MgO; g) [La/Nd]_{PM} vs MgO; h) [Gd/Yb]_{PM} vs MgO.

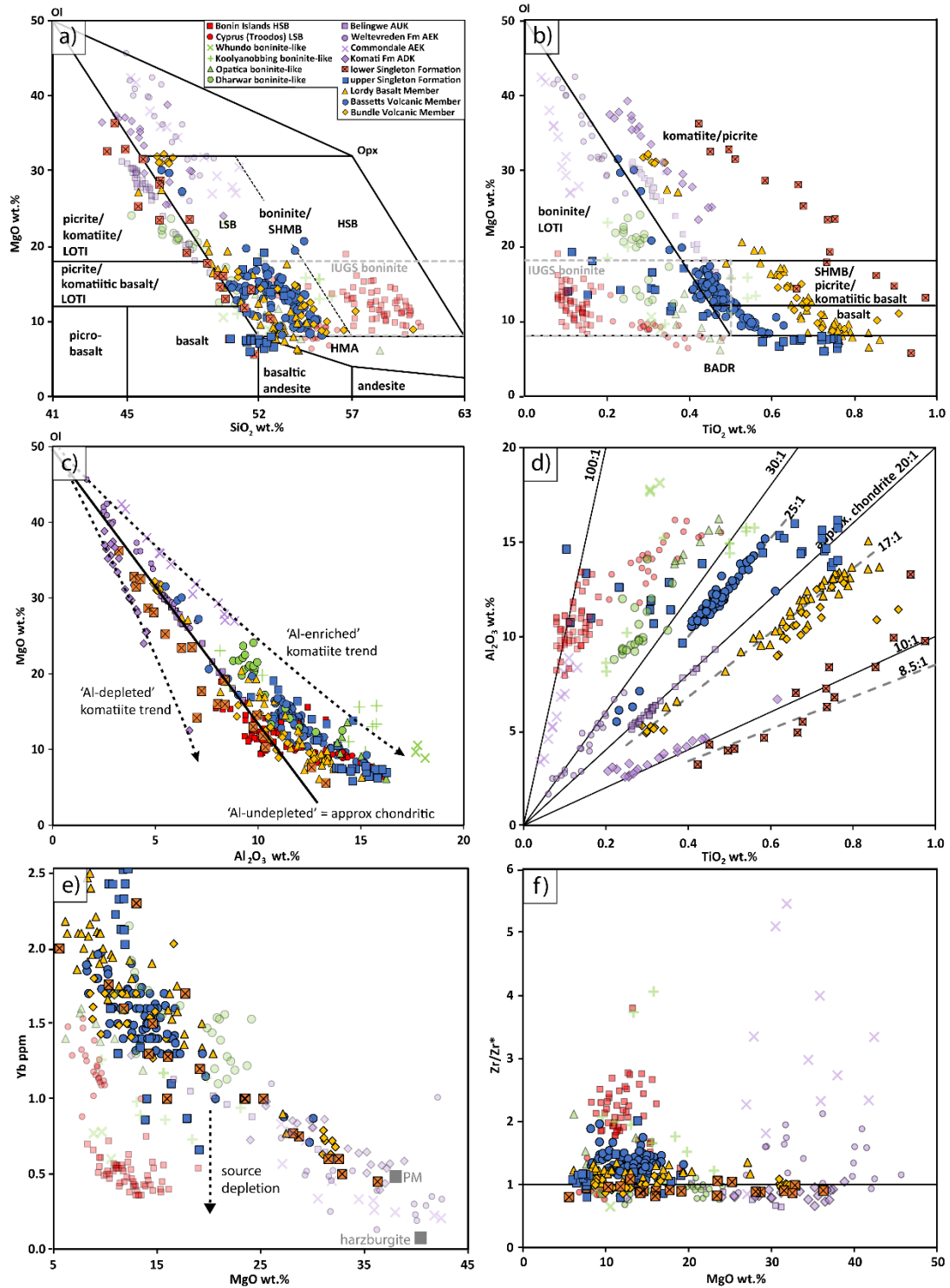


Figure 3.14. Major and trace element variation and discrimination diagrams comparing Norie and Polelle Group mafic volcanics (including olivine-rich cumulates) to potential analogues: a) MgO vs SiO₂ and b) MgO vs TiO₂ discrimination diagrams (both after Pearce and Reagan 2019; SHMB - siliceous high-Mg basalt); c) MgO vs Al₂O₃; d) Al₂O₃ vs TiO₂; e) Yb vs MgO; and f) Zr/Zr* vs MgO. Data sources: Ogasawara HSB (High-Si boninite; Kanayama, 2012), Troodos LSB (low-Si boninite König, 2008, Osozawa, 2012, Golowin, 2017), Opatika (Boily and Dion, 2002), Whundo (Smithies, 2005), Dharwar (Manikyamba, 2005), Weltevreden Formation AEK and Komati Formation ADK (Al-enriched komatiite, Al-depleted komatiite; Robin-Popieul, 2012), Comondale AEK (non-cumulates only; Wilson, 2003b, Hoffmann and Wilson, 2017), Belingwe AUK (Al-undepleted komatiite; Puchtel, 2009).

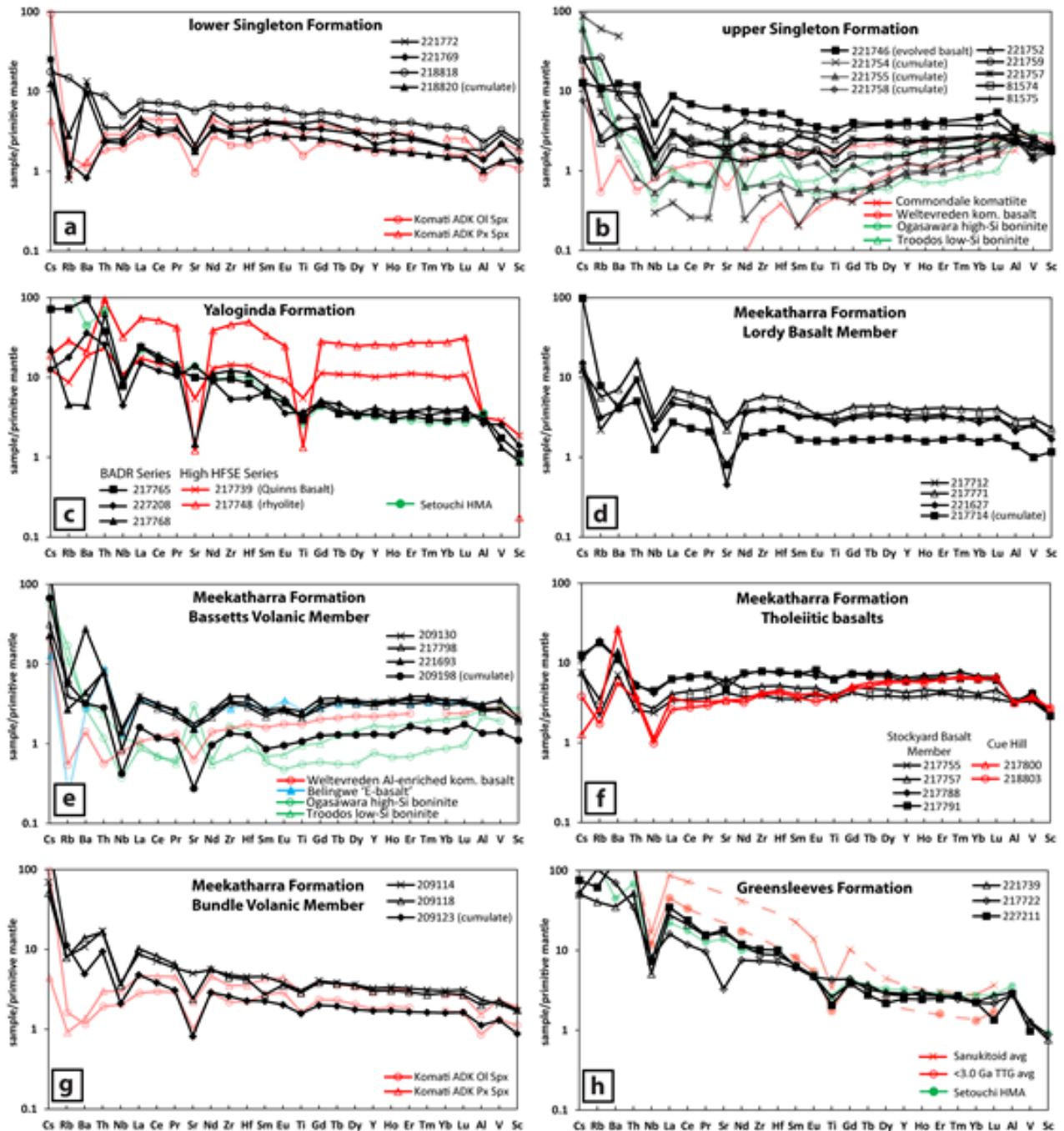


Figure 3.15. Trace element patterns for northwest Youanmi Terrane normalised to primitive mantle (Sun and McDonough 1989). Partially transparent patterns used for comparisons include Komati Formation Al-depleted komatiites (BD4 and BD7; Robin-Popieul, 2012), Weltevreden Formation Al-enriched komatiites (WP107 and WP108; Robin-Popieul, 2012), Commondale Al-enriched komatiite (27.37; Wilson, 2003b), Ogasawara high-Si boninite (Kanayama, 2012), Troodos low-Si boninite (CY119; Osozawa, 2012), Setouchi HMA (OTO-7; Tatsumi, 2005), Belingwe 'E-Basalt' (BX229; Shimizu, 2005), Sanukitoid avg and < 3000 Ma TTG (tonalite-trondhjemite-granodiorite) avg (Martin, 2005).

Table 3.3. Chemostratigraphic characteristics of Norie and Polelle Groups.

Stratigraphic Group and Formation	Member	Age (Ma)	Type Locality	IUGS classification (chemical description)	SiO ₂	Mafic character -istics	REE patterns	εNdT	Melt fraction (simple batch melt model)	Source region	Intrusive affinities	Tectonic implications
Polelle Group: Greensleeves Formation	upper (informal)	c. 2750 to 2740	Wattagee Hill	Andesite to rhyolite (calc-alkaline, BADR-series)	High	Mostly low Mg, low Ni, Cr	Strongly enriched LREEs, depleted to flat HREEs, occasionally concave between Dy-Yb	-2.2 to +0.5 (n=2)	not modelled	Metasomatised mantle; locally contaminated by old crust	Cullculli Suite (hornblende-biotite sanukitoids and TTGs)	Subduction and/or underplating of meta-somatised mantle
Polelle Group: Greensleeves Formation	Woolgra Andesite	c. 2760 to 2740	Polelle Syncline	Basaltic andesite to rhyolite (calc-alkaline, BADR-series)	High	High Mg, Ni, Cr	Strongly enriched LREEs, depleted to flat HREEs, occasionally concave between Dy-Yb	+0.8 to +1 (n=2)	not modelled	Metasomatised mantle		
Polelle Group: Meekatharra Formation	Cue basalt (informal)	<2800	Cue Hill	Basalt (siliceous high-Mg basalt)	High	Moderate Mg, High Fe, low Ni, Cr	Strongly depleted LREEs through to HREEs	-	c. 5% 2nd stage melt of 10% depleted DMM	Metasomatised refractory mantle	Boodanoo and Warriedar Suites (hornblende bearing gabbros)	Subduction and/or underplating of meta-somatised mantle
Polelle Group: Meekatharra Formation	Bundle Volcanics	<2800	Polelle Syncline	Basaltic andesite to andesite (siliceous high-Mg basalt)	High	High-Mg, Ni, Cr	Strongly enriched LREE through to gently sloping HREEs (possible garnet signature)	+0.2 (n=1)	not modelled	Metasomatised mantle; possible melting depth of ≥ 3 GPa		
Polelle Group: Meekatharra Formation	Stock-yard Basalt	<2800	Polelle Syncline	Basalt to andesite (tholeiitic basalt)	Normal to High	Low to moderate Mg, low Ni, Cr	Depleted to flat LREEs and typically flat HREEs, but occasionally depleted HREEs (garnet signature)	+0.80 to +1.2 (n=2)	not modelled	Weak to moderately depleted un-metasomatised mantle; replenished upwelling asthenosphere	None identified	Extension/rifting
Polelle Group: Meekatharra Formation	Bassetts Volcanics	<2800	Polelle Syncline	Basaltic andesite to andesite (boninite-like siliceous high-Mg basalt)	High	High Mg, Ni, Cr	Concave REEs, strongly enriched La-Sm, [Gd/Yb] _{PM} ~0.9.	-0.5 (n=2)	c. 20-25% 2nd stage melt of 10% DMM	Metasomatised refractory mantle	Boodanoo and Warriedar Suites (hornblende bearing gabbros)	Subduction and/or underplating of meta-somatised mantle
Polelle Group: Meekatharra Formation	Lordy Basalt Member	<2800	Polelle Syncline	Basalt to andesite (siliceous high-Mg basalt)	High	High Mg, Ni, Cr	Moderately enriched LREEs, flat HREEs	-0.2 to +0.1 (n=2)	not modelled	Metasomatised mantle melts or contamination of fertile asthenospheric melts		
Norie Group: Yaloginda Formation	Undifferentiated (BADR series)	2805 to 2815	Polelle Syncline	Basaltic andesite to rhyolite (siliceous high-Mg basalt to high-Mg andesite)	High	High Mg, Ni, Cr	Strongly enriched LREEs, [Gd/Yb] _{PM}	-0.1 to +1.4 (n=4)	not modelled	Metasomatised lithosphere	Mount Kenneth Suite (felsic intrusions with calc-alkaline affinity)	

Table 3.3. Continued

Stratigraphic Group and Formation	Member	Age (Ma)	Type Locality	IUGS classification (chemical description)	SiO ₂	Mafic character -istics	REE patterns	εNdT	Melt fraction (simple batch melt model)	Source region	Intrusive affinities	Tectonic implications
Norie Group: Yaloginda Formation	Kantie Murdana, Youan-garra, Yuinmery Volcanics	c. 2814 to 2817	Meeline Suite Intrusions	Rhyolite (locally andesitic) (tholeiitic rhyolite)	High	Low Mg, Ni, Cr	Weakly enriched LREEs, flat HREEs, very high concentrations	0 (n=1)	not modelled	Fractionated tholeiitic liquids derived from melts of crust/lithospheric mantle	Mount Kenneth Suite (felsic intrusions with tholeiitic affinity)	Local expressions of extension/rifting
Norie Group: Singleton Formation	Quinns Basalt	>2817	Quinns Mining District	Basalt to andesite (tholeiitic basaltic andesite)	High	Low Mg, Ni, Cr	Weakly enriched LREEs, flat HREEs, high concentrations	-	not modelled			
Norie Group: Singleton Formation	upper (informal)	>2817	Gabanintha	Basalt to basaltic andesite (boninite-like rocks and high-Mg basaltic andesites)	High	High Mg, Ni, Cr	Depleted to enriched LREEs, [Gd/Yb] _{PM} 0.7 to 1.1, locally concave patterns	+0.9 to +0.2 (n=5)	c. 20-25% melt of DMM source	Metasomatised mantle (variably depleted)	Meeline Suite (tholeiitic intrusions)	Subduction and/or underplating of meta-somatised mantle
Norie Group: Singleton Formation	lower (informal)	>2817	Gabanintha	Basalt, picrite (Al-depleted komatiite-like high-Mg basalt, picrite and orthocumulate)	Normal	High Mg, Ni, Cr	Flat LREEs, depleted HREEs; locally convex patterns	+1.2 (n=1)	c. 10% melt of DMM source or c. 25% melt of weakly depleted mantle at ≥ 3 GPa	low-moderate degree melting (mostly Cpx) in fertile upwelling asthenosphere; garnet left in source		Extension, rifting; possible mantle plume

3.4.2.1. Singleton Formation

The Singleton Formation in the Gabanintha area (Figs 3.1-3.3) can be separated into two distinct geochemical sub-units, corresponding to the lower part and upper part of the formation.

3.4.2.1.1. Lower Singleton Formation

Fine-grained volcanic rocks in the lower Singleton Formation (Fig 3.3) contain 49.9-52.7 wt% SiO₂, with high MgO (10.3-16.1 wt%), Mg-numbers [$\text{Mg}^{2+}/(\text{Mg}^{2+} + \text{Fe}_{\text{Total}}) \times 100$] (62-71), Ni (243-647 ppm) and Cr (810-2020 ppm) (Fig 3.13). Samples with ≥ 18 wt% MgO contain abundant olivine phenocrysts and while these rocks are described elsewhere as komatiitic (e.g., Barley, 2000), their MgO concentrations have clearly been inflated via olivine accumulation. Based on fine grained sample compositions and olivine fractionation trends, liquid compositions are estimated to be 16-20 wt% MgO and hence picritic (Electronic Appendix 3.4a). However, the rocks have major element contents and trace element patterns similar to Al-depleted komatiitic basalts (e.g., Komati Formation, Barberton; Robin-Popieul, 2012) (Figs 3.14a, d, 3.15a). In the case of the komatiitic basalts, and probably the Singleton Formation basalts and picrites, their unfractionated to slightly depleted LREEs indicate a weakly depleted mantle source, while their high $[\text{Gd}/\text{Yb}]_{\text{N}}$ (1.2-1.9; Fig 3.14g) and low Al₂O₃/TiO₂ (8-11 for lower Singleton Formation picrites; Fig 3.14d) indicates retention of garnet as a residual phase (Arndt, 2008).

A single sample yielded $\epsilon_{\text{Nd}2820}$ of 1.2 (Table 3.2).

3.4.2.1.2. Upper Singleton Formation

Fine-grained volcanic rocks from the upper Singleton Formation (Fig 3.3) are relatively magnesian (6.1-12.6 wt% MgO) and under the IUGS classification (Le Maitre, 2002) most samples classify as basalt, with lesser basaltic andesite and picrite (48.8-52.8 wt% SiO₂ and 1.6-3.5 wt% Na₂O + K₂O). They are relatively primitive, with moderate to high Mg-numbers (48 to 68), Ni (93-462 ppm) and Cr (284-1476 ppm), and have relatively low (0.57-0.76 wt%) TiO₂ concentrations. Although they do not meet the major element criteria for boninite by either the IUGS (Le Bas, 2000; MgO > 8 wt%, SiO₂ > 52 wt%, TiO₂ < 0.5 wt%) or more recent Pearce and Reagan (2019) scheme

(Figs 3.14a,b; $\text{Si}_8 > 52$, $\text{Ti}_8 < 0.5$), most samples have LREE-depleted or concave mantle normalised trace element patterns (Fig 3.15b) and low Ti/V typically observed in Cenozoic boninite-related suites.

Sub-volcanic rocks have SiO_2 content (48.8 to 53.5 wt%) similar to volcanic rocks from the same localities, but reach higher MgO (7.3-19.1 wt%), Ni (105-822 ppm), Cr (320-3170 ppm), and lower TiO_2 (0.1-0.6 wt%) concentrations. Approximately 20% of sub-volcanic samples classify as boninite by the IUGS scheme and 40% classify as boninite by the Pearce and Reagan (2019) scheme, although compositions with < 0.2 wt% TiO_2 correspond to samples containing abundant stubby to acicular pyroxene pseudomorphs (\pm Cr-spinel) with little groundmass (i.e., pyroxene orthocumulates) and are therefore subject to cumulate effects. Sub-volcanic units containing > 0.2 wt% TiO_2 are mostly subophitic with similar incompatible trace element patterns to the volcanic units (at slightly lower concentrations; Fig 3.15b).

Pyroxene orthocumulate samples have very low incompatible trace element concentrations, with patterns that are either strongly LREE-MREE depleted (e.g., 221755 in Fig 3.15b) or LREE-enriched and MREE depleted (i.e., concave; e.g., 221758, 221759 in Fig 3.15b) – these patterns resemble boninites from the Troodos Ophiolite in Cyprus (e.g., Osozawa, 2012) and Ogasawara Islands (previously Bonin Islands; e.g., Kanayama, 2012). Two cumulate samples (221754 and 221756* [*not plotted]) have trace element patterns similar to some Al-enriched komatiites (e.g., Weltevreden Formation and Comondale komatiites; Wilson, 2003a,b; Puchtel, 2013), however, they appear to have suffered post-volcanic metasomatism based on minor LREE-loss (relative to Zr-Hf, i.e., high Zr/Zr^* [where $\text{Zr}^* = \text{Nd}_{PM}^{0.5} \times \text{Sm}_{PM}^{0.5}$]), LILE gains (very high Cs, Ba, Rb; K_2O 1.4 wt% in 221754) and lower MgO/ TiO_2 compared to other samples in this group (Figs 3.13d, 3.15b), and are therefore not considered further in the discussion below.

Six samples yield a narrow range in $\epsilon_{\text{Nd}2820}$ from +0.2 to +0.9* (Table 3.2; *excluding altered cumulate sample 221754 with $\epsilon_{\text{Nd}2820} +2.0$, since $^{147}\text{Sm}/^{144}\text{Nd}$ is assumed to have been modified by metasomatism).

3.4.2.2. Yaloginda Formation

The Yaloginda Formation (Figs 3.1, 3.2) can also be divided into two distinct chemical groups. First, the ‘high-HFSE series’ in the lower parts of the Yaloginda Formation comprises basaltic andesites, dacites and rhyolites (Quinns Basalt and Rhyolite, and Kantie Murdana Volcanics; Figs 3.1, 2.2) with high HFSE-REE concentrations and relatively flat mantle normalised trace element patterns. They are spatially and temporally associated with layered intrusive complexes of the Meeline Suite. One representative trace element pattern is shown in Fig 3.15c; this unit will be discussed in greater detail in a subsequent study of felsic lithologies. Sm-Nd isotope data for sample 193923 indicate an $\epsilon_{\text{Nd } 2815}$ of 0.0 (WACHEM database, GSWA, 2018b).

The second chemical group in the Yaloginda Formation is a series of high-Mg basaltic andesite, andesite, dacites and rhyolite (hence ‘BADR-series’). Samples from stratigraphically lower levels contain 52.9-55.1 wt% SiO_2 with high MgO (8.9-11.7 wt%), Mg-numbers (57-68), Ni (246-441 ppm) and Cr (797-2092 ppm) – most samples are consistent with a high-Mg (or primitive) andesite classification, i.e., $\text{SiO}_2 > 54$ wt% and $\text{MgO} > 6$ wt% (Wood and Turner, 2009) and Mg-number 50-60 (> 60 for primitive andesite; Kelemen, 2007). They have mantle normalised trace element patterns that are LREE-enriched ($[\text{La}/\text{Sm}]_{\text{PM}} \sim 2.3$, $[\text{Gd}/\text{Yb}]_{\text{PM}} 1.3$) and have prominent negative Nb-anomalies relative to Th and La (Fig 3.15c). These characteristics are comparable to Cenozoic high-Mg andesites from volcanic arc settings, such as the Setouchi Volcanic Belt in SW Japan (e.g., Tatsumi, 2005). Overlying the Yaloginda Formation high-Mg andesites is a sequence of andesitic to dacitic rocks with moderate concentrations of MgO (6.5-14 wt%), Fe_2O_3 (8.1-3.9 wt%), TiO_2 (0.9-0.6 wt%), Ni (150-10 ppm) and Cr (296 to < 10 ppm), which decrease with increasing SiO_2 (56.4-63.4 wt%) as is expected for a transition from crystallization of mafic to felsic mineral assemblages.

Sm-Nd isotope data for two samples yield $\epsilon_{\text{Nd}2815}$ -0.1 and +0.2 (Table 3.2), while another yields $\epsilon_{\text{Nd}2815}$ +1.5 (sample 185930; WACHEM database, GSWA, 2018b).

3.4.2.3. *Meekatharra Formation*

The Meekatharra Formation (Figs 3.1, 3.2) can be divided into four distinct chemical members, the Lordy Basalt Member, Bassetts Volcanic Member, Stockyard Basalt Member and Bundle Volcanic Member:

3.4.2.3.1. *Lordy Basalt Member*

Fine-grained volcanic rocks contain 49.2-54.6 wt% SiO₂, 6.1-20.4 wt% MgO, and their Mg-numbers range from 53 to 76. Samples containing > 16 wt% MgO are rare, and these contain abundant fine-grained (< 1mm), mostly euhedral olivine crystals. Hence, liquid compositions were almost certainly \lesssim 16 wt% MgO. Ni (68-861 ppm) and Cr (87-2757 ppm) concentrations in the Lordy Basalt Member vary significantly. TiO₂ (0.53-0.86 wt%) is relatively low (but not as low as to classify as boninite, < 0.5 wt%), and Al₂O₃ (9.2-15 wt%) is moderate, resulting in relatively constant, slightly sub-chondritic Al₂O₃/TiO₂ (15-18). According to the IUGS classification scheme (Le Bas, 2000), various samples in this unit classify as picrite, basalt or basaltic andesite, whereas in the Pearce and Reagan (2019) scheme, most samples classify as siliceous high-Mg basalt (Fig 3.14 a,b).

Trace element patterns are transitional between those of the overlying Bassetts Volcanic Member and Bundle Volcanic Member (Fig 3.15d), with fractionated REE patterns ([La/Nd]_{PM} 1.4-1.5, [La/Yb]_{PM} 1.4-2.0), strongly negative Nb anomalies ([Th/Nb]_{PM} 4.2-4.5 and [Nb/La]_{PM} 0.4-0.5) and moderately positive Zr-Hf anomalies (Zr*/Zr = 1.15-1.30). In these very well-preserved samples, Zr-Hf anomalies are considered to be an igneous feature. REE and HFSE ratios remain relatively constant over a significant fractional crystallization interval (20.4-9.1 wt% MgO), indicating liquid evolution controlled mainly by olivine, which has low partition coefficients for those incompatible elements.

Sm-Nd isotopic data for two samples yield $\epsilon_{\text{Nd}2800}$ of -0.2 and +0.1 (Table 3.2).

3.4.2.3.2. *Bassetts Volcanic Member*

Fine-grained samples from this unit yield high SiO₂ (51.8-56.7 wt%), MgO (8.1-17.2 wt%), and Mg-numbers (63-77). Samples with > 15 wt% MgO contain abundant orthopyroxene phenocrysts and

those with 19-21 wt% MgO are orthopyroxene orthocumulates, implying liquid compositions had \leq 15 wt% MgO. Ni (109-513) and Cr (203-1980 ppm) concentrations again vary significantly, but correlate with MgO, reflecting olivine and orthopyroxene control. TiO₂ is low (0.39-0.60 wt%) and Al₂O₃ is relatively high (10.0-15.2 wt%), resulting in consistently super-chondritic Al₂O₃/TiO₂ ratios (24.4–27.5) that clearly differentiate the Bassetts Volcanic Member from the rest of the Meekatharra Formation samples (Al₂O₃/TiO₂ 10-20). Most samples classify as boninite in the IUGS scheme (Le Bas, 2000), but rare examples containing < 10 wt% MgO exceed the upper 0.5 wt% TiO₂ limit and are instead classified as basaltic andesite (Fig 3.14b). According to the Pearce and Reagan (2019) scheme, most samples classify as siliceous high-Mg basalts, with only the lowest TiO₂ samples classifying as boninite. CaO ranges from 7.5-11.1 wt% and CaO/Al₂O₃ (0.65-0.82) is in the range of high-Ca boninite (CaO/Al₂O₃ > 0.7-1; Crawford, 1989).

Mantle normalised trace element patterns have subtly concave shapes, with minima near Nd (Fig 3.15e), like most Archean boninite-like rocks (e.g., Boily and Dion, 2002; Manikyamba, 2005; Angerer, 2013). They feature strong negative Nb anomalies [Th/Nb]_{PM} (4.8-5.7) and positive Zr-Hf anomalies (Zr*/Zr = 1.3-1.4). [Nb/Yb]_{PM} (0.42-0.48) and [Gd/Yb]_{PM} (0.92-0.98) ratios are lower than in modern N-MORB (0.53 and 1.0 respectively; Sun and McDonough, 1989), indicating a moderately depleted mantle source. In contrast, REE patterns are mildly LREE enriched ([La/Nd]_{PM} (1.4-1.6) and [La/Yb]_{PM} (1.0-1.3)).

REE concentrations and [Gd/Yb]_{PM} ratios in the Bassetts Volcanic Member are higher than in most Cenozoic boninites and Archean boninite-like rocks, including those from the upper Singleton Formation (this study). If these signatures are indicative of their primary melts, then they suggest a less refractory mantle source than for ‘typical’ boninite. As is the case throughout the Meekatharra Formation, REE and HFSE ratios show little variation as MgO decreases (17.2-9.0 wt%), confirming that olivine and orthopyroxene dominated the crystalizing mineral assemblages.

Sm-Nd isotopic data for two samples yield identical $\epsilon_{\text{Nd}2800}$ of -0.5 (Table 3.2).

3.4.2.3.3. *Stockyard Basalt Member*

The Stockyard Basalt Member is chemically distinct from other volcanic units in the Meekatharra Formation. Sample compositions vary between low- to moderate-Mg basalt and basaltic andesite (90% of samples contain 49.6-56.2 wt% SiO₂ and 4.1-8.0 wt% MgO). Based primarily on incompatible element concentrations, the unit can be separated into two sub-populations. The first population (population 1; Murrouli Range, Fig 3.2) is slightly more magnesian than the second (population 2; Polelle Syncline and Murrouli Range, Fig 3.2), and contains significantly lower TiO₂ (0.7-1.0 wt% vs 1.3-1.7 wt%), HFSE (especially Nb and Zr) and REE concentrations than population 2. Despite large concentration differences for incompatible elements between the two populations, mantle normalised trace element patterns are broadly similar (Fig 3.15f); most are Th- and Nb-depleted ($[\text{Th}/\text{Yb}]_{\text{PM}}$ 0.6-1.0, $[\text{Nb}/\text{Yb}]_{\text{PM}}$ 0.5-1.1) and LREE depleted relative to MREE-HREEs, which are relatively unfractionated. Exceptions to that more common trace element pattern, include several samples from population 1 with convex-down (hump-shaped) patterns ($[\text{La}/\text{Sm}]_{\text{PM}}$ 0.51-1.11 and $[\text{Gd}/\text{Yb}]_{\text{PM}}$ 0.96-1.47), possibly indicating retention of garnet in their mantle source, and five samples from population 2 that are Th-enriched with strong negative Nb anomalies ($[\text{Th}/\text{Nb}]_{\text{PM}}$ 1.4-2.0), undepleted LREEs, weakly depleted HREEs ($[\text{La}/\text{Sm}]_{\text{PM}}$ 0.93-1.12 and $[\text{Gd}/\text{Yb}]_{\text{PM}}$ 1.06-1.30), and small positive Zr-Hf anomalies (Zr/Zr^* 1-1.2).

Two samples yielded slightly positive $\epsilon_{\text{Nd}2800}$ +0.8 and +1.2 (Table 3.2).

3.4.2.3.4. *Bundle Volcanic Member*

Fine-grained samples from the Bundle Volcanic Member contain high, but variable SiO₂ (50.9-62.3 wt%), MgO (5.7-16.6 wt%) and Mg-numbers (55-74). Ni (96-566 ppm) and Cr (267-1470 ppm) concentrations vary significantly but correlate with MgO. TiO₂ is moderately high (0.6-1.1 wt%), and Al₂O₃ (9.0-13.6 wt%) is lower than other high-Mg mafic volcanic rocks in the Meekatharra Formation (at equivalent MgO concentrations), resulting in lower Al₂O₃/TiO₂ (11-18). Their compositions broadly overlap with the Lordy Basalt Member, but can be distinguished by their slightly lower Al₂O₃ and CaO, and higher SiO₂ concentrations.

Bundle Volcanic Member samples have very uniform mantle normalised trace element patterns that are typically more LREE-enriched ($[La/Yb]_{PM} \sim 3.1$ vs ~ 1.6 and $[La/Sm]_{PM} 1.5-2.5$ vs $1.3-2.0$), and have higher $[Gd/Yb]_{PM}$ ($1.4-1.5$ vs $1.0-1.2$) than the Lordy Basalt Member, and they also lack the Zr-Hf anomalies observed in the other high-Mg mafic volcanic rocks of the Meekatharra Formation ($Zr/Zr^* = 1 \pm 0.1$) (Figs 3.14f, 3.15g). They have strong negative Nb anomalies ($[Th/Nb]_{PM} 4.4-4.9$ and $[Nb/La]_N 0.4-0.5$), indicating an enriched mantle source or interaction with continental crust, and $[Nb/Yb]_{PM}$ ratios greater than primitive mantle values ($1.2-1.6$), again indicating an enriched mantle source, or possibly retention of garnet in the mantle source.

A single sample from this unit yielded $\epsilon_{Nd2800} +0.2$ (Table 3.2).

3.4.2.4. Greensleeves Formation

The Greensleeves Formation (Figs 3.1, 3.2) consists of an inferred differentiation series of basaltic andesite-andesite-dacite-rhyolite (BADR). The analysed samples map this trend, from 55.2 to 73.4 wt% SiO_2 and 7.3 to 0.01 wt% MgO ($> 1.3\%$ in samples with < 70 wt% SiO_2). Mg-numbers vary from 66 to 45 (but mostly > 50) in basaltic andesite to dacite compositions. Compared to other Archean felsic rocks, including TTGs, Greensleeves basaltic andesite-dacitic compositions are relatively high in Ni (49-272 ppm for andesite, 25-106 ppm for dacite) and Cr (78-713 ppm for andesite and 34-204 ppm for dacite). Trace element patterns are strongly LREE-enriched ($[La/Yb]_{PM} > 13 \pm 5$). Compared to ‘typical’ Archean TTGs (e.g., Martin, 2005), Greensleeves Formation samples are more magnesian, contain higher Ni and Cr, and have less fractionated trace element patterns - in these compositional characteristics they are transitional between high-Si adakites (HSA; Martin, 2005), and Cenozoic HMA (Tatsumi, 2005).

3.5. DISCUSSION

3.5.1. Comparison of Archean boninite-like rocks with Cenozoic boninites

‘Boninites’ are defined by the IUGS as volcanic rocks with $SiO_2 > 52$ wt%, $MgO > 8$ wt% and $TiO_2 < 0.5$ wt% (Le Bas, 2000). A more recent classification scheme (Pearce and Reagan, 2019) has suggested including rocks with lower SiO_2 concentrations in the boninite classification if their

fractionation trends project backwards to $\text{SiO}_2 \geq 52 \text{ wt\%}$ and $\text{TiO}_2 \leq 0.5 \text{ wt\%}$ at 8 wt\% MgO (Si_8 , Ti_8) which includes boninitic rocks with a significant olivine phenocryst component. Rocks meeting that definition can vary significantly in terms of their incompatible trace element characteristics, which is thought to reflect variable degrees of source depletion and conditions of melting (Crawford, 1989). For example, boninites from the Ogasawara Islands contain high MgO (8-15 wt%) and SiO_2 (57-60 wt%) and very low TiO_2 (0.1-0.2 wt%) and HREE concentrations, indicating a near-clinopyroxene-free source with melting involving mostly orthopyroxene. Boninites from the Troodos Ophiolite in Cyprus, on the other hand, have lower MgO ($\leq 10 \text{ wt\%}$) and SiO_2 (53-56 wt%), but higher TiO_2 (0.2-0.4 wt%) and HREE concentrations, indicating a depleted lherzolite source and melting that included clinopyroxene. These two type examples are sometimes described as high-Si and low-Si boninites, respectively (Kanayama, 2012; Umino, 2017; Pearce and Reagan 2019).

Many Archean ‘boninite-like’ rocks display high-Mg ($\geq 8 \text{ wt\%}$), low-Ti ($\leq 0.5 \text{ wt\%}$) and strongly depleted incompatible trace element characteristics similar to Cenozoic boninites, but contain lower SiO_2 ($< 52 \text{ wt\%}$) (Kerrick, 1998; Wyman, 1999; Polat, 2002, Manikyamba, 2005). By analogy with post-Archean counterparts (Brown and Jenner, 1989, Pearce and Reagan, 2019), such rocks are sometimes described as ‘low-Ti tholeiites’ (LOTI; Kerrich, 1998; Wyman, 1999) but were termed ‘Whitney-type’ boninites by Smithies (2004).

Some Archean suites do in fact meet the chemical definition of boninite *s.s.* (Fig 3.14 a, b, e), including examples from the *c.* 2790 Ma Opatika Sub-Province (Superior Province, Canada; Boily and Dion, 2002), *c.* 2700 Ma Gadwal greenstone belt (Dharwar Craton, India; Manikyamba, 2005), and *c.* 3120 Ma Whundo Group of the West Pilbara Terrane (Pilbara Craton, Western Australia; Smithies, 2005). These examples have MgO vs TiO_2 and HREE characteristics of low-Si boninites (as defined by Pearce and Reagan, 2019: Fig 3.14 a, b, e). However, these rocks generally differ from Archean LOTI basalts in having, on average, slightly higher SiO_2 (*c.* 52-54 wt% at 8 wt% MgO; at the lower end of the Cenozoic boninite range) and concave REE patterns, indicating a second, LREE-enriched source component. As is the case for some Archean LOTI basalts (e.g., Wyman, 1999), these examples occur within stratigraphic sequences containing other subduction-associated lithologies such

as calc-alkaline intermediate to felsic volcanics (including adakites) and intrusions (such as sanukitoids) that have been taken as evidence for subduction or subduction-like processes (Boily and Dion, 2002; Smithies, 2005). A comparison between the chemical attributes of Cenozoic boninites, and those of Archean LOTI and boninite-like rocks, is presented in Table 3.4.

Similarities between boninites and the Archean Al-enriched Comondale suite have long been noted (Wilson, 2003a, b). Under the new Pearce and Reagan (2019) classification scheme, the suite is now classed as “komatiitic boninite”, based on their combination of boninite compositions and spinifex textures, although those textures are defined by orthopyroxene spinifex rather than olivine spinifex (Barr, 2009). Various studies of the Al-enriched Comondale ultramafic suite have preferred either mantle plume (e.g., Robin-Popieul, 2012) or supra-subduction zone settings for melting (e.g., Wilson, 2003a; Hoffmann and Wilson, 2017), but there is general agreement that the sources of the Al-enriched magmas must have yielded earlier Al-depleted, high $[Gd/Yb]_N$ komatiitic melts at high pressure, where majorite garnet is stable, before yielding Al-enriched, low $[Gd/Yb]_N$ melts at lower pressures – i.e., melting a source with a strong majorite garnet signature. In contrast, Phanerozoic boninites and LOTI are commonly envisioned to be the associated with intense mantle depletion at shallow depths in a proto-arc wedge or a back arc environment (i.e., less than *c.* 2 Gpa or *c.* 60 km: Stern and Bloomer, 1992; Hickey-Vargas, 2018; Wolkie, 2018). In at least some cases, however, the initial mantle depletion associated with Archean LOTI may have been produced or enhanced by high temperatures associated with a mantle plume (Wyman, 2003; Smithies, 2004), similar to a scenario invoked for Tongan boninites by Danyushevsky (1995).

Table 3.4. Comparison between Modern boninites and Archean LOTI and boninite-like suites.

Geologic period and chemical suite	Cenozoic high-Si boninite	Cenozoic low-Si boninite	Archean LOTI suite	Archean LOTI suite	komatiitic boninite	Archean Boninite-like suite	Archean Boninite-like suite	Archean Boninite-like suite	Archean Boninite-like suite	Archean Boninite-like suite	Archean Boninite-like suite
Locality	Ogasawara Islands	Cyprus - Troodos upper pillow lavas	Isua	Abitibi	Comondale	Whundo	Opatica	Dharwar	upper Singleton Formation (Norie Group): Sub-volcanic/cumulate	upper Singleton Formation (Norie Group): volcanic/fine grained	Bassetts Volcanic Member (Polelle Group): fine grained
MgO wt%	9-19	6-13	7-16	9-13	30-42	8-10	6-13	12-24	13-19	8-12	8-17
SiO ₂ wt%	55-61	53-56	47-54	48-53	45-51	50-53	49-58	45-52	50-53	48-53	52-57
TiO ₂ wt%	<0.1-0.2	0.2-0.4	0.2-0.4	0.3-0.5	≤ 0.1	0.3	0.4-0.5	0.2-0.4	0.1-0.4	0.5-0.7	0.4-0.6
Si ₈ wt%	57-61	53-56	49-54	48-54	54-57	51-53	53-58	49-54	53-55	50-54	52-58
Ti ₈ wt%	0.1-0.2	0.2-0.4	0.2-0.4	0.3-0.5	0.2-0.3	0.3	0.4-0.5	0.3-0.5	0.1-0.5	0.6-0.7	0.4-0.6
Mg-number	65-79	57-72	58-75	63-72	86-92	63-68	62-72	67-80	71-78	57-68	63-77
Al ₂ O ₃ /TiO ₂	63-137	36-62	44-93	38-65	64-84	55-58	33-38	30-50	25-140	20-25	24-27
[Th/Nb] _{PM}	1.9-7.1	0.7-2.2	0.9-4.9	1.1-1.5	0.2-0.8 (Th typically not reported)	2.1-5.6	3.1-5.3	2.4-7.3	1.5-4.7	1.7-5.1	4.8-5.7
[La/Sm] _{PM}	0.9-2.1	0.6-1.5	0.6-1.4	1.0-1.5	0.1-1.5 (two outliers >5)	1.4-2.4	1.6-2.1	1.5-2.6	1.1-2.5	1.1-2.2	1.4-1.6
[Gd/Yb] _{PM}	0.6-0.9	0.4-0.9	0.3-0.6	0.4-0.6	0.2-0.4	0.7-0.8	0.7-0.9	0.6-0.7	0.4-1.0	0.7-1.1	0.9-1
REE pattern shape	Concave. Minima varies between Sm to Tb	Concave. Minima at Pr.	Flat LREEs, strongly LREE-MREE depleted	Flat LREEs, strongly LREE-MREE depleted	Flat LREEs, strongly LREE-MREE depleted	Concave. Minima at Tb	Weakly concave. Minima at Sm	Weakly concave. Minima at Sm	LREE depleted to concave	LREE depleted to LREE enriched	Weakly concave. Minima at Sm
Zr/Zr*	1-3.8	0.8-1.2	1.1-2.4	1.0-1.4	0.8-5.4	0.6-0.9	0.9-2.1	0.7-1.1	0.9-1.1	0.9-1.4	1.3-1.4
Reference	Kanayama <i>et al.</i> , 2012	Osozawa <i>et al.</i> , 2012; Konig <i>et al.</i> , 2008; Golowin <i>et al.</i> , 2017	Polat <i>et al.</i> , 2002	Wyman <i>et al.</i> , 1999	Wilson 2003b; Barr <i>et al.</i> , 2009	Smithies <i>et al.</i> , 2004	Boily and Dion, 2002	Manikyamba <i>et al.</i> , 2005	This study	This study	This study

Another class of hypotheses applied to some Archean boninite-like rocks is that they are the contamination products of other mantle magma types. The suggestion that siliceous high-Mg basalts may be contaminated examples of Archean boninitic magmas (Sun, 1989) is rarely cited in the recent literature, but numerous studies have proposed a contaminated komatiite model for komatiitic basalts or siliceous high-Mg basalts (e.g., Arndt and Jenner, 1986; Arndt, 2001; Shimizu, 2005; Barnes, 2012), which, like boninites, have high Si and Mg, and low Ti, as well as strongly enriched LREEs. Shimizu (2005) reported several siliceous high-Mg basalts (e.g., BX235, BX229) from the Belingwe greenstone belt that have strikingly similar characteristics to boninite-like rocks in the Meekatharra Formation, including concave REE patterns (Fig 3.15e), high SiO_2 (c. 54 wt% at 9 wt% MgO) and high $\text{Al}_2\text{O}_3/\text{TiO}_2$ ratios (c. 25). The time interval between the siliceous high-Mg basalt-hosting Zeederbergs Formation and the underlying komatiite- and komatiitic basalt-hosting Reliance Formation is poorly constrained, falling between a few million years and up to c. 70 My (Prendergast and Wingate, 2013). Shimizu suggested that komatiitic magmas ponded in the crust, where they were contaminated and underwent fractional crystallization to generate the boninite-like characteristics of these lavas. However, it is difficult to conceive of an assimilant mixture that would result in both relative depletion of the MREEs and enrichment of the LREEs, while also generating positive Zr/MREE anomalies that are not observed in the associated Al-undepleted komatiites. Moreover, Reliance Formation komatiites that host xenolithic garnets and clinopyroxenes, or their depleted basalt fractionation products, do not display boninite-like REE patterns or the high Th/LREE found in the siliceous high-Mg basalts (Shimizu, 2004; 2005).

3.5.2. Classification and source characteristics of northwestern Youanmi Terrane mafic-ultramafic volcanic rocks

The following discussion focusses on high-Mg mafic volcanic units within the Norie and Polelle Groups that potentially preserve chemical attributes (e.g., trace element ratios) of their mantle sources. Table 3.3 summarizes the chemical attributes and petrogenetic interpretations of each chemostratigraphic unit defined based on the results above.

3.5.2.1. Singleton Formation Al-depleted high-Mg basalts and olivine cumulates

The stratigraphically lowest unit in the study area is the lower Singleton Formation, which is dominated by high-Mg basalts, picrites and olivine orthocumulates. These have been described in other studies as (Al-depleted) komatiites (Reudavey, 1990; Watkins and Hickman, 1990; Barley, 2000; Hallberg, 2000; Van Kranendonk, 2013), but all samples with > 16 wt% MgO contain cumulus olivine (picrites and olivine orthocumulates; 21-36 wt% MgO; Fig 3.4c-f). Using the methods of Robin-Popieul (2012), we estimate the more primitive liquids contained 16-20 wt% MgO (Electronic Appendix 3.4a), which is marginal between komatiite (> 18 wt% MgO; Le Bas, 2000) and picrite (12-18 wt% MgO; Le Bas, 2000), but notably lower than most well-known Al-depleted komatiites (e.g., 26 wt% MgO for the Komati Formation, South Africa; Robin-Popieul, 2012).

Higher concentrations of Al₂O₃ and TiO₂ (at similar MgO) compared to most Al-depleted komatiites and basalts (e.g., Komati Formation) indicate that clinopyroxene was the main mineral phase consumed during melting, while less magnesian compositions (< 16 wt% MgO and Mg-numbers 62-71 in fine-grained rocks versus 22-33 wt% MgO and Mg-numbers 66-87 in spinifex textured rocks of the Komati Formation) indicate a smaller melt fraction than typically inferred for komatiite. Simple trace element modelling using Petromodeler (Ersoy, 2013) indicates their REE patterns, with relatively unfractionated LREE-MREEs and high [Gd/Yb]_{PM} ratios (avg 1.55 vs 1.4 in Komati Formation), requires melting at high pressures where garnet is stable (≥ 3 GPa, assuming an un-metasomatised source). The main characteristics of these trace element patterns can be recreated via a range of melt-crystallization models and two scenarios are considered here (see Electronic Appendix 3.4b). The first model is via 10% batch melting of depleted garnet lherzolite at 3 GPa using a depleted MORB mantle (DMM) source composition, mineral/melt partition coefficients and melt modes of Salters and Stracke (2004), and 15% fractional crystallization. The second model is via 25% batch or dynamic melting of a more fertile mantle (35% depleted mantle and 65% primitive mantle) at 9 GPa using mineral/melt partition coefficients and melt modes of Robin-Popieul (2012; derived in part from Borg and Draper, 2003) and 10% fractional crystallization. Both models require minor interaction with a crustal component to slightly enrich Th, La and Ce – either via crustal assimilation (r-factor = 0.1; assimilating

a Narryer Terrane 3300–3700 Ma granite composition) or mixing with metasomatised lithosphere (not modelled). Both scenarios are consistent with asthenospheric upwelling in a rift setting.

3.5.2.2. Singleton Formation boninite-like rocks

The oldest suite of rocks with boninite-like characteristics occurs in the *c.* 2815 Ma upper Singleton Formation. These rocks were largely ignored in earlier studies, but they represent a petrogenetically important chemical end-member unit, occurring close to the onset of the major 2820–2730 Ma magmatic episode that dominates the northwestern Youanmi Terrane.

Approximately 20% of high-Mg samples (> 8 wt% MgO) from the upper Singleton Formation meet the major element classification criteria for boninite under the IUGS scheme (Le Bas, 2000), and approximately 40% (all samples with > 14 wt% MgO) meet those of the more recent scheme by Pearce and Reagan (2019) (Fig 3.14a,b), which accounts for compositions modified by olivine and orthopyroxene fractionation. However, on the plot of MgO vs TiO₂ (Fig 3.14b), most samples define a fractionation trend with a strong clinopyroxene influence (towards lower MgO/TiO₂ than expected for olivine or orthopyroxene control), and approximately half of those samples that plot in the boninite field contain cumulus clinopyroxene phenocrysts. Since the compositions of pyroxene orthocumulate samples are subject to cumulate effects, the most primitive liquid composition was almost certainly less magnesian, transitional between finer grained sub-volcanic rocks and primitive volcanic rocks (12–14 wt% MgO, 0.3–0.55 wt% TiO₂, 51–52.5 wt% SiO₂) and marginal between basalt and boninite.

Most samples have incompatible element patterns with MREEs depleted relative to HREEs ([Gd/Yb]_{PM} 0.66–1.07) and low [Nb/Yb]_{PM} (0.52–0.85) and TiO₂, requiring a moderately depleted mantle source, such as the one that generated the underlying basalts and picrites. Simple trace element melt-modelling was able to approximate the MREE-HREE patterns with a 20–25% batch melt of a source similarly depleted to modern N-MORB source (Workman and Hart, 2005) (Electronic Appendix 3.4b).

The variable LILE-LREE enrichment observed in trace element patterns of the upper Singleton Formation clearly reflects varying contributions of a crustal component (e.g., via assimilation, mantle metasomatism, magma mixing) which is discussed in following sections. Dividing the upper

Singleton Formation into two populations at a $[\text{La/Gd}]_{\text{PM}}$ ratio of 1.25 distinguishes unenriched-mildly enriched patterns (30% of samples) from moderate-strongly enriched patterns (70% of samples). The more LREE-enriched samples ($[\text{La/Gd}]_{\text{PM}} > 1.25$) generally have slightly lower TiO_2 , CaO , V and Sc , and slightly higher SiO_2 , Ni and Cr , which possibly reflects a greater partial melt (greater Opx contribution, relative to Cpx). Together with higher concentrations of Ba and Th , this may indicate variable metasomatism in the source. Bizimis (2000) studied the trace element contents of clinopyroxenes from supra-subduction zone peridotites and found that the melting rate of clinopyroxenes during hydrous mantle melting is less than in dry melting, but that the rate of orthopyroxene depletion is greater.

3.5.2.3. Meekatharra Formation boninite-like rocks

The second suite of boninite-like rocks in the study area, the *c.* 2800 Ma Bassetts Volcanic Member of the Meekatharra Formation, occurs throughout the northern Youanmi Terrane and is well-exposed in the Polelle Syncline (Fig 3.2). The Bassetts Volcanic Member can be readily distinguished from other mafic volcanic rocks in the study area by their low- TiO_2 (< 0.5 wt%), above-chondritic $\text{Al}_2\text{O}_3/\text{TiO}_2$ ratios (*c.* 25), concave REE patterns, and negative Nb-Ta and positive Zr-Hf anomalies. Most samples meet the IUGS definition of boninite (Le Bas, 2000), but samples containing < 10 wt% MgO typically exceed the upper TiO_2 limit (0.5 wt%), and locally may drop below the lower SiO_2 limit (52 wt%). In the newer Pearce and Reagan (2019) scheme, most Bassetts Volcanic Member lavas plot above the upper TiO_2 vs MgO boundary of the boninite field, within the picrite/komatiitic basalt/siliceous high-Mg basalt field (Fig 3.14a,b).

Boninite-like rocks from the Bassetts Volcanic Member have asymmetrically concave REE patterns, similar to many Phanerozoic low-Si boninite suites, but at generally higher MREE-HREE contents (Fig 3.15e). On average, they also contain higher TiO_2 and are less MREE-depleted than Phanerozoic low-Si boninites, indicating a less depleted mantle source. Simple melt-modelling indicates a mantle source that was 10% depleted relative to N-MORB-source mantle and required higher degrees of partial melting (20-25% batch melt) than the earlier boninite-like rocks to match MREE-HREE concentrations in more primitive samples (Electronic Appendix 3.4b). Trace element

patterns of Bassetts Volcanic Member samples feature ubiquitous Zr-Hf anomalies, which are not observed in the earlier boninite-like rocks. In the case of these very well-preserved samples, the features are considered to be of igneous origin. In all of the contamination scenarios that we modelled, the Zr-Hf anomalies could not be reproduced (Electronic Appendix 3.4b). In Cenozoic boninites, positive Zr-Hf anomalies (high Zr/Zr^* and high Hf/Hf^* [$Hf^* = Nd_{PM}^{0.25} \times Sm_{PM}^{0.75}$]) have typically been attributed to enrichment of sub-arc mantle by fluids (Bizimis, 2000) or melts (e.g., König, 2010; Kanayama, 2012) released from hydrated oceanic crust during subduction. Bizimis (2000) found that enrichments in LREE-MREE and HFSE (Zr) were linked to continuous hydrous flux of the mantle in models for subduction settings that initiated refertilization after 9% and 10% melting of a MORB source. One important piece of evidence regarding the nature of the mantle at 2800 Ma, when the Bassetts Volcanic Member erupted, is the presence of the hornblende-rich Narndee Igneous Complex ($\epsilon_{Nd2800} = -0.7$ to $+2.0$) in the central part of the Youanmi Terrane. Ivanič (2015) showed, isotopically, that the parental magmas of the Narndee Igneous Complex had hydrous mantle sources.

3.5.2.4. Meekatharra Formation depleted tholeiites

A second suite of Meekatharra Formation basalts, near the town of Cue (Fig 3.2), have lower SiO_2 (49.7-51.8 wt%), are less magnesian (mostly 5-7 wt% MgO, Mg-number 40-50) and contain higher TiO_2 (mostly 0.4-0.8 wt%) than boninite, yet they are relevant to this discussion because of their low $[Gd/Yb]_{PM}$ (mostly 0.7-0.85), which suggests a moderately refractory mantle source, similar to the source inferred for boninite-like rocks in the Bassetts Volcanic Member. Simple melt-modelling indicates their source was also 10% depleted relative to N-MORB-source mantle, but with lower degrees of partial melting (5% batch melt, assuming an anhydrous un-metasomatised source) than for boninite-like rocks in the study area (Electronic Appendix 3.4b). Their lower MgO, Mg-number and higher TiO_2 , compared to coeval boninite-like rocks in the Bassetts Volcanic Member, can therefore be explained by lower degrees of melting and possibly higher degrees of fractional crystallization. Trace element patterns for the Cue basalts have low $[La/Yb]_{PM}$ (mostly < 0.6) and small Nb-depletions (Fig 3.15f), which precludes significant source enrichment or crustal contamination and

therefore constitutes our best constraint on the trace element ratios of the mantle source prior to LILE-LREE enrichment.

3.5.3. Mode of mantle-crust interaction

The following sections discuss two competing hypotheses for LILE-LREE enrichment in boninite-like rocks: melting of a mantle source metasomatised by subduction or sagduction and crustal contamination of initially unenriched mafic-ultramafic primary melts.

3.5.3.1. *Th/Yb-Nb/Yb systematics*

In modern oceanic settings, negative Nb anomalies on mantle normalised trace element patterns (i.e., high Th/Nb or low Nb/La) are widely attributed to the relative immobility of Nb (compared to other incompatible lithophile elements) in hydrous fluids to the extent that high Th/Nb is commonly used as a proxy for subduction enrichment (Pearce and Stern 2006; Pearce 2008).

Many Archean greenstones have high Th/Nb, leading to suggestions that modern-style plate tectonic processes were operating during the Archean (see discussion in Smithies, 2018). However, high Th/Nb can also be produced (or enhanced) in mantle-derived melts by assimilation of high Th/Nb continental crust, or by mixing with high Th/Nb crustal melts.

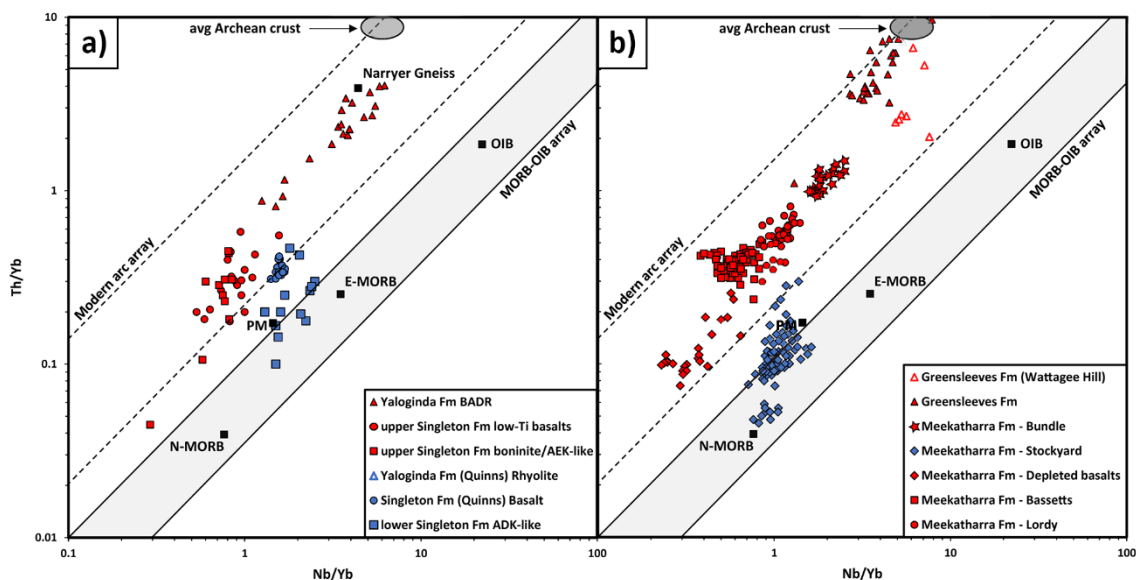


Figure 3.16. Th/Yb vs Nb/Yb after (Pearce 2008). (a) Norie Group; (b) Polelle Group. Samples containing > 68 wt% SiO₂ have been excluded.

One method of evaluating Th/Nb systematics uses Pearce's (2008) plot of Th/Yb vs Nb/Yb. Discrete trends in this plot may be able to differentiate between two main modes of mantle-crust interaction: hydrous subduction-linked mantle metasomatism versus crustal assimilation. The clearly dominant Th/Yb-Nb/Yb trend in our study area is oriented parallel to the mantle array and almost entirely within the modern arc array (red symbols in Fig 3.16a, b). This trend originates at Th/Yb equal to, and Nb/Yb lower than, modern N-MORB and increases at relatively constant Th/Nb ratios towards typical Archean continental crust values. In detail, the trend comprises several discrete groups of samples relating to geographically or temporally discrete segments of the greenstone package, and therefore likely reflects variable source fertility, melting regimes and crust-mantle interaction. Nearly all high-Mg compositions fall on this trend (except those belonging to lower Singleton Formation) and very few compositions plot between this trend and the modern mantle array, suggesting that the high Th/Nb ratios of these rocks were inherited from the mantle source, or at least prior to ascending through the crust. The crustal contributions to parent magmas of samples that define this trend are discussed in the following sections (see 'Sm-Nd isotopic variation').

Three volcanic units plot as discrete clusters along a smaller sub-vertical trend, separated from the main Th/Yb-Nb/Yb trend: (1) In the Polelle Group, Stockyard Basalt Member compositions plot as two clusters between 'N-MORB' and 'primitive mantle' values (Fig 3.16b); (2) In the Norie Group, lower Singleton Formation compositions straddle the upper limit of the modern MORB-OIB array (Fig 3.16a); and (3) Quinns Basalt Member (high-HFSE basaltic andesite) compositions straddle the lower limit of the modern arc arrays (Fig 3.16a). Considering Th/Yb-Nb/Yb in isolation, these clusters could be interpreted as a contamination vector (e.g., Pearce, 2008). However, most of the samples that define the trend have trace element compositions indicating low-degrees of crustal interaction: the lower Singleton Formation and Stockyard Basalt Member have mantle-like $[Th/Nb]_{PM}$ (mostly < 1 and < 1.2 respectively) and unfractionated or depleted LREE patterns ($[La/Nd]_{PM}$ 0.9-1.1 and 0.7-1.0 respectively). Internal Th/Yb-Nb/Yb variation within each volcanic unit may reflect near-surface contamination (e.g., two outliers at higher Th/Yb for the lower Singleton Formation and five outliers at higher Th/Yb for the Stockyard Basalt Member), but the volcanic units themselves cannot be

petrogenetically related to one another by crustal contamination. For example, compositions from the Quinns Basalt Member have relatively high $[\text{Th}/\text{Nb}]_{\text{PM}}$ (1.7-2.2) and are mildly LREE-enriched ($[\text{La}/\text{Nd}]_{\text{PM}}$ 1.2-1.3), but their near chondritic MREE-HREE ratios ($[\text{Gd}/\text{Yb}]_{\text{PM}}$ 1.0-1.2) are inconsistent with a crustal contamination origin from parental melts to either the lower Singleton Formation ($[\text{Gd}/\text{Yb}]_{\text{PM}}$ 1.5-1.9) or Stockyard Basalt Member ($[\text{Gd}/\text{Yb}]_{\text{PM}}$ 1.0-1.4). Instead, they resemble Fe-Ti-P rich basalt-andesite series rocks or “Icelandites” (e.g., the basaltic icelandites of NE Iceland: Jónasson, 2005; and Archean examples from the Kidd Creek Volcanic Complex, Abitibi belt, Canada: Wyman, 1999).

3.5.3.2. Sm-Nd isotopic variation

The total Nd isotopic range for the samples reported here is surprisingly small (ϵ_{NdT} from +1.2 to -0.5; excluding sample 221754 with ϵ_{NdT} +2, because LREE loss likely affected $^{147}\text{Sm}/^{144}\text{Nd}$; Table 3.2), and all data points plot along a c 2820 Ma isochron (not shown). Interpretation of these results must take into account the analytical uncertainty (c. ± 0.5 units for ϵ_{NdT}). However, the observed isotopic range for the volcanic rocks is very similar to that previously reported for the broadly coeval mafic-ultramafic complexes in the region, such as the c. 2813 Ma Windimurra Igneous Complex (+1.8 to -1.0) and the c. 2800 Ma Narndee Igneous Complex (+2.0 to -0.7; Ivanic, 2015).

Moreover, subtle isotopic differences between the Norie Group (ϵ_{NdT} +1.5 to -0.1; including data from Geological Survey of Western Australia, 2018b) and Polelle Group (ϵ_{NdT} +1.2 to -2.2; including data from Geological Survey of Western Australia 2018b) correlate with differences in Th/Yb-Th/Nb systematics (Fig 3.16), suggesting greater crustal influence in the Polelle Group. The consistency of the results, their similarity with the data for coeval intrusive mafic complexes, and correlations with chemical features, suggest that primary Sm-Nd isotope systems remained largely undisturbed and calculated ϵ_{NdT} values represent primary magmatic signatures.

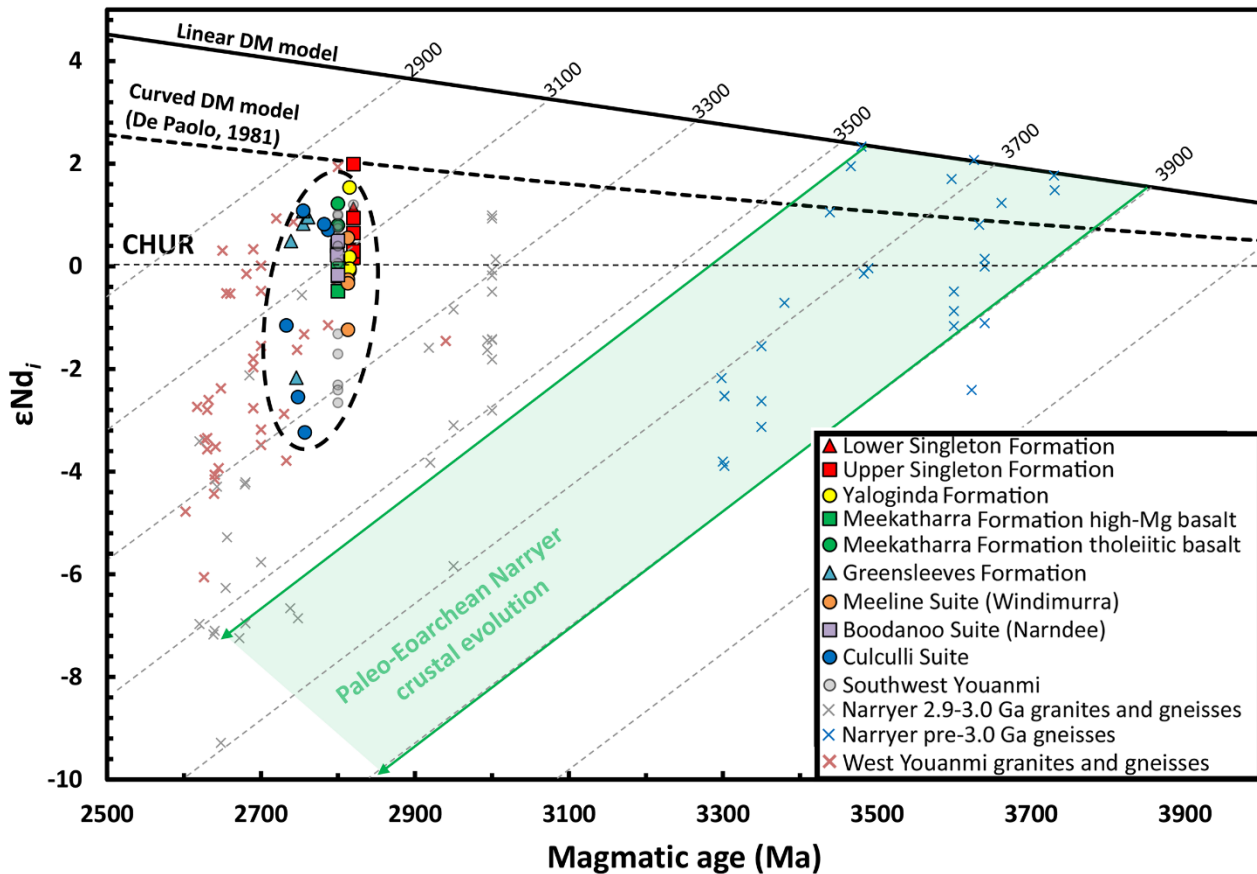


Figure 3.17. Whole-rock Sm-Nd isotope systematics; $\epsilon_{\text{Nd}t}$ vs magmatic age. Diagonal grey dashed lines indicate crustal isotope evolution pathways assuming $^{147}\text{Sm}/^{144}\text{Nd} = 0.115$. Additional data sources: Southwest Youanmi Terrane data Windimurra and Narndee (Ivanic, 2015); Yaloginda Formation, Greensleeves Formation and Culculli Suite (WACHEM database; GSWA, 2018b); southwest Youanmi Terrane (unpublished data); northwestern Youanmi Terrane granites and gneisses (Champion, 2013 and references within) Narryer Terrane granites and gneisses (De Laeter, 1985, Nutman, 1993).

Nd isotopic compositions of the Neoarchean mantle are difficult to ascertain due to alteration effects and crustal assimilation (e.g., Lahaye, 1995; Arndt, 2001; Frei, 2002; Said and Kerrich, 2010). Global models for the evolution of depleted mantle (e.g., DePaolo, 1981; Goldstein, 1984) are a guide and suggest $\epsilon_{\text{Nd}2800}$ values between +3.8 and +2.1 (Fig 3.17). Nd isotope compositions in this range exist in some juvenile Neoarchean granite-greenstone terranes (e.g., Abitibi-Wawa, Canada: Lahaye, 1995; Polat and Kerrich, 2002; and eastern Dharwar, India: Dey, 2013) but lower ϵ_{Nd} values in Neoarchean mantle-derived magmatic rocks are common (e.g., summary in Mole, 2018). The data suggest that the magmas, which formed the rocks studied here, interacted with older crustal components (crust or crustal melts, mantle lithosphere, or slab melts \pm sediment component) that had much lower $\epsilon_{\text{Nd}t}$.

Published Sm-Nd isotope data for the northwestern Yilgarn region indicate that $\epsilon_{\text{Nd}2800}$ ranged from +4 (*c.* 2800 Ma olivine cumulates, Wyman and Kerrich, 2012) to -11.5 (3600 Ma Meeberrie Gneiss, Narryer Terrane, Nutman, 1993) (Fig 3.17). Norie Group volcanic rocks show little variation in their Sm-Nd isotopic compositions, and nearly all samples have juvenile ϵ_{NdT} (+1.5 to -0.1), consistent with similar aged, juvenile gabbros of the Windimurra Igneous Complex in the central Youanmi Terrane (Nebel, 2013), indicating little interaction with ancient continental crust from *c.* 2820-2800 Ma. In contrast, Polelle Group volcanic rocks and coeval intrusions (*c.* 2799-2735 Ma) show greater isotopic variation (ϵ_{NdT} +1.2 to -3.2). Nearly half have mildly to moderately evolved ϵ_{NdT} , including three high-Mg mafic volcanic rocks (ϵ_{NdT} -0.2 to -0.5) and four rhyolitic and granitic rocks (ϵ_{NdT} -2.2 to -3.2), indicating mixing or contamination with an ancient continental crust component (Figs 3.17-3.18). Lu-Hf isotopic compositions from the northwestern Youanmi Terrane (zircon Lu-Hf; Ivanic, 2012) show similar overall trends: isotopic ratios between 2810-2760 Ma are mostly juvenile (ϵ_{HfT} +3.6 to -0.5; 95% > ϵ_{HfT} 0) and become more variable and evolved from 2760 to 2735 Ma (ϵ_{HfT} +2.4 to -10; 33% > ϵ_{HfT} 0).

Crustal basement of the type represented by the > 2900–3700 Ma Narryer Terrane, if it extended to the study area at the time (e.g., Wyche, 2012), must be considered in interpretations of Nd isotope results for the Norie and Polelle Group volcanic rocks. For example, of the four rhyolitic and granitic samples with moderately evolved ϵ_{NdT} (-2.2 to -3.2), three contain inherited zircon xenocrysts with $^{207}\text{Pb}/^{206}\text{Pb}$ ages of 2950, 2960 and 3420 Ma (outlined in Fig 3.18). The 2950-2960 xenocryst ages are equivalent to the older parts of the supracrustal sequence, exposed along the southwest and western margins of the Youanmi Terrane. The 3420 Ma xenocryst age in sample 185939 (a single zircon grain; GSWA, 2018a), which is located 65 km to the west of our study area (Fig 3.2), is consistent with the age of some granitic gneisses in the Narryer Terrane (*c.* 40km west from that sample locality).

Assuming a simple 2-component mixing system at 2800 Ma, the boninite-like rocks with the lowest ϵ_{Nd} (Bassetts Volcanic Member; $\epsilon_{\text{Nd}2800}$ to -0.5) would be modelled as a mix of 72-81% mantle component ($\epsilon_{\text{Nd}2800}$ +3.9 to +2.1) and 19-28% of a model crustal component ($\epsilon_{\text{Nd}2800}$ -11.5; Meeberrie

Gneiss); the model proportions also depend on the Nd concentrations assigned to the endmembers, but likely approximate the maximum possible crustal contribution for the intra-crustal contamination scenario.

One set of samples, dominated by high-Mg basaltic andesite to rhyolite series rocks of the Yaloginda and Greensleeves Formations, shows increasing $[La/Nd]_{PM}$ and SiO_2 at constant Nd-isotopic ratios (ϵ_{NdT} 0 to +1; Fig 3.18a,b). It is highly unlikely that samples plotting along these trends were affected by contamination of old continental crust (requiring a contaminant with even higher $[La/Nd]_{PM}$, SiO_2 and ϵ_{NdT} 0 to +1), but the trend could reflect mantle enrichment by relatively young crust, such as the (2920–2980 Ma) lower supracrustal rocks in the Youanmi Terrane.

The remaining samples fall along a trend toward high $[La/Nd]_{PM}$ and SiO_2 with decreasing ϵ_{NdT} (Fig 3.18 a, b), extending to felsic rocks that contain xenocrystic zircons, which could be perceived as a contamination trend. However, a plot of Th/Nb vs ϵ_{NdT} (Fig 3.18c) shows most geological units fall on a mixing curve involving crust that is less isotopically evolved and therefore younger (on average) than that which contaminated xenocryst bearing felsic rocks. Samples at the more isotopically evolved end of the dominant Th/Nb- ϵ_{NdT} trend correspond to high-Mg basaltic andesites (Mg-number of *c.* 60) with pronounced Zr-Hf depletions (see ‘Mount Magnet East HMA’ of Wyman, 2019), which in post-Archean subduction-related rocks are generally attributed to sediment melting under conditions where residual zircon remains behind (Elliott, 1997; Hermann and Rubatto, 2009). When these rocks and other mafic-intermediate rocks from the southwestern Youanmi Terrane are also considered, it is clear that samples with similar Mg-numbers (*c.* 60) display a wide range of ϵ_{NdT} on a near-vertical trend that does not extend to the xenocryst-bearing felsic samples (Fig 3.18d).

Collectively, the isotopic data plotted in Figure 3.18 show three types of non-mantle contributions. One is the previously mentioned trend involving young crust, for which there is no correlation between the extent of input and the resultant isotopic signature. The second is crustal contamination from old basement rocks corresponding to the trend for xenocryst-bearing felsic samples. The third type of contribution, which is observed in most mafic-intermediate rocks of the

Norie and Polelle Groups, is derived from reservoirs of intermediate age, which allows Th/Nb and $[\text{La/Nd}]_{\text{PM}}$ to monitor the extent of its contribution to mafic magmas.

Based on isotopic ratios, zircon inheritance and Th/Yb-Nb/Yb systematics, the nature and extent of crust-mantle interaction progressively increased from low-levels of mixing in the Norie Group (*c.* 2820-2800 Ma), to moderate degrees of interaction in the Polelle Group (2799-2735 Ma). Th/Yb-Nb/Yb systematics and large volumes of homogenized melt compositions observed in each volcanic unit require that the contamination process occurred deep in the crust, lithospheric mantle, or the mantle wedge. Crustal reprocessing is, however, likely to be a major factor for felsic rocks, as is demonstrated by Yilgarn-wide whole rock ϵ_{NdT} mapping of granites, which shows that two-stage depleted mantle ages of 3000 to 3300 My are common (Champion, 2013; Smithies, 2018).

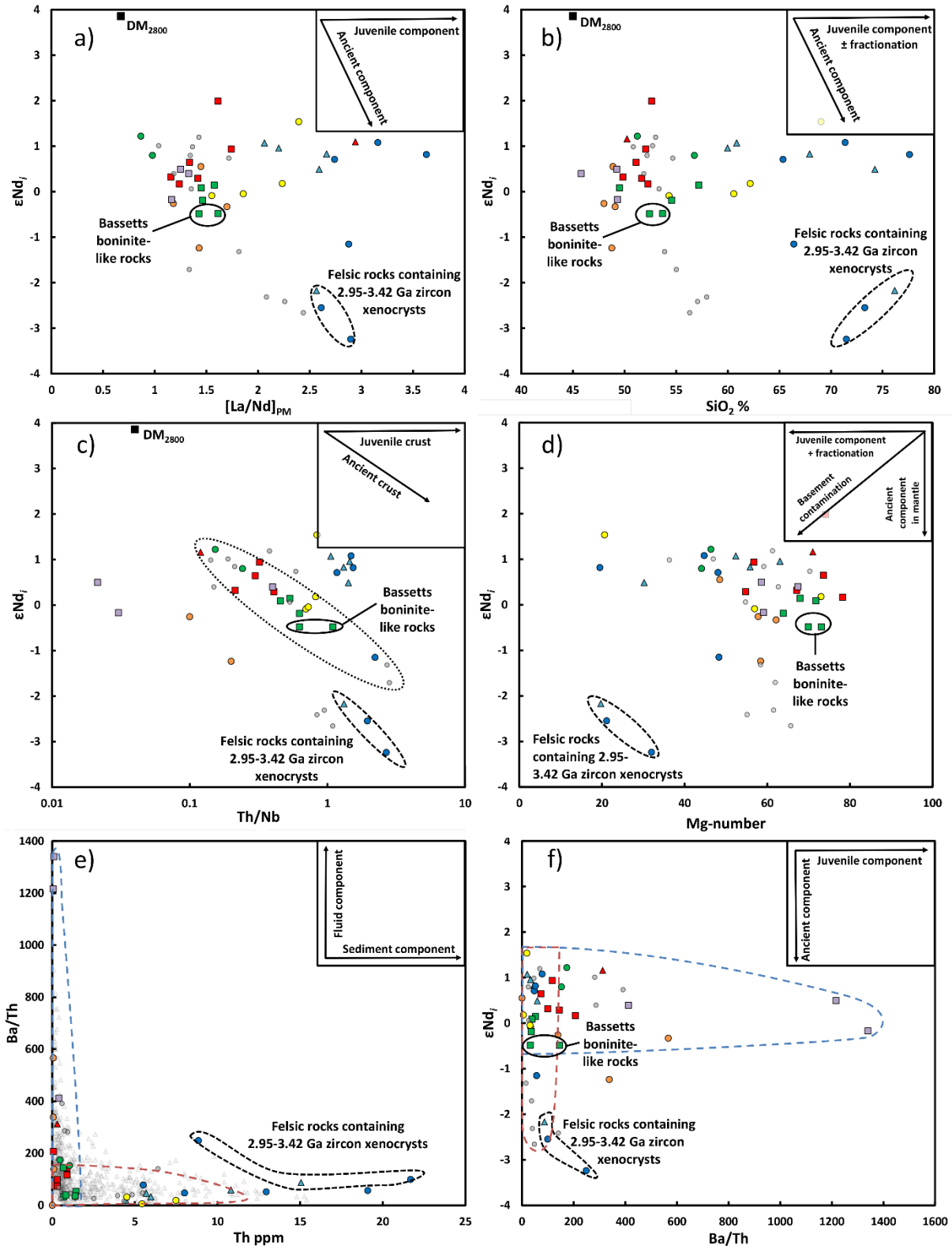


Figure 3.18. Integrated whole rock chemistry and Nd-isotopic systematics. a) ϵ_{Nd_i} vs $[La/Nd]_{PM}$; b) ϵ_{Nd_i} vs SiO_2 ; c) ϵ_{Nd_i} vs Th/Nb ; d) ϵ_{Nd_i} vs Mg -number; e) Ba/Th vs Th ; f) ϵ_{Nd_i} vs Ba/Th . Transparent grey triangles in panel e) indicate compositions of northwestern Youanmi Terrane samples lacking isotopic data, other symbols as per Fig 3.17. Outlier with $\epsilon_{Nd_i} +2.0$ relates to altered cumulate sample 221754. Additional data sources: Windimurra and Narndee (Ivanic, 2015); Yaloginda Formation, Greensleaves Formation and Cullculli Suite (WACHEM database; GSWA, 2018b), southwestern Youanmi Terrane (unpublished data).

3.5.3.3. Subduction vs sagduction geodynamic models

Consensus for a transition to geodynamic processes resembling modern subduction in the mid- to late Archean appears to be growing and is based not only on lithological and geochemical arguments, but also on metamorphic evidence (e.g., Brown and Johnson, 2018) and detailed structural studies of the complex sequences of events associated with orogens, often in “orogenic gold” districts (Blewitt, 2010; Bleeker, 2015).

Given that drip or “sagduction” Archean geodynamic models have a long history (e.g., Ayers and Thurston, 1985, and references therein), they need to be considered in the context of our results. In most cases, the sag or drip models are primarily concerned with cratonization where a stagnant lid or an existing proto-craton is transformed into a long-lived terrane through the formation of intra-crustal granite rocks. What the proposed sags or drips generally lack is a close spatial-temporal analogue for a developing mantle wedge, although its absence may not be obvious in 2D illustrations or computer models. In this regard, Archean rocks that resemble Phanerozoic proto-arc suites may provide key evidence for the viability of sag/drip scenarios.

The setting of the rocks studied here likely involved existing evolved crust and includes rock types, such as siliceous high-Mg basalt, that are not typical of Phanerozoic juvenile arcs. Nonetheless, many of the rock types observed in the northern Youanmi Terrane can be viably amalgamated into a subduction scenario: high-Mg basalts and picrites; moderately LREE-depleted tholeiites; and LOTI basalts, boninites and related rocks from variably “re-enriched” depleted mantle sources are recurring features of juvenile arc systems (Bloomer, 1995; Meffre, 1996; Baziotis, 2017; Patriat, 2019). The later intermediate-felsic volcanic sequences can be equated to more mature arc settings. In addition, the mantle hydration history associated with the Norie and Polelle Groups and contemporaneous mafic intrusive suites are consistent with the progressive influence of subduction zone processes. Sagduction models, in contrast, involve the incorporation of water into melt pathways via hydrated basaltic crust that sinks into the mantle. This process is a key requirement for intra-crustal granite generation but does not provide mechanisms for significant addition of water to the asthenosphere. Not only do models of descending drips or sinking crust fail to create isolated depleted wedge mantle

analogues, they are not capable of focussing metasomatic fluids into evolving boninitic source regions. These are generic weaknesses of sagduction models, and our results provide additional specific reasons to adopt an alternative model.

3.5.3.4. Nature of mantle metasomatism

The samples for which ϵ_{NdT} are available are plotted in Figure 3.18e on the Ba/Th vs Th plot of Hawkesworth (1997), where they display a similar distribution to that observed in island arc settings. Most geological units fall on distinct trends, where multiple samples are available. A trend to high Ba/Th at low Th is defined by the Narndee and Windimurra Igneous Complexes, Singleton Formation (basalts and picrites, boninite-like rocks and variably LREE-enriched tholeiites), and Meekatharra Formation (tholeiitic basalts, siliceous high-Mg basalts and boninite-like rocks). This trend corresponds to the fluid-related mantle metasomatism trend documented by Hawkesworth (1997) for the Marianas, Tonga, and some other intra-oceanic arcs. A second trend at low Ba/Th to high Th is defined by basaltic andesite-rhyolite samples of the Norie and Polelle Group samples (including adakitic compositions) and similar aged high-Mg andesites from the south western Youanmi Terrane (assigned to the Meekatharra Formation; Geological Survey of Western Australia, 2018c).

Hawkesworth attribute this latter trend in the Aeolian Islands and the Philippines to sediment-related mantle enrichment. Northwestern Youanmi Terrane samples that fall along this trend also show many of the classic features of sediment-related mantle enrichment, such as strong Th-LREE enrichment and negative or positive Zr-Hf anomalies (related to residual zircon or zircon melting in the source respectively), and therefore plausibly represent a classic ‘sediment’ trend in an arc mantle wedge setting. In a geochronological context, these results collectively imply that a switch from fluid- to sediment modified sources occurred twice within the studied Norie – Polelle sequence (Fig 3.18 and Table 3.3) and was associated with two transitions from depleted to metasomatised mantle, as also demonstrated by the Th/Yb vs Nb/Yb plots of the Norie and Polelle Groups (Fig 3.16).

3.5.4. Significance of textural observations from northwestern Youanmi Terrane mafic-ultramafic ultramafic rocks.

3.5.4.1. Lower Singleton Formation

Mafic-ultramafic rocks of Singleton Formation in the Gabanintha area have previously been classified as komatiite and komatiitic basalt (Fig 3.3; Jackson 1990, Reudavey 1990, Watkins and Hickman 1990, Barley *et al.*, 2000, Hallberg 2000, Pidgeon and Hallberg 2000, Van Kranendonk *et al.*, 2013), but in each case, the classification was based on compositions of olivine cumulate rocks (i.e., picrites or olivine orthocumulate). Our data show that fine grained rocks (e.g., Fig 3.4a, b), on the other hand, mostly have basaltic compositions (SiO_2 49.9-52.7 wt% and MgO 10.3-16.1 wt%), whereas samples containing ≥ 18 wt% MgO all contain abundant olivine phenocrysts (e.g., Fig 3.4c-f), and therefore do not represent liquid compositions. Furthermore, several of those earlier studies identified textural features uncommon for komatiites, including abundant amygdales in both fine grained and picritic rocks, and a pyroclastic component within the volcanic sequence (Reudavey 1990, Barley *et al.*, 2000, Hallberg 2000). Both of those features indicate a relatively high volatile content and are consistent with a hydrous mantle origin.

3.5.4.2. Boninite-like rocks

Volcanic rocks of the upper Singleton Formation show textural evidence for magma mixing (or rather, incomplete mixing), such as rafts of more mafic groundmass ‘intruding’ slightly lighter bulk rock groundmass (Fig 3.5b), and mafic globules in leucocratic domains, within otherwise mafic groundmass (Fig 3.5e,f). Alternatively, the mafic globules could reflect immiscible domains of a solute-bearing hydrous fluid exsolved from the silicate liquid-crystal mush before or during emplacement, as proposed for globular/orbicular features by Ballhaus (2015). Such a mechanism could also be responsible for the common occurrence of ‘varioles’ in boninite-like rocks and siliceous high-Mg basalts of the Meekatharra Formation (Fig 3.7). Boninite-like rocks in the Bassetts Volcanic Member (Meekatharra Formation) are typically vitrophyric or microlitic textured, like many Cenozoic boninites (e.g., Taylor, 1994, Falloon and Crawford, 1991), with zoned pigeonite-augite phenocrysts (Electronic Appendix 3.3). Locally, the Bassetts Volcanic Member also exhibits dendritic pyroxene and platy pyroxene spinifex textures, which have rarely been described in the literature (see discussion in Lowrey *et al.*, 2017), but have been reported in one Cenozoic boninite from New

Zealand (Wood, 1980). Compositions in the freshest cores of zoned clinopyroxenes range from pigeonite to clinoenstatite ($\text{Wo}_4\text{En}_{83}\text{Fs}_{13}$ to $\text{Wo}_{15}\text{En}_{68}\text{Fs}_{17}$; Electronic Appendix 3.3, Fig 3.10), and in cross polarized light they show tightly spaced polysynthetic twinning along the c-axis (Fig 3.8f). Polysynthetic twinning in clinoenstatite from Phanerozoic boninites has been attributed to stacking disorder arising from the transition of protoenstatite to clinoenstatite during rapid cooling (Dallwitz, 1966, Komatsu 1980). Another consideration is the transition from pigeonite(-clinoenstatite) cores to augite rims, which contain unusually high concentrations of incompatible minor elements Al and Ti; an early study of lunar basalts by Grove and Bence (1977) showed that pyroxene-liquid partitioning behaviour of Al and Ti were strongly dependent on the cooling rate. In our samples, rapid crystallization of Al-Ti-poor pigeonite cores likely resulted in correspondingly Al-Ti-rich halos surrounding the cores: the higher than normal Al and Ti concentrations in augite rims therefore re-enforce a high cooling rate model.

All textures observed in boninite-like rocks and siliceous high-Mg basalts in our study area indicate rapid crystallization and undercooling, to varying degrees, during emplacement (Lowrey *et al.*, 2017, and references within). Recognition that variolitic or ‘globular’ textures can result from immiscibility between exsolved hydrous fluids, and silicate magma (Ballhaus, 2015), is petrogenetically significant for high-Mg mafic volcanics in our study area, since it requires a H_2O -rich parent magma. Considered together with the primitive compositions seen in our data, the petrographic evidence indicates that lavas were very hot, phenocryst poor, and likely wet during emplacement, which in turn indicates a rapid ascension through the crust and reaffirms that crustal assimilation prior to eruption was minimal.

3.5.5. Geodynamic Synthesis

The Th/Yb-Nb/Yb trends in *c.* 2800 Ma northwestern Youanmi Terrane rocks indicate that mixing between crustal and mantle components occurred either in the mantle, or in mixing zones within the lower crust, before ascending to surface, otherwise contamination trends would be apparent. This is supported by whole-rock Sm-Nd and zircon Lu-Hf data (this study; Ivanic, 2012, 2015), which predominantly show a trend towards increasingly LILE-LREE enriched compositions at

near-constant (ϵ_{NdT} -0.5 to +1.5) isotopic ratios. Together with contemporaneous hydrous mantle-related magmatism of the 2799 \pm 7 Ma Boodanoo and 2801 to 2793 Ma Warriedar Suites (Ivanic, 2015; Ivanic, 2016), the evidence favours a subduction origin or another process that might replicate key features of the subduction process.

Based on the recurrence of multiple rocks types in the northwestern Youanmi Terrane that commonly occur in Phanerozoic arcs, the geochemical evidence for two-fold mantle depletion and re-enrichment associated with mantle hydration and the distinct isotopic-geochemical trends observed, we favour a subduction-like process for Norie and Polelle magmatism, although the mode of Archean subduction may have been different to the styles that dominate in the Phanerozoic (e.g., Perchuk, 2019). Subduction of relatively young crust at *c.* 2800Ma resulted in hydrous metasomatism of mantle sources and modified the LREE-MREE characteristics of many magmas without significantly influencing their Nd isotopic signatures. Sediments, with variably evolved isotopic ratios, were increasingly important in the genesis of intermediate to felsic magmas during both Norie and Polelle Group volcanism, although mixed fluid-sediment contributions appear to have also occurred. The fluid-to-sediment re-setting of metasomatic sources can be accommodated in a variety of subduction-linked scenarios: “short-lived” Norie Group subduction (*c.* 20 million years) may have been terminated by a reconfiguration of plates, such as in a subduction zone step back, which also initiated Polelle Group magmatism.

Post *c.* 2780 Ma, we identify a volcanic hiatus in our study area of up to 20 Ma, which separates the Meekatharra Formation from the Greensleeves Formation, but its tectonic significance is not yet clear and may be a local feature within a larger scale subduction system.

3.6. CONCLUSIONS

Boninitic and LOTI basalt suites occur in many Archean cratons and have played an important role in assessments of tectonic styles operating during Earth’s early history. The 2820-2735 Ma northwestern Youanmi Terrane stratigraphy contains perhaps the best preserved and most complete set of rock types that would be considered diagnostic of subduction magmatism in the modern

geologic record (boninite, LOTI basalt, tholeiitic basalt, high-Mg basalt-andesite-dacite, sanukitoid and hornblende-rich gabbros).

Using a combination of new whole-rock compositions and Sm-Nd isotopic data we have demonstrated that:

- (1) Previously reported Al-depleted komatiites in the lower Singleton Formation are instead high-Mg basalts, picrites and olivine orthocumulates. Wyman (2019) noted their similarities to Phanerozoic arc-picrites in terms of magma liquid compositions and field characteristics. Nonetheless, the rocks also bear a strong similarity to Barberton Al-depleted komatiitic rocks with respect to MgO concentration, trace element patterns and incompatible element ratios (e.g., $\text{Al}_2\text{O}_3/\text{TiO}_2$). Their emplacement at the lowest stratigraphic level leaves open the possibility that the first cycle of subduction magmatism in the Youanmi region at c. 2820 Ma was triggered by the ascent of a nearby plume.
- (2) High-Mg basalts and picrites of the lower Singleton Formation and tholeiitic basalts in the Stockyard Basalt Member erupted with minimal interaction with crust, which in turn indicates locally thinned lithosphere and upwelling asthenosphere, consistent with two episodes of rifting at c. 2820 Ma and sometime between 2799-2787 Ma.
- (3) Th/Yb-Nb/Yb systematics and Nd isotopes suggest $\text{LILE} \pm \text{LREE}$ enrichment was a characteristic of their mantle source, which evolved in composition over time.
- (4) The mantle sources of boninite-like rocks in the upper Singleton Formation and Meekatharra Formation were metasomatised by fluids derived mainly from reservoirs that were (on average) younger than the sediments that modified the sources of the Greensleeves Formation and coeval Cullculli Suite magmas.
- (5) Integration of the available geochemical, geochronological and isotopic data implicates two consecutive cycles of depletion and metasomatism in c. 2800 Ma mafic magma sources in the northwestern Youanmi Terrane. This requirement cannot be achieved in sagduction or crustal drip models within the temporal and spatial restrictions imposed by our results. Conversely,

two subduction initiation events, 25 million years apart, may be attributed to subduction step-back or plate arrangements.

Chapter 4: Chemostratigraphy of the northwestern Youanmi Terrane

Chapter 3 showed evidence supporting a primitive arc setting for *c.* 2820 to 2790 Ma boninite-like rocks and associated mafic volcanic rocks in two greenstone belts in the northwestern Youanmi Terrane. At the time that the work was written and published, a concurrent PhD project in an adjacent study area, the Yalgoo-Singleton belt (Fig. 4.1), was abandoned. That adjacent study area contains a variety of lithologies that are critical to understanding the magmatic and geodynamic history of the northwestern Youanmi Terrane. Hence, using a considerable database of geochemical and isotopic data (Electronic Appendices 1.1-1.2), this chapter examines a broader period of magmatism, from *c.* 2820 to 2738 Ma, and extends the study area eastward and southward to incorporate several other greenstone belts of Youanmi Terrane (Fig. 4.1). A subset of the whole rock geochemical ($n = 151$ out of 1395) and Sm-Nd isotopic data ($n = 13$ out of 115) interrogated here were inherited from the supervisor of the abandoned PhD project and the student (R. Teslyuk) is acknowledged as the originator of those samples (Electronic Appendices 1.1-1.2) – no interpretative content (beyond field observations such as lithology and textures present in sample) was inherited from the abandoned PhD project. In this Chapter, the stratigraphy is classified into 16 chemostratigraphic units, which are interpreted to be compatible with widely hydrated and metasomatised mantle sources and subduction-related magmatism.

4.1. SAMPLE SCREENING

All samples collected during this study represent the (visually) least altered and most lithologically, texturally, and mineralogically homogeneous specimens available. However, given this study also interrogates samples from previous studies, and considering many samples were collected from regions close to known Au- and base metal mineralisation, it was necessary to further screen samples for the effects of hydrothermal alteration on the concentrations of important major elements, such as SiO₂, CaO, Na₂O, and K₂O, which are not always discernible by visual inspection. Samples with compositions that are clearly altered, such as those with LOI that far exceeds results typical of the rest

of the unit, were excluded from this dataset. Rocks with $\text{SiO}_2 > 57 \text{ wt\%}$ were excluded from the dataset if their aluminium saturation index (ASI; $\text{Al}_2\text{O}_3 / (\text{CaO} + \text{Na}_2\text{O} + \text{K}_2\text{O})$ on a molar basis) exceeded 1.1 (i.e. the sample was peraluminous) or if they contained $<1 \text{ wt\% Na}_2\text{O}$ or $<3.5 \text{ wt\% Na}_2\text{O} + \text{K}_2\text{O}$ as these low alkali concentrations almost certainly reflect alkali depletion during alteration. Rocks with $\text{SiO}_2 > 77.5 \text{ wt\%}$ (silica concentrations higher than values achievable through normal igneous processes) were initially removed for all Units, but were re-entered into the dataset for three high-silica rhyolite Units (Units 3, 9 and 14) that are proximal to VMS hydrothermal systems and are typically silicified. For all Units, emphasis is placed on trace elements that remain immobile (i.e., they appear to retain their magmatic ratios; Th, HFSEs, REEs, transition metals) even in samples where major elements show significant mobility.

4.2. STRATIGRAPHIC CORRELATION BY CHEMICAL SIMILARITIES

Bivariant plots of incompatible elements and patterns of mantle-normalised incompatible trace element concentrations, plotted on spider diagrams, have proven useful for identifying groups of samples derived from a shared parent magma (e.g., Lowrey *et al.*, 2019). This is because such sample groups often show little variation in their incompatible element ratios over large crystallization windows (e.g., from basalt to andesite), providing fractionation was dominated by minerals with low affinities for the elements being compared (e.g., olivine, pyroxene, plagioclase) and/or the bulk mineral-melt partition co-efficient for the fractionating assemblage(s) did not change significantly. Correlations of volcanic rocks based on their incompatible trace element characteristics are now routinely used, together with geochronology and geological context (field relationships, younging indicators etc.), to inform their regional stratigraphic frameworks across the Yilgarn Craton (e.g., Smithies *et al.*, in review). This ability to correlate stratigraphy based on chemically characterized geological units does depend, however, on how dismembered the greenstone belts are and how much chronological control there is. Seismic data indicate a particularly complicated network of overprinting shear zones in this region (e.g., Zibra, 2020) and it is acknowledged that all stratigraphic implications of this work are tentative because facing directions are not always known.

4.3. Age, distribution, petrography and chemical characteristics of stratigraphic units

This section summarizes the chemical and petrographic characteristics of samples in the context of any known or inferred chronological information and their geographic distributions. Based on natural breaks in zircon U-Pb ages (Fig. 3.3), the stratigraphy is separated into two broad episodes of magmatism at 2817–2782 Ma (‘magmatic episode 1’) and 2761–2738 Ma (‘magmatic episode 2’). Magmatic components from these two episodes are then divided into sixteen chemostratigraphic ‘Units’ based on geochronological and geochemical similarities within a consistent geological context (i.e., consistent field relationships and younging indicators). Units are numbered in chronological order, from oldest to youngest. This section presents a high level of detail that serves as an essential reference and provides the evidence necessary to document the full range of igneous lithologies that, collectively, are consistent with a c.2820 to 2738 Ma subduction ‘succession’.

Figure 4.1 and Table 4.1 are provided as keys to accompany the chemostratigraphic descriptions that follow – Figure 4.1 shows the geospatial arrangement of the chemostratigraphic units while Table 4.1 summarizes the chronological, lithological and chemical attributes of each unit. Together, they show significant chemostratigraphic variations between greenstone belts in the northern Youanmi Terrane.

Interpretations for samples from the Meekatharra to Cue area (Lowrey *et al.*, 2019) and Mount Magnet and Mount Singleton areas (Wyman, 2019) have previously been reported and are only summarized in this study. Major elements are plotted against SiO₂ for dominantly felsic units, and against MgO for dominantly mafic units. Tantalum is included on extended trace element patterns for dominantly felsic units, but not for dominantly mafic units where measured concentrations are close to the lower detection limit for the later. Likewise, Sr is included in trace element patterns for felsic units but excluded from patterns for mafic units, which predominantly show effects of alteration rather than fractionation. Pearce’s Th/Yb vs Nb/Yb diagram (Pearce, 2014), which was designed as a tectonic discrimination diagram for basaltic rocks, is shown for all units, regardless of their SiO₂ content. This is simply to illustrate trends in Th/Nb within and between chemical units – no

geodynamic interpretations for felsic rocks are based on their plotting within the modern arc basalt fields on this diagram.

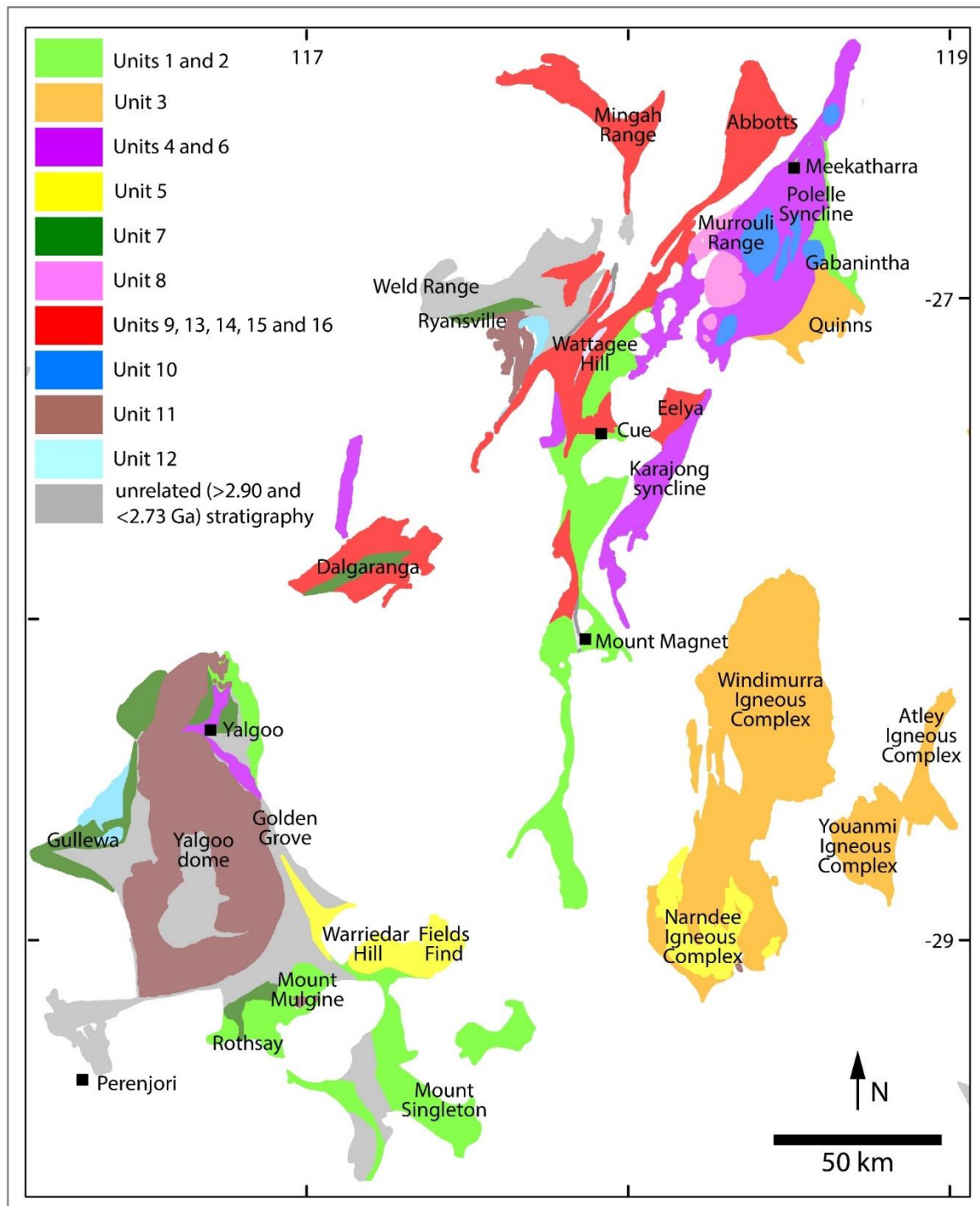


Figure 4.1 – Simplified chemostratigraphic map. Several Units are too small to map their geographic distribution at the scale of this study, so where two or more Units regularly occur in local stratigraphies together, they have been mapped together.

Table 4.1 summary of chemostratigraphic units								
	Unit	Age		Description	GSWA stratigraphic unit	Chemical affinity	Interpretation	εNdT
Magmatic Episode 1	1	c. 2820 Ma	No direct dating; ages inferred from field relationship to Unit 3 in the Gabanintha area.	Olivine-pyroxene rich mafic-ultramafic volcanic and sub-volcanic rocks	Singleton Formation	High-Mg, high-Ti tholeiitic rocks with high Gd/Yb	Deep (>90km) asthenospheric melting (Lowrey <i>et al.</i> , 2019)	+1.3 to +0.6
	2	c. 2820 Ma	No direct dating; ages inferred from field relationship to Unit 3 in the Gabanintha area.	Pyroxene-rich mafic-ultramafic volcanic and sub-volcanic rocks	Singleton Formation	High-Mg, low-Ti tholeiitic basalt to boninitic	Relatively low-pressure melting of refertilised refractory mantle sources (Lowrey <i>et al.</i> , 2019)	+1.8 to +0.4
	3	2817 to 2813 Ma	Quinns mining district (2817 ± 3 Ma); Windimurra and Youanmi Igneous Complexes (2813 ± 3 Ma). (GSWA, 2021).	Intermediate to felsic volcanic, volcanoclastic and shallow-level intrusive rocks (such as granophyre) and associated intrusive complexes	Yaloginda Formation and Meeline Suite	Tholeiitic basalts to rhyolites with weakly enriched, but highly elevated incompatible trace element concentrations	Relatively low-pressure asthenospheric melting and low-pressure fractional crystallization	+1.2 to +0.1
	4	2815 to 2803 Ma	Thirteen ages between 2815 and 2803 Ma in the Meekatharra-Karajong and Yalgoo-Singleton greenstone belts, and Narndee and Atley igneous complexes (Wang, 1998; Fletcher and McNaughton, 2002; GSWA, 2021).	Hornblende-bearing (mafic to) felsic volcanic rocks and intrusive equivalents	Yaloginda Formation and Mount Kenneth Suite	Sanukitoid (and sanukitoid-like)	Relatively low-pressure melting of metasomatised mantle sources	+3 to -1.5
	5	2799 ± 7	2799 ± 7 Ma hornblende gabbro at Narndee; The Fields Find, Warriedar Hill and Mount Magnet localities are undated.	Hornblende-rich ultramafic-mafic intrusions and volcanic equivalents	Boodanoo Suite and Singleton Formation?	High-Mg, moderate-Ti compositions, low Zr/Zr*. Fields Find, Warriedar Hill and Mount Magnet samples have high Gd/Yb, whereas Narndee has relatively flat MREE-HREE patterns; Alaskan-type intrusions (Wyman, 2019) and extrusive equivalents.	Relatively low-pressure melting of metasomatised mantle sources (Wyman, 2019)	Mostly +1.3 to -0.2 with two high outliers at +2.89 and +1.9 and one low outlier at -0.8
	6	c. 2793 Ma	2793 ± 5 Ma interflow sediment near Meekatharra, crosscut by 2787 Ma granite pluton at Murrouli Range	Predominantly mafic (to intermediate) volcanic rocks including pyroxene spinifex textured basalts and massive or pillowed basalts	Meekatharra Formation	Intermediate-Th, siliceous high-Mg basalts, boninite-like rocks, tholeiitic basalts	Relatively low-pressure high-degree melting of variably refertilised refractory mantle sources and upwelling asthenosphere (Lowrey <i>et al.</i> , 2019)	+2 to -0.3; one low outlier at -1.7
	7	c. 2793 Ma	2793 ± 4 Ma interflow sediment near Yalgoo and intercalated with 2793 ± 8 Ma rhyolite near Gullewa.	Predominantly mafic volcanic rocks including pyroxene spinifex-textured basalts	Meekatharra Formation	High-Th, siliceous high-Mg basalts	Relatively low-pressure high-degree melting of metasomatised mantle sources	-1.4 to -3.2
	8	2787 to 2782 Ma	2787 ± 3 Ma and 2782 ± 7 Ma granitic rocks in the Murrouli Range; 2782 ± 5 Ma porphyritic andesite in the Murrouli Range (GSWA, 2021)	Hornblende-biotite bearing granitic plutons (containing dioritic clots) and porphyritic felsic volcanic or sub-volcanic rocks	Nannine Tonalite (previously Cullculli Suite)	Sanukitoid (and sanukitoid-like)	Relatively low-pressure melting of metasomatised mantle sources	+1.0 and +0.9

Table 4.1 continued

Magmatic Episode 2	9	c. 2760 Ma	Three ages between 2761 and 2759 Ma in the Eelya and Cue areas (Pidgeon and Hallberg, 2000; Hayman <i>et al.</i> , 2015; GSWA, 2021)	Biotite-(hornblende-) bearing granitic rocks and volcanic equivalents.	Greensleeves Formation and Eelya Suite (previously Cullculli Suite)	High-Si granites and rhyolites with enriched and elevated LILE-LREEs and elevated HREEs	Low-pressure fractional crystallization of LILE-LREE-enriched tholeiitic magmas	No data
	10	2761 to 2746 Ma	Six ages between 2761 and 2746 Ma in the Meekatharra belt.	Hornblende-(biotite-) and pyroxene- bearing intermediate to felsic volcanic(lastic) rocks and porphyritic intrusions.	Greensleeves Formation and Cullculli Suite	Sanukitoid (and sanukitoid-like)	Relatively low-pressure melting of metasomatised mantle sources	+1.2 to -0.4
	11	2766 to 2741 Ma	Fourteen ages between 2766 and 2741 Ma in the Yalgoo-Singleton and Mingah-Ryansville belts.	Biotite-bearing granitic rocks	Rothsay Suite	Sodic to moderately potassic granites analogous to transitional TTG (TTTG)	Deep (or not so deep) melting of crust that includes a felsic component	+1 to -1.9
	12	2754 to 2747 Ma	Two hornblende-rich granites near Gullewa give 2754 ± 4 Ma (GSWA 2021) and 2747 ± 3 (Fletcher and McNaughton, 2002) ages; a biotite-hornblende granite near Ryansville gave a crystallization age of 2748 ± 5 Ma.	Hornblende-biotite-bearing granitic plutons (containing dioritic clots) and intermediate volcanoclastic rocks and lamprophyre dykes	Rothsay Suite - Cagacaron Syenogranite	Shoshonitic plutons, volcanoclastics and lamprophyres; variably high to ultra-high K_2O and P_2O_5 concentrations.	Relatively low-pressure melting of K_2O - P_2O_5 rich metasomatised mantle sources	-1.5 to -3.1
	13	c. 2750 Ma	No direct dating; age is equivocal and inferred from field relationships to Unit 14 in the Abbots, Dalgara, Mingah and Wattagee Hill areas.	Basalt to andesite containing abundant Fe-Ti oxides.	Meekatharra Formation?	High-LILE-LREE tholeiitic basalt to andesite	Low-pressure fractional crystallization of LILE-LREE-enriched tholeiitic magmas	-3.2 to -4.1
	14	2752 to 2745 Ma	Eight ages between 2752 ± 4 Ma and 2743 ± 4 Ma in the Eelya mining district, Mingah Range and Dalgara area (Wang, 1998; Pidgeon and Hallberg, 2000; GSWA 2021).	Predominantly rhyolites, locally granophyric	Greensleeves Formation and Eelya Suite	High-Si rhyolites with enriched and elevated LILE-LREEs and elevated HREEs	Low-pressure fractional crystallization of LILE-LREE-enriched tholeiitic magmas	-2.0 and -3.6
	15	2750 to 2738 Ma	Nine ages between 2750 ± 9 Ma and 2738 ± 4 Ma in the Abbots greenstone belt, Mingah Range and Wattagee Hill area (Wang, 1998; GSWA 2021). One sample of tuff from the Abbots greenstone belt gave a 2734 ± 5 Ma age (Wang, 1998), outside of the c. 2743 to 2742 Ma window of uncertainty given by the other nine samples from this unit.	Hornblende-(biotite) and pyroxene bearing intermediate to felsic volcanic(lastic) rocks and porphyritic intrusions.	Greensleeves Formation	Sanukitoid (and sanukitoid-like)	Relatively low-pressure melting of metasomatised mantle sources	+0.6
	16	equivocal; c. 2750 to c. 2725 Ma	No direct dating and inferred ages are equivocal; samples presently assigned to Wattagee Formation in the Wattagee Hill area (Van Kranendonk <i>et al.</i> , 2013) are indistinguishable from samples along strike that are assigned to Meekatharra Formation in the Cuddingwarra Hill and Yalgowra Hills areas (Van Kranendonk <i>et al.</i> , 2013).	Gabbros and basalts, locally with abundant acicular pyroxene phenocrysts	Meekatharra Formation or Wattagee Formation	High-Mg basalts and low-Mg tholeiitic basalts with	Relatively low-pressure asthenospheric melting	No data

4.3.1. Magmatic Episode 1

4.3.1.1. Unit 1

Unit 1 consists of mafic volcanic and sub-volcanic rocks, including Al-depleted high-Mg basalt, picrite and olivine-pyroxene cumulate assigned to the *c.* 2820 Ma Singleton Formation. The type localities are at Gabanintha (Lowrey *et al.*, 2019) and Mount Singleton (Wyman, 2019). These mafic rocks are not suited to direct dating methods, but their age range can be inferred from their geological relationships to Unit 3 rocks, i.e., they have likely been deposited around the same time and interpreted to be extrusive equivalents of the *c.* 2820–2810 Ma Meeline Suite mafic intrusive complexes (Lowrey *et al.*, 2019). The chemical characteristics of Unit 1 have been described in detail by Lowrey *et al.* (2019) and Wyman (2019). According to the total alkali-silica scheme, most samples classify as basalt or basaltic andesite, except for samples that contain significant volumes of olivine phenocrysts, which classify as picrobasalts. All samples contain low-K₂O and follow tholeiitic lines of liquid descent. At Gabanintha and Mount Singleton, where metamorphic grades are predominantly greenschist facies, there is a notable break in MgO concentration between fine grained samples containing ≤ 16 wt% and olivine rich cumulates that contain ≥ 23 wt% MgO (Fig 4.2a-f). Amphibolite with similar incompatible element characteristics north of Gabanintha and northwest of Mount Singleton contain 5–19 wt% MgO. Compositions within the komatiitic field are extremely rare but given their potential significance in previous geodynamic interpretations (Barley *et al.*, 2000; Van Kranendonk *et al.*, 2013), Lowrey *et al.* (2019) assessed this unit in detail and concluded that liquid compositions likely contained approximately 16 wt% MgO, less than that of true komatiite and not necessitating anomalously high mantle temperatures (see also arguments in Wyman, 2019). Nevertheless, the low Al₂O₃/TiO₂ (Fig 4.2d) and the incompatible trace element characteristics (Fig 4.3) of these rocks resembles those of Al-depleted komatiites, suggesting these rocks were derived by melting of relatively primitive mantle in the presence of residual garnet (\pm amphibole) (Lowrey *et al.*, 2019) and consequently of a relatively deep source (>90 km depth), near to the beginning of the *c.* 2820–2780 Ma magmatic episode 1.

Th/Yb–Nb/Yb systematics indicate only limited crustal contributions to their parent magmas and the relatively constant Th/Nb over the crystallization range from 16–5 wt% MgO implies that this contribution occurred at a very early stage, likely in the mantle source or at the base of the lithosphere.

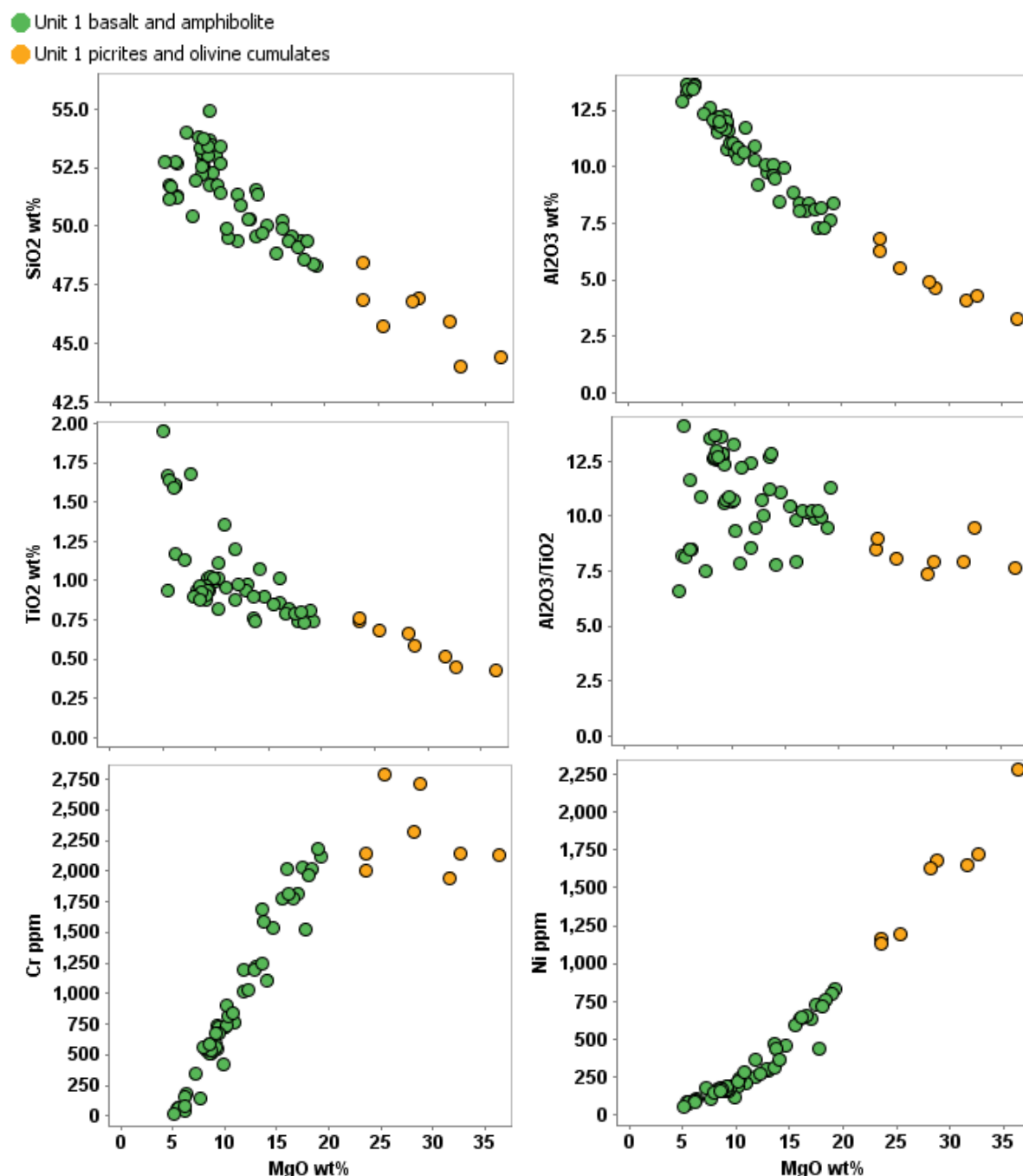


Figure 4.2. Major and compatible trace element variation diagrams for Unit 1 samples: a) SiO₂ vs MgO; b) Al₂O₃ vs MgO; c) TiO₂ vs MgO; d) Al₂O₃/TiO₂ vs MgO; e) Cr vs MgO; f) Ni vs MgO.

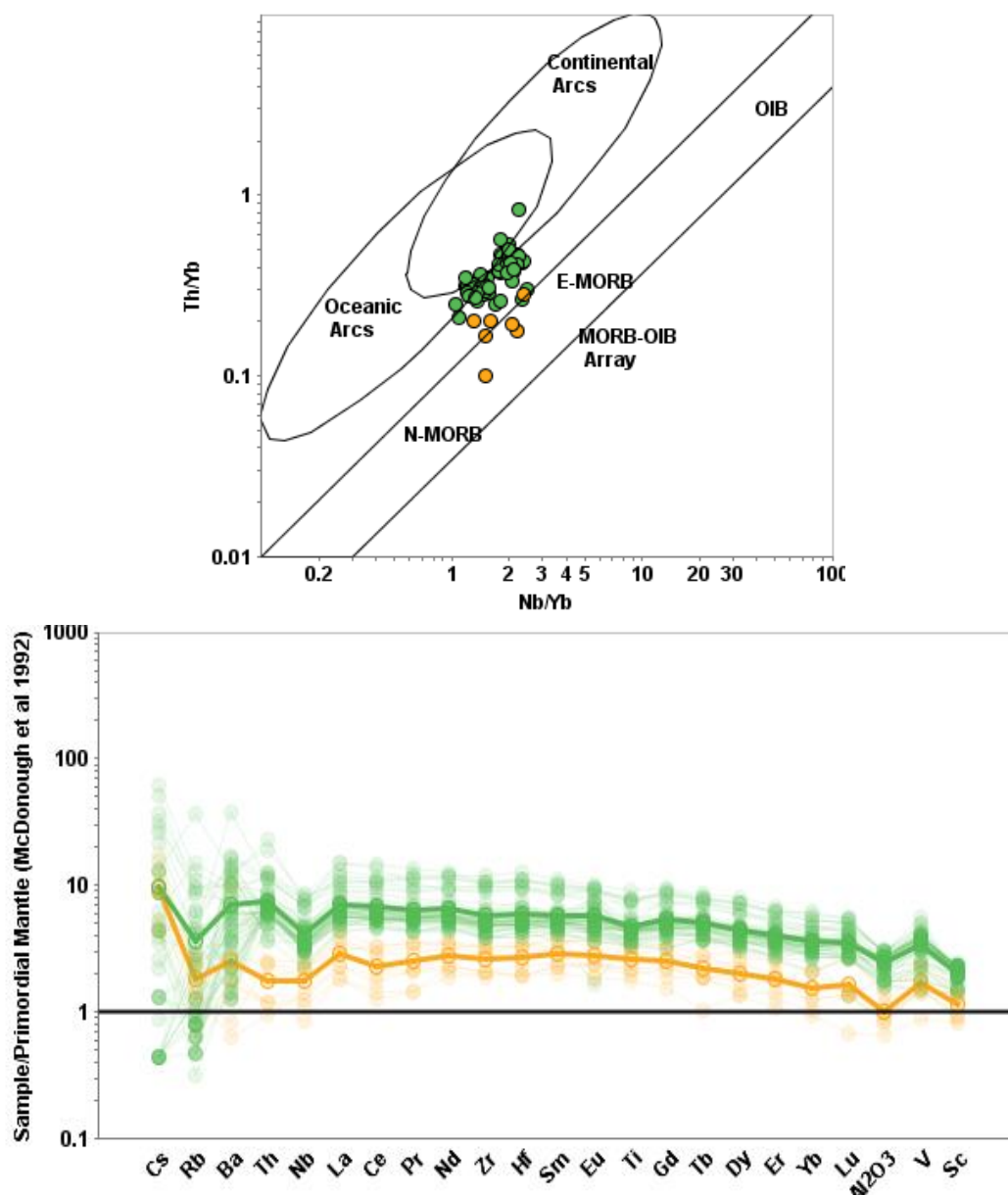


Figure 4.3 a) Th/Yb vs Nb/Yb (after Pearce, 2014) for Unit 1; b) mantle normalised trace element patterns for Unit 1. Symbols as per Fig 4.2. Averages for trace element patterns of each grouping shown as bold lines.

4.3.1.2. Unit 2

Unit 2 consists of mafic volcanic and sub-volcanic rocks, including low-Ti, high-Mg basalt to basaltic andesite assigned to the *c.* 2820 Ma Singleton Formation, which locally contains rocks with boninite-like compositions. These rocks are interpreted to conformably overlie Unit 1 in the Gabanintha and Mt Singleton areas (Lowrey *et al.*, 2019), and are therefore inferred to relate to the same broad magmatic event as Unit 3 and the coeval *c.* 2820–2810 Ma Meeline Suite mafic intrusive complexes. The chemical characteristics of Unit 2 have been described in detail by Lowrey *et al.* (2019) and Wyman (2019), but here the distribution is extended to the Yalgoo, Mount Mulgine, and Fields Find

areas (Figs 1, 4; Electronic Appendix 1.1). Basaltic rocks from Cue to Mount Magnet that are presently assigned to the *c.* 2800–2790 Ma Meekatharra Formation (Unit 4) in basement geological maps (GSWA, 2020) are also tentatively assigned here to Unit 2: there is no clear indication based on geochronology or field relationships that these basalts belong to the Singleton Formation or Meekatharra Formation but their compositions are more similar to demonstrably Unit 2 compositions than to demonstrably Unit 4 compositions.

According to the total alkali vs silica classification scheme, most Unit 2 samples are basalt or basaltic andesite. Unit 2 is dominated by relatively high-Mg basalts (7–15 wt% MgO) but includes a significant number of samples that have fractionated to compositions with less than 3 wt% MgO.

Samples that contain > 15 wt% MgO (including a number of samples that are not plotted below in Figs 4.3 and 4.4 due to strong alteration) plot along a MgO-SiO₂ trend that is offset to higher SiO₂, clearly distinguishing them as pyroxene ± olivine cumulates rather than komatiites (Fig 4.4a). Unit 2 samples can be easily distinguished from coeval Unit 1 samples by their significantly lower TiO₂ and higher Al₂O₃/TiO₂ at any given MgO concentration (Fig 4.2c-d and Figs 4.4 c-d).

It is clear from bivariate plots of incompatible elements (e.g., Th, La, Nb and Zr vs TiO₂; Fig 4.5a-d) that Unit 2 includes numerous sub-units (i.e., trends or clusters) that represent batches of magmas from specific geographic locations. The vectors shown on these plots reflect the sum of various magmatic processes, including degree of partial melting, fractionation and crustal assimilation. For example, whereas most sub-units follow broadly similar increases in Th, La, Nb and Zr with TiO₂, one sub-unit of basalts from immediately north of Yalgoo (dark blue points on Fig 4.5a-d) plot at significantly higher Th, La, Nb and Zr versus TiO₂ and likely represent an unusually high degree of crustal assimilation or mixing with a felsic magma. Nevertheless, nearly all of the Unit 2 sub-units appear to have compositions that evolved from high-MgO parental liquids from moderately MREE-depleted mantle sources and show variable contributions from LILE-LREE rich crustal components. On a plot of Th/Yb vs Nb/Yb (Fig 4.6a), Unit 2 samples have a relatively broad range of values and follow a trend that originates at lower-Nb/Yb and higher Th/Yb relative to N-MORB and define a vector that is approximately parallel to the modern mantle-array. Lowrey *et al.*, 2019 interpreted this

trend to imply that the depleted mantle source itself had been mixed with a Th (-LILE-LREE) enriched crustal component. Mantle normalised trace element patterns for Unit 3 vary from strongly LREE-MREE-depleted to LREE-enriched and MREE-depleted (Fig 4.6b), the latter equating to concave-shaped REE patterns; both of these trace element pattern types are typical of boninite and low-Ti tholeiitic (LOTI) basalt associations.

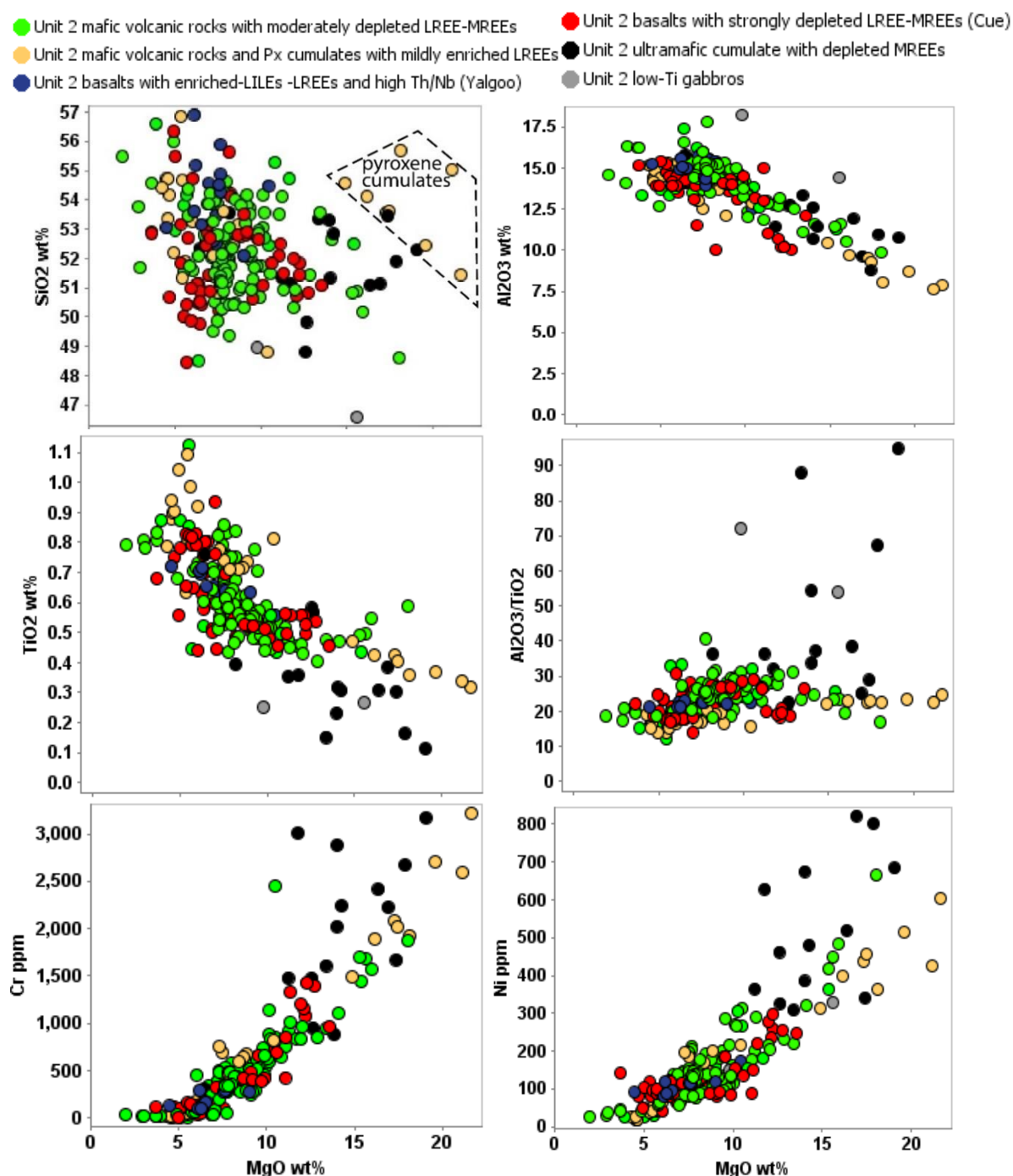


Figure 4.4. Major and compatible trace element variation diagrams for Unit 2 samples: a) SiO₂ vs MgO; b) Al₂O₃ vs MgO; c) TiO₂ vs MgO; d) Al₂O₃/TiO₂ vs MgO; e) Cr vs MgO; f) Ni vs MgO.

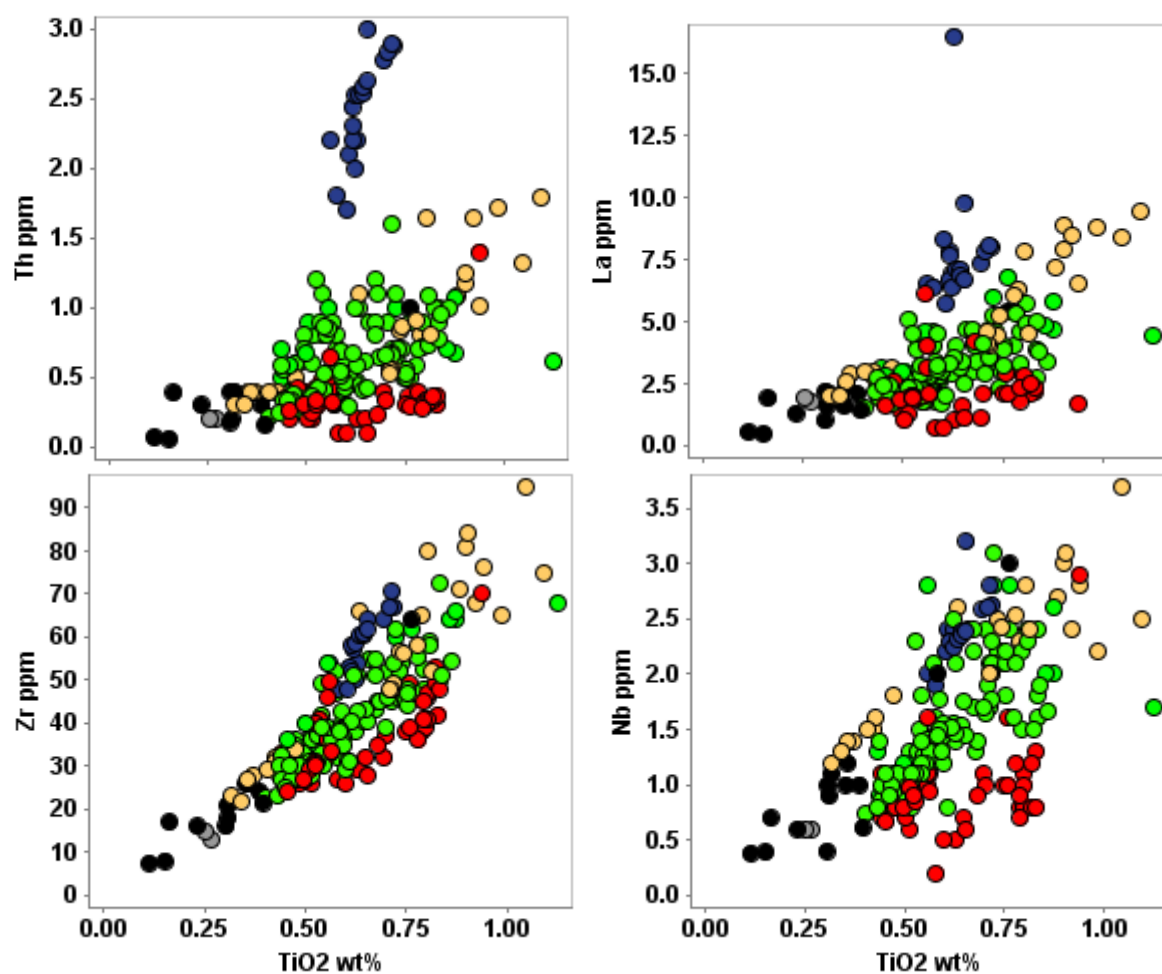


Figure 4.5 incompatible trace element systematics for Unit 2 samples: a) Th vs TiO_2 ; b) La vs TiO_2 ; c) Zr vs TiO_2 ; d) Nb vs TiO_2 . Symbols as per Fig .4.4.

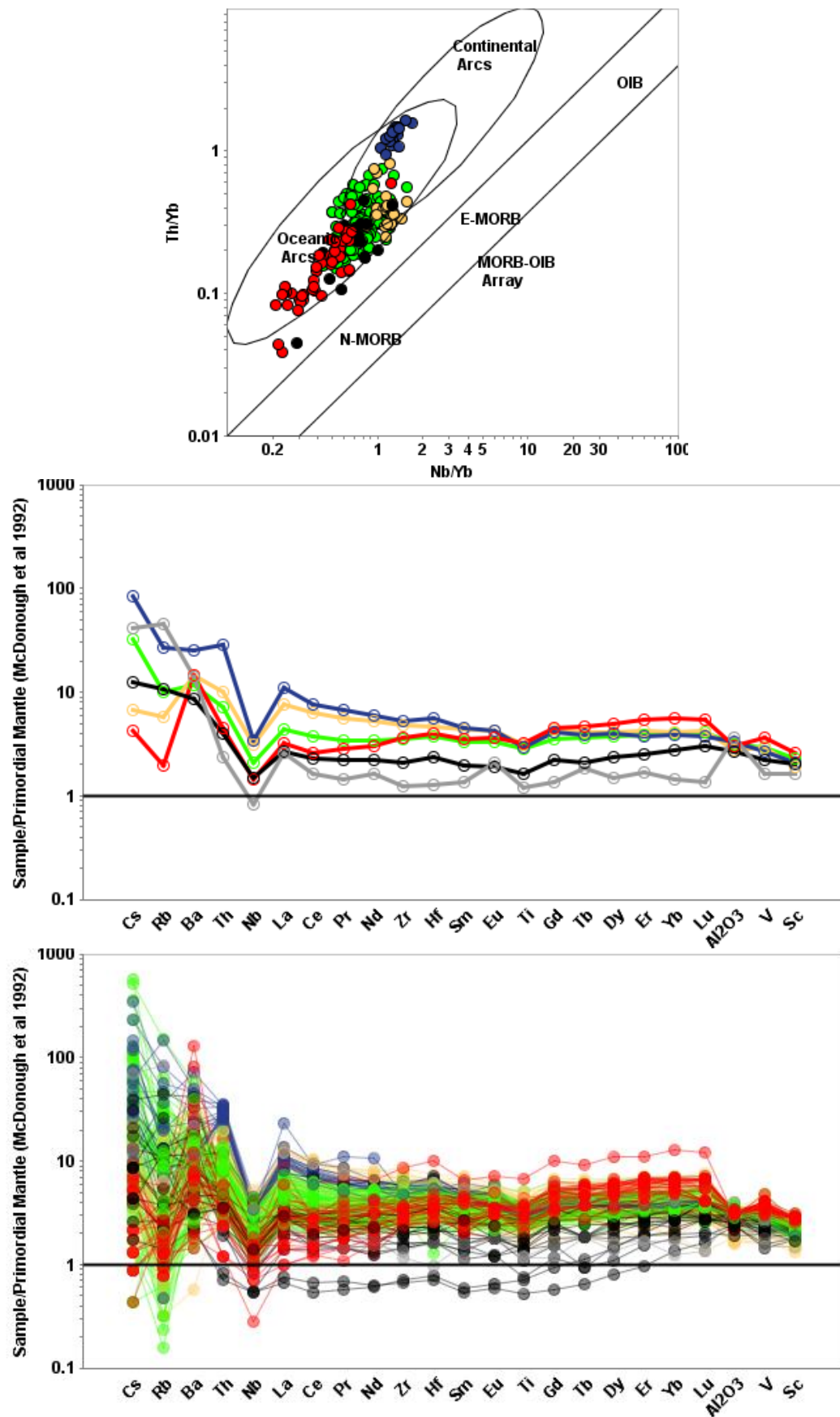


Figure 4.6 a) Th/Yb vs Nb/Yb (after Pearce, 2014) for Unit 2; b) comparison of Unit 2 mantle normalised trace element patterns, averaged for each color group; c) mantle normalised trace element patterns for all samples in Unit 2. Symbols as per Fig 4.4.

4.3.1.3. Unit 3

Unit 3 consists of *c.* 2818–2813 Ma mafic, intermediate and felsic volcanic, volcanoclastic and shallow-level intrusive rocks (such as granophyre) presently assigned to the 2818–2799 Ma Yaloginda Formation (Table 4.1), specifically those with strong tholeiitic affinities. These have currently only been identified in close proximity to large mafic igneous complexes, likely indicating a shared petrogenetic origin. Intrusive rocks assigned to the Meeline Suite, including the Windimurra Igneous Complex, are analogous to the supracrustal rocks of Unit 3 in terms of age, distribution, composition (albeit subject to cumulate effects) and petrogenetic implications (e.g., Ivanic, 2019), although the discussion is limited here to the lesser studied volcanic components.

Compositions of volcanic rocks from the Quinns area (Fig 4.1) are split bimodally between basaltic andesite and high-silica rhyolite (Figs 4.7a,b), whereas a more continuous fractionating series is preserved in the Youanmi Igneous Complex, including basalt, andesite, dacite and rhyolite (Figs 4.7a,b). The vast majority of the Unit 3 dacite–rhyolite samples in the initial dataset used to map their geographic distribution are eliminated from the dataset when the alteration filters using $ASI > 1.1$ and $SiO_2 > 77.5\%$ are applied. It is worth noting that these samples show significant alteration effects in nearly all of the major elements, but their incompatible trace elements remain largely unaffected and can be used to discriminate the samples between the tholeiitic and calc-alkaline intermediate-felsic series. Among the unaltered samples, mantle normalised trace element patterns remain remarkably constant throughout the fractionated range of compositions (Fig 4.8b), with elevated HFSE and HREE concentrations compared to similarly siliceous samples from other units, and very low $(La/Yb)_N$, reflecting a tholeiitic liquid line of descent dominated by crystallization of olivine, pyroxene and plagioclase. Late crystallization of magnetite-ilmenite (and possibly rutile) is indicated by the rapid decrease in Fe_2O_3 and TiO_2 at approximately 70% SiO_2 (Figs 4.7d, e) and by the presence of Ti-V-rich magnetitite layers in adjacent layered intrusions, consistent with reduced magma conditions.

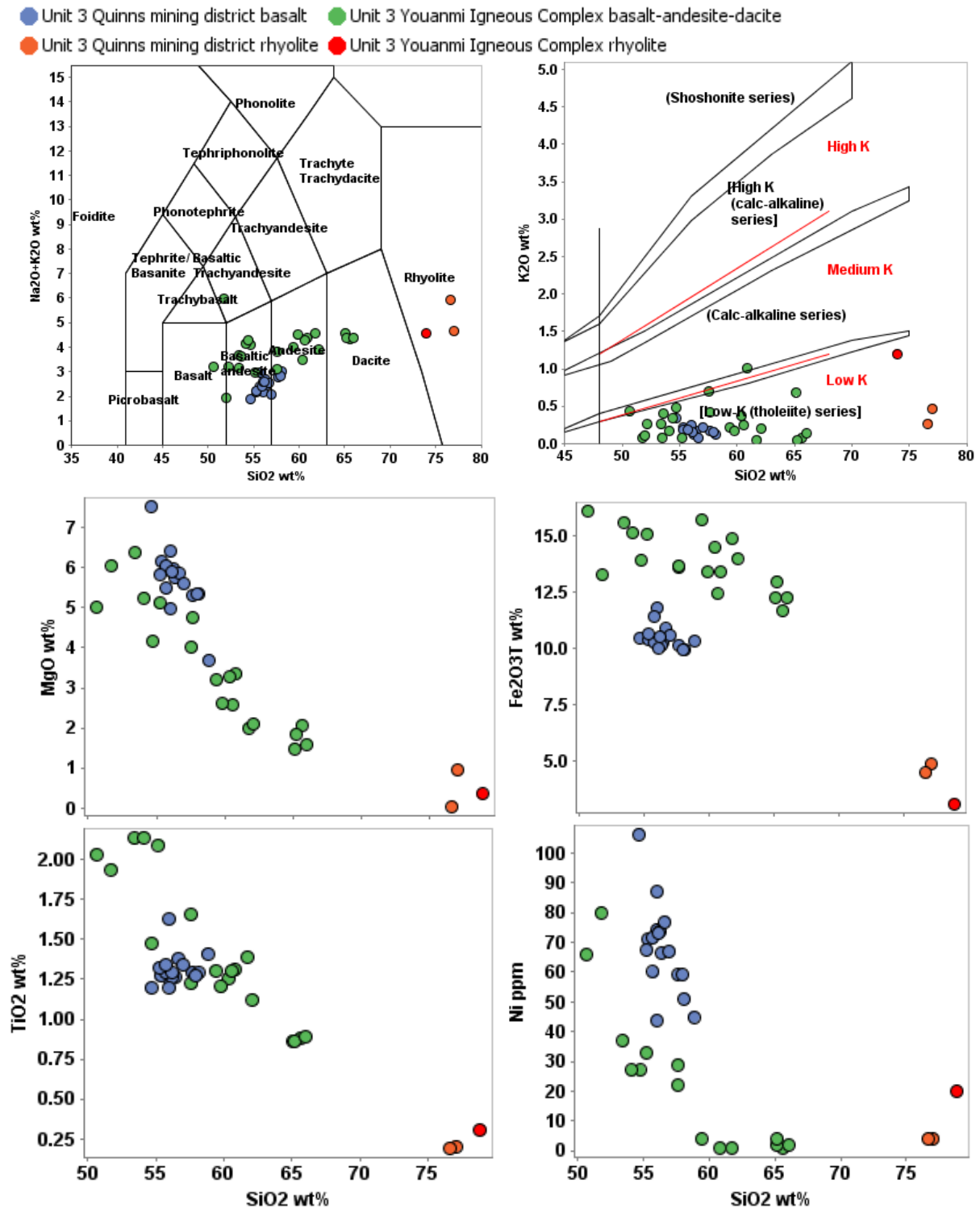


Figure 4.7. Major and compatible trace element variation diagrams for Unit 3 samples: a) Total alkalis vs SiO₂; b) K₂O vs SiO₂; c) MgO vs SiO₂; d) Fe₂O₃ vs SiO₂; e) TiO₂ vs SiO₂; f) Ni vs SiO₂.

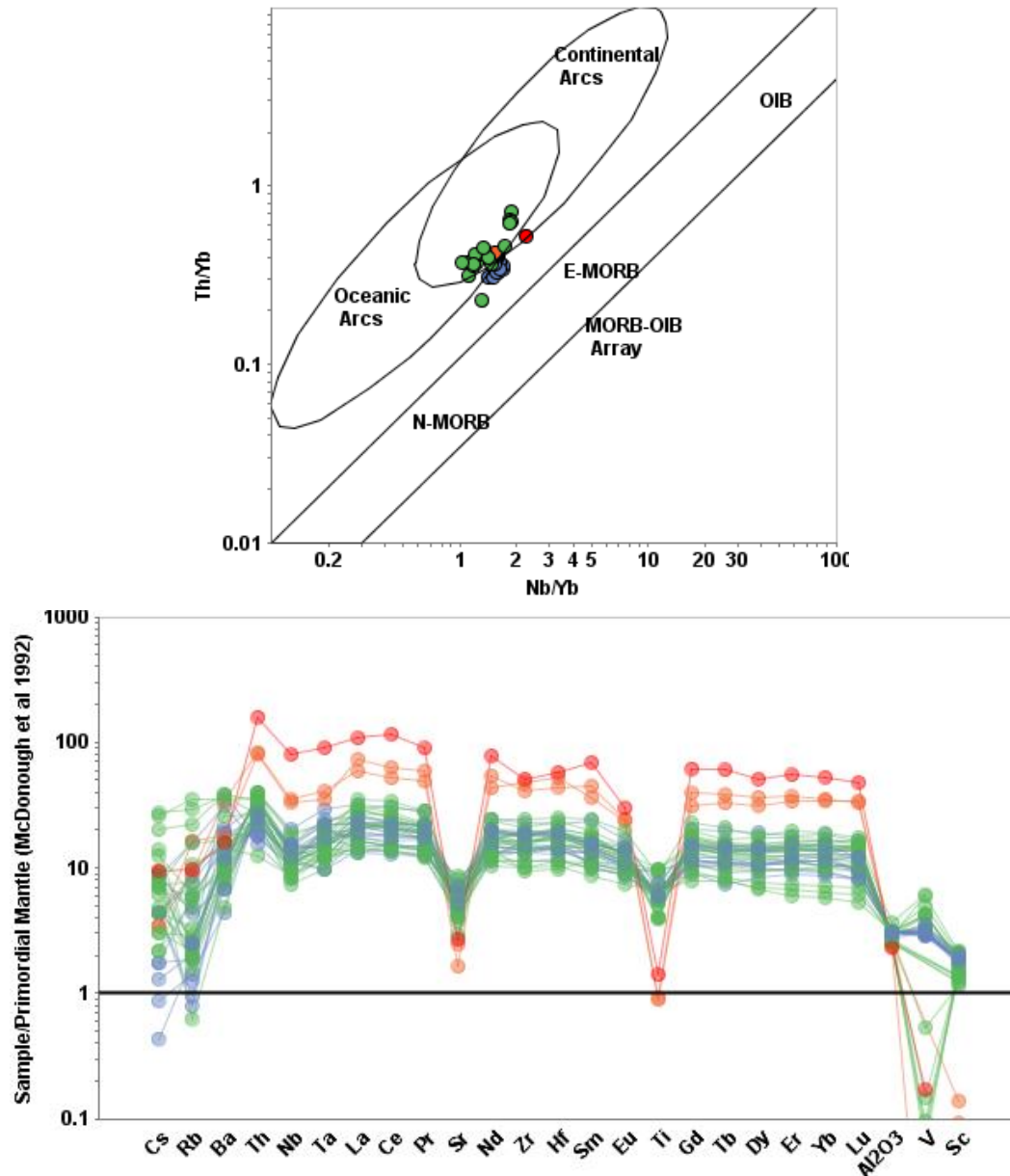


Figure 4.8 a) Th/Yb vs Nb/Yb (after Pearce, 2014) for Unit 3; b) mantle normalised trace element patterns for Unit 3. Symbols as per Fig 4.7

4.3.1.4. Unit 4

Unit 4 consists of predominantly 2815–2799 Ma felsic volcanic rocks assigned to the Yaloginda Formation in the Meekatharra–Karajong belt, and in the Mount Magnet and Yalgoo areas. The depositional ages of these felsic volcanic rocks have been determined from several samples in the Meekatharra area and range between 2815 and 2799 Ma (GSWA, 2021). Reported ages for the Mount Kenneth Suite intrusions also range between 2815 and 2803 Ma (GSWA, 2021) and, with similar chemical characteristics (Electronic appendix 1.1), they may be a sub-volcanic equivalent to the Yaloginda Formation. Porphyritic-textured examples are commonly amygdular, typically with fine

groundmass and euhedral phenocrysts of plagioclase and clinopyroxene (\pm hornblende), commonly occurring together as glomerophenocrysts, with accessory oxide minerals. Fragmental rocks, mostly volcanic breccias or hyaloclastites with lesser tuffs in high-Si units, contain angular clasts of the same porphyritic textured material and are chemically indistinguishable in most instances. Porphyritic textured volcanic and sub-volcanic rocks span a broad range of compositions and based on the IUGS total alkali vs SiO_2 scheme (Fig 4.9a), can be classified as basaltic andesite (rarely basalt), andesite, dacite, and locally rhyolite (hence BADR series). Most samples follow a calc-alkaline line of liquid descent (Fig 4.9c) and samples containing c. 60 wt% SiO_2 have Mg-numbers ≥ 60 , and Cr and Ni concentrations ≥ 100 ppm (Figs 4.9d,i,j), meeting Shirey and Hanson's (1984) definition for 'sanukitoid' i.e., silica-oversaturated melts with high Mg-numbers, high Ni, Cr and LILE abundances.

Samples from the Meekatharra belt have extended trace element patterns that show enrichments in LILE and LREE-MREE, and relatively flat HREE (Fig 4.10c). Samples from the Mount Magnet area are more siliceous than the Meekatharra samples (63–70 wt% SiO_2) but follow a similar liquid line of descent to the Meekatharra samples (Fig 4.9c-j), with similar enrichments in LILE and LREE-MREE but depletion through the HREEs (Fig 4.10e), consistent with hornblende fractionation from a parent melt that was originally similar in composition to the Meekatharra Unit 4 samples.

A small group of samples from the Meekatharra area that have ≥ 9 wt% MgO (samples 227201-227209) contain abundant pyroxene phenocrysts (now altered to amphibole) and therefore do not reflect liquid compositions. Another small group of samples from immediately east of Mount Magnet (Fig 4; known locally as Hybrazil) also have very primitive compositions, but have extremely high-Th/Nb (4.10a), and strongly negative Zr-Hf anomalies (4.10f), that Wyman (2019) argued cannot be accounted for by contamination of non-arc mantle magmas with evolved Murchison crust. Although the Hybrazil volcanic rocks likely inherited high Th/Nb and negative Zr-Hf from their mantle source, their ultra-low K_2O concentrations are incompatible with their very high Th concentrations and likely reflects K_2O loss during low-temperature alteration. These samples also have notably lower ϵ_{NdT} than other Yaloginda Formation samples, and the significance of this is not yet understood.

- Unit 4 felsic volcanic rocks from Meekatharra belt
- Unit 4 felsic volcanic rocks from Meekatharra belt with abundant Px phenocrysts
- Unit 4 felsic volcanic rocks from Meekatharra belt with high-Ti-P2O5
- Unit 4 felsic volcanic rocks from Hyabrazil
- Unit 4 felsic volcanic rocks from Mount Magnet
- Unit 4 felsic volcanic rocks from Yalgoo

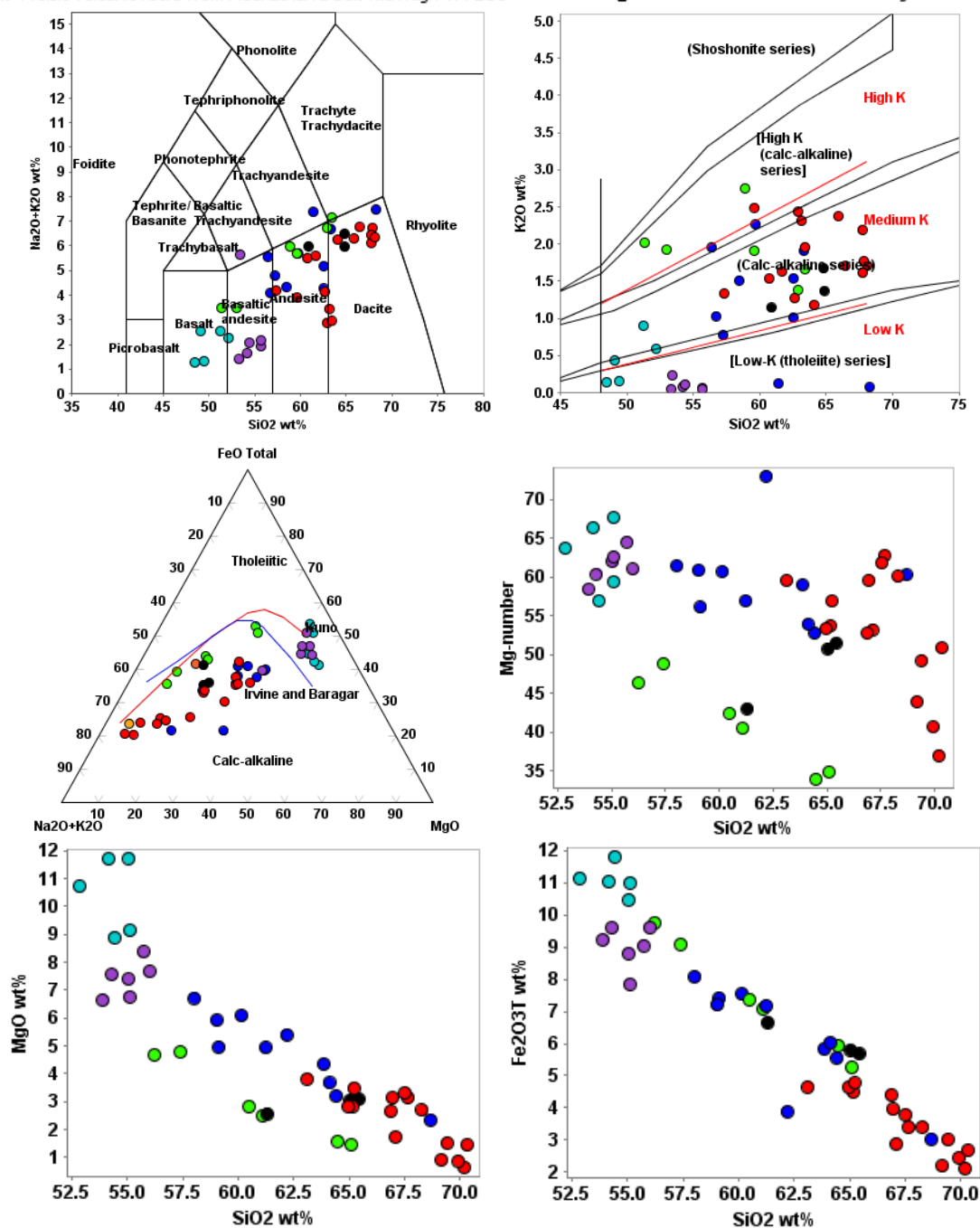


Figure 4.9. Major and compatible trace element variation diagrams for Unit 4 samples: a) Total alkalis vs SiO₂; b) K₂O vs SiO₂; c) AFM ternary diagram (total Fe); d) Mg-number vs SiO₂; e) MgO vs SiO₂; f) Fe₂O₃ vs SiO₂. Continued.

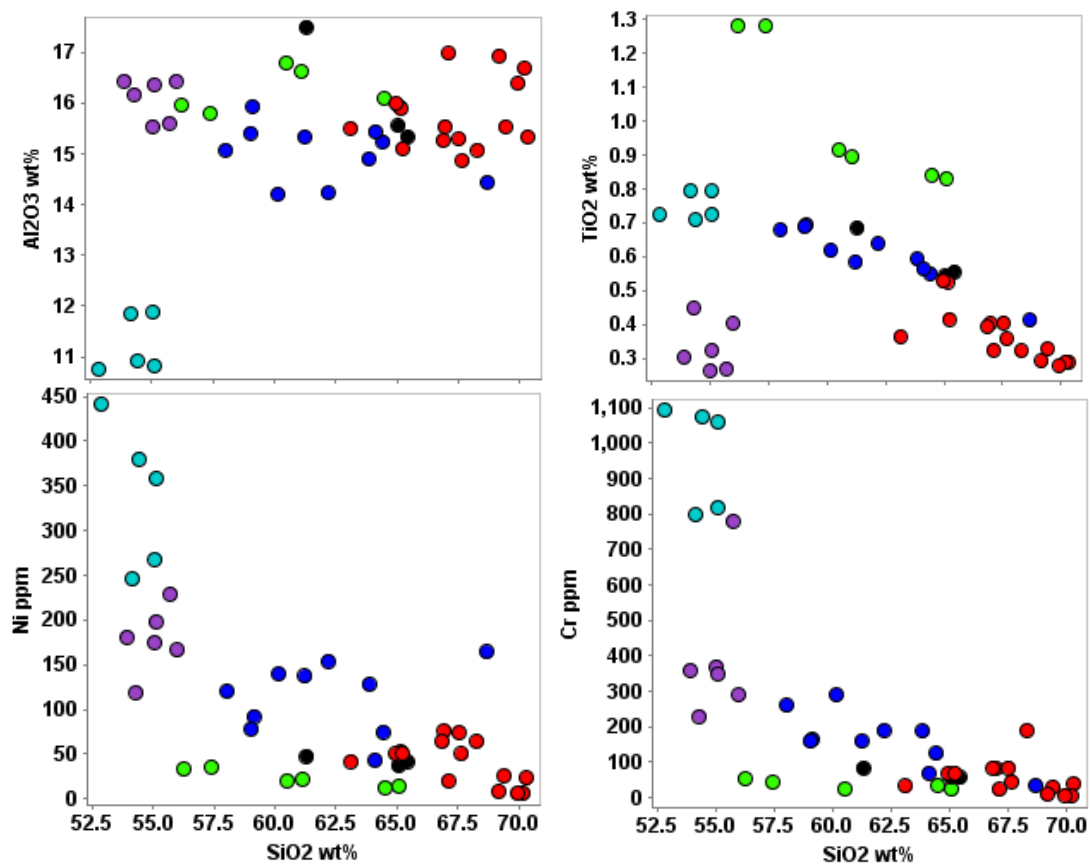


Figure 4.9 Continued. g) Al₂O₃ vs SiO₂; h) TiO₂ vs SiO₂; i) Ni vs SiO₂; j) Cr vs SiO₂.

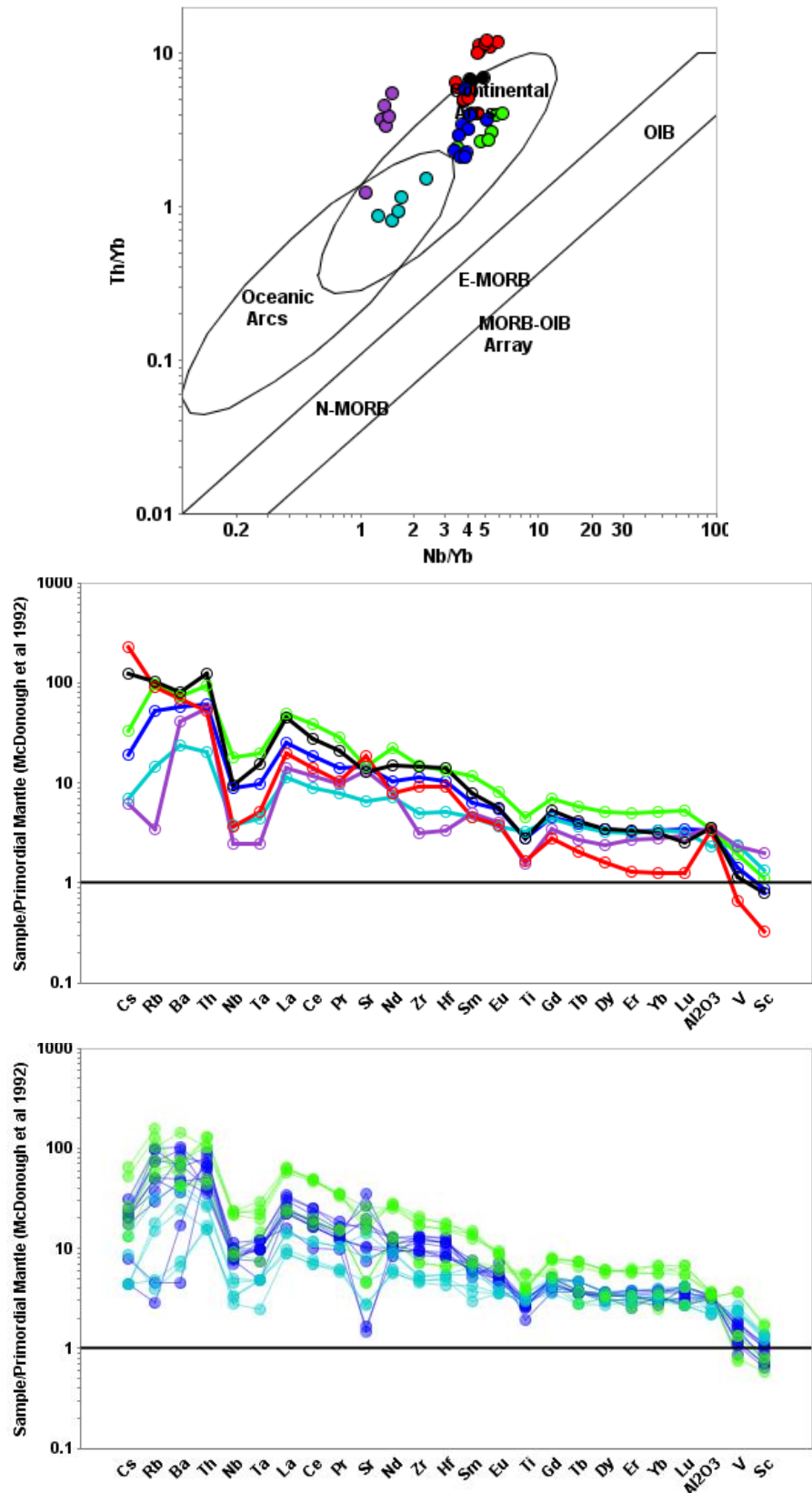


Figure 4.10 Incompatible trace element plots for Unit 4 a) Th/Yb vs Nb/Yb (after Pearce, 2014); b) comparison of mantle normalised trace element pattern averages for each Unit 4 locality; c) mantle normalised trace element patterns for Unit 3 samples from the Meekatharra area. Symbols as per Fig 4.9. Continued.

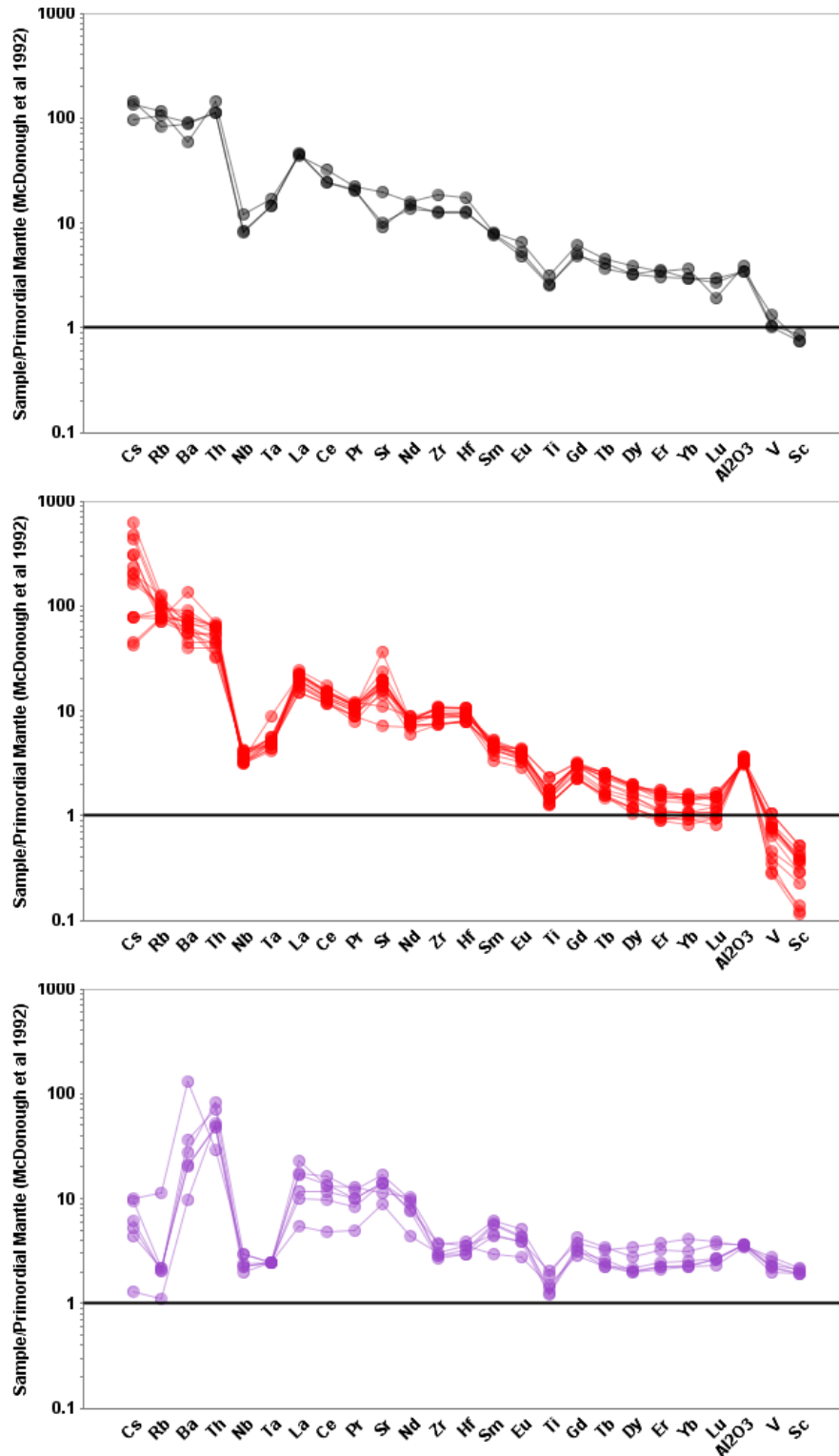


Figure 4.10 continued d) mantle normalised trace element patterns for Unit 4 samples from the Yalgoo area; e) mantle normalised trace element patterns for Unit 4 samples from the Saturn and Morning Star deposits in the Mount Magnet area; f) mantle normalised trace element patterns for Unit 4 samples from the Hybrazil area immediately east of Mount Magnet. Symbols as per Fig 4.9.

4.3.1.5. Unit 5

Unit 5 consists of *c.* 2800 Ma mafic intrusive rocks, predominantly hornblende-gabbros, in the Narndee and Fields Find igneous complexes (assigned by GSWA to the Boodanoo Suite) and fine-grained mafic rocks in the Warriedar Hill region (Fig 4.1) which, based on strikingly similar compositions, are likely to be the volcanic equivalent to the underlying hornblende-gabbros in Fields Find Igneous Complex (Fig 4.1). Undated hornblende-gabbroic rocks from Mount Magnet (Alaskan-type intrusions of Wyman, 2019) also share these trace element patterns and are tentatively assigned here to Unit 5.

Gabbroic samples at Narndee include hornblende peridotite and hornblende norite, which both contain up to 8% modal igneous hornblende, generally as oikocrysts (Ivanic, 2019), indicating water-rich parental magma. Compositions for most samples show significant cumulate effects, such as plagioclase accumulation (high $\text{Al}_2\text{O}_3/\text{TiO}_2$, positive Sr and Eu anomalies). Several of the fresher hornblende rich samples show strongly negative Zr-Hf anomalies (low Zr/Zr^* ; Fig 4.11h). Gabbros from Warriedar Hill, Fields Find and Mount Magnet, also contain abundant hornblende, but as phenocrysts, and lack evidence for plagioclase accumulation. A compositional break between 12.5 and 17 wt% MgO is interpreted to separate olivine + hornblende cumulates from gabbroic and basaltic rocks that more closely reflect their parental magma compositions. Trace element patterns are very similar between the cumulates and lower-Mg gabbros and basalts and show ubiquitous negative Nb(-Ta) and Zr-Hf anomalies and HREEs are depleted relative to LREE-MREEs (Fig 4.12c, d). Wyman (2019) described these rocks as Alaskan-type magmas which were attributed to melting of subduction modified sub-cratonic mantle.

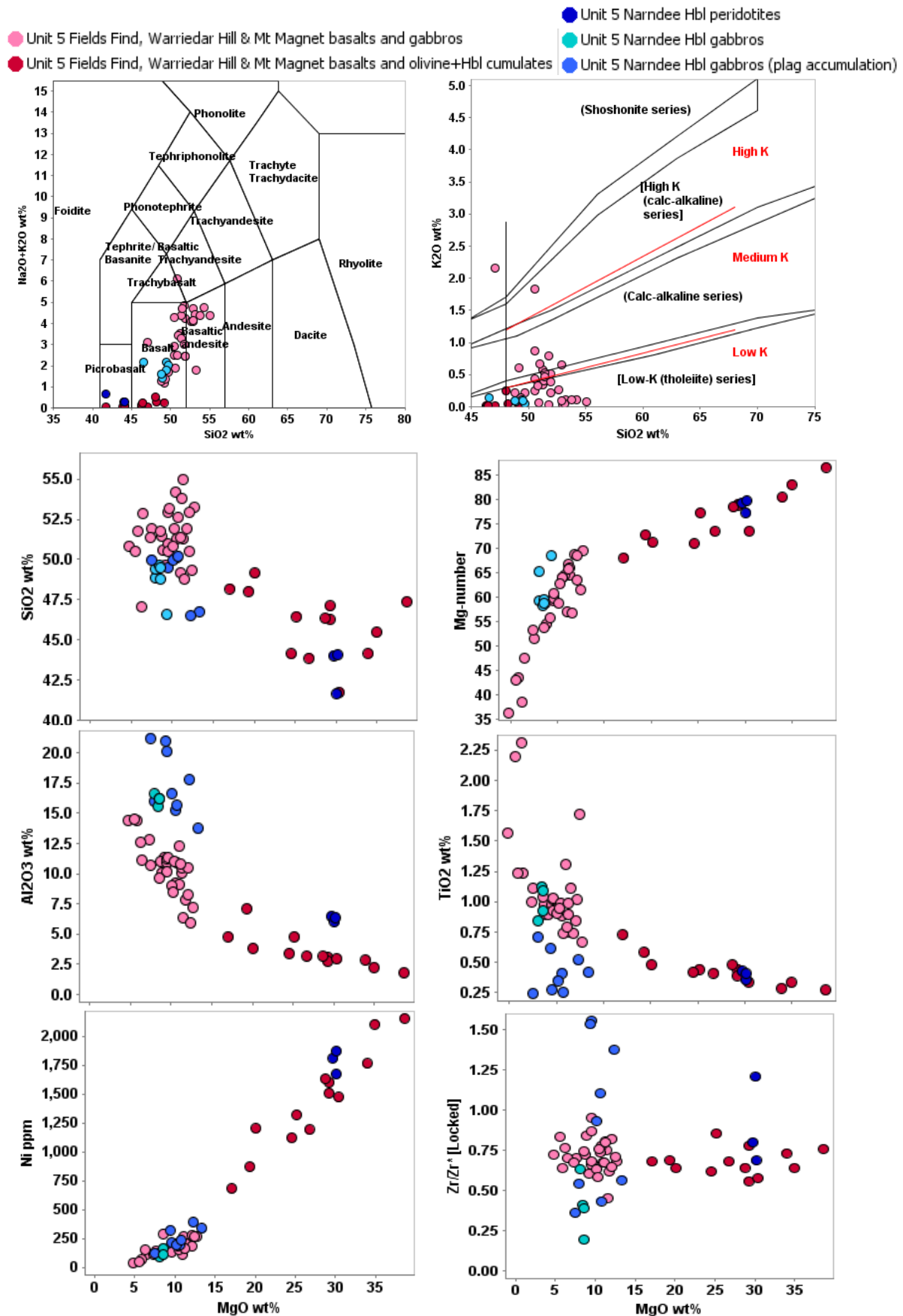


Figure 4.11. Major and compatible trace element variation diagrams for Unit 5 samples: a) Total alkalis vs SiO_2 ; b) K_2O vs SiO_2 ; c) SiO_2 vs MgO ; d) Mg-number vs MgO ; e) Al_2O_3 vs MgO ; f) TiO_2 vs MgO ; g) Ni vs MgO ; h) Zr/Zr^* vs MgO .

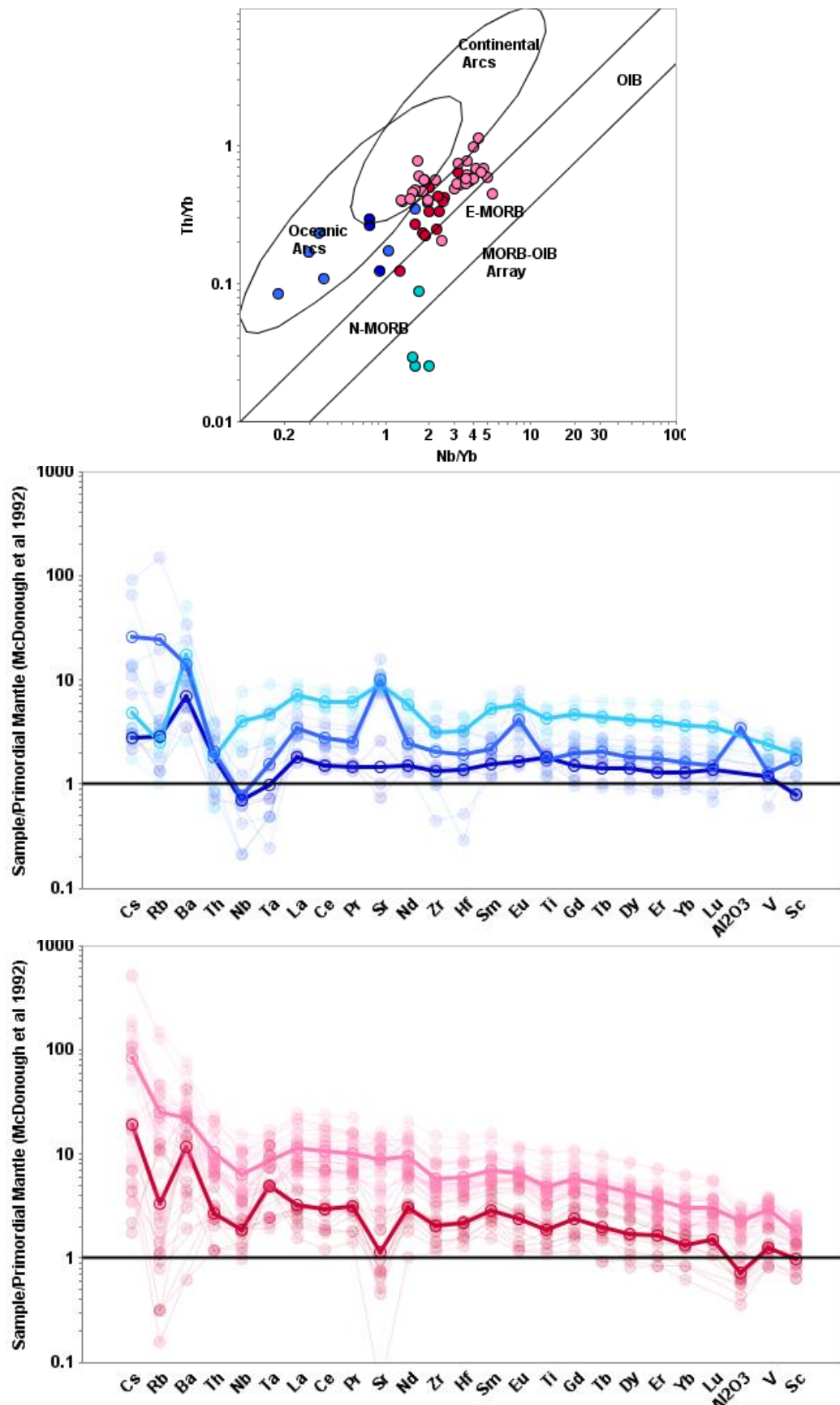


Figure 4.12 Incompatible trace element plots for Unit 5 a) Th/Yb vs Nb/Yb (after Pearce, 2014); b) mantle normalised trace element patterns for Unit 5 samples from the Narndee Igneous Complex; c) mantle normalised trace element patterns for Unit 5 samples from the Fields Find, Warriear Hill and Mount Magnet areas. Symbols as per Fig 4.11. Averages for trace element patterns of each grouping shown as bold lines.

4.3.1.6. Unit 6

Unit 6 consists of *c.* 2790 Ma mafic-intermediate volcanic rocks assigned to the Meekatharra Formation in the Meekatharra-Karrajong belt. Their depositional age is constrained between that of the underlying 2799 ± 2 Ma felsic volcanoclastic rocks in the Meekatharra area, and that of intrusions of 2787–2782 Ma granitic rocks in the Murrouli Range (Fig 4.1). The chemical characteristics of mafic volcanic rocks in Unit 6 have been described in a previous study of their type locality in the Meekatharra area (Lowrey *et al.*, 2019). Rocks with similar compositions and textures have since been identified, though in smaller volumes, at similar stratigraphic levels during recent field studies of the Yalgoo and Dalgaranga areas (Fig 4.1; Electronic Appendix 1.1). Lowrey *et al.*, (2019) described four chemical sub-units that are grouped here as Unit 6: (1) a siliceous high-Mg basalt with moderate Th-LILE-LREE enriched trace element patterns, and flat MREE-HREE patterns (Lordy Basalt Member; Fig 4.14c); (2) a low-Ti siliceous high-Mg basalt with boninite-like (concave-shaped) trace element patterns (Bassetts Volcanic Member; Fig 4.14d); (3) a low-Th tholeiitic basalt with weakly depleted LREEs and flat MREE-HREE patterns (Stockyard Basalt Member; Fig 4.14e); and, (4) a siliceous high-Mg basalt with more strongly enriched Th-LILE-LREE-MREE enriched trace element patterns (Bundle Volcanic Member; Fig 4.14f). Lowrey *et al.* (2019) concluded that these interlayered siliceous high-Mg basalts, boninite-like rocks and tholeiitic basalts were consistent with melts derived from metasomatised lithospheric mantle and upwelling asthenosphere.

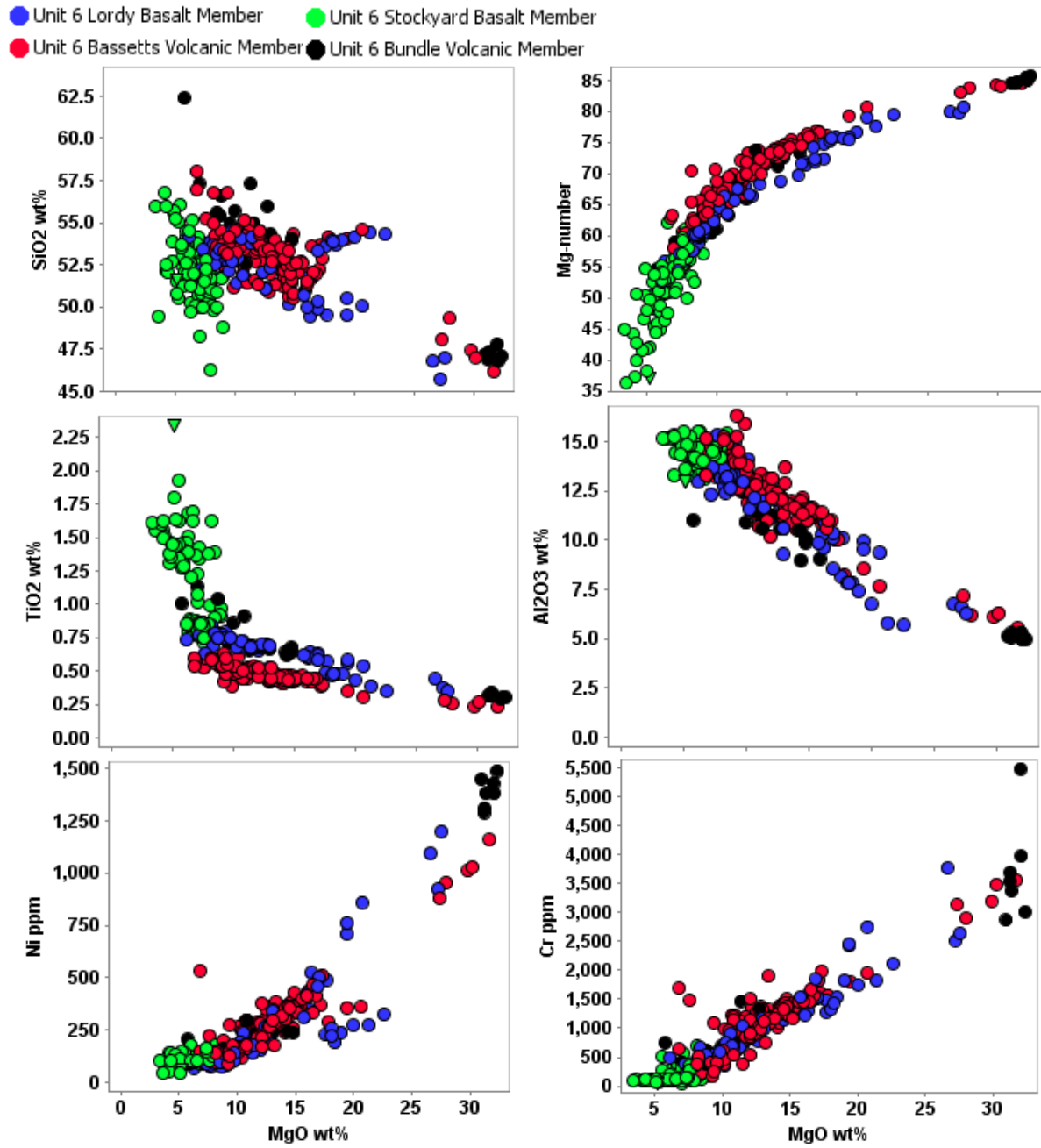


Figure 4.13. Major and compatible trace element variation diagrams for Unit 6 samples: a) SiO₂ vs MgO; b) Mg-number vs MgO; c) Al₂O₃ vs MgO; d) TiO₂ vs MgO; e) Ni vs MgO; f) Cr vs MgO.

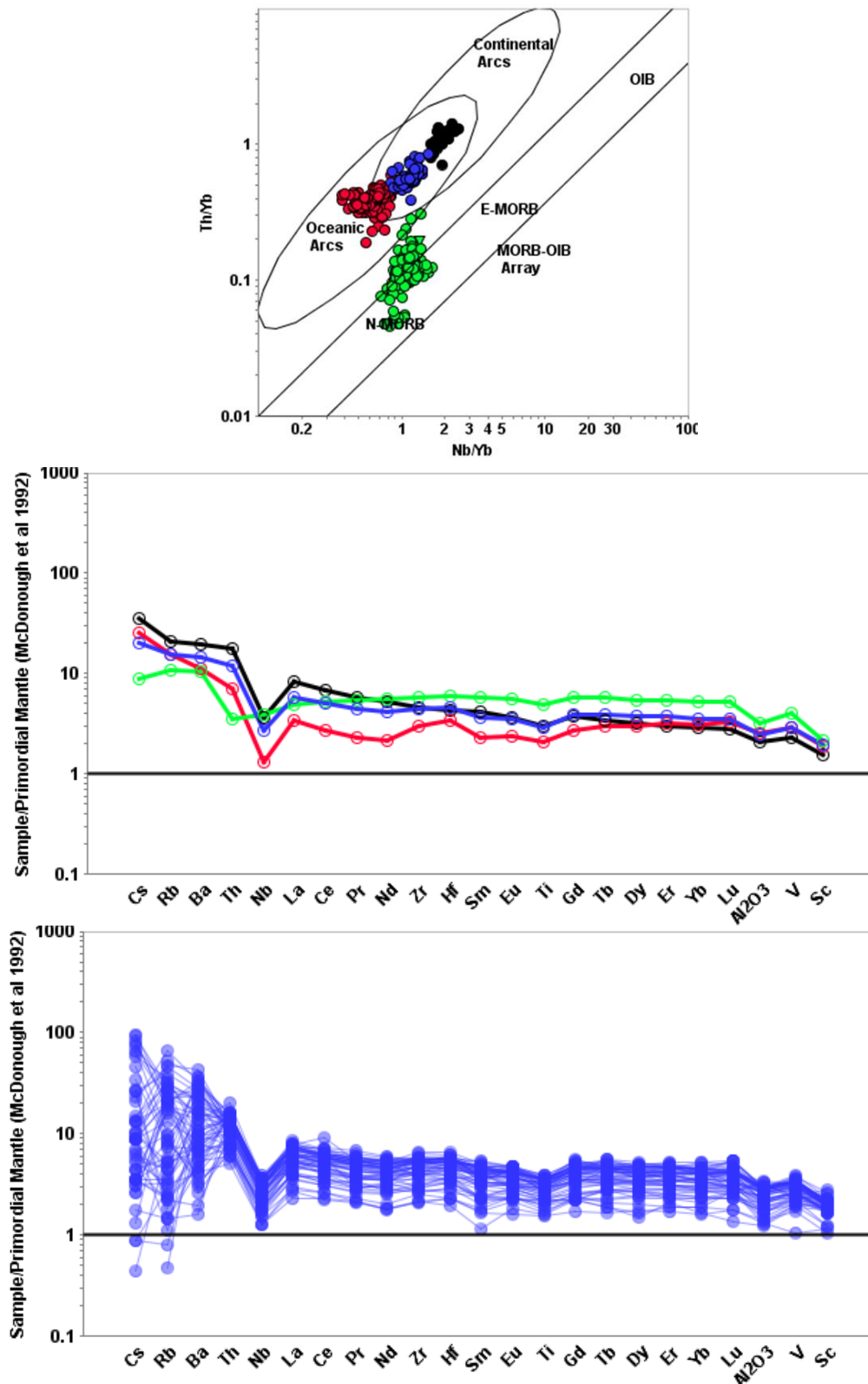
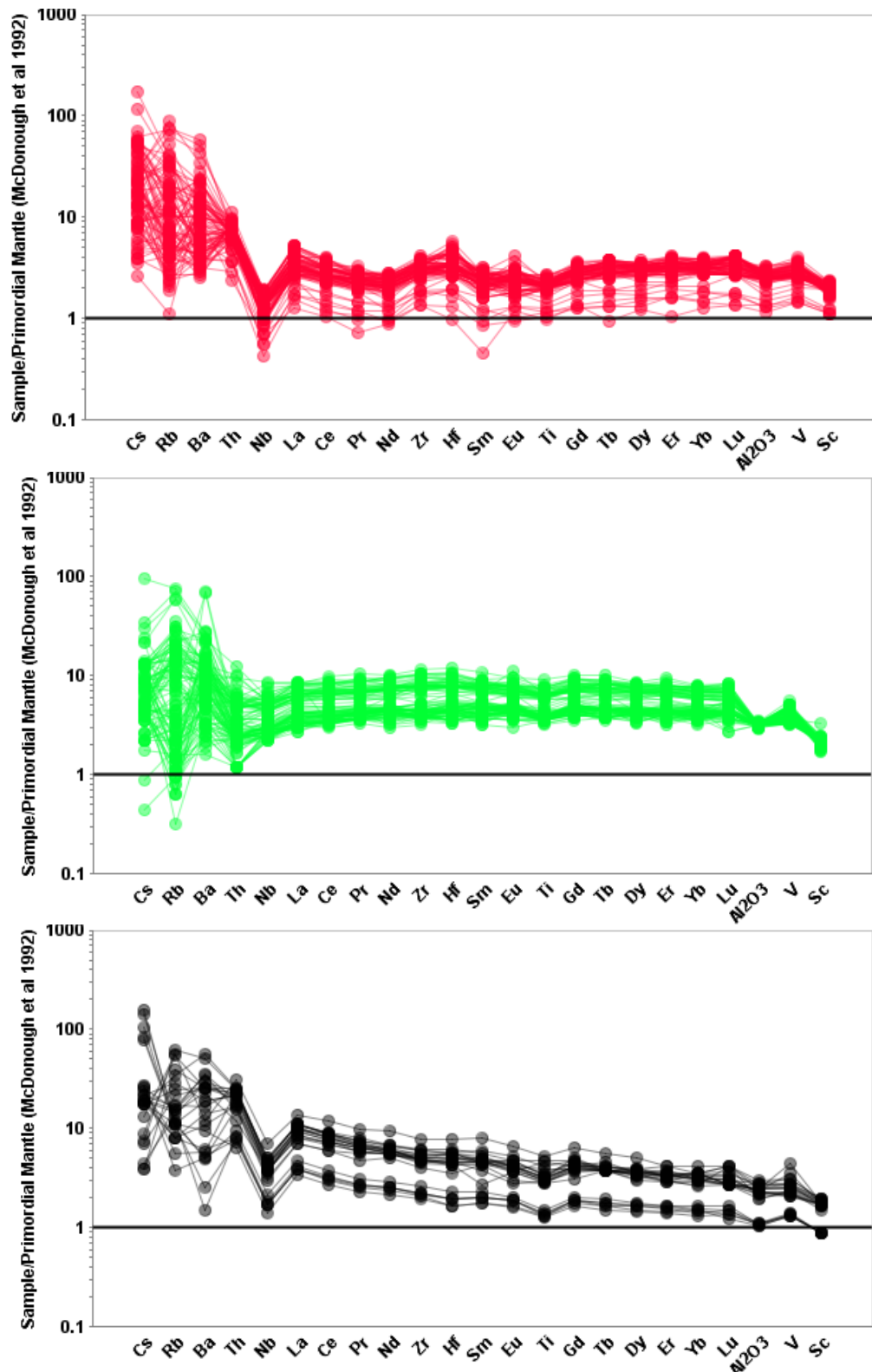


Figure 4.14 Incompatible trace element plots for Unit 6 a) Th/Yb vs Nb/Yb (after Pearce, 2014); b) comparison of mantle normalised trace element pattern averages for each Unit 6 sub-unit; c) mantle normalised trace element patterns for the Lordy Basalt Member. Symbols as per Fig 4.13. Continued



4.3.1.7. Unit 7

Unit 7 consists of *c.* 2793 Ma predominantly mafic volcanic rocks, with lesser andesitic to rhyolitic compositions, assigned to the Meekatharra Formation. Mafic volcanic rocks in Unit 7 are underlain by a volcanic sandstone in the Yalgoo area with a maximum depositional age of 2793 ± 8 Ma and intercalated with a 2793 ± 8 Ma rhyolite in the Gullewa area (GSWA, 2021). These dated felsic rocks and other Unit 7 samples with $\geq 60\%$ SiO₂ have trace element patterns that are similar to the main population of associated mafic volcanic rocks, but at higher overall concentrations, indicating that they have evolved from a shared parental magma predominantly by low-pressure fractional crystallization, involving mainly olivine and clinopyroxene.

Unit 7 samples have trace element patterns that are strongly LREE-enriched, with strongly negative Nb-Ta anomalies and relatively constant Th/Nb ratios (e.g., 0.85 ± 0.2 at Gullewa, 1.05 ± 0.1 at Yalgoo, 1.04 ± 0.15 at Ryansville), negligible to weakly positive Zr-Hf anomalies (Zr/Zr^* 1.12 ± 0.05 at Gullewa, 0.98 ± 0.09 at Yalgoo, 0.99 ± 0.07 at Ryansville) with fractionated HREEs ($[Gd/Yb]_{PM}$ 1.26 ± 0.11 at Gullewa, 1.22 ± 0.15 at Yalgoo, 1.29 ± 0.15 at Ryansville).

● Unit 7 siliceous high-Mg basalt ● Unit 7 andesite-dacite-rhyolite

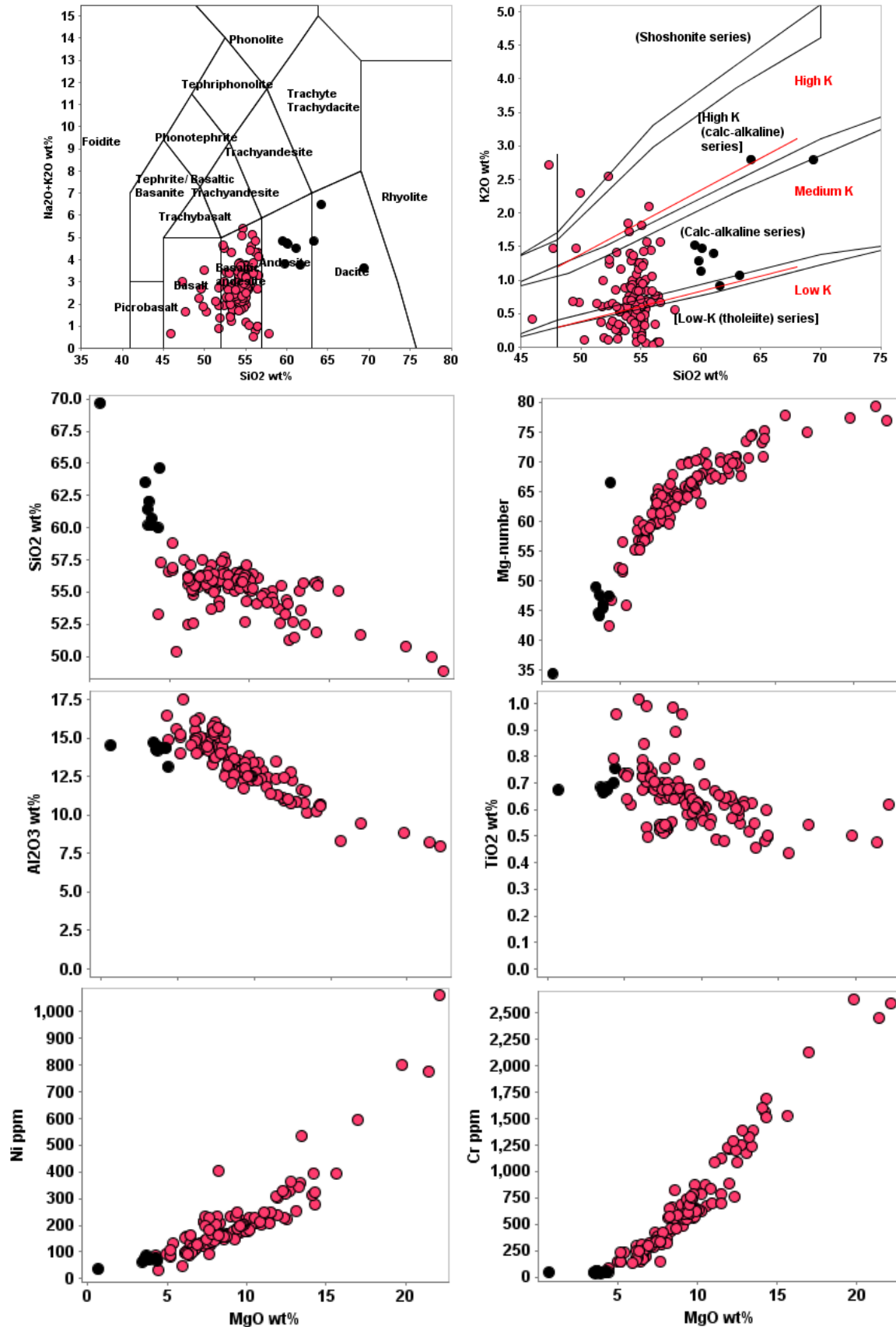


Figure 4.15. Major and compatible trace element variation diagrams for Unit 7 samples: a) Total alkalis vs SiO₂; b) K₂O vs SiO₂; c) SiO₂ vs MgO; d) Mg-number vs MgO; e) Al₂O₃ vs MgO; f) TiO₂ vs MgO; g) Ni vs MgO; h) Cr vs MgO.

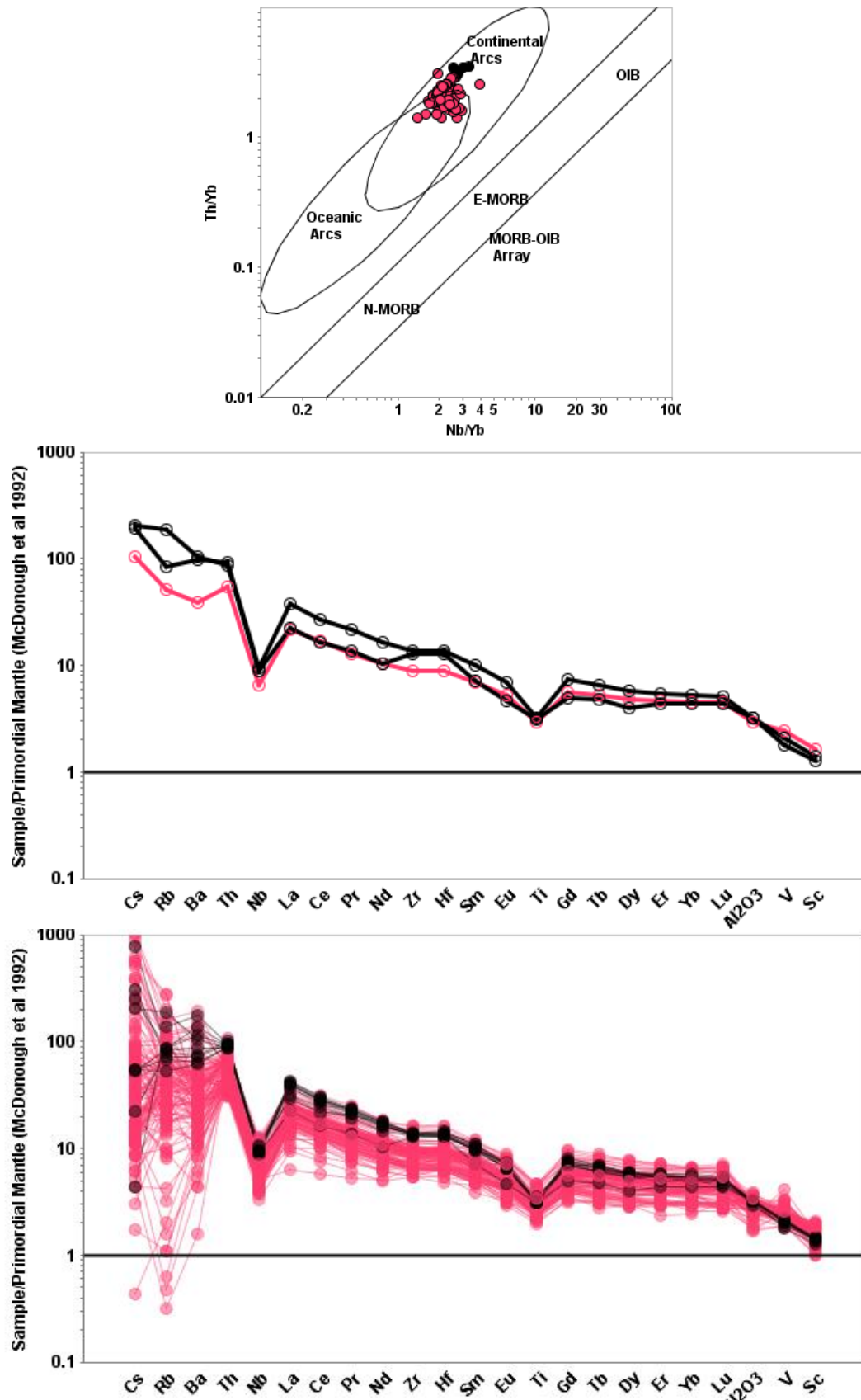


Figure 4.16 Incompatible trace element plots for Unit 7 a) Th/Yb vs Nb/Yb (after Pearce, 2014); b) comparison of mantle normalised trace element pattern averages for each mafic and felsic volcanic rocks in Unit 7; c) mantle normalised trace element patterns for all Unit 7 samples. Symbols as per Fig 4.15.

4.3.1.8. Unit 8

Unit 8 consists of a hornblende-bearing granitic unit that comprises several plutons in the Murrouli Range–Reedy area (25km SW of Meekatharra, Fig 4.1). They have been assigned by GSWA to the Cullculli Suite in the formal stratigraphy (Van Kranendonk and Ivanic, 2009), but their 2787–2782 Ma zircon ages are distinctly older than the Cullculli Suite’s dominant zircon age peak at 2761–2746 Ma (Fig 1.2).

These poorly exposed granitic plutons are medium- to coarse-grained and variably hornblende-rich, with mafic enclaves of either hornblende-gabbro or biotite-magnetite-rich diorite. In the Murrouli Range, a 2782 ± 7 Ma porphyritic andesite unit (GSWA, 2021), with similar extended trace element patterns to the hornblende-bearing granite samples of this Unit, is interleaved with tholeiitic basalt assigned to the Meekatharra Formation. It is unclear from the field relationships whether this unit is volcanic, and coeval with the Meekatharra Formation, or a porphyritic dyke related to the plutons.

Compositions in this Unit (n=13) range from 57.0–77 wt% SiO₂ and 5.1–0.2 wt% MgO, although the more siliceous examples (>75 wt% SiO₂) are almost certainly silicified to some extent. Their trace element patterns exhibit a concave inflection between Dy–Lu and mildly positive Zr–Hf anomalies, both of which are likely related to hornblende fractionation. Like Unit 4, the high Mg-numbers, Ni and Cr concentrations of primitive end-member samples in Unit 8 are consistent with Shirey and Hanson’s (1984) definition for sanukitoid, indicating mantle sources were enriched by crustal components.

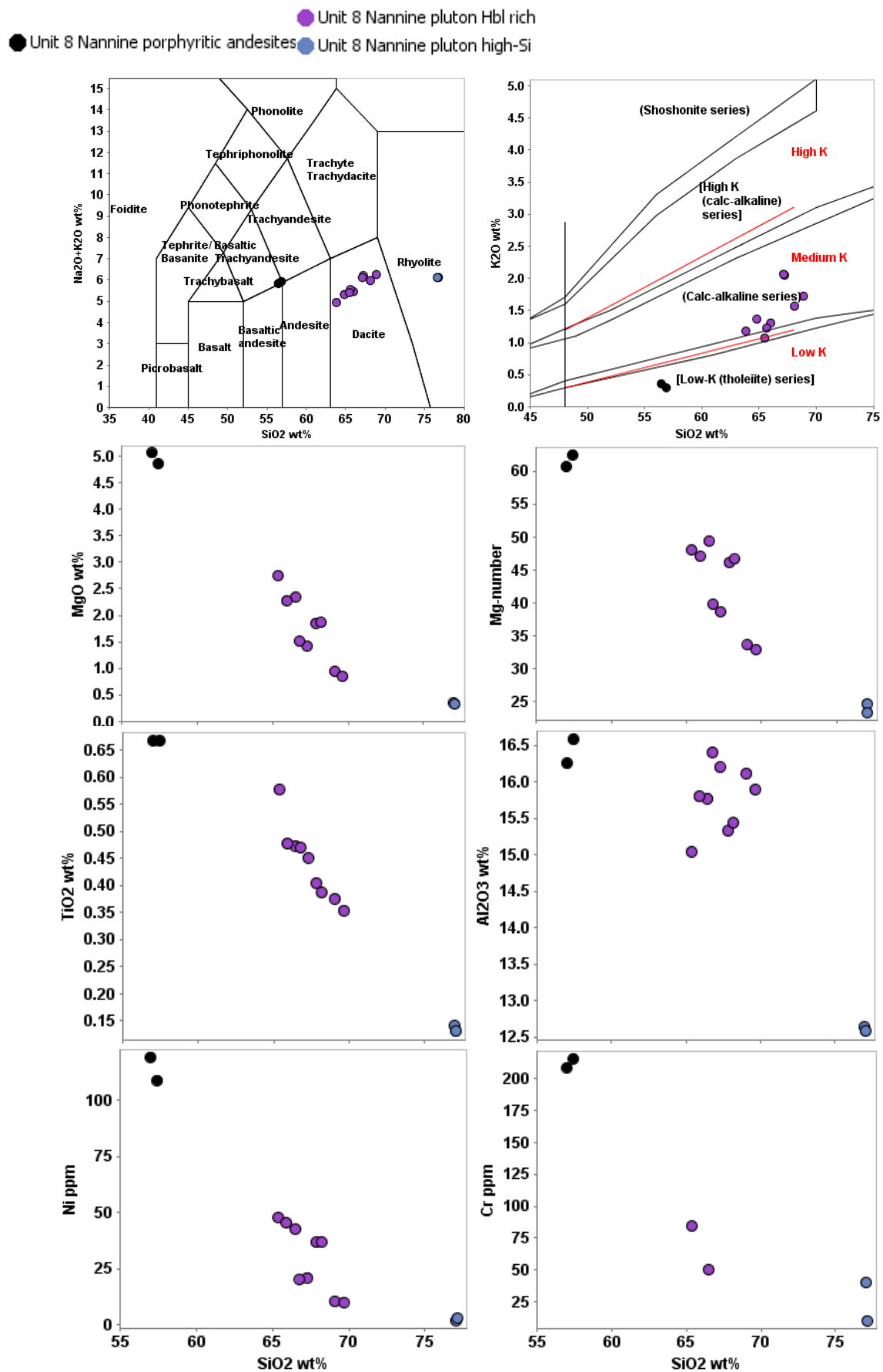


Figure 4.17. Major and compatible trace element variation diagrams for Unit 8 samples: a) Total alkalis vs SiO₂; b) K₂O vs SiO₂; c) MgO vs SiO₂; d) Mg-number vs SiO₂; e) Al₂O₃ vs SiO₂; f) TiO₂ vs SiO₂; g) Ni vs SiO₂; h) Cr vs SiO₂.

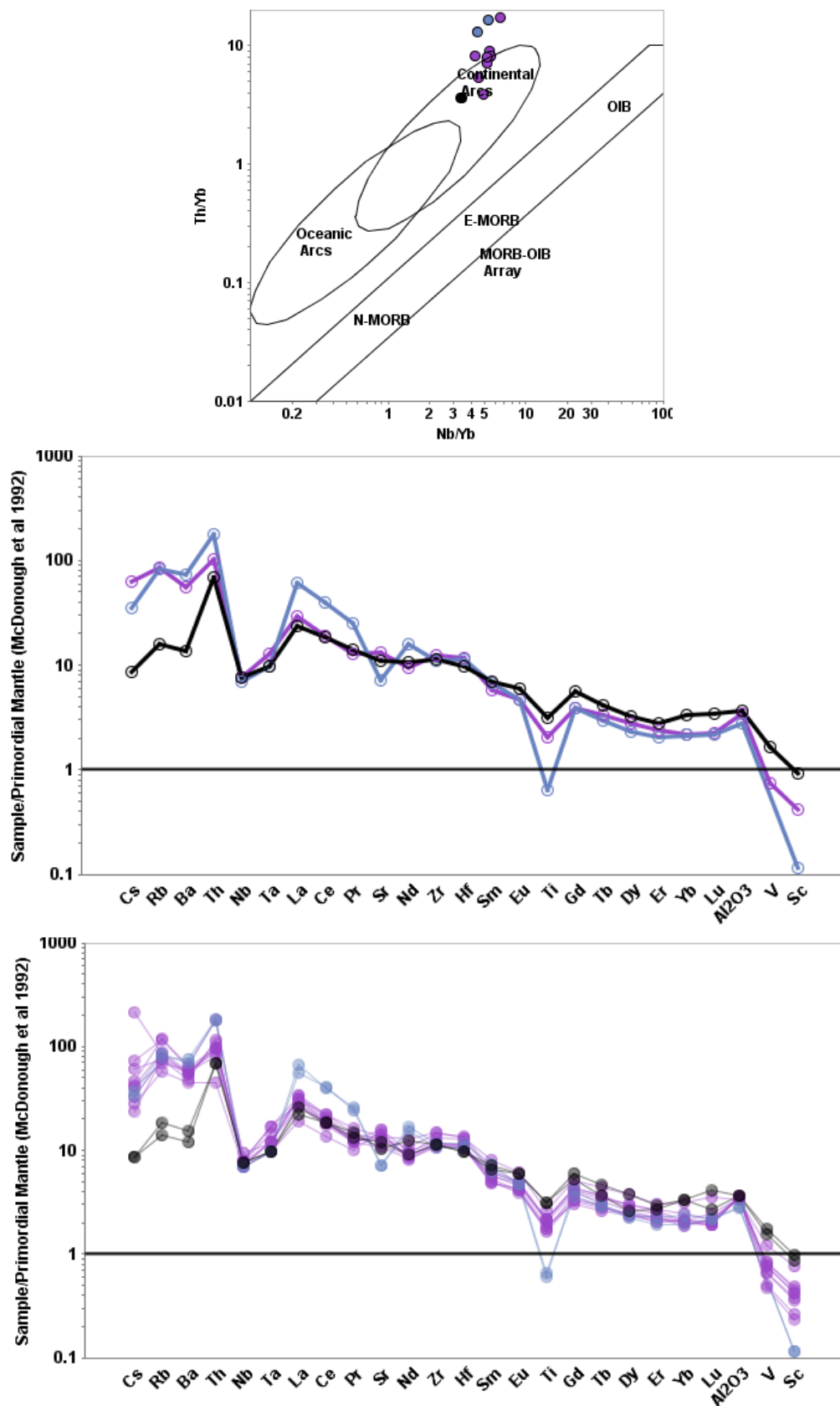


Figure 4.18 Incompatible trace element plots for Unit 8 a) Th/Yb vs Nb/Yb (after Pearce, 2014); b) comparison of mantle normalised trace element pattern averages for each color group; c) mantle normalised trace element patterns for all Unit 8 samples. Symbols as per Fig 4.17.

4.3.2. Magmatic Episode 2

4.3.2.1. Unit 9

Unit 9 consists of *c.* 2760 Ma high-SiO₂ felsic volcanic, volcanoclastic and intrusive rocks in the Eelya mining district (30km NE of Cue, *c.* 2759 Ma; GSWA, 2021; Hayman *et al.*, 2015) and Wattagee Hill area (~5km NW of Cue, *c.* 2761 Ma, Pidgeon and Hallberg, 2000) as well as granodiorite in the Cue area (*c.* 2759 Ma; Pigeon and Hallberg, 2000; described as ‘Cue Tonalite’ by Van Kranendonk and Ivanic, 2009) (Fig 4.1). Previously, Champion and Cassidy (2002) classified the granodiorite in the Cue area in their ‘Mafic granite’ group (their ‘Gem of Cue Clan’) and the higher silica Eelya pluton in their ‘high-HFSE granite’ group (their ‘Nannine Clan’) which GSWA then formally assigned to the Cullculli Suite and Eelya Suite respectively (Van Kranendonk and Ivanic, 2009). Here, based on the striking similarity between trace element patterns of the Cue granodiorites and other Eelya Suite samples, it is suggested that they share a similar magmatic history and are included together in Unit 9. Presently, no Nd isotopic ratios have been determined for Unit 9.

Compared to similarly fractionated high-silica rhyolites in Unit 3, which has a clearly tholeiitic affinity, Unit 9 samples have lower HFSE and MREE-HREE concentrations and are more LILE- and LREE-enriched, resulting in La/Yb that is transitional between the tholeiitic series (Unit 3) and calc-alkalic series (Units 8, 10 and 14) samples. Most incompatible elements (LILE, HFSE, REE) increase together with SiO₂ so that the trace element patterns of more primitive samples are broadly parallel to the more evolved ones, whereas Eu, Sr, Ti and V decrease with increasing SiO₂, resulting in increasingly negative anomalies for these elements. This type of liquid evolution is consistent with fractional crystallization of a mineral assemblage dominated by plagioclase (Sr, Eu anomalies) and ilmenite-magnetite (Ti, V anomalies) from a LILE-enriched magma. However, primitive end-member samples in Unit 9 (e.g., 2760 Ma Cue Tonalite; 66% SiO₂, 2.3% MgO, Mg-number ~48, 40 ppm Ni and Cr) are locally hornblende-rich, indicating these melts contained moderate amounts of H₂O in their parent magma, albeit in insufficient concentrations to promote amphibole crystallization over pyroxene, or to inhibit plagioclase crystallization. The hornblende in the Cue Tonalite is therefore

likely to have crystallized later in the fractionation process, as H₂O concentration increased following significant fractionation of anhydrous minerals (e.g., olivine, pyroxene and plagioclase).

The Peter Well Granodiorite, a pluton in the Eelya mining district, is poorly exposed but includes intensely recrystallised tonalite-granodiorite (\pm biotite \pm hornblende) that locally contains clotty inclusions mafic minerals (biotite-oxide minerals-hornblende). These hydrous minerals may indicate a relatively oxidated parent melt which is inconsistent with a purely tholeiitic fractionation assemblage. Likewise, the granodiorite at Cue is locally hornblende-rich, indicating these melts contained at least moderate amounts of H₂O in their parent magma, despite the chemical evidence for significant plagioclase fractionation (negative Eu-Sr anomalies) and minimal hornblende fractionation (flat and elevated middle-heavy REE patterns).

Based on these compositional and mineralogical characteristics, Unit 9 rocks are considered to be transitional between the calc-alkaline and tholeiitic magma series.

- Unit 9 Cue Hbl-bearing granite
- Unit 9 Eelya granite and felsic volcanic rocks
- Unit 9 Emily Well volcanics

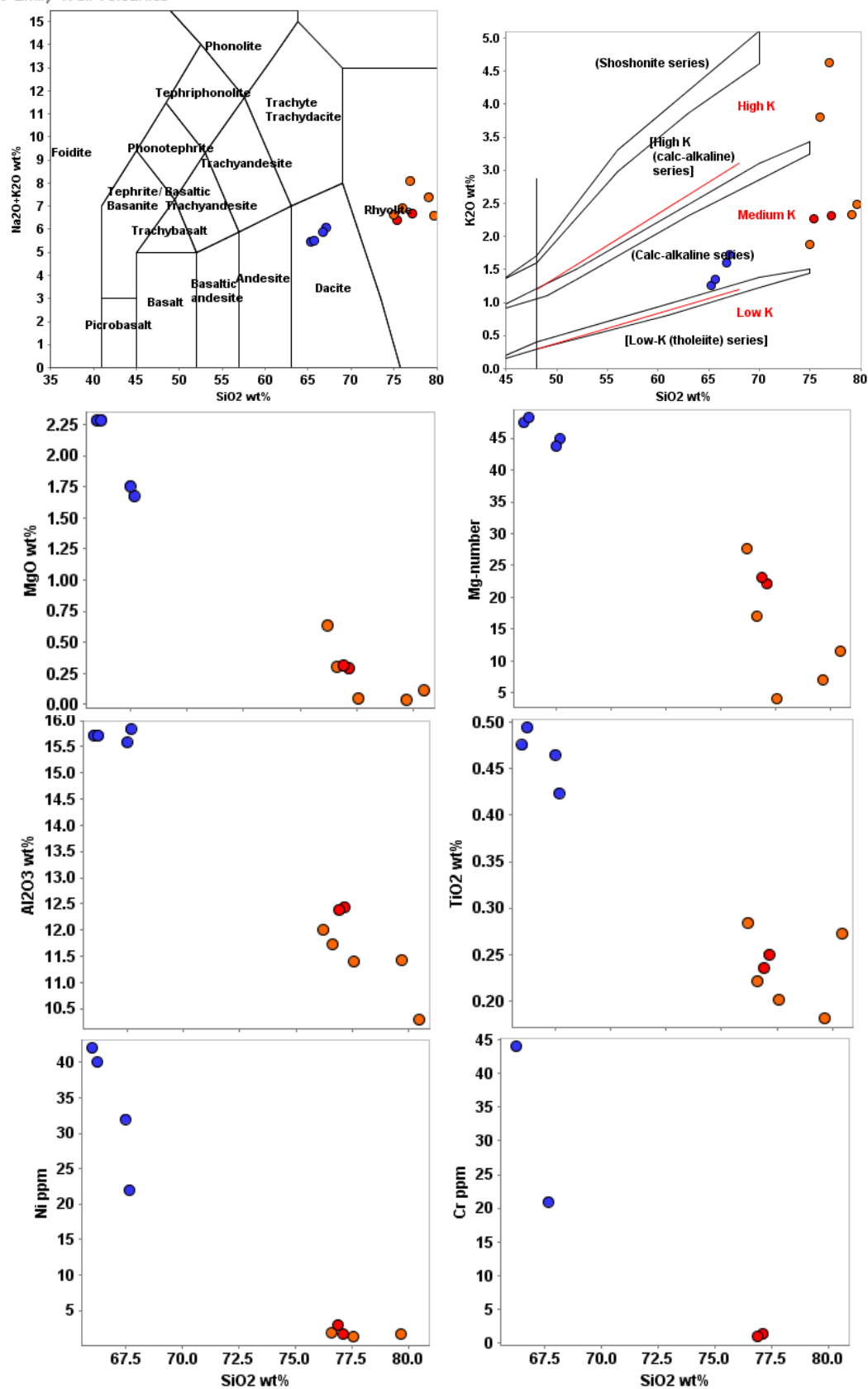


Figure 4.19. Major and compatible trace element variation diagrams for Unit 9 samples: a) Total alkalis vs SiO₂; b) K₂O vs SiO₂; c) MgO vs SiO₂; d) Mg-number vs SiO₂; e) Al₂O₃ vs SiO₂; f) TiO₂ vs SiO₂; g) Ni vs SiO₂; h) Cr vs SiO₂.

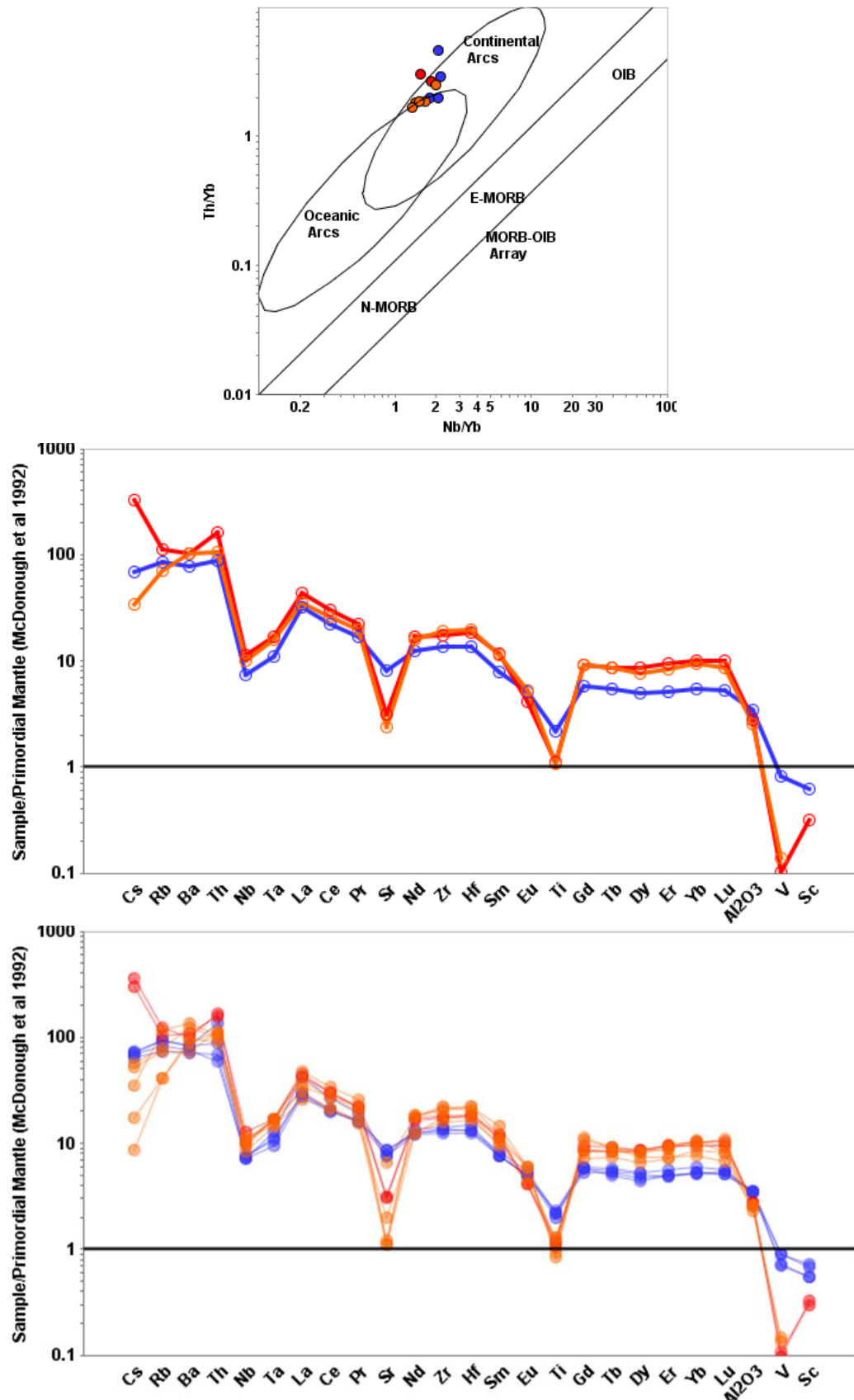


Figure 4.20 Incompatible trace element plots for Unit 9 a) Th/Yb vs Nb/Yb (after Pearce, 2014); b) comparison of mantle normalised trace element pattern averages for each color group; c) mantle normalised trace element patterns for all Unit 9 samples. Symbols as per Fig 4.19.

4.3.2.2. Unit 10

Unit 10 consists of 2761–2746 Ma intermediate to felsic volcanic (and volcanoclastic) rocks (assigned to the Woolgra Andesite Member of the Greensleeves Formation; Van Kranendonk and Ivanic, 2009) and their intrusive equivalents (assigned to the Cullculli Suite; Van Kranendonk and Ivanic, 2009) in the Meekatharra greenstone belt. Three volcanic samples yielded crystallization ages of 2761 ± 6 Ma and 2755 ± 5 Ma (GSWA, 2021) and three porphyritic intrusive rocks yielded crystallization ages of 2760 ± 8 Ma, 2755 ± 6 Ma and 2746 ± 5 Ma (Fletcher and McNaughton, 2002; GSWA, 2021).

Porphyritic textured rocks are commonly amygdular and typically have a fine-grained groundmass with euhedral plagioclase, clinopyroxene and hornblende phenocrysts (commonly as glomerophenocrysts). Fragmental rocks (mostly volcanic breccias or hyaloclastites with lesser tuffs in high-Si units) contain angular clasts of the same porphyritic textured material and are chemically indistinguishable in most instances. Intrusions vary from thin porphyritic dykes and sills to medium- or coarse-grained granitic plutons – the latter commonly contain abundant hornblende and mafic clots of either hornblende-gabbro or biotite-magnetite-rich diorite. On a TAS diagram, compositions define a relatively uninterrupted fractionating series from andesite (57.5 wt% SiO_2 and 4–5 wt% $\text{Na}_2\text{O} + \text{K}_2\text{O}$), through to rhyolite (73 wt% SiO_2 and 7 wt% $\text{Na}_2\text{O} + \text{K}_2\text{O}$) with most compositions in the dacite field (Fig 4.21a). On a plot of SiO_2 versus K_2O , most samples plot in the low-K to moderate-K field, transitional between tholeiitic and calc-alkaline fields (Fig 4.21b). Primitive end-member samples meet Shirey and Hanson's (1984) definition for sanukitoid, i.e., silica-oversaturated melts with high Mg-numbers, high Ni, Cr and LILE abundances (Fig 4.21c–h). A small number of high-Si samples have notably lower HREE concentrations than the vast majority of rocks in the same plutons, resulting in much higher La/Yb, similar to Archean TTG – considering the co-magmatic relationship with hornblende-rich rocks, these lower-HREE concentrations at high-Si likely reflect fractional crystallization of hornblende. Alternatively, they may be younger granitic rocks that postdate the main pluton.

● Unit 10 felsic volcanic rocks and porphyritic plutons

● Unit 10 felsic volcanic rocks and porphyritic plutons (high Sr/Y) ● Unit 10 TTG-like component of pluton

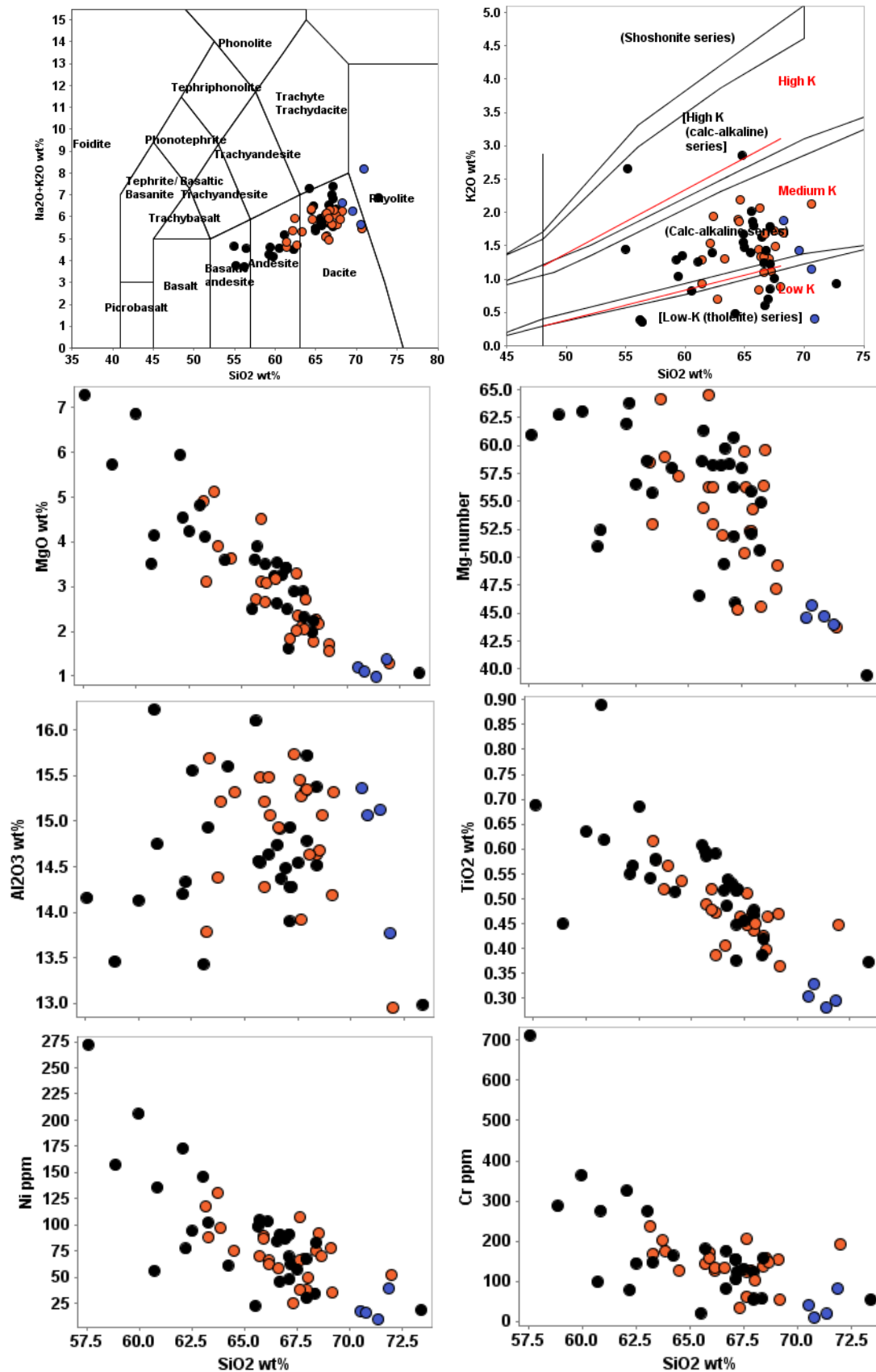


Figure 4.21. Major and compatible trace element variation diagrams for Unit 10 samples: a) Total alkalis vs SiO₂; b) K₂O vs SiO₂; c) MgO vs SiO₂; d) Mg-number vs SiO₂; e) Al₂O₃ vs SiO₂; f) TiO₂ vs SiO₂; g) Ni vs SiO₂; h) Cr vs SiO₂.

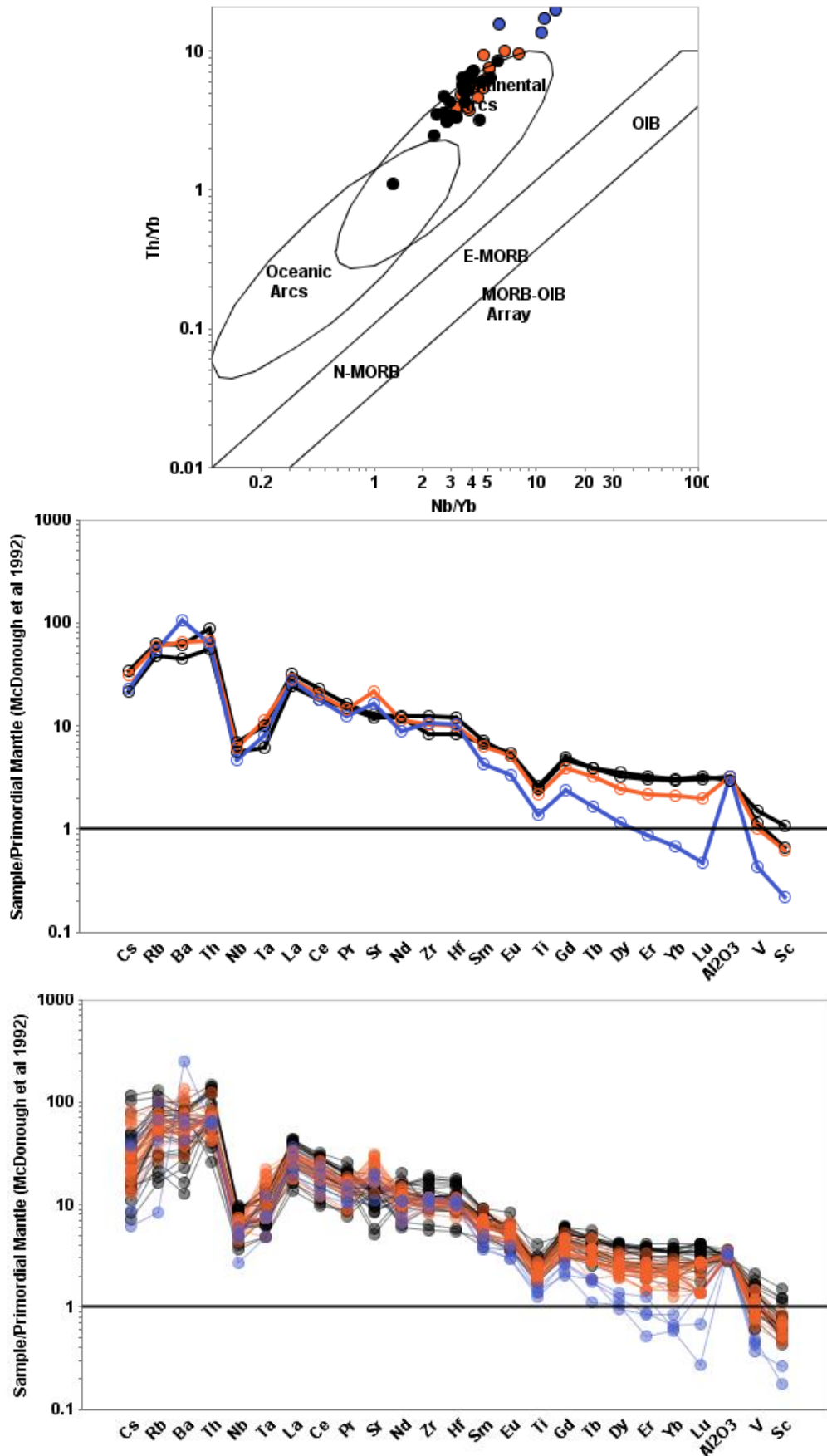


Figure 4.22. Incompatible trace element plots for Unit 10 a) Th/Yb vs Nb/Yb (after Pearce, 2014); b) comparison of mantle normalised trace element pattern averages for each color group; c) mantle normalised trace element patterns for all Unit 10 samples. Symbols as per Fig 4.21.

4.3.2.3. Unit 11

Unit 11 consists predominantly of 2763–2742 Ma moderately sodic to weakly potassic granitic rocks of the Rothsay Suite, which occur in and around the Yalgoo Dome, and 2748–2744 Ma unassigned granitic rocks from Mount Magnet to the Ryansville area (GSWA, 2021).

They are typically plagioclase, and K-feldspar phyrlic with a quartz-biotite \pm epidote \pm titanite \pm magnetite groundmass (Clos *et al.*, 2018). All samples have high to very high SiO₂ (66.7–76.4%, mostly >71%) and all major and minor elements decrease with increasing SiO₂, except for K₂O, which increases (MnO shows no correlation with SiO₂, but all samples contain $\leq 0.1\%$ and is therefore subject to detection limit issues). Hence, although this series of granitic rocks begins with moderately sodic compositions (K₂O/Na₂O ~ 0.5 at 70% SiO₂), they increase to weakly-potassic compositions over a very narrow silica interval (K₂O/Na₂O ~ 1.0 at 74% SiO₂ and K₂O/Na₂O 1.2–1.5 at 76% SiO₂). Nearly all samples with K₂O/Na₂O < 1.0 have high Sr/Y (30–200), while most samples with K₂O/Na₂O > 1.0 have low Sr/Y (10–30), and low Sr/Y samples typically have strongly negative Sr anomalies. All samples have very steep trace element patterns (high La/Yb 25–380) and, at 70–72 % SiO₂, they contain high Al₂O₃ (>15 %), Sr (200–800 ppm), Ba (500–3000 ppm) and have low HREEs (Yb ≤ 0.9 ppm), the later typically associated with melting in equilibrium with residual hornblende and/or garnet, thus meeting most of the characteristics described for Archean TTGs (Smithies, 2000). However, most of the samples in this unit are more potassic than typical TTG (K₂O/Na₂O 0.5–1.5 vs <1.0) and approximately 80% of samples fall below the proposed 500 ppm Sr lower limit for TTG, likely because they have fractionated plagioclase and K-feldspar.

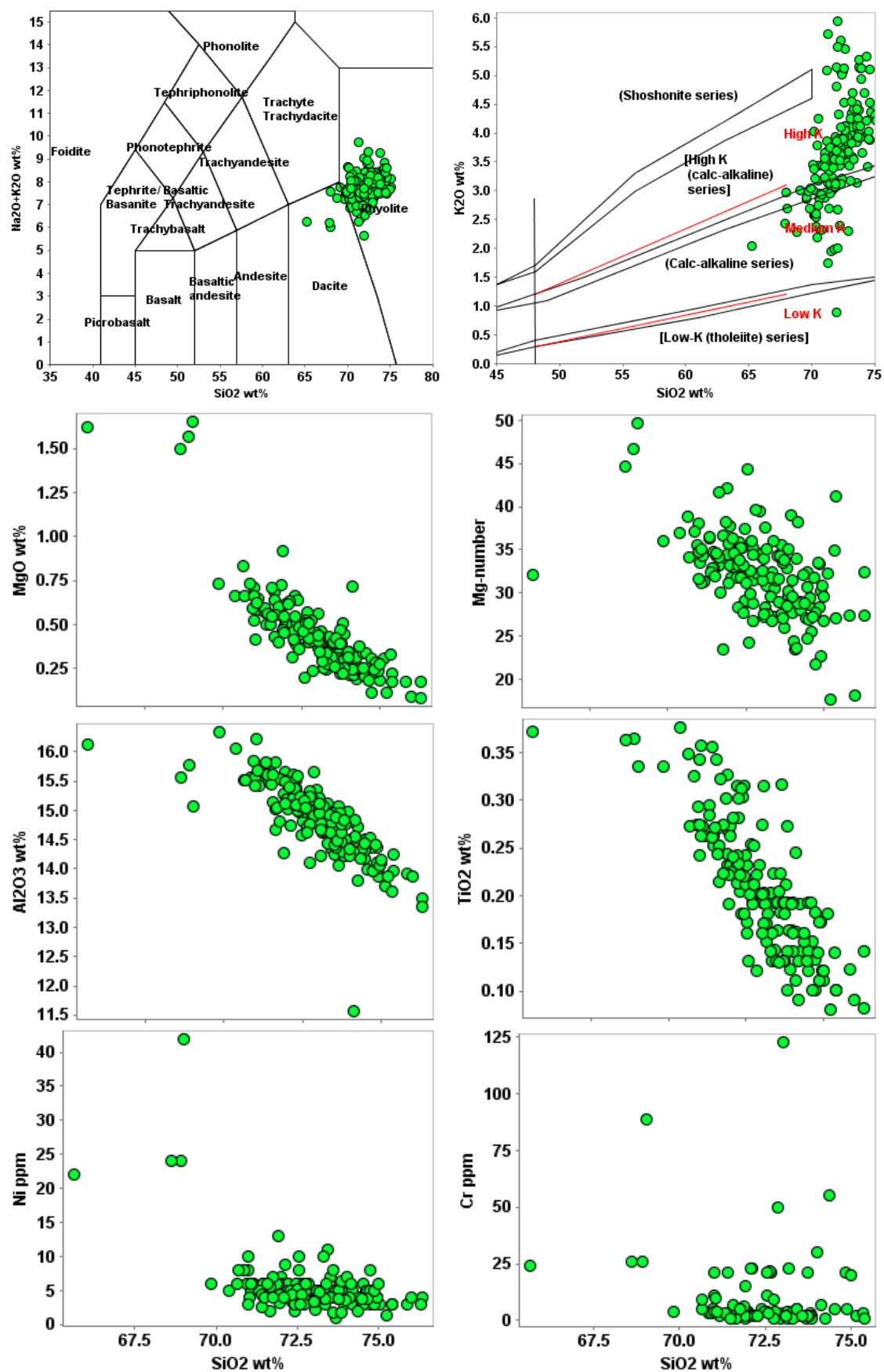


Figure 4.23. Major and compatible trace element variation diagrams for Unit 11 samples: a) Total alkalis vs SiO₂; b) K₂O vs SiO₂; c) MgO vs SiO₂; d) Mg-number vs SiO₂; e) Al₂O₃ vs SiO₂; f) TiO₂ vs SiO₂; g) Ni vs SiO₂; h) Cr vs SiO₂.

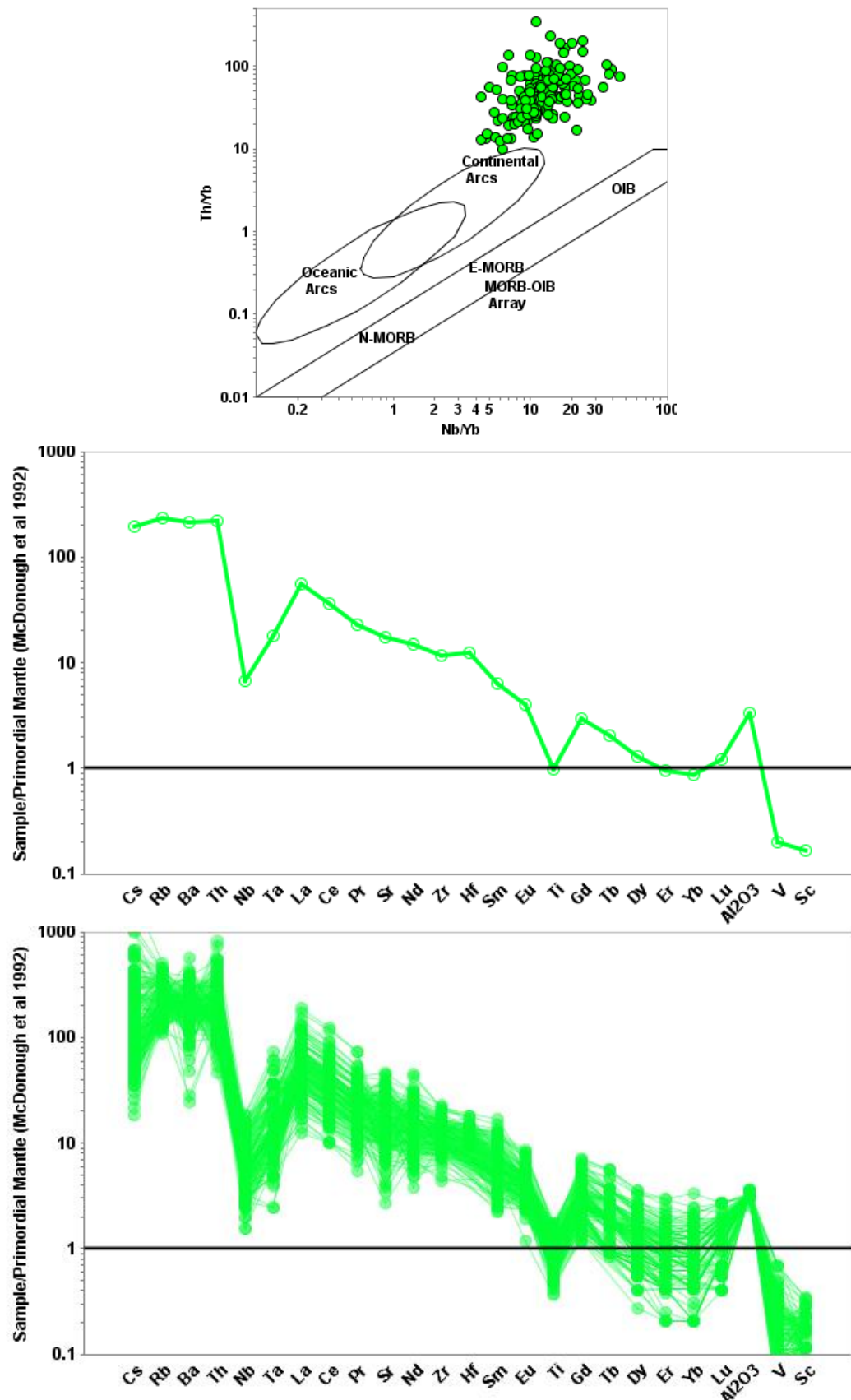


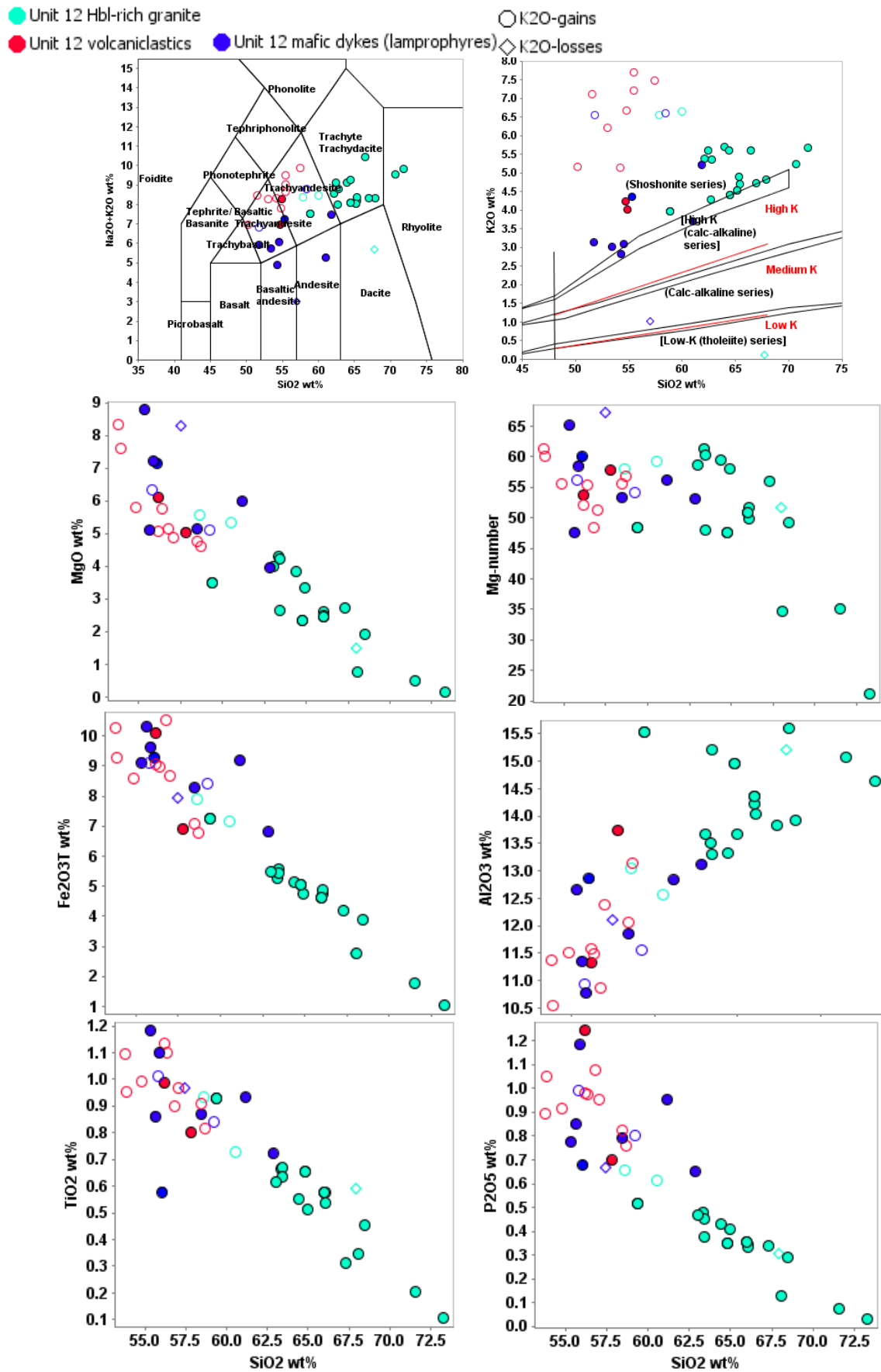
Figure 4.24 Incompatible trace element plots for Unit 11 a) Th/Yb vs Nb/Yb (after Pearce, 2014); b) mantle normalised trace element pattern for average of Unit 11 compositions; c) mantle normalised trace element patterns for all Unit 11 samples.

4.3.2.4. Unit 12

Unit 12 consists of *c.* 2754 to 2747 Ma high-Mg, hornblende-biotite rich ultrapotassic granitic rocks (shoshonitic plutons), mafic dykes (shoshonitic lamprophyres) and volcanoclastic units (trachyandesites) in the Gullewa mining district (40 km SW of Yalgoo) and hornblende-biotite rich shoshonitic plutons and lamprophyric dykes approximately 20km SE of Ryansville (Fig 4.1).

Although the trachyandesites and lamprophyres have not yet been directly dated, their spatial association with the shoshonitic plutons and their stratigraphic positions are permissive of a co-genetic relationship. Their chemical characteristics are broadly similar to sanukitoid rocks, including high-MgO, Ni and Cr concentrations (relative to SiO₂) and strong LREE enrichment, however, they contain significantly higher P₂O₅ and K₂O concentrations, as well as much higher La/Yb ratios and have subtle (in some cases significant) negative Zr-Hf anomalies.

Thirteen samples, predominantly volcanoclastic rocks, contain higher than expected K₂O and two samples contain lower than expected K₂O compared to the dominant K₂O-SiO₂ trend, likely reflecting potassium redistribution due to low-temperature fluid alteration given their locality in the Gullewa Au mining district. This alteration appears to correlate with some loss in Na₂O and gain in Ba, but the other major and trace element concentrations appear largely unaffected (Figs 4.25, 4.26). Among the samples that have not been flagged as altered, the most primitive samples (lamprophyres and compositionally similar aphanitic mafic dykes) contain approximately 3 wt% K₂O, showing that their parental magmas were strongly enriched in K₂O and P₂O₅, reflecting mantle sources that likely contained phlogopite and apatite.



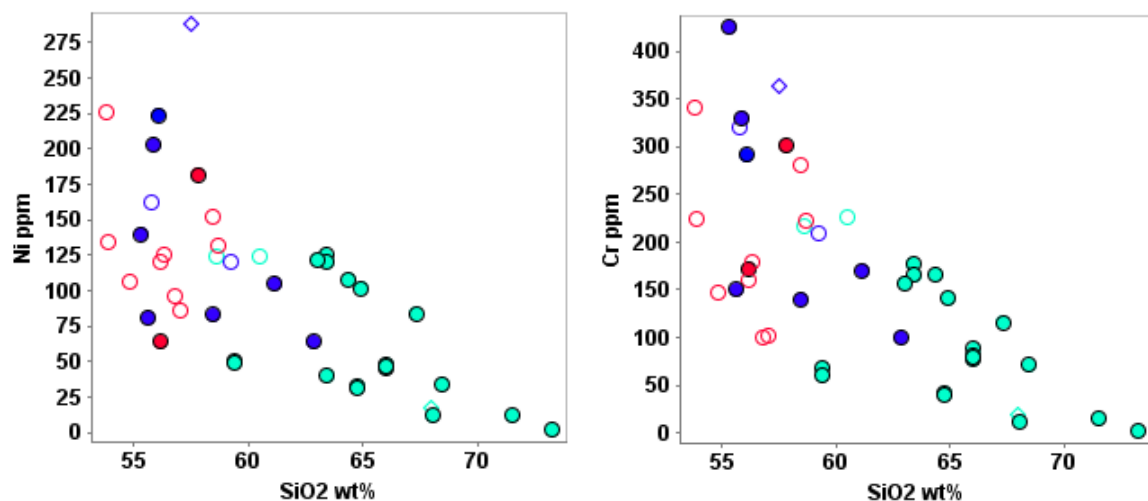


Figure 4.25 continued. I) Ni vs SiO₂; j) Cr vs SiO₂.

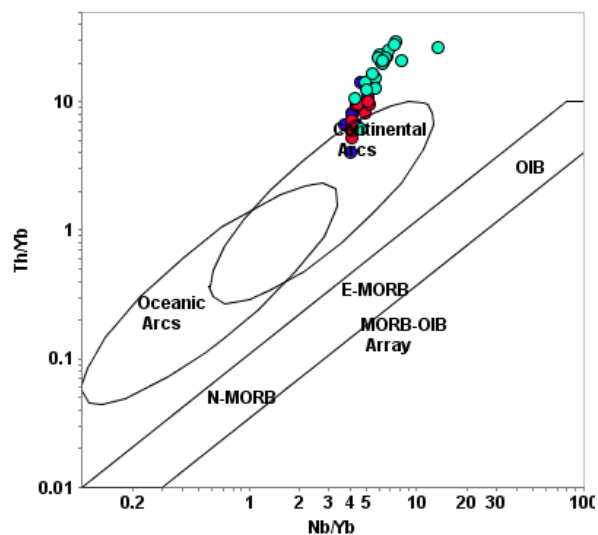
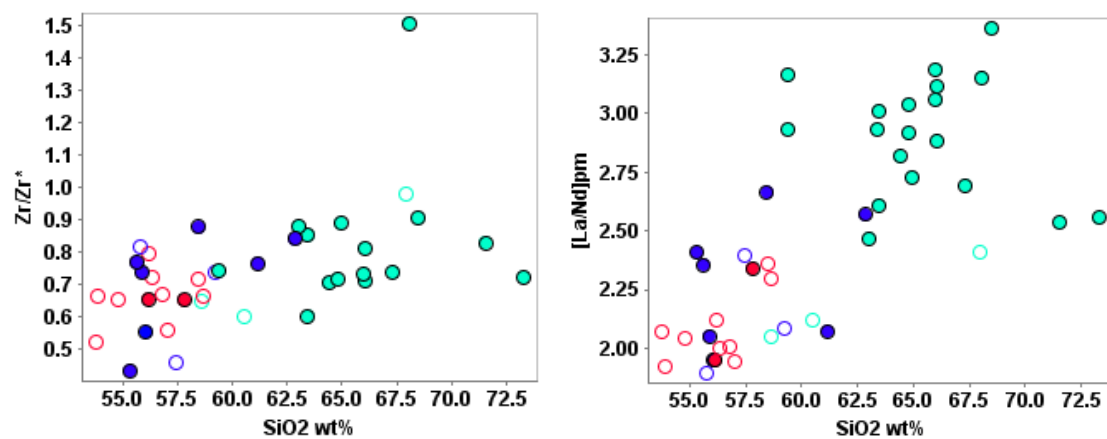


Figure 4.26 Incompatible trace element plots for Unit 12 a) Zr/Zr* vs SiO₂; b) [La/Nd]_{PM} vs SiO₂; c) Th/Yb vs Nb/Yb (after Pearce, 2014). Continued.

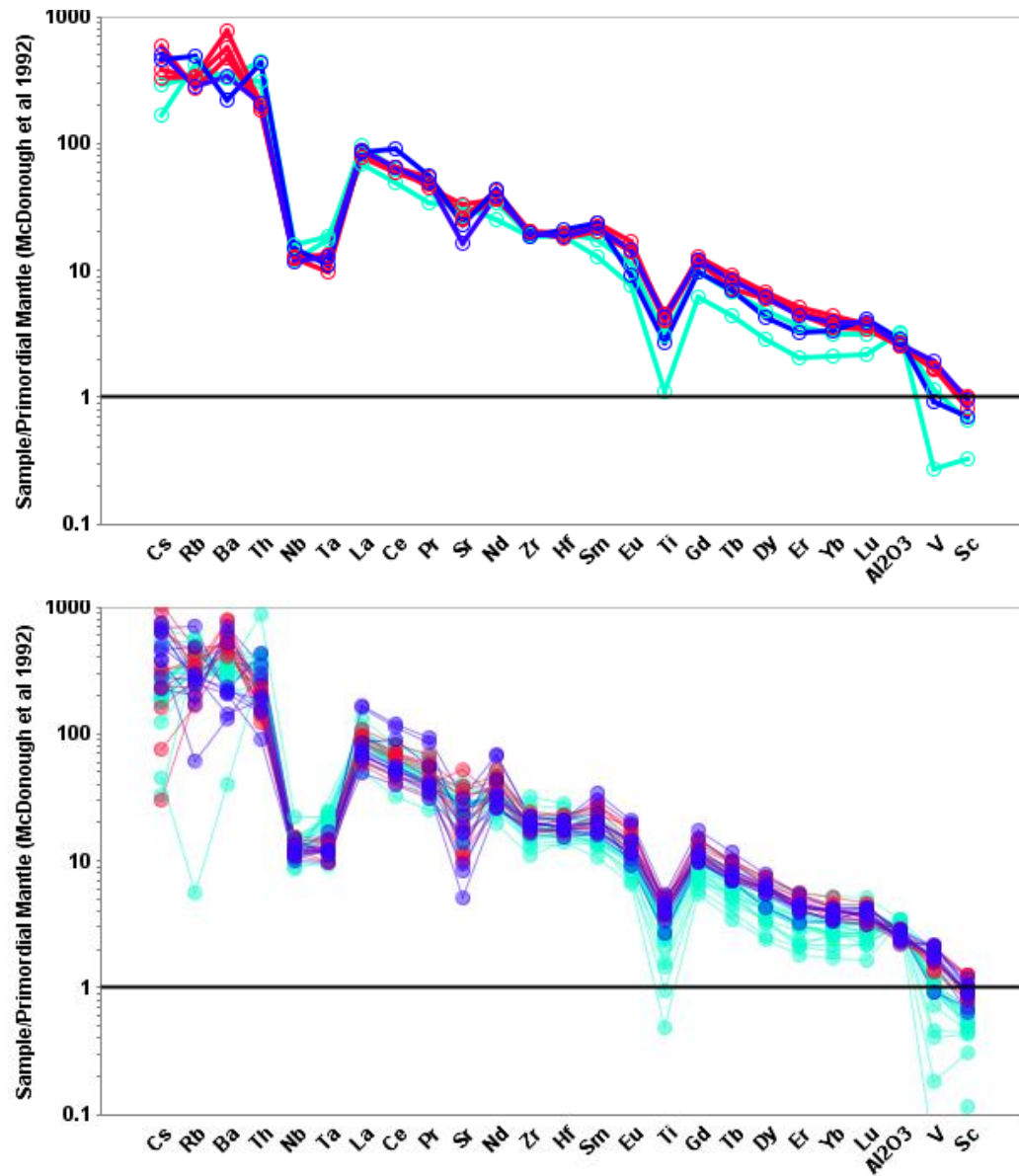


Figure 4.26 continued. d) Comparison of Unit 12 mantle normalised trace element pattern, averaged for each color group; e) mantle normalised trace element patterns for all Unit 12 samples. Symbols as per 4.25.

4.3.2.5. Unit 13 and Unit 14

Units 13 and 14 are discussed (and plotted in Figs 4.27-4.28) together because they appear to share a co-genetic relationship. Unit 13 contains mafic to intermediate volcanic and gabbroic rocks in the Dalgaranga, Abbots, Wattagee Hill and Mingah Range localities. Although field relationships are equivocal (see ‘stratigraphic correlations’ discussion below), these rocks appear to have been emplaced at *c.* 2750 based on recurring stratigraphic association with *c.* 2750 to 2745 Ma felsic volcanic rocks of Unit 14 and 15. On a plot of total-alkali versus SiO₂, most samples classify as basaltic andesite, while on K₂O versus SiO₂, most samples plot in the low-K tholeiitic field. Their trace element patterns are strongly LILE-LREE enriched, with strong negative Nb anomalies, and their MREE-HREE patterns are typically flat. One subset of gabbroic rocks (black points in Fig 4.27a-j) show MgO increasing with SiO₂, reflecting pyroxene accumulation. Another subset of samples from the Wattagee Hill area (red points in Figs 4.27a-j) have distinctly higher TiO₂, Fe₂O₃ and SiO₂, as well as lower MgO, Ni and Cr, showing evidence for accumulation of Fe-Ti oxides. Collectively, Unit 13 samples follow a typical tholeiitic line of liquid decent (e.g., Fig 4.27c).

Unit 14 includes high-silica rhyolites and granitic intrusions with crystallization ages ranging from 2752–2745 Ma in the Eelya mining district (Wang, 1998; GSWA, 2021), Mingah Range (GSWA, 2021) and Dalgaranga (Pigeon and Hallberg, 2000; Champion and Cassidy, 2002) areas. Samples from Unit 14 have nearly identical trace element patterns to Unit 9, and can only distinguished from one another with high precision zircon geochronology. The chemical characteristics of Unit 14 are therefore, like Unit 9, consistent with fractional crystallization of high-LILE tholeiitic magmas.

All Unit 14 samples contain >69% SiO₂, classifying as rhyolite on a total alkali vs silica diagram (Fig 4.27a). Extended trace element patterns of the Unit 14 felsic rocks are broadly parallel to the mafic rocks in Unit 13, except the felsic rocks have pronounced negative Eu, Sr, Ti and V anomalies (Fig 4.28), indicating a relationship by fractional crystallization of an assemblage dominated by plagioclase and ilmenite-magnetite.

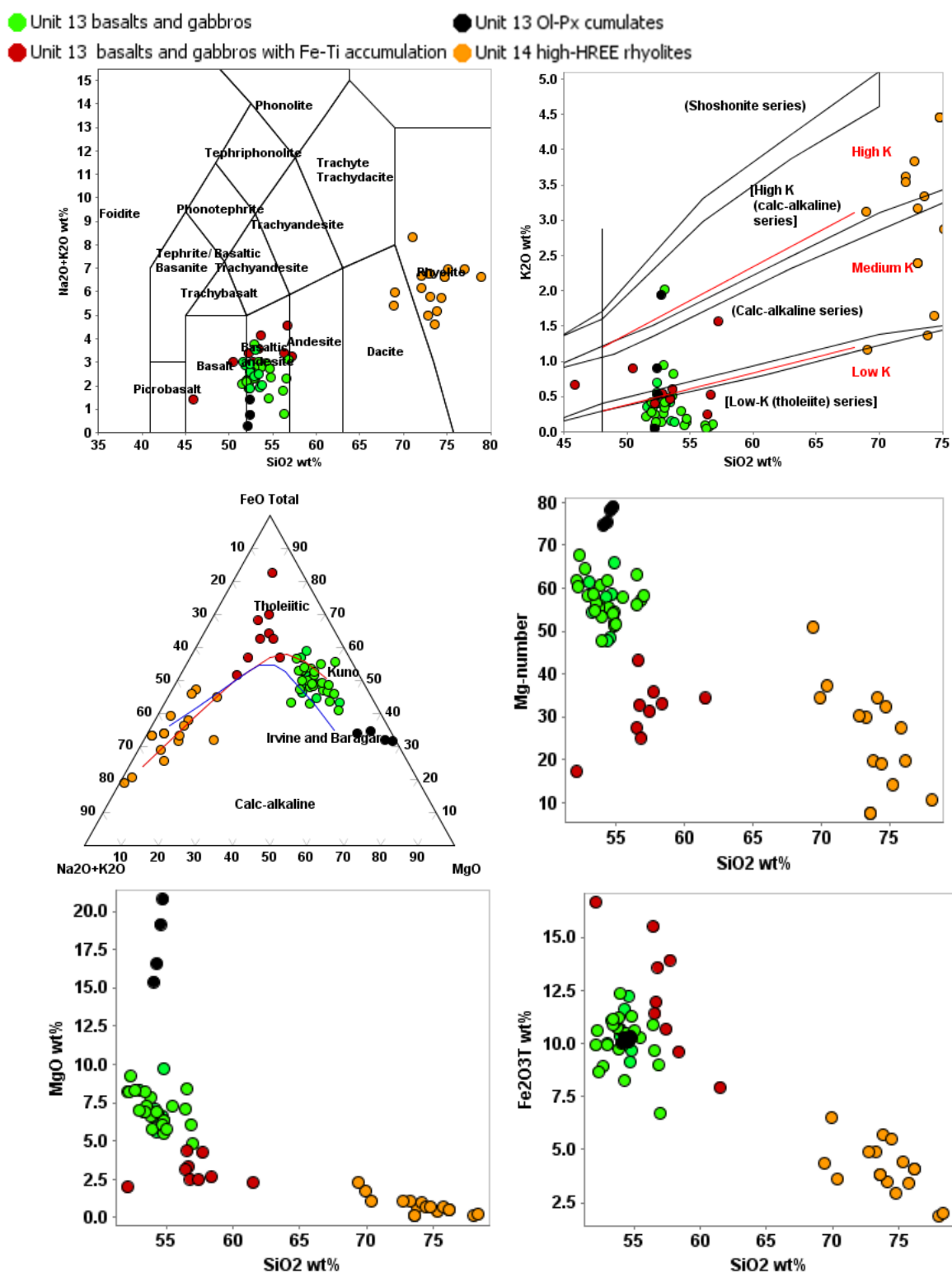


Figure 4.27. Major and compatible trace element variation diagrams for Unit 13 and 14 samples: a) Total alkalis vs SiO₂; b) K₂O vs SiO₂; c) AFM ternary diagram (total Fe); d) Mg-number vs SiO₂; e) MgO vs SiO₂; f) Fe₂O₃ vs SiO₂. Continued.

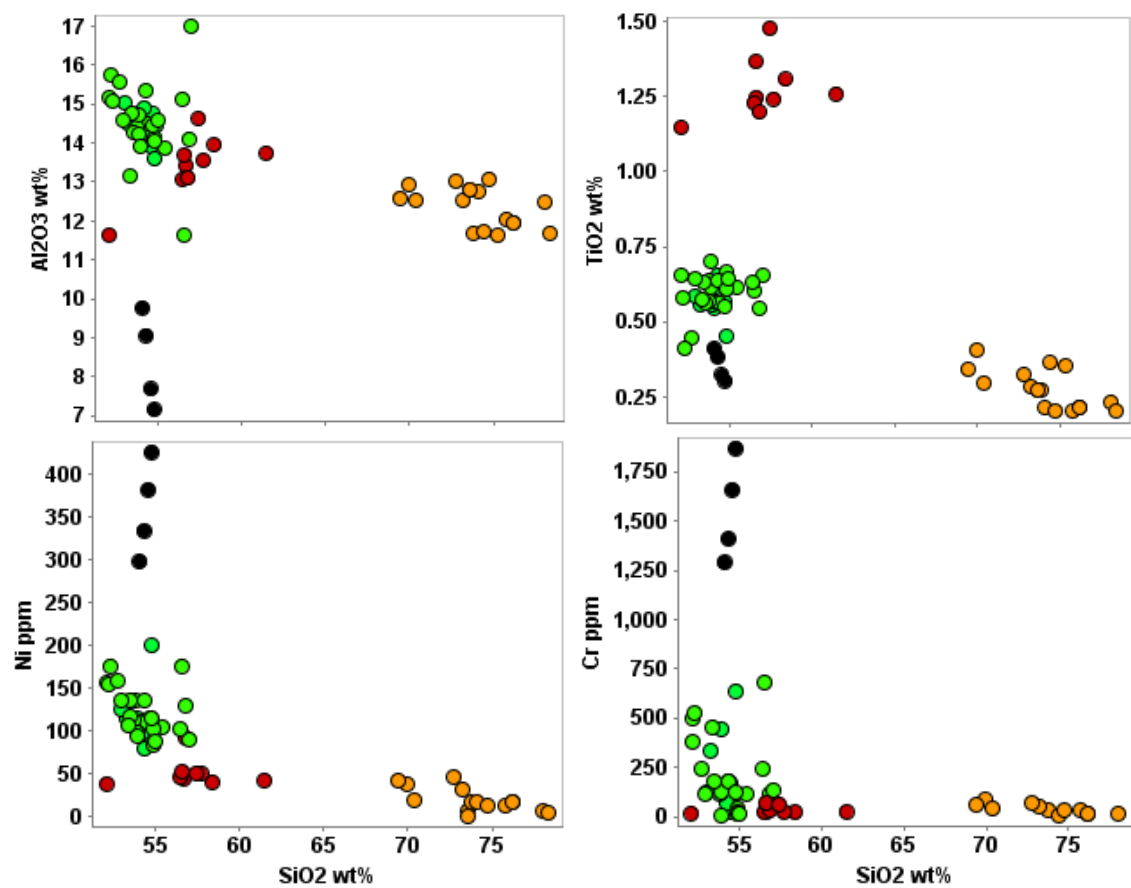


Figure 4.27 Continued. g) Al₂O₃ vs SiO₂; h) TiO₂ vs SiO₂; i) Ni vs SiO₂; j) Cr vs SiO₂.

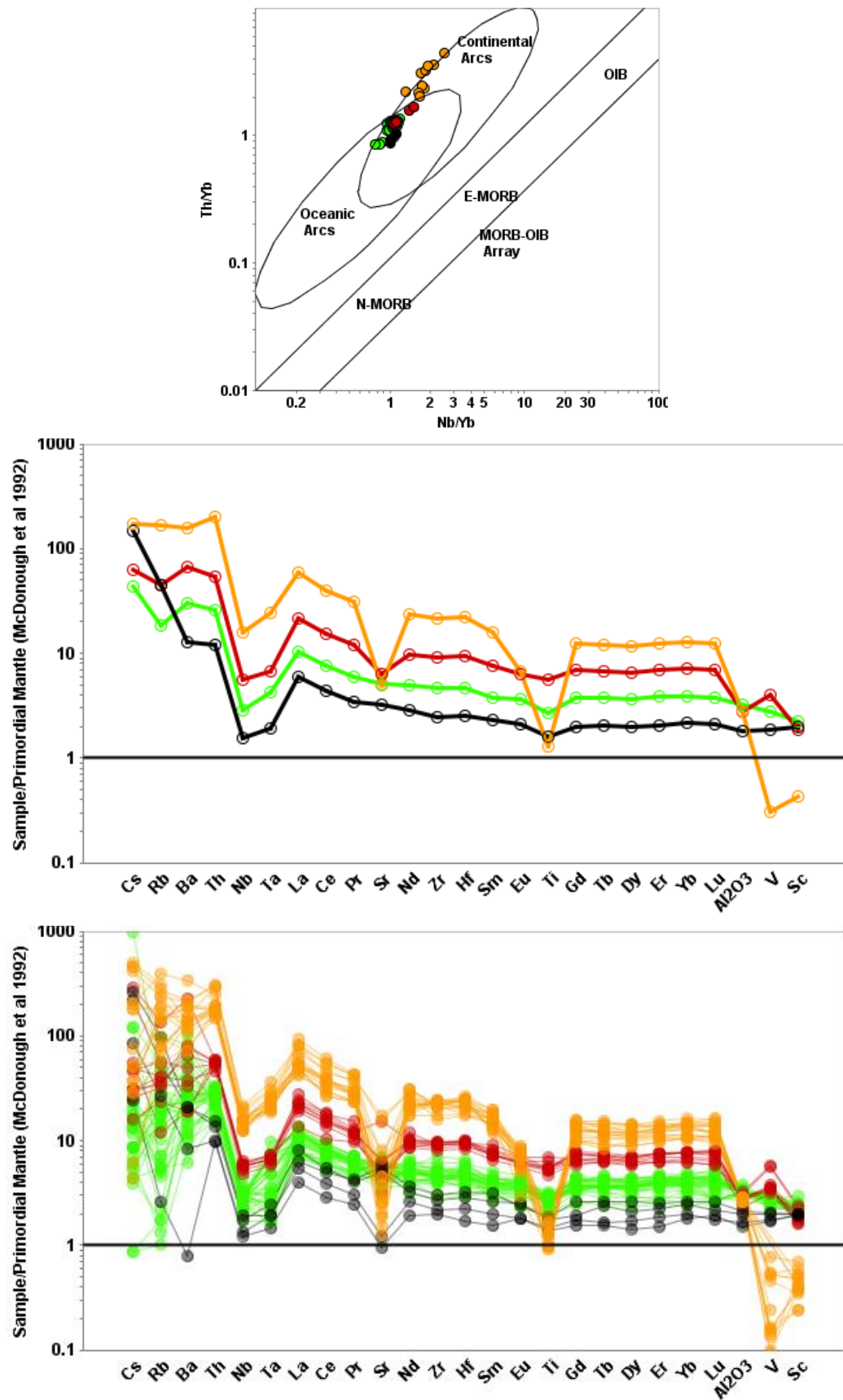


Figure 4.28 Incompatible trace element plots for Units 13 and 14 a) Th/Yb vs Nb/Yb (after Pearce, 2014); b) comparison of Unit 13 and 14 mantle normalised trace element patterns, averaged for each color group; c) mantle normalised trace element patterns for all Unit 13 and 14 samples. Symbols as per 4.27.

4.3.2.6. Unit 15

Unit 15 consists of 2750–2734 Ma intermediate to felsic volcanic (and volcanoclastic) rocks assigned to the Greensleeves Formation in greenstone belts between the Abbots and Cue mining districts. Most of the rocks sampled for this study were fragmental (volcanic breccias or hyaloclastites with lesser tuffs in high-Si units). The most primitive samples plot within the andesite field on the TAS classification diagram (*c.* 55.3% SiO₂ and 4–5 Na₂O + K₂O), while the most fractionated samples plot slightly into the rhyolite field. Most compositions are dacitic and there is no significant break in compositions on the TAS diagram (Fig 4.29a). Samples from Unit 15 have similar trace element patterns to Unit 10 and are similarly consistent with fractional crystallization involving hornblende.

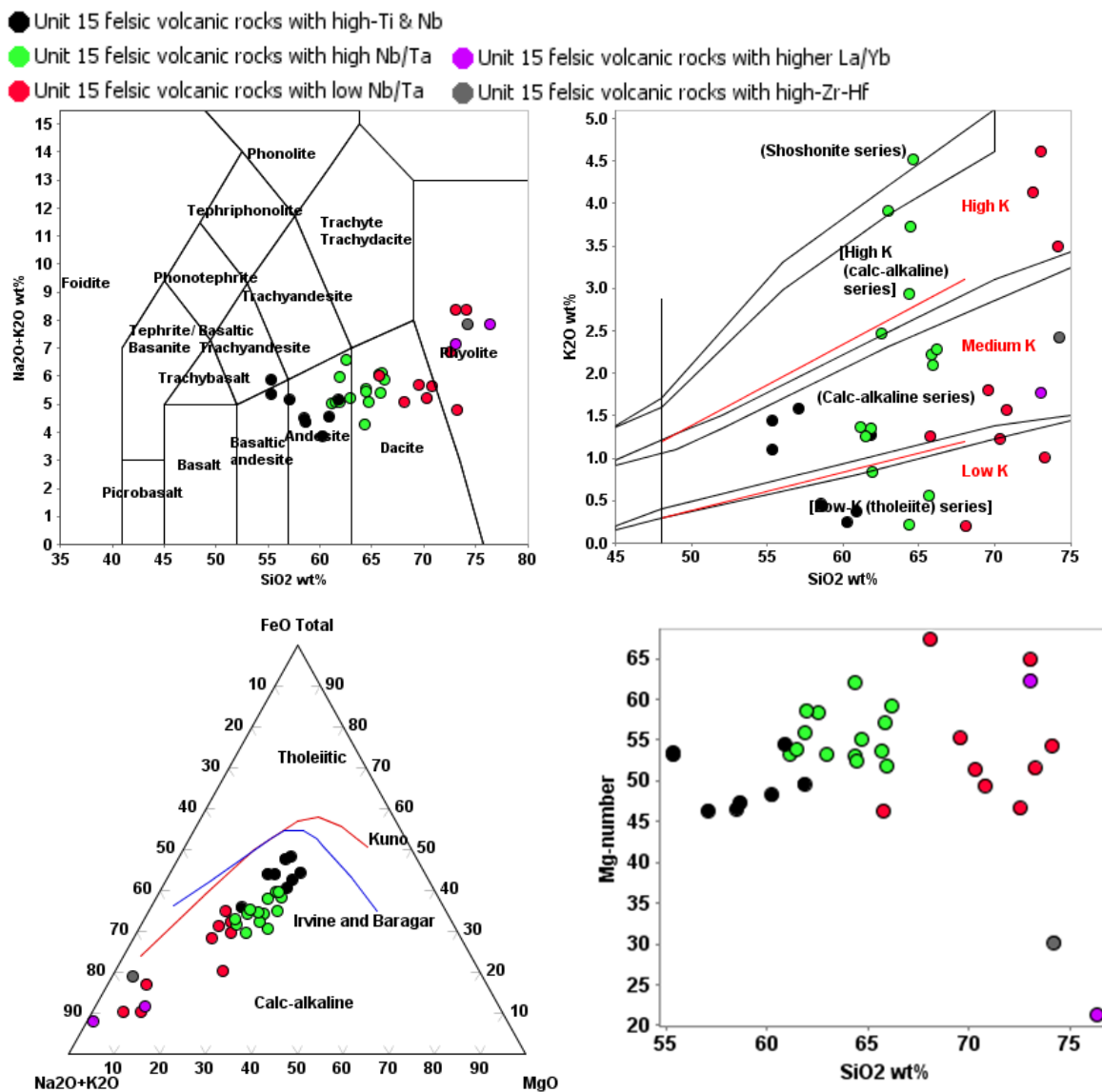


Figure 4.29. Major and compatible trace element variation diagrams for Unit 15 samples: a) Total alkalis vs SiO₂; b) K₂O vs SiO₂; c) AFM ternary diagram (total Fe); d) Mg-number vs SiO₂. Continued.

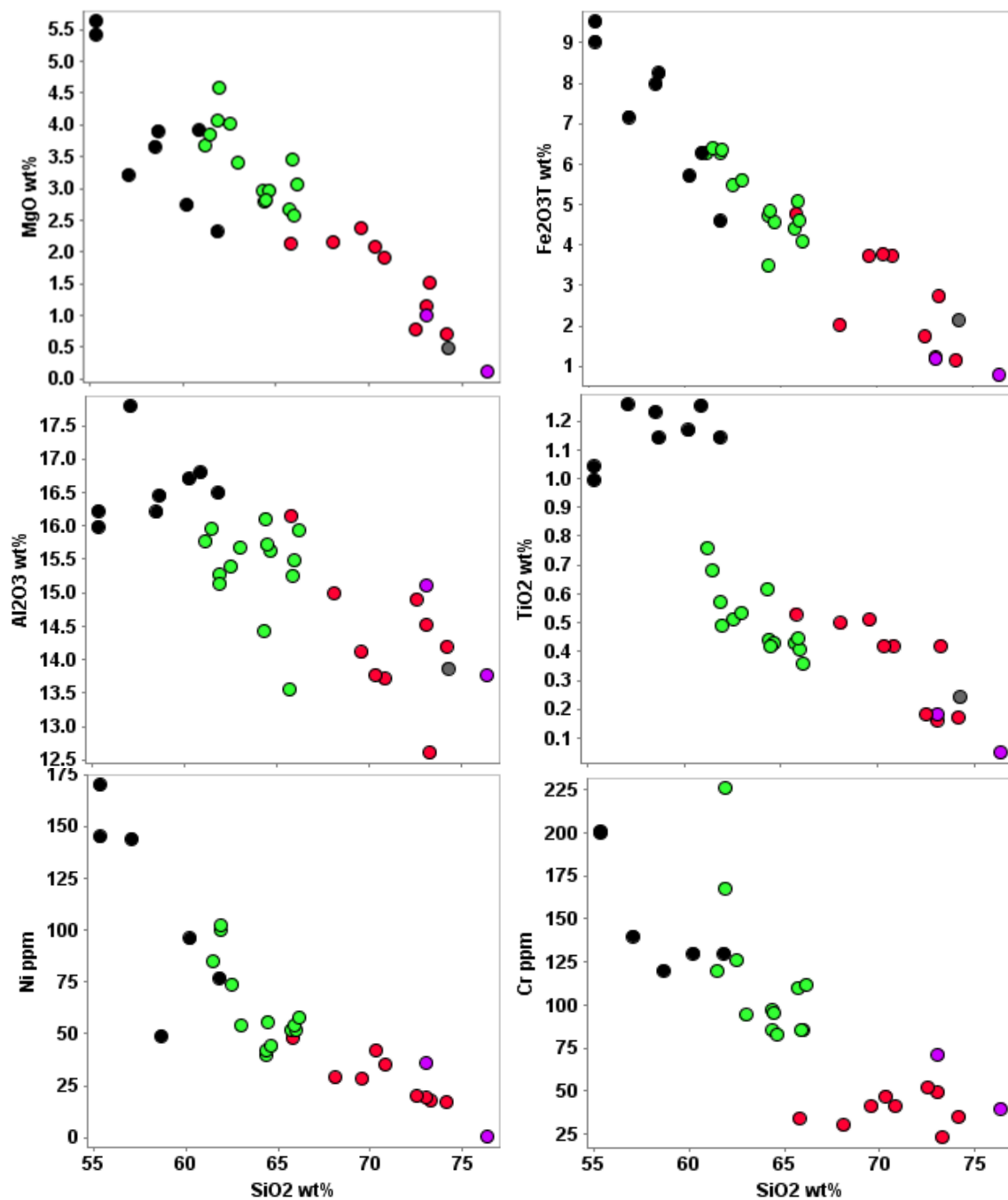


Figure 4.29 Continued. e) MgO vs SiO₂; f) Fe₂O₃ vs SiO₂; g) Al₂O₃ vs SiO₂; h) TiO₂ vs SiO₂; i) Ni vs SiO₂; j) Cr vs SiO₂.

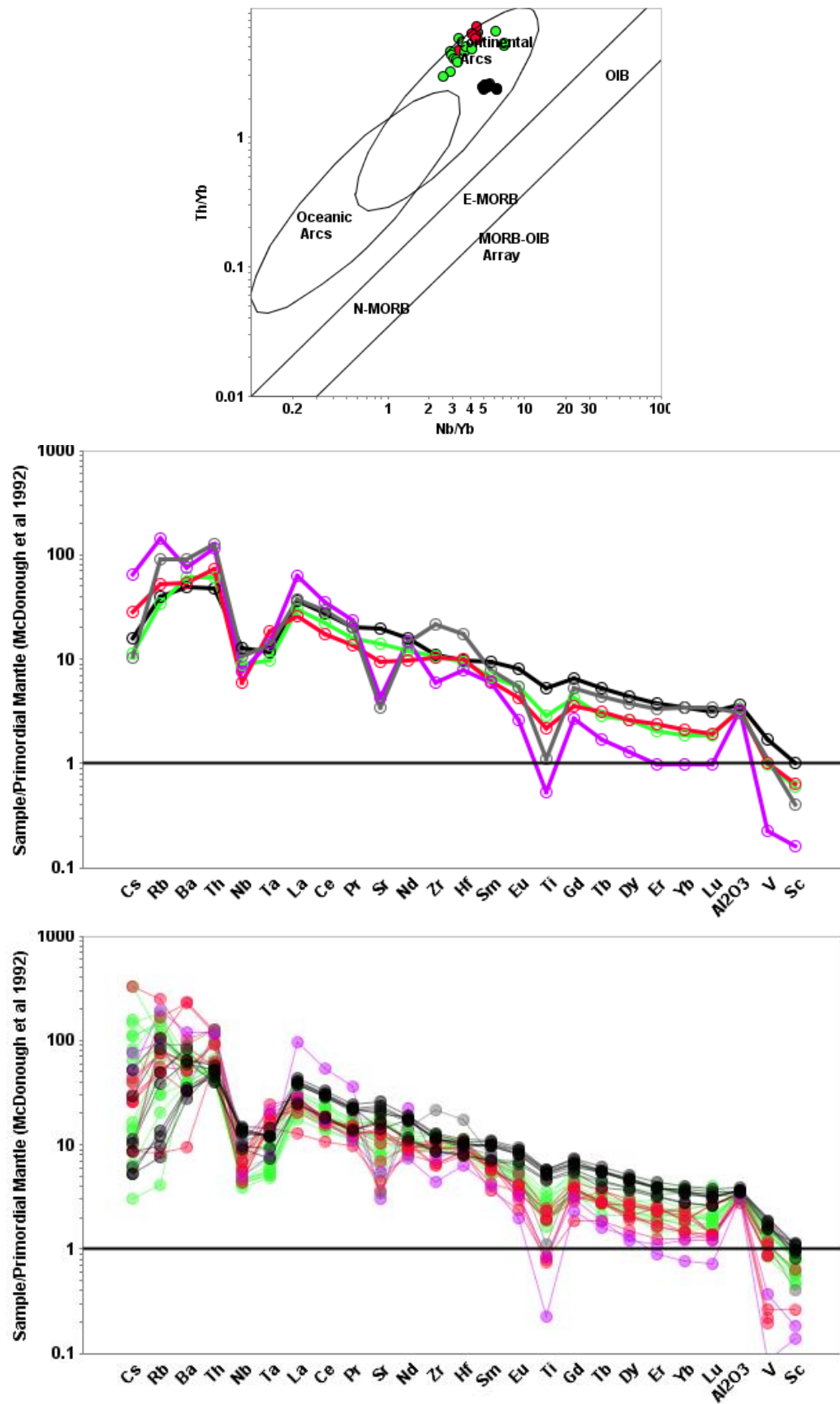


Figure 4.30 Incompatible trace element plots for Unit 15 a) Th/Yb vs Nb/Yb (after Pearce, 2014); b) Comparison of Unit 15 mantle normalised trace element pattern, averaged for each color group; c) mantle normalised trace element patterns for all Unit 15 samples. Symbols as per 4.29.

4.3.2.7. Unit 16

Unit 16 consists of gabbros and basalts that in the Cuddingwarra Hill, Wattagee Hill and Yalgowra Hills areas. On a plot of SiO₂ vs total alkalis (Fig 4.31a) they define a bimodal distribution between basaltic and basaltic andesite, the latter predominantly representing pyroxene accumulation. These rocks are presently assigned to the Glen Group but field relationships and available geochronology are equivocal and the unit may be part of Polelle Group. As their compositions do not differ greatly from other basalts in either Magmatic Episode 1 or 2 (specifically Units 3, 6 and 13), this uncertainty of stratigraphic position is not expected to be greatly significant to the geodynamic interpretations presented here, but it will be the subject of ongoing fieldwork by the GSWA.

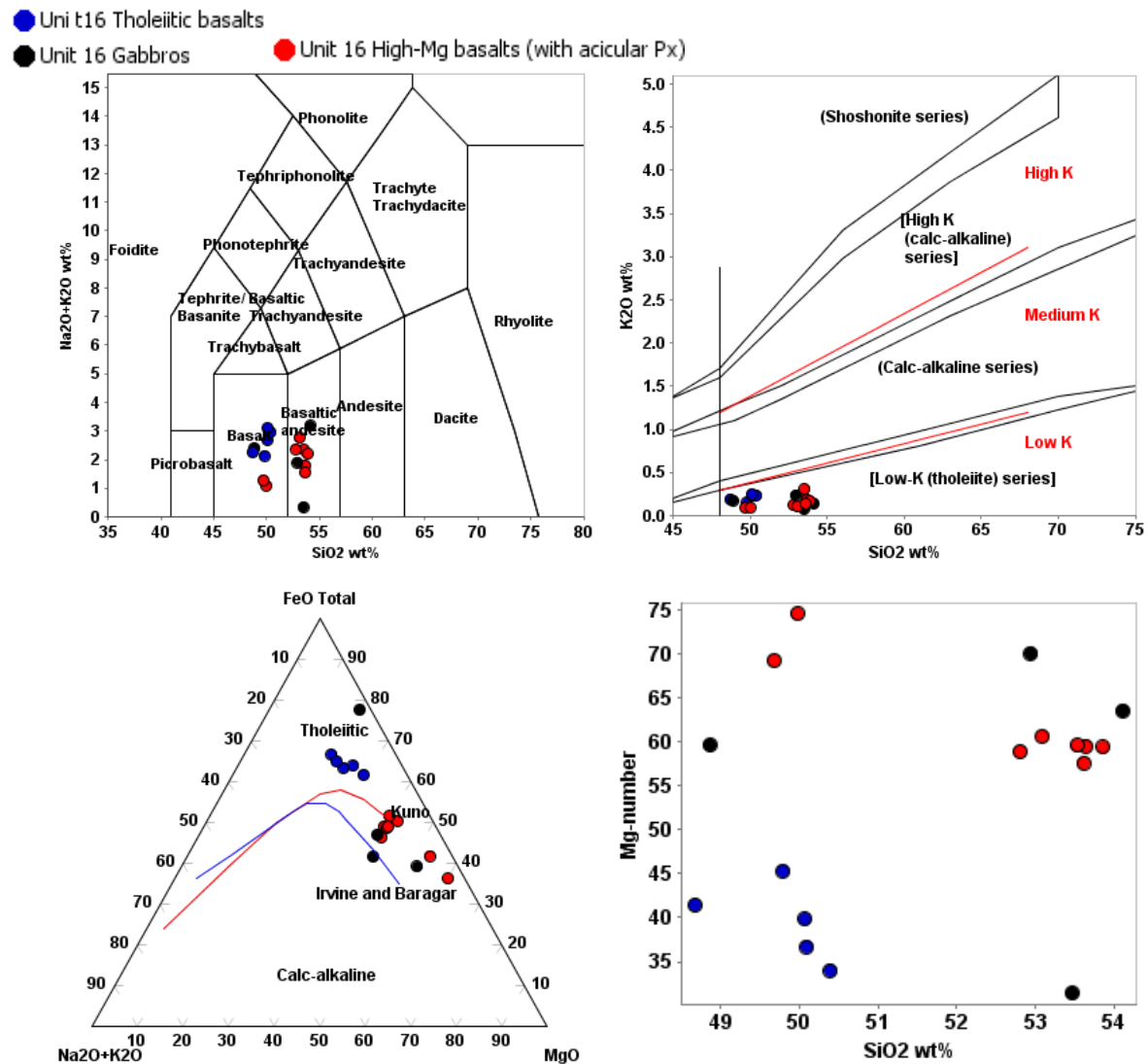


Figure 4.31. Major and compatible trace element variation diagrams for Unit 16 samples: a) Total alkalis vs SiO₂; b) K₂O vs SiO₂; c) AFM ternary diagram (total Fe); Mg-number vs SiO₂; Continued.

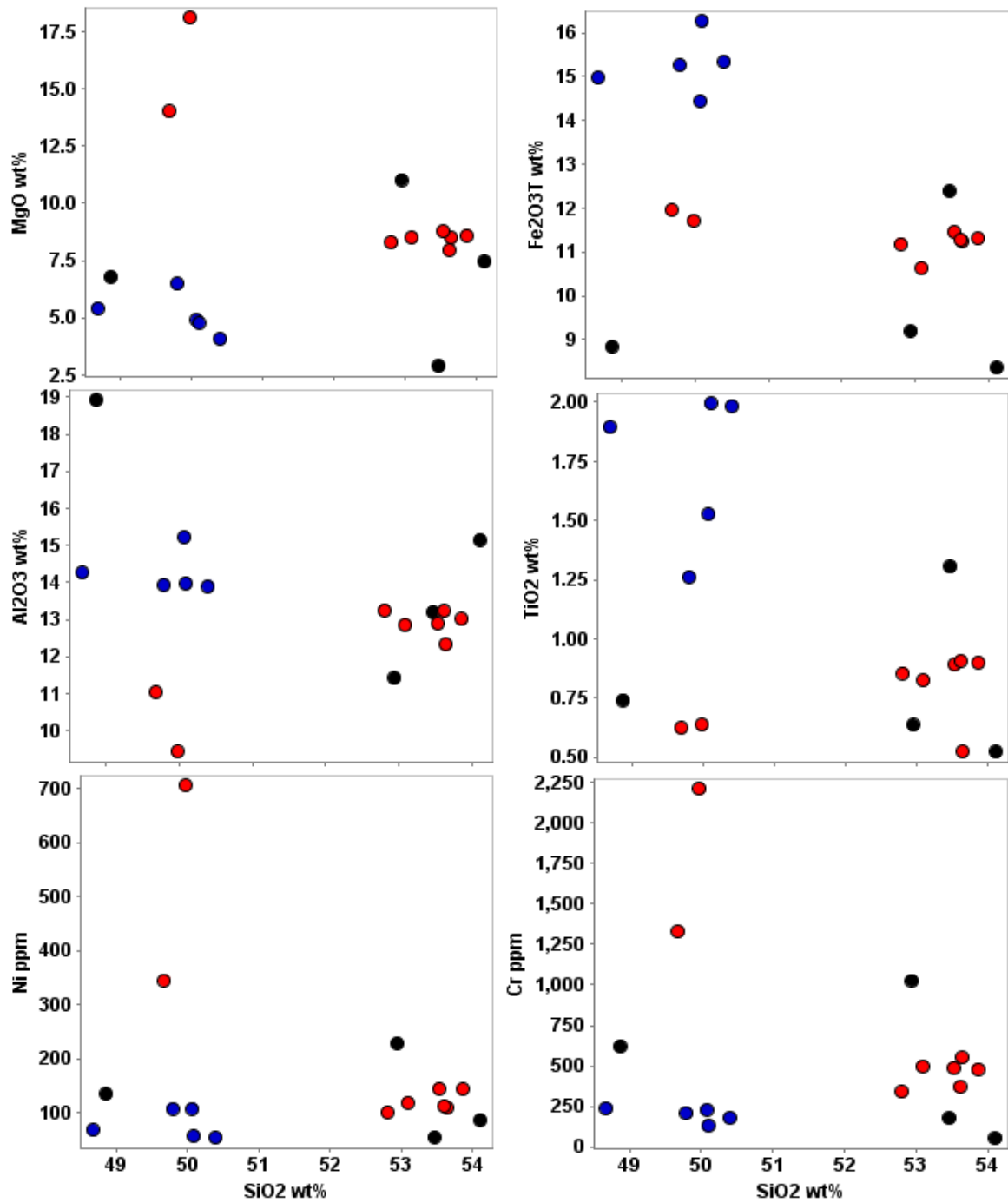


Figure 4.31 Continued. d) MgO vs SiO₂; e) Fe₂O₃ vs SiO₂; f) Al₂O₃ vs SiO₂; g) TiO₂ vs SiO₂; h) Ni vs SiO₂; i) Cr vs SiO₂.

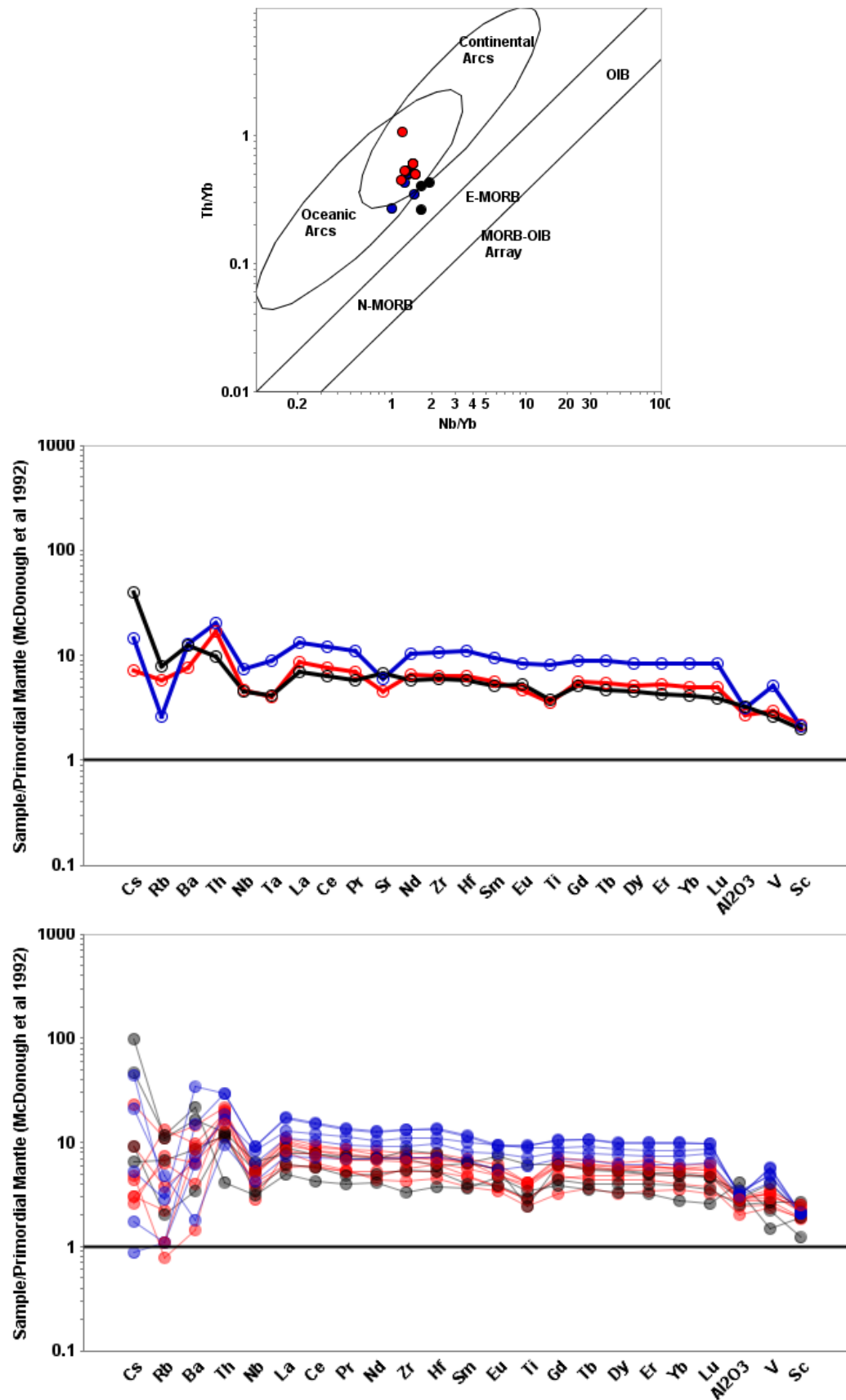


Figure 4.32 Incompatible trace element plots for Unit 16 a) Th/Yb vs Nb/Yb (after Pearce, 2014); b) Comparison of Unit 16 mantle normalised trace element pattern, averaged for each color group; c) mantle normalised trace element patterns for all Unit 16 samples. Symbols as per Fig 4.31.

4.4. Required Stratigraphic Changes

The following are several significant changes to previously assigned stratigraphy that are required based on this chemostratigraphic assessment. These changes are based on the ‘marker units’ that have trace element characteristics that are generally unmistakable for other units of similar major element compositions and compatible with the latest geochronological data.

1. Tholeiitic basalts in the Murrouli Range, previously considered the type locality for the *c.* 2820 Ma Murrouli Basalt (Formation) (Van Kranendonk and Ivanic, 2009) are compositionally comparable to the Stockyard Basalt Member in the Meekatharra Formation and includes a thin unit with boninite-like compositions that is indistinguishable from the Bassetts Volcanic Member in the Meekatharra Formation. Re-assigning the Murrouli Range sequence to the Meekatharra Formation is consistent with all available geochronological constraints: the sequence is intruded by 2787–2782 Ma tonalites, providing a minimum depositional age constraint, and there is no evidence to indicate that they are older than other similar mafic volcanic rocks in the Meekatharra Formation. All remaining occurrences of the Murrouli Basalt that are plausibly *c.* 2820 Ma have since been reassigned to a new unit called the Singleton Formation.
2. Previously, the Cullculli Suite (Van Kranendonk and Ivanic, 2009) included hornblende-bearing granitic rocks from 2787–2733 Ma. However, there are three peaks in zircon U-Pb ages: (1) the 2787-2782 Ma Nannine Tonalite in the Murrouli Range area; (2) 2761 – 2746 Ma plutons in the Meekatharra greenstone belt; (3) a single 2733 ± 6 Ma biotite-hornblende tonalite pluton between the Mingah Range and Weld Range belts. While all three of these groupings have sanukitoid (or sanukitoid-like) compositions, the separable chronology contravenes the definition of a suite. Based on this study, the *c.* 2733 Ma pluton has already been reassigned to the Big Bell Suite (which may itself require splitting into smaller Suites), but it is also recommend that the Nannine Tonalite be promoted to Suite level in the stratigraphic hierarchy, leaving Cullculli Suite to contain only those plutons from 2761–2746 Ma.

3. Previously, the Greensleeves Formation was defined as a single unit of felsic volcanic rocks with zircon ages from 2761–2734 Ma. This assessment indicates that the Greensleeves Formation is comprised of at least four chemically or chronologically distinct units with a *c.* 5 Ma hiatus between Units 9 and 10 (2761–2755 Ma; fractionated tholeiitic and high-Mg calc-alkaline rocks) and Units 14 and 15 (2750–2734; high-Mg calc-alkaline and fractionated tholeiitic rocks), which typically occur in separate greenstone belts. The preliminary interpretation is that a mafic volcanic Unit 13, which has distinctive trace element patterns, occurs between two felsic episodes, or at least underlies the younger Units 14 and 15 in several localities.
4. High-Th siliceous basalts in the Ryansville area were previously assigned to the Wattagee Formation of the Glen Group, interpreted to conformably overlie clastic sediments of the Ryansville Formation (Van Kranendonk, 2010). However, most of the contacts in this region are faulted and there appears to be little geochronological evidence to support this interpretation. Based on compositional similarities to high-Th siliceous basalts (Unit 7) that outcrop in the Gullewa, Yalgoo and Ryansville areas, the Ryansville examples should be reassigned to the Meekatharra Formation.

An additional and presently unresolved issue is that mafic volcanic rocks in the Wattagee Hill area (Unit 13), presently assigned to the Glen Group (Van Kranendonk *et al.*, 2013), have multiple geochemical characteristics (e.g., their LILE-LREE enriched REE patterns and Nd isotopic ratios) that are indistinguishable from mafic volcanic rocks assigned to the Polelle Group in the Abbots, Mingah and Dalgaranga areas (also assigned here to Unit 13). At the later three localities, the mafic volcanic rocks in question are interpreted to underlie *c.* 2752–2738 Ma felsic volcanic rocks of the Greensleeves Formation (Units 14 and 15), whereas in the Wattagee Hill area the mafic volcanic rocks were interpreted by Van Kranendonk *et al.* (2013) to overlie the Greensleeves Formation based on magmatic differentiation trends in *c.* 2735 Ma mafic sills that intrude the felsic volcanic rocks and a 2725 ± 4 Ma age from a rhyolitic unit that is intercalated with the mafic volcanic rocks. Although this uncertainty is not resolvable at present, the interpretation that the mafic (Unit 13) and felsic (Unit

14) volcanic rocks in these localities are related via fractional crystallization suggests that they were emplaced at approximately the same time.

4.5. Geospatial organisation

Figure 4.1 shows the arrangement of distinct belts of different chemostratigraphic units present within the northern Youanmi Terrane. The eastern part of the study area, from Meekatharra to Mount Singleton, is dominated by Units 1–5, 8 and 10, which include boninite-like rocks, siliceous high-Mg basalts, MORB-like tholeiitic basalts, HREE-depleted picrites and high-Mg hornblende-rich gabbros, while felsic lithologies are predominantly sanukitoids and sanukitoid-like basalt-andesite-dacite-rhyolite series rocks and fractionated tholeiitic rocks. The variety of lithologies in the eastern part of the study area require wide-spread hydrated, LILE-LREE enriched mantle and are best explained by oceanic arc or back-arc magmatism (Lowrey *et al.*, 2019; Wyman, 2019). The western part of the study area, from the Abbots greenstone belt to Dalgaranga and Yalgoo to Gullewa, is dominated by Units 7, 9, and 11–16. Mafic rocks in the eastern part of the study area are predominantly pyroxene spinifex textured high-Th siliceous high-Mg basalts (with notably higher Th-LREE than stratigraphic equivalents in the eastern belts) and LILE-LREE enriched tholeiitic basalts-andesites and locally shoshonitic lamprophyres, all of which have very high Th/Nb and low ϵ_{NdT} . Felsic lithologies in the western part of study area are predominantly transitional TTG and fractionated tholeiitic felsic rocks with lesser volumes of shoshonitic hornblende-biotite rich plutons and volcanoclastic rocks and sanukitoid (and sanukitoid-like) volcanic rocks.

The distinctly lower ϵ_{NdT} of most samples in the western side (excluding the transitional TTGs) and strong LILE-LREE enrichment in most lithologies, particularly in magmatic episode 2, implicates an isotopically and chemically evolved (i.e., ancient and felsic) component in the petrogenesis of most lithologies and is more consistent with a continental setting, which is elaborated upon in Chapter 5.

4.6. CONCLUSIONS

This study benefits from nearly two orders of magnitude more high-precision trace element analyses than were available to previous lithostratigraphic interpretations and it is becoming apparent

that, although broadly of similar ages, there are significant differences in the compositions of supracrustal rocks between greenstone belts. Some of these differences may simply be due to local compositional variation in country rock substrata (assimilant composition), however, given distinctive ‘marker’ units such as boninite like rocks and Al-depleted picrites, which are quite sensitive to contamination, can be traced sporadically for hundreds of kilometres along strike (i.e. between Meekatharra and Mount Singleton in a NNE-SSW orientation), with little variation in composition, assimilant variation does not sufficiently explain these differences. That there is far less continuity in the E-W orientation (i.e. between greenstone belts), than in the N-S orientation (i.e. along strike within greenstone belts) possibly indicates that there was a N-S control on the emplacement of these rocks originally. Possible explanations include magmatic asymmetry and/or primary belt- or corridor-like nature to the magmatism, but this is likely emphasized by losses of segments the supracrustal sequence, possibly due to E-W shortening and ‘stoping out’ by younger granites (Zibra, 2020).

1. A large, high quality geochemical and isotopic dataset on felsic magmatic rocks from the northern Youanmi Terrane has augmented previous work on mafic magmatic rocks and provided one of the most complete chemostratigraphic records between 2820 and 2730 Ma.
2. Together with existing geochronology, a detailed unit by unit chemostratigraphic framework has been established consisting of (but not limited to) tholeiitic, sanukitoid (and sanukitoid-like), transitional TTG, shoshonitic, and boninitic rocks, forming 16 chemically distinct units.
3. Details of these compositions indicate a wide variety of magmatic processes and mantle sources involved during the development of the Norie and Polelle Groups and the Annean Supersuite. These include (assimilation-)fractional crystallization, hydrated crustal sources, and metasomatised mantle sources in operation over about 80 Ma.
4. The timeline of magmatic events is strongly compatible with an arc accretion tectonic setting.
5. The distribution of chemical assemblages indicate a ~300 x 50 km corridor of sediment-fluxed mantle wedge-sourced volcanic rocks in the western side of the study area and a ~400 x 50 km corridor of back arc-like volcanic rocks on the eastern side.

Chapter 5: Petrogenetic implications and geodynamic synthesis

This section contains petrogenetic interpretations for intermediate-felsic lithologies that based on the chemostratigraphic assessment outlined in Chapter 4. The petrogenesis of mafic magmatic rocks from the Meekatharra to Cue area (Lowrey *et al.*, 2019), Mount Magnet and Mount Singleton areas (Wyman, 2019) and mafic intrusive complexes of the Central Youanmi Terrane (Ivanic, 2019) have been discussed extensively previously, so mafic rocks are only referred to here where it is necessary to provide context for the intermediate-felsic rocks. Methods for this section are described in Chapter 1, whole rock compositions are tabulated in Electronic Appendix 1.1 and Sm-Nd isotopic compositions are tabulated in Electronic Appendix 1.2. Chemostratigraphic Unit names follow from Chapter 4.

5.1. SPATIOTEMPORAL ASSESSMENT OF SM-ND DATA

The previous chapters of this study have shown that the greenstone belts on the eastern side of the study area, wholly within the CIZ, include a stratigraphic ‘succession’ of chemically distinctive lithological units such as boninite-like rocks, MORB-like tholeiitic basalts and sanukitoids (and sanukitoid-like rocks) that seldom occur in the belts that fall outside of, or straddle the western margin of the CIZ. Using Th/Yb-Nb/Yb systematics and Nd isotopes, it was shown in Chapter 3 that LILE±LREE enrichment in 2820–2790 Ma rocks from the Meekatharra–Cue area was a characteristic of their mantle sources, which evolved in composition over time. Here, the assessment of Sm-Nd ratios is extended eastward and southward to include samples from other greenstone belts in the study area (Fig 5.1). A full dataset is included in Electronic Appendix 1.2, however a number of samples have been excluded from the tables and figures in this Chapter for the following reasons. Firstly, isotopic ratios of ultramafic cumulates are excluded because their low REE concentrations result in greater analytical uncertainty and because they are prone to alteration, which has been shown to affect the concentrations of LREEs (Lowrey *et al.*, 2019). Samples containing >70% SiO₂ are also excluded because saturation in accessory phases potentially adds additional and less-predictable influences on

compositional trends and because many of these rocks are derived from crustal melts in any event.

The remaining dataset contains 79 Sm-Nd isotopic ratios, including 48 new data.

5.1.1. Mantle source components

The most commonly used depleted mantle model (DM) assumes linear depletion, with $\epsilon_{\text{NdT}} = 0$ at 4.5 Ga and $\epsilon_{\text{NdT}} = +10.4$ at 0 Ga (Goldstein, 1984). However, depleted mantle model values (DM_T) are significantly higher than the ϵ_{NdT} reported for many primitive Archean magmatic rocks, e.g., the freshest and least-altered komatiites from the c. 3.5-3.3 Ga Barberton greenstone have ϵ_{NdT} approximately +0.5 (Puchtel *et al.*, 2013) whereas DM_{3300} is + 2.9, indicating that the Archean mantle was less homogeneously depleted than it has been since the Phanerozoic.

In the northwestern Youanmi Terrane, there have been a small number of samples that have ϵ_{NdT} approximating or higher than DM_{2800} ($\epsilon_{\text{NdT}} + 3.9$), however most of these were from altered olivine cumulates or gabbros (e.g., Wyman and Kerrich, 2012; Nebel *et al.*, 2013; Ivanic *et al.*, 2015) that are more prone to disturbance of isotopic ratios due to changes in REE concentrations. Two felsic rocks reported by other studies (andesite sample 198298 with $\epsilon_{\text{Nd2813}} +3.0$ and tonalite sample 98968104 with $\epsilon_{\text{Nd2813}} +4.0$) have higher ϵ_{NdT} than most of the mafic rocks in this study area and the significance of this is not presently understood. The vast majority of northwestern Youanmi samples, however, have $\epsilon_{\text{NdT}} \leq +2$, including tholeiitic basalts and gabbroic rocks that based on trace element ratios do not appear to have assimilated significant volumes of felsic crust, nor been significantly altered (Chapters 3–4; Lowrey *et al.*, 2019). This indicates that the mantle sources to the c. 2820–2782 Ma (magmatic episode 1 of this study) northwestern Youanmi Terrane primitive magmas were either less depleted than DM or had been broadly refertilised by less radiogenic crustal components. On this basis, the modelled DM and derivative crustal evolution models, such as T2DM, are treated with caution and are used simply as qualitative indicators for crust-mantle interaction and to identify regions of relatively juvenile magmatism and crustal reworking.

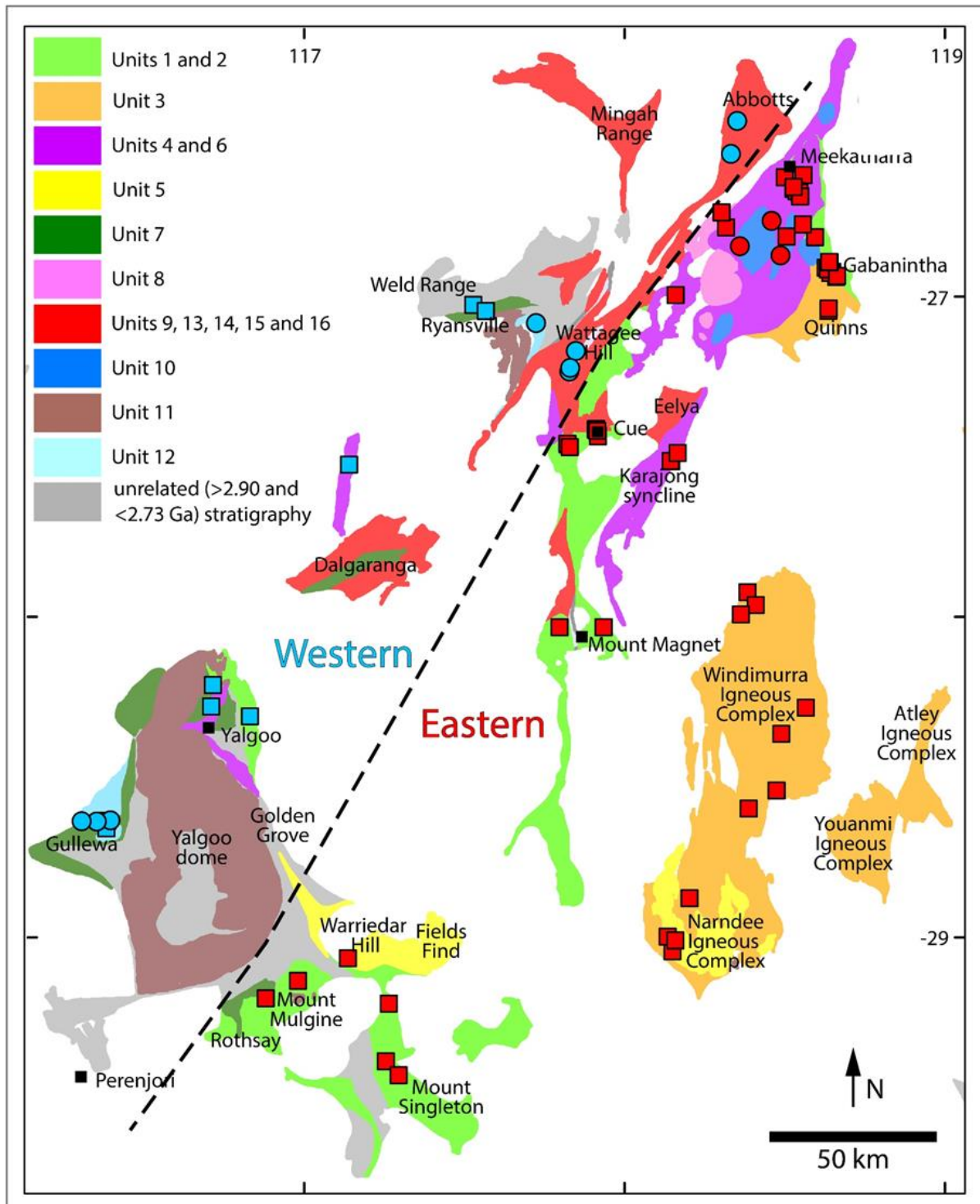


Figure 5.1 Locations of Sm-Nd analyses (including publically available data; Lu et al., 2021) overlaid on the chemostratigraphic unit map and classified into magmatic episode 1 (square symbols) and magmatic episode 2 (circle symbols) as well as whether they are from the eastern (red symbols) and western (blue symbols) sides of the study area.

Figure 5.2 plots ϵ_{NdT} against crystallization age for *c.* 2820–2738 Ma aged magmatic rocks and shows a minor break in ϵ_{NdT} values at around -1. A spatial assessment of the data reveals an

apparently strong geographic control in the distribution of the isotopic ratios: samples eastward of a line (approximately) from Meekatharra to the southern end of the Yalgoo Dome (Fig 5.1.) have ϵ_{NdT} mostly from +2.1 to -0.3, while samples west of that line have ϵ_{NdT} mostly from -1.4 to -4.1 (Fig 5.2).

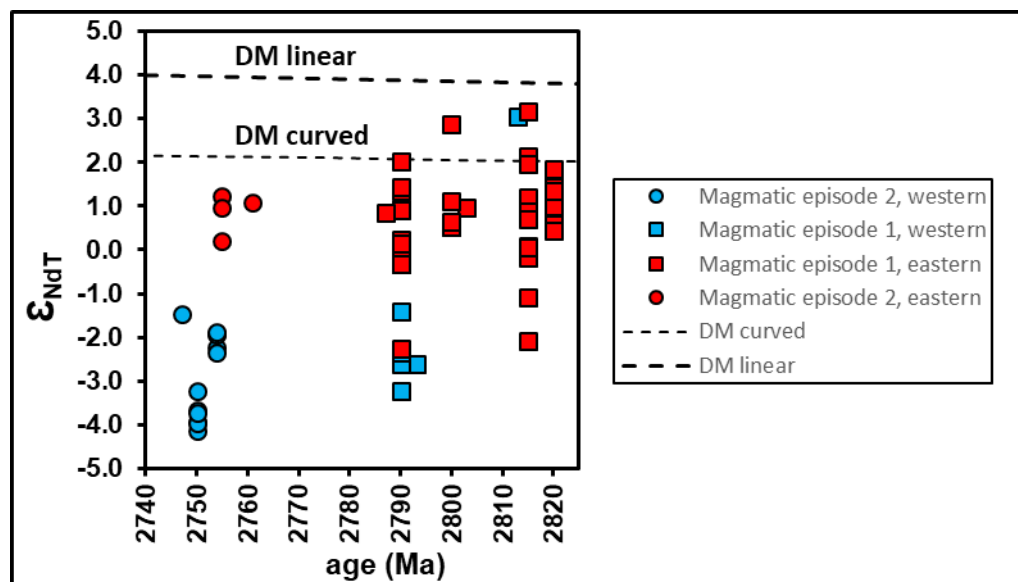


Figure 5.2. ϵ_{NdT} versus crystallization age for c. 2820–2738 Ma aged magmatic rocks in the study area

Table 5.1. ϵ_{NdT} for c. 2820 to 2738 Ma magmatic rocks from this study area			
		Magmatic episode 1	Magmatic episode 2
Eastern	Range	+3.2 to -2.2	+ 1.2 to -0.2
	Average	+0.8 (σ 1.1)	+0.9 (σ 0.3)
Western	Range	+3.0 to -3.2	+1 to -4.1
	Average	-1.1 (σ 2.1)	-2.2 (σ 1.2)

Table 5.1 shows the ϵ_{NdT} ranges and averages for samples grouped by magmatic episode and by whether they are located east or west of the dashed line in Fig 5.1. The isotopic range from magmatic episode 1 is broader and skewed towards more juvenile ϵ_{NdT} values than magmatic episode 2. Additionally, samples from the eastern side of the study area are generally more juvenile than samples from the western side, particularly those from magmatic episode 2 (Fig 5.2). Although sample localities are widely spaced, the data are representative enough of the stratigraphy to show that ancient, evolved (crustal) source components had a stronger influence on magmas in the western part of the study area than in those from the east.

The generally higher ϵ_{NdT} and more juvenile T2DM model ages of samples from the eastern side of the study area can be explained by melting of mantle sources that included variable (but relatively minor) contributions from isotopically evolved crustal components with compositions similar to *c*. 3050–2920 Ma crust from the Weld Range to Golden Grove and from Southern Cross to Ravensthorpe (GSWA 2020) (Fig 5.3). In Chapter 3, it was suggested that the mantle sources of boninite-like rocks and other mafic lithologies in magmatic episode 1 were metasomatised by fluids from a subducted slab, while the mantle sources of intermediate-felsic samples from magmatic episode 2 were metasomatised by young sedimentary components. That hypothesis has remained compatible with the additional data collected from the eastern side of the study area since Chapter 3 was published (Electronic Appendix 1.2), however the implications of Sm-Nd ratios from the western side of the study area are more complicated because of the wider variety of intermediate–felsic lithologies.

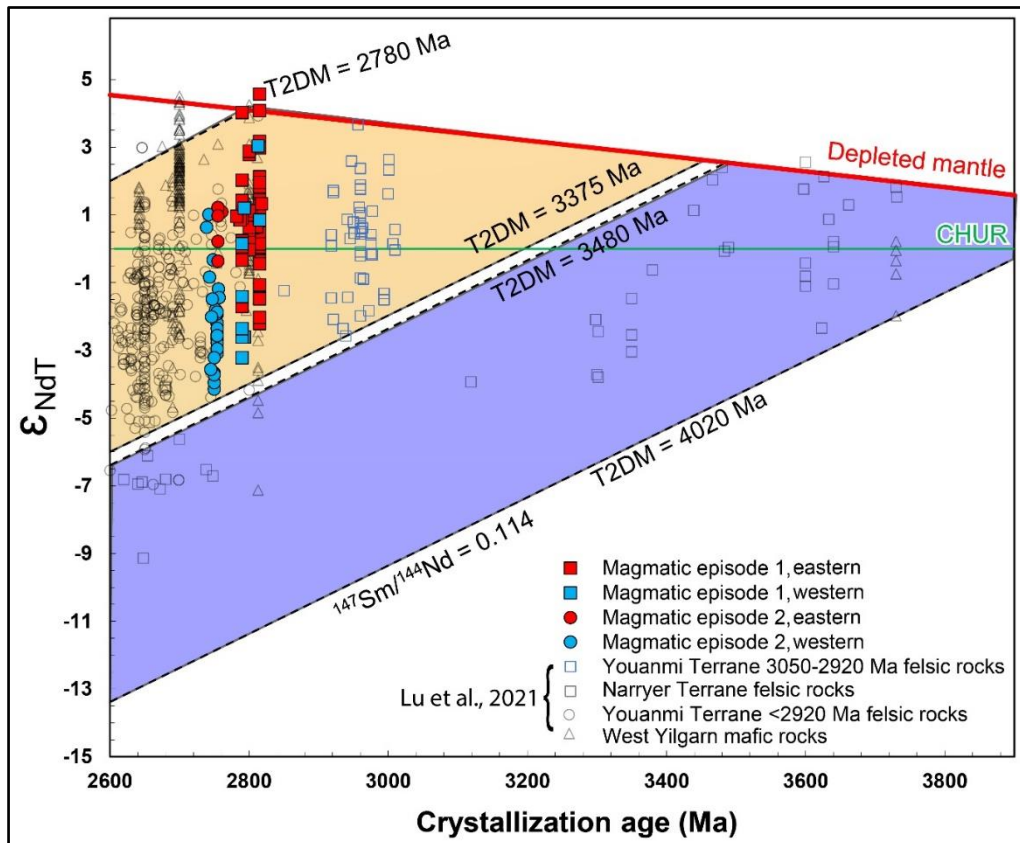


Figure 5.3. ϵ_{NdT} vs magmatic age showing crustal evolution pathways for Murchison (orange) and Narryer (purple) Terrane samples. Diagonal black dashed lines indicate crustal isotope evolution pathways assuming $^{147}\text{Sm}/^{144}\text{Nd} = 0.114$. Additional data was compiled by Lu et al., 2021.

The higher ϵ_{NdT} and more ancient T2DM model ages for samples from the western side of the study area, require source metasomatism with relatively greater contributions from 3050–2920 Ma crust, and (or) assimilation of 3050–2920 Ma basement crust in some lithological units. The chemostratigraphic units in the western side of the study area that are best constrained in terms of Nd-isotopic range include the siliceous high-Mg basalts of Unit 7 (Meekatharra Formation), transitional TTGs of Unit 11 (Rothsay Suite), shoshonitic rocks of Unit 12 (also Rothsay Suite), and transitional tholeiitic rocks of Units 13 and 14 (Meekatharra and Greensleeves Formations).

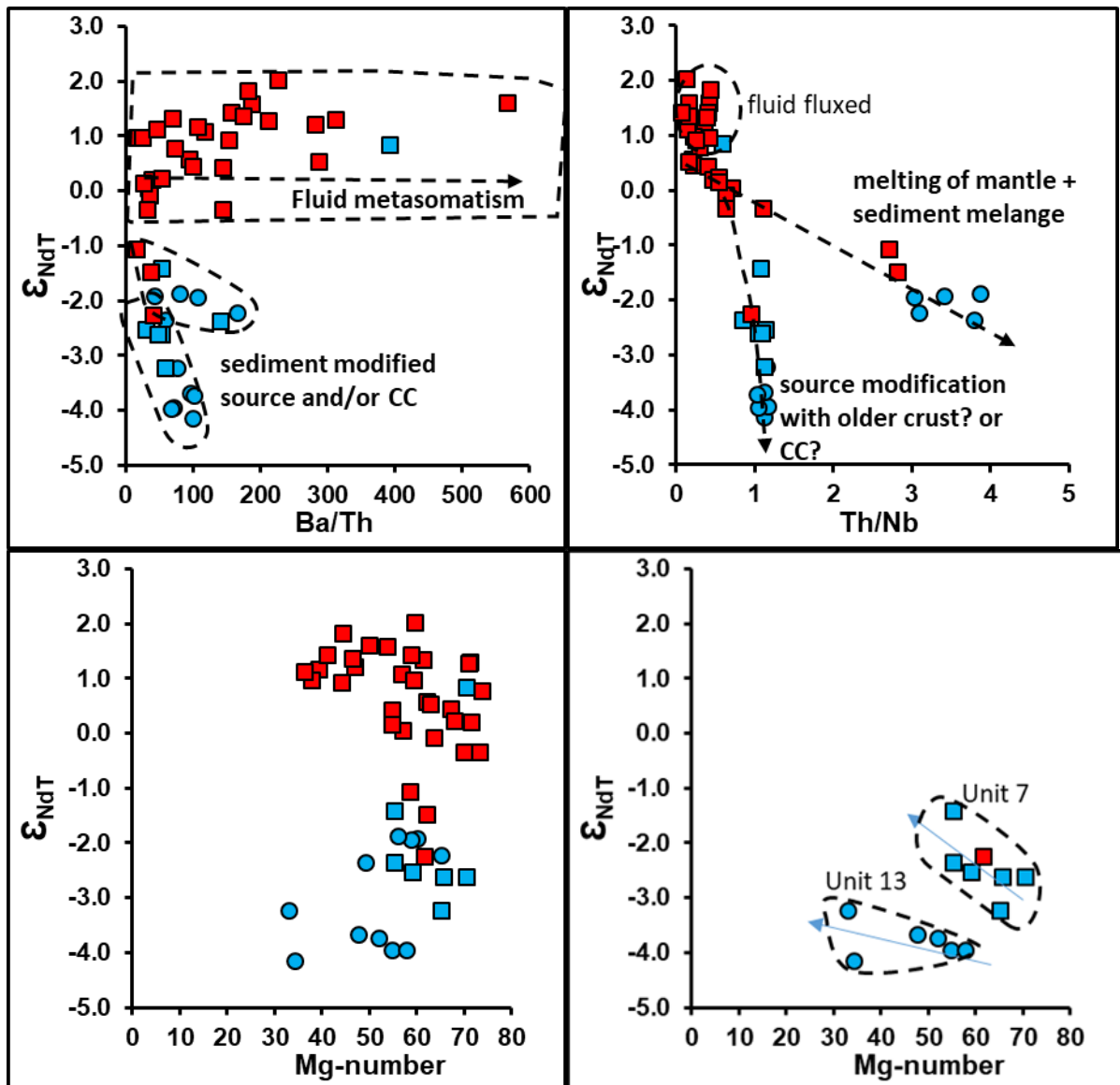


Fig 5.4. Sm-Nd isotopic and whole rock chemical systematics: a) ϵ_{NdT} vs Ba/Th; b) ϵ_{NdT} vs Th/Nb; c) ϵ_{NdT} vs Mg-number; d) ϵ_{NdT} vs Mg-number for Units 7 and 13 only. Symbols as per Figure 5.3. Note, this figure only shows results from this study.

Figure 5.4a shows one trend with variable Ba/Th at relatively constant ϵ_{NdT} , which is interpreted here to reflect mantle sources that have been variably metasomatised by fluids during dehydration of altered crust, and two shorter trends towards low ϵ_{NdT} with increasing Ba/Th, which are consistent with melting of a sediment modified source or crustal contamination involving 3050–2920 Ma aged material, or both. Figure 5.4b shows two distinct trends for the samples that have $\epsilon_{\text{NdT}} < 0$. In one of the trends, Th/Nb increases with decreasing ϵ_{NdT} , while in the other trend Th/Nb remains constant at ~ 1 over approximately 2 ϵ_{Nd} units.

Samples that plot on the trend with constant Th/Nb ~ 1 and variable ϵ_{NdT} are not easily reconciled with a single petrogenetic process. Most of the samples that plot along this trend belong to Units 7 and 13, which contain (or are related to units that contain) inherited 3035–2950 Ma zircons and, very rarely, Paleo-Eoarchean zircons (Table 1.1), that together with the low ϵ_{NdT} , could be interpreted as evidence for assimilation of basement crust. However, the strikingly different major element and incompatible trace element compositions of these two Units are not easily relatable to one another by fractionation or assimilation fractional crystallization, and intra-unit trends, such as increasing ϵ_{NdT} with decreasing Mg-number (Fig 5.4d), are not consistent with assimilation fractional crystallization involving an isotopically ancient assimilant. On the contrary, if assimilation fractional crystallization was involved, then the ϵ_{NdT} –Mg-number trends suggest the parental magmas had lower ϵ_{NdT} than the assimilant, which would in turn indicate that the mantle sources of Units 7 and 13 had been metasomatised by ancient crustal components, and that any subsequent assimilation involved more radiogenic 3050–2920 Ma basement crust. Inherited zircons have so far only been identified in felsic end member samples (i.e., geochronology samples), consistent with both hypotheses, leaving the origins of this isotopic trend presently unresolvable.

The second trend in Figure 5.4b, where Th/Nb increases with decreasing ϵ_{NdT} trend, is more easily explained. All of the samples on this trend, which include shoshonitic rocks (lamprophyres, trachytic andesites and hornblende-rich granites) and primitive andesites from the Hybrazil area, have mildly to strongly negative Zr-Hf anomalies ($\text{Zr}/\text{Zr}^* 0.4\text{--}0.9$), i.e., decoupling of Zr and Hf from Sm and Nd, that in subduction-zone magmas have been attributed to hydrous partial melting of pelagic

sediments on the slab, in equilibrium with residual zircon (e.g., Tollstrup *et al.*, 2010, Hirai *et al.*, 2018). Furthermore, the shoshonitic samples (Unit 12) that plot on this trend, which include primitive compositions (Mg-numbers ≤ 65), are very K₂O- and P₂O₅-rich, indicating phlogopite- and apatite-rich mantle sources. Collectively, high Th/Nb, K₂O, P₂O₅ and low Zr/Zr* in rocks with Mg-numbers ≥ 60 are best explained by melting of sediment-mantle mélange sources, and it is interpreted that the other samples plotting on the trend where Th/Nb increases with decreasing ϵ_{NdT} shared similarly sediment-rich mantle sources.

5.2. PETROGENETIC IMPLICATIONS OF INTERMEDIATE TO FELSIC MAGMATIC ROCKS

Based on the chemostratigraphic assessment in Chapter 4, intermediate to felsic rocks from between 2818 to 2738 Ma in the northwestern Youanmi Terrane can be divided into three broad categories: (1) groups of samples that follow typical tholeiitic liquid lines of descent and are either unenriched in LILEs and LREEs (relative to primitive mantle; Unit 3) or strongly enriched in LILEs and LREEs (Units 9 and 14); (2) groups of samples that share the high-Mg, Ni, Cr characteristics of sanukitoid (Shirey and Hanson, 1984), or more siliceous compositions that can be related by liquid lines of descent to sanukitoid compositions (i.e., sanukitoid-like)(Units 4, 8, 10 and 14); and (3) groups of moderately- to ultra-potassic rocks that resemble ‘transitional TTGs’ (Unit 11; e.g., Champion and Smithies, 2007) or ‘shoshonitic’ rocks (Unit 12) respectively. Each of these categories contain a range of variably evolved chemical compositions, but samples within each category are considered to have followed broadly similar petrogenetic processes, summarized below and tabulated in Chapter 4 (Table 4.1).

5.2.1. Tholeiitic and transitional-tholeiitic rocks

Basaltic to rhyolitic volcanic rocks from Unit 3 (Magmatic Episode 1) follow a tholeiitic line of liquid descent and have mantle normalised MREE-HREE patterns that remain flat and elevated over a broad fractional crystallization window. These characteristics are consistent with either low-pressure fractionation dominated by olivine, pyroxene and plagioclase, in upper crustal tholeiitic magma chambers undergoing periodic magma recharge, or by partial melting of basaltic rocks (e.g. Hart *et*

al., 2004), or a combination of both. Hart *et al.*, (2004) studied the relationship between bimodal mafic and felsic volcanic rocks and VMS mineralisation in the Abitibi Subprovince of the Superior Province (Canada) – a subset of their rhyolitic samples (their F_{IV} type) have similar trace element patterns to andesitic-rhyolitic samples from Unit 3. Hart *et al.* (2004) propose that this type of rhyolite forms via low-pressure (<10 km) moderate-degree partial melting of basaltic rocks – the heat source being high-temperature, ultramafic-mafic magmas that intruded the crust within the zone of brittle fracture permeability (10-15km), the latter interpretation being important for the generation of significant VMS-hosting hydrothermal alteration systems. Applying this model to the tholeiitic felsic volcanics in the western Youanmi is suitable for explaining Unit 3 localities where compositions are bimodal mafic and felsic, e.g. in the Quinns mining district (Figs 4.1, 4.7) and can explain the intimate association between Unit 3 rhyolites and VMS mineralisation (e.g. Hollis *et al.*, 2015; Duuring *et al.*, 2016) as well as the close spatial, temporal and compositional similarities of Unit 3 rhyolites to the voluminous layered intrusions of the tholeiitic c. 2815 Ma Meeline Suite (e.g., Windimurra; Ivanic, 2019). However, the range of magma compositions at the Youanmi and Atley Igneous Complexes (Figs 4.1 and 4.7), with no distinct compositional break between mafic and felsic end-members, suggests that low-pressure fractionation dominated by olivine, pyroxene and plagioclase also played a role in at least some of the intermediate-felsic magmas. Collectively, the range of approximately chondritic ϵ_{NdT} (+1.2 to +0.1) in Unit 3 and Meeline Suite samples is consistent with generally shallow melting of relatively undepleted asthenospheric sources.

Basaltic andesites and gabbros, high-Si rhyolites and granodiorites from Units 9, 13 and 14 (Magmatic Episode 2) have flat and elevated MREE-HREE patterns, broadly similar to Unit 3, however, their strong LILE-LREE enrichments and very low ϵ_{NdT} (-2.0 to -4.1 in Units 13 and 14; Electronic Appendix 1.2) indicate significant involvement of an ancient crustal component. The incompatible trace element patterns of Units 9, 13 and 14 are in most respects transitional between typical tholeiitic felsic rocks, such as those in Unit 3, and sanukitoid (or sanukitoid-like) felsic rocks, such as those in Units 4, 8, 10 and 14. These transitional tholeiitic rocks are analogous to VMS-associated rocks of the Abitibi belt's Blake River Assemblage that have been ascribed to mixing of

asthenospheric derived tholeiitic magmas and subduction related calc alkaline magmas or to melting of mantle hybridized by slab melts (Lafleche *et al.*, 1992; Wyman, 2003).

Although transitional tholeiites in this study area have the least radiogenic Sm-Nd isotopic ratios of the intermediate-felsic rock categories discussed here, their Nd isotopic systematics are inconsistent with assimilation of ancient crust, e.g., figure 5.4d shows a trend towards higher ϵ_{NdT} with decreasing Mg-number, which suggests that the parental melts to the transitional tholeiites had acquired their strongly non-radiogenic isotopic signatures early on. It is still possible that crustal assimilation contributed to the high Th/Nb in Unit 3, but the assimilated material would have to have been isotopically more juvenile than the basaltic melt itself. Nevertheless, ruling out basement assimilation as the origin for the very low ϵ_{NdT} leaves crustal recycling of isotopically and chemically evolved crust into the mantle source as the most reasonable explanation for their enrichment. An estimate of the crustal compositions involved, based on two-stage depleted mantle model (T2DM) ages implicates *c.* 3212–3375 Ma crustal components, however, this is also compatible with recycling of *c.* 3050–2920 Ma crustal components based on compositional data compiled by Lu *et al.*, (2021) (Fig 5.5a). An origin involving crustal recycling is also consistent with the observation that some samples in this category contain igneous hornblende, such as the granodiorite at Cue, indicating their parental magmas contained moderate amounts of H₂O.

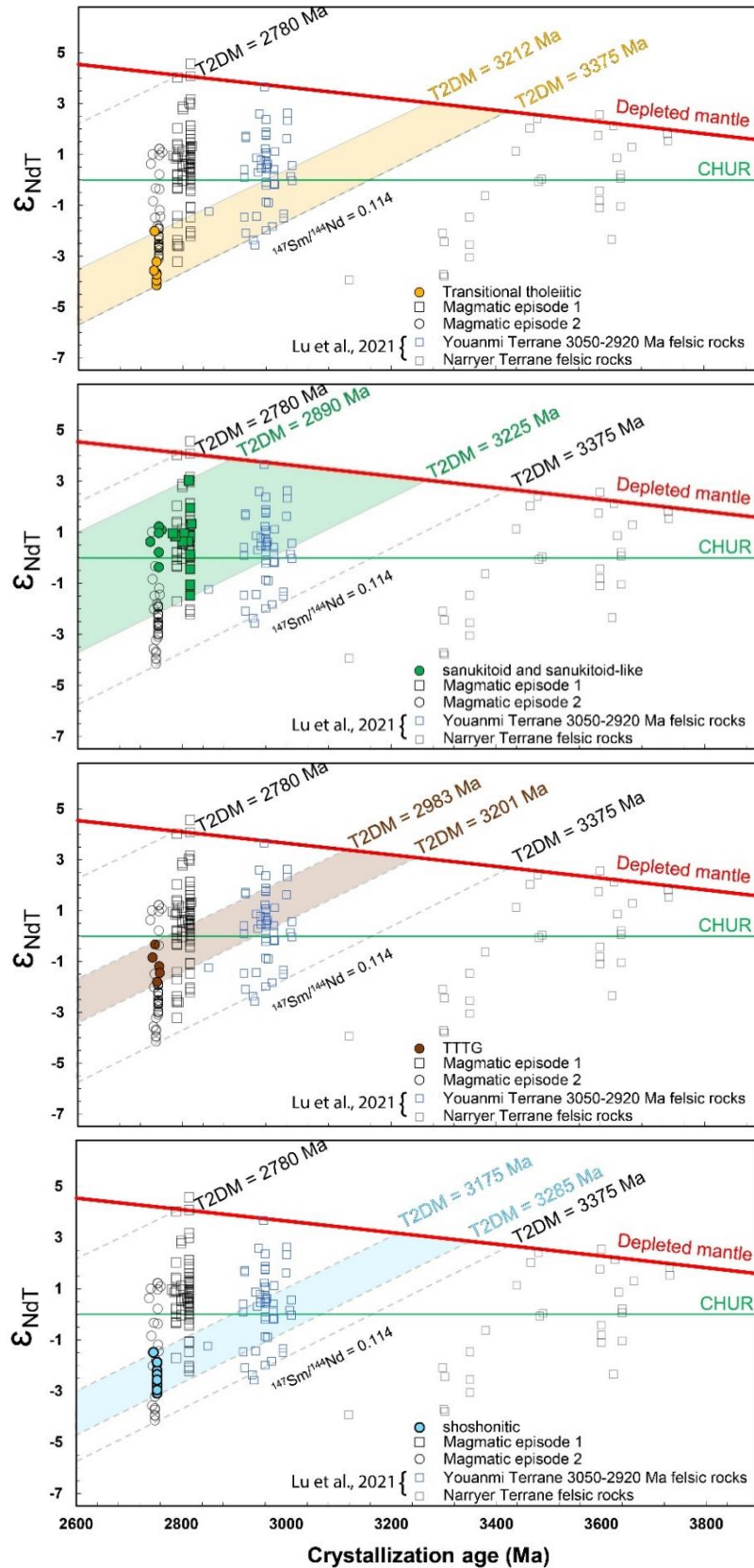


Figure 5.5. ϵ_{NdT} vs magmatic age for intermediate-felsic magmatic rocks: a) transitional tholeiitic rocks (includes basaltic andesites from Unit 13 and rhyolites from Unit 14); b) sanukitoid and sanukitoid-like rocks; c) transitional TTG rocks; d) shoshonitic rocks (including Hbl-Bt-granites, trachyandesitic volcanoclastics and lamprophyres). Diagonal grey dashed lines indicate an envelope of crustal isotope evolution pathways for magmatic episode 1 and 2 (assuming $^{147}\text{Sm}/^{144}\text{Nd} = 0.114$). Shaded polygons indicate envelope of crustal evolution pathways specific to each lithological category.

5.2.2. Sanukitoids and sanukitoid-like rocks

Four chemostratigraphic units (Units 4 and 8 in magmatic episode 1 and Units 10 and 14 in magmatic episode 2) contain samples that meet Shirey and Hanson's (1984) definition for 'sanukitoid', i.e., silica-oversaturated melts with high Mg-numbers, high Ni, Cr and LILE abundances. These units include a variety of basalt-andesite-dacite-rhyolite (BADR) rocks and coeval intrusive rocks that follow calc-alkaline fractionation trends.

Calc-alkaline felsic magmas, in general, can form by a wide variety of petrogenetic processes, but the high MgO (Mg-number), Ni and Cr of sanukitoids requires that their parental magmas were in equilibrium with mantle. Assimilation of basement crust is precluded as a primary process for LILE-LREE enrichment because these felsic magmas have ϵ_{NdT} mostly +1 to 0, which is comparable to those of contemporaneous mafic magmatic rocks, and fractionation does not seem to strongly affect their ϵ_{NdT} (Fig 5.4c), whereas assimilation of regional basement as a primary cause for LILE-LREE enrichment would be expected to also lower their ϵ_{NdT} . Crustal assimilation also fails to explain the source for H₂O required to produce hornblende, which is a common feature of these rocks. Given intermediate-felsic magmas in magmatic episode 1 were emplaced together with hydrous mafic magmas, such as hornblende gabbros (Ivanic, 2015), Alaska-type gabbros (Wyman 2019) and volcanic equivalents (this study), picrites and boninite-like magmas (Lowrey *et al.*, 2019), and in magmatic episode 2 together with shoshonitic rocks, it is fair to assume that their LILE-LREE enrichments are the result of crustal recycling into, and hybridization with, their mantle source prior to or during melting. The high-Mg numbers of sanukitoid and sanukitoid-like rocks indicate high melting temperatures, relative to other calc-alkaline magmas, and may relate to upwelling asthenosphere, e.g., in a slab edge/window position, as proposed for boninites dredged from the northern termination of the Tonga Trench (Falloon *et al.*, 2008). Slab-edge/window settings have also been implicated for high-degree slab melting and adakite petrogenesis (e.g., Thorkelson and Breitsprecher, 2005).

In magmatic episode 2, the least-evolved end member compositions have relatively low Sr/Y (10–30), though at 63% SiO₂ there is a marked increase in Sr concentration, resulting in higher Sr/Y

(30–65) compositionally similar to adakite. In the modern geologic record, adakitic magmas reflect primary slab melts, slab melts hybridized by peridotite, or melts derived from peridotite metasomatised by slab melt (Rapp *et al.*, 1999). It is possible that higher Sr/Y rocks are related to plagioclase accumulation rather than differences in source composition. However, given that primitive end-member samples can be explained by melting of metasomatised arc wedge mantle above a subducting slab, the high Sr/Y adakitic rocks may reflect magmas derived from melting of the slab itself, or given their high Cr and Ni, slab melts that have equilibrated with peridotite. Although, given magmatic episode 2, appears to be post-orogenic in timing, these samples are more likely to reflect partial melting of a foundering slab or part of the slab that has broken off and melted due to influx of hot upwelling asthenosphere.

An estimate of the age of crustal components being recycled into their mantle sources based on T2DM model ages range from *c.* 2890–3225 Ma (Fig 5.5b), however it is more likely that these T2DM model ages reflect hybridization between primitive to depleted mantle with *c.* 3050–2920 Ma crustal components.

5.2.3. Transitional TTGs and Shoshonites

In the western side of this study area, *c.* 2763–2742 Ma potassic granite plutons occur in two belts; (1) in the Yalgoo to Singleton greenstone belt and (2) approximately 20 km southeast of Ryansville and towards the Mingah Range area (Fig 4.1), most of which have been formally assigned to the Rothsay Suite. The vast majority of these plutons have compositions resembling transitional TTG (TTTG) of Champion Smithies (2007), which have higher K₂O, LILEs, Th, and U than typical sodic TTGs. Where TTG magmas are typically interpreted to require high pressure melting of a mafic source (subducting basalt slab or underplating of lower basaltic crust or just thick crust – or indeed not-so thick crust), TTTGs from several Archean cratons have been shown to require more evolved, higher-K sources, i.e., mafic crust infused with felsic components, such as TTG for example (Moyen *et al.*, 2003; Champion and Smithies, 2007; Farina *et al.*, 2015). The range of ϵ_{NdT} values for TTTG rocks in this study area (+0.9 to -2.1) is consistent with melting of *c.* 3050–2920 Ma basement crust or crust of similar composition (Fig 5.5c).

The second, less common, variety of potassic granite in western side of this study area classify as quartz monzonites according to TAS classification schemes (Middlemost, 1994) and plot within the ultra-potassic ‘shoshonitic’ field of Peccerillo and Taylor (1976). The shoshonitic granites are typically easy to distinguish from the TTTGs by their hornblende-biotite(-titanite) rich mineralogy, often including mafic clots or enclaves (e.g., sample 229222, a mafic clot with broadly similar composition incompatible trace element ratios to the hornblende-biotite-granite itself) in the granitic body, and by their notably higher-MgO, -K₂O, -P₂O₅, Ni and Cr compositions. However, in one location near Ryansville, where hornblende-biotite granites and shoshonitic lamprophyres are observed inter-fingering together (Fig 5.6), there is a small compositional overlap between TTTG compositions and the shoshonitic granites (Fig 5.7), possibly related to hybridization between TTTG magmas and the shoshonitic lamprophyres.

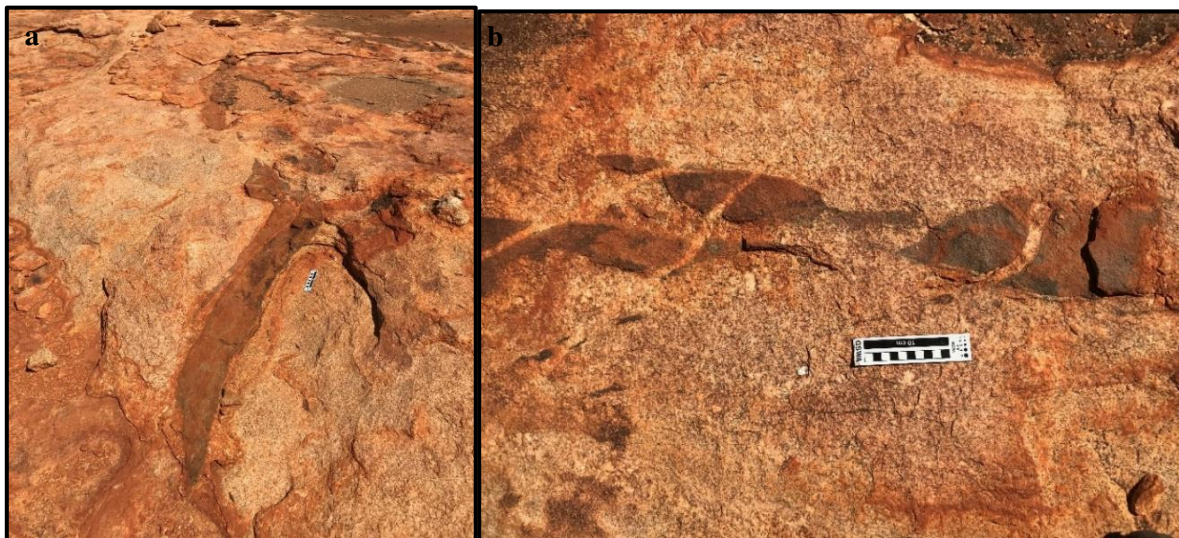


Fig 5.6.a and b. Co-magmatic mafic dykes with shoshonitic compositions and cusped margins inter-fingering with granitic magmas of variably shoshonitic to TTTG compositions; photos provided by Tim Ivanic.

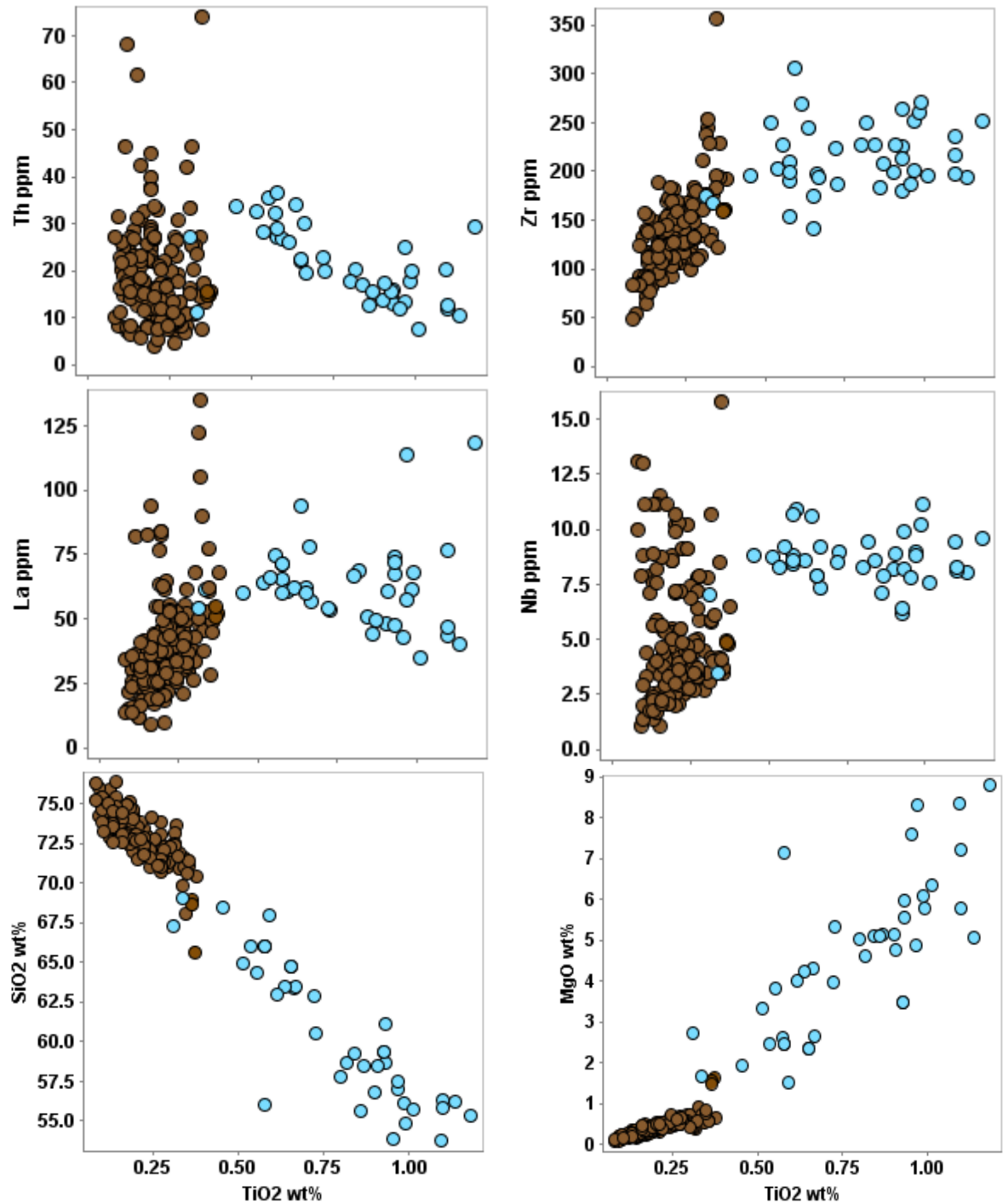


Figure 5.7. Incompatible trace element comparison between TTTGs and shoshonitic rocks (including hornblende-biotite granites, trachyandesitic volcanoclastics and lamprophyres): a) Th vs TiO₂; b) Zr vs TiO₂; c) La vs TiO₂; d) Nb vs TiO₂; e) SiO₂ vs TiO₂; f) MgO vs TiO₂.

With Mg-numbers, Ni and Cr concentrations comparable to sanukitoids, the shoshonitic rocks require a parental melt with a mantle source, while studies of Phanerozoic magmas with similarly high-K₂O and -P₂O have drawn clear conclusions that such melts require phlogopite (e.g. Conceição & Green, 2004) and apatite in their source (e.g. O'Reilly & Zhang, 1995), which in turn requires

source-metasomatism involving a more compositionally evolved (felsic) crustal component compared to sanukitoid sources. The very low ϵ_{NdT} values for shoshonitic rocks in this study area (-1.6 to -3.1) and old T2DM ages (*c.* 3175–3285 Ma; Fig 5.2d) indicate that metasomatism of their mantle source involved Paleoarchean components, which may have been *c.* 3730–3300 Ma ‘Narryer-aged’ crustal components, or indeed *c.* 3050–2920 Ma crustal components, based on the range of isotopic values in publically available datasets (e.g., Lu *et al.*, 2021)(Fig 5.5d).

The compositions of the TTTG and shoshonitic rocks in this study area are generally similar to potassic granites and shoshonitic rocks (including shoshonitic lamprophyres) from post-orogenic continental collision settings, such as the Mesozoic Tibetan Plateau for example, where close spatial and temporal associations between shoshonitic diorites and lamprophyres, and potassic granites with adakite-like Sr/Y ratios are well documented (Chung *et al.*, 2003; Gao *et al.*, 2003; Guo *et al.*, 2007; Wang *et al.*, 2008; Yang *et al.*, 2015; Lu *et al.*, 2015). In this study area, the shoshonitic and TTTG rocks are clearly part of the same broad magmatic event at *c.* 2761 to 2740 Ma, with metasomatised K-rich mantle and K-rich crustal sources respectively and given the apparent *c.* 20 Ma hiatus between magmatic episodes 1 and 2, could well reflect a post-orogenic event relating to collapse of the arc system (i.e., slab break off or delamination) that was formed during magmatic episode 1.

5.3. GEODYNAMIC SETTING

5.3.1. Non-subduction models for crust-mantle interaction

Recently, non-subduction models for crust-mantle interaction have been favoured to explain Archean arc-like magmas, particularly where there is strong evidence for vertical tectonic processes at the outcrop and regional scale such as ‘dome and keel’ structures in the Pilbara (e.g., Johnson *et al.*, 2017; Smithies *et al.*, 2021), or significant numbers of komatiites, as is the case in the Kalgoorlie Terrane and the Abitibi belt (Smithies *et al.*, 2019; Mole *et al.*, 2021). In the northwestern Youanmi Terrane, however, the sequence of primitive arc-like rocks in magmatic episode 1 overlain by evolved-arc like rocks in magmatic episode 2 requires a dominantly metasomatised source region becoming progressively enriched over the tectonic period – *c.* 2817 to *c.* 2738 Ma (Chapter 3). The zircon record and lithostratigraphy indicate a *c.* 35 Ma period of essentially uninterrupted magmatism

(magmatic episode 1), followed by a *c.* 20 Ma period of quiescence and then a second *c.* 20–30 Ma period of magmatism (magmatic episode 2), that included lamprophyres, shoshonites, sanukitoids (and sanukitoid-like rocks) and transitional TTGs which are interpreted here as post-orogenic suites. This stop-start nature of magmatism is not easily reconciled with non-subduction models that would require multiple plumes, several 10's Ma apart, to ascend from the D'' layer at the core–mantle boundary (Campbell *et al.*, 1989; Van Kranendonk *et al.*, 2013) towards the same region in the upper crust or, in the case of delamination/drip models, repeated destabilisation and separation of the dense lower crust. Furthermore, certain chemical characteristics of the *c.* 2820–2738 Ma stratigraphy are difficult to reconcile with alternative models, such as crustal drip tectonics.

5.3.1.1. High field strength element anomalies

One feature that may potentially discriminate between mantle hybridization by subduction versus other crust-mantle interactions (i.e., sags/drips or delamination) is the decoupling of HFSE (particularly Zr and Hf) from similarly incompatible REEs. Decoupling of Zr and Hf from Sm and Nd in subduction-zone magmas has been attributed to hydrous partial melting of pelagic sediments on the slab, in equilibrium with residual zircon, which produces strongly negative Zr-Hf anomalies (Zr/Zr^* and $Hf/Hf^* \ll 1$ or $\gg 1$; e.g., Tollstrup *et al.*, 2010, Hirai *et al.*, 2018). This implies melting temperatures that are high enough for sediments to melt (750–800°C at 2 GPa, 800–825°C at 3 GPa, 1000–1050°C at 4 GPa; Johnson and Plank, 1999), but low enough that zircon remains as a residual phase. Hermann and Rubatto (2009) conducted melting experiments on pelagic sediments under a range of pressure-temperature conditions relevant to slab melting (2.5–4.5 GPa and 750–1050 °C) and found zircon (among other accessory minerals) persisted up to 1000 °C, 4.5 GPa and to high degrees of partial melting (i.e., 55% at 900 °C). They argued that it was unlikely zircon would be eliminated during melting at less than 850 °C in a large range of pelite compositions.

Non-subduction models can be constructed to account for Zr-Hf depleted crustal melts generated from melting in a crustal drip or delamination regime. A key issue, however, is the extent to which hydrous fluids with sediment-like O-isotopic compositions can be delivered to potential mantle source regions. Subduction zones acting over millions of years can demonstrably deliver significant water

and sediment melts to the partially isolated and broadly linear environments of a mantle wedge as they lower the temperature of the local mantle. A major criticism of drip models is that they cannot deliver a similar fluid load (Rollinson, 2007) and the lack of an analogue to the constricted mantle wedge setting requires that the one-pass crustal drips release their fluids radially or diffusely into the convecting upper mantle. Without a sustained “cold finger” effect acting in the vicinity of the crustal drip, it is not established that water in the drip would not be “zone refined” upwards back into the crust as the drip developed, instead of remaining in the descending crustal body until required by drip tectonic models. Indeed, the hydrated mafic crust is commonly envisioned to form early low Sr/Y TTG prior to drip formation and then younger high Sr/Y TTG after being caught in a downward-moving drip without any further addition of hydrous fluids (Nebel *et al.*, 2018; Mole *et al.*, 2021).

Proponents for drip models have argued that negative Nb–Ta–Ti anomalies observed in Archean TTGs, which in the recent geologic record are typically attributed to residual rutile, titanite and/or ilmenite during melting of subduction-modified mantle, could equally be expected during partial melting at pressures and temperatures characteristic of oceanic plateau lower crust (e.g., Bédard, 2006). Assuming that negative Zr-Hf anomalies, which are common in Neoarchean calc-alkaline or shoshonitic lamprophyres and sanukitoid-series rocks (e.g., in the Yilgarn Craton and Superior Province), reflect residual zircon signatures, then it is challenging to reconcile with those same models. Upper crustal material would need to drip through the middle and lower crust, sediments would need to partially melt only after they have been transported into the mantle, and zircon would need to remain stable to impart low Zr/Zr*. This challenge is exacerbated by the fact that prominent negative Zr-Hf depletions are usually relatively late features in any given major Archean volcanic sequence. In the Abitibi belt, for example, the feature becomes prominent only in the later stages of volcanism in the Blake River Assemblage or in orogenic shoshonitic lamprophyres, syenites, etc. (Wyman *et al.*, 2002).

Whether other magmatic process can generate low Zr/Zr*, such as melting in equilibrium with residual amphibole or garnet, is worth further consideration, however it is noted that low Zr/Zr* is not

observed in the vast majority of Archean high pressure TTGs, which are widely considered to be high-pressure eclogite melts.

5.3.2. Towards an arc accretion model

The identification of subduction-related magmas in the Youanmi Terrane, requires a revised model for the tectonic evolution of this part of the Yilgarn Craton between 2820 and 2738 Ma. The impediments to forming a geospatially consistent arc accretion model are that (1) structural complexity has juxtaposed many diverse magmatic rock types, so the distribution of chemostratigraphic units identified in Figure 5.1 only represent broad trends. (2) Metamorphic data is lacking that might show cooler thermal gradients in particular domains at *c.* 2820–2738 Ma. (3) The intrusion of extremely voluminous post-2730 Ma granitic rocks into the Youanmi Terrane mean that it is impossible to know if all components of the two magmatic episodes have been sampled. However, the following sections, detail further refinements to the arc accretion model for the northern Youanmi Terrane published by Lowrey *et al.* (2019; Chapter 3).

5.3.2.1. Crustal architecture and the Cue Isotopic Zone

Earlier craton-scale isotopic investigations of the Yilgarn (e.g., Champion, 2013) identified an anomalous zone of isotopically ‘juvenile’ (low T2DM neodymium model aged) granites in the Youanmi Terrane, which has since been infilled with new isotopic data by the Geological Survey of Western Australia (Lu *et al.*, 2021). The isotopically juvenile zone occurs between Meekatharra in the north, to Mount Singleton in the south, and is referred to here as the ‘Cue Isotopic Zone’ (CIZ) after the town of Cue in the centre of the anomaly (Fig 5.8a). The T2DM model age contours are only derived from felsic samples (i.e., granites and felsic volcanic rocks) and include rocks that pre-date and post-date the magmatic period studied here. Importantly, because the younger granites are interpreted to be derived by melting of lower to middle crustal sources (Champion and Cassidy, 2002), their isotopic ratios (and any entrained xenocrystic zircons) potentially provide an insight into the isotopic compositions and relative ages of source rocks within those crustal domains, including the *c.* 2820–2740 Ma stratigraphy studied here. The relatively radiogenic isotopic ratios of granitic rocks

inside the CIZ indicate that crust in that region was, on average, much younger than most of the Youanmi Terrane and the Western Yilgarn more generally.

Two possible explanations for this isotopically anomalous feature are that (1) the CIZ represents a focal point for ‘juvenile’ magmatism (i.e., the *c.* 2820–2710 Ma magmatic period) that was not expressed as strongly outside of the zone, and/or (2) the CIZ represents an area where isotopically ancient crust (>2920 Ma; Southern Cross Supergroup and Thundelarra Supersuite, and/or older unassigned sequences) was attenuated, or absent. It is difficult to determine whether *c.*2820–2710 Ma magmatism was more prolific inside the CIZ than outside, as magmatic ages in this range are common to both the east and west of the CIZ. However, two lines of evidence do suggest that >2920 Ma basement crust was either attenuated, or absent, inside the CIZ. Firstly, the lower part of the Youanmi Terrane stratigraphy, the Southern Cross Supergroup and Thundelarra Supersuite, has not yet been identified within the CIZ, but is widely distributed immediately outside the CIZ margin. Secondly, among samples that have been dated, very few xenocrystic zircons with Pb-Pb ages > 2900 Ma occur within the CIZ (9 out 1004 zircons labelled ‘igneous’ or ‘xenocrystic’ in the GSWA [2021] geochronology dataset and only 1 zircon reported by Wang [1998]), but are relatively common outside of the CIZ (Table 1.1; Fig 5.8b).

The GSWA zircon dataset also shows that zircons older than the lower Youanmi Stratigraphy are extremely rare, with single >3050 Ma xenocrystic zircons identified in only five samples, all of which are from Magmatic Episode 2 (or later) and located on the margin of the CIZ: (1) *c.* 3258 Ma in a basaltic andesite that is intercalated with 2735–2700 Ma sedimentary rocks in the Yalgoo Singleton Belt (sample 198295; GSWA 2021); (2) *c.* 3263 Ma in a *c.* 2752 Ma felsic tuff in the Weld Range (sample 96-120; Wang, 1998); (3) *c.* 3423 Ma in a *c.*2746 Ma felsic volcanoclastic in the Mingah Range (sample 185937, GSWA 2021); (4) *c.* 3499 Ma in a *c.* 2744 Ma felsic tuff from the Abbotts belt (sample 93-970, Wang, 1998); (5) *c.* 3940 Ma in a *c.* 2746 Ma felsic tuff from the Dalgara belt (sample W298, Pigeon and Hallberg, 2000)(Fig 5.xb).

The pattern of all >3050 Ma zircons occurring in supracrustal rocks deposited during Magmatic Episode 2 is possibly significant for several reasons: (1) a dearth of >3050 Ma zircons in >*c.*2760 Ma

magmatic rocks, including TTTGs that include source components from throughout the crustal section, suggests that >3050 Ma felsic crust was not present in the Youanmi Terrane basement prior to 2760 Ma and is compatible with the Narryer and Youanmi Terranes being separate terranes at that time; (2) >3050 Ma zircons come from samples in belts that are located closest to the Narryer Terrane; and, (3) a sudden appearance of zircons with ages in the range of Narryer Terrane gneisses, in the Youanmi Terrane during magmatic episode 2 coincides with the proposed timing of collision between the Narryer and Youanmi Terranes and can be explained by sediments being shed from the Narryer Terrane into volcano-sedimentary basins after joining with the Youanmi Terrane.

Here it is interpreted that the paucity of basement derived inherited > 2900 Ma zircons and notably more radiogenic isotopic ratios within the CIZ reflects a rift developing in c.3050-2920 crust at c. 2820–2790 Ma. Given the CIZ is positioned 150-250 km southeast of a possible suture zone at the Youanmi-Narryer Terrane boundary, the CIZ potentially represents a back-arc rift, consistent with the variety of observed lithologies in magmatic episode 1, such as boninites, MORB-like tholeiitic basalts, HREE depleted picrites and calc-alkaline high-Mg BADR-series rocks. Mantle sources enriched in K₂O and P₂O₅ together with negative Zr-Hf anomalies in shoshonitic rocks from magmatic episode 2 are consistent with melts originating from sediment-modified mantle mélanges and may reflect a change in the material being subducted or could reflect lithospheric melting during a post-orogenic upwelling event related to slab break off or delamination.

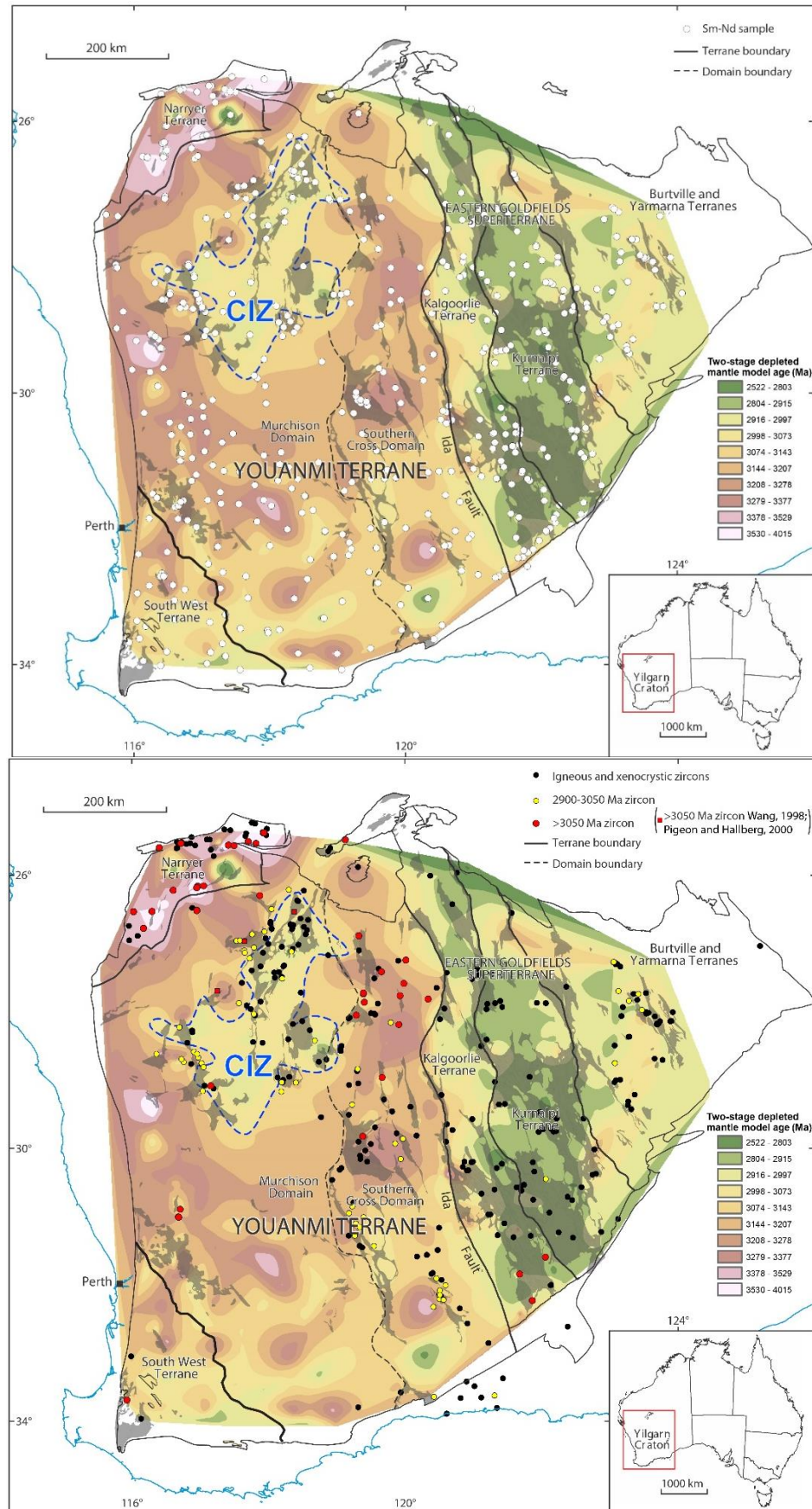


Figure 5.8. Contour map of two-stage depleted mantle model ages derived from Sm-Nd isotopic ratios modified after Lu et al., 2021; a) showing Sm-Nd samples used to contour T2DM; b) showing igneous and xenocrystic zircon Pb-Pb ages from GSWA database (circle symbols; GSWA, 2021) and from Wang (1998) and Pidgeon and Hallberg (2000) (square symbols) .

5.4. FURTHER WORK

The following section briefly considers a number of impediments to forming an arc accretion model that remain but are beyond the scope of this study and warrant further investigation.

5.4.1. Earlier crust building episodes in the western Yilgarn

Detail of the distribution, ages and compositions of basement components and crustal architecture prior to the 2820–2738 Ma magmatic period is needed to further refine the geodynamic arguments presented above.

5.4.1.1. 3050–2920 Ma Southern Cross Supergroup and Thundelarra Supersuite

The distribution of 3050–2920 Ma stratigraphic components are well known, but they are presently under-sampled and compositional information is limited to a small number of local-scale studies (e.g., Golden Grove and Weld Range; Guillianse, 2014). Data emerging from a new GSWA regional study of the 3050–2920 Ma supracrustal and granitic rocks along the Youanmi side of the Youanmi-Narryer Terrane boundary indicate that granitic gneisses are notably more potassic (77% of samples $K_2O/Na_2O \geq 1$), have low Sr/Y ratios (90% of samples $Sr/Y \leq 30$) and Mg-numbers not exceeding 40, suggesting low-pressure melting of crust that included felsic components. Furthermore, *c.* 2985 Ma sanukitoids near Ravensthorpe in the far south of the Youanmi Terrane (Witt, 1998) and zircons with hydrous REE signatures in *c.* 3010 Ma granites from the Wongan Hills (Lu *et al.*, 2019) suggest hydrated, metasomatised mantle sources prior to the magmatic period studied here. Hence, the mantle within this study area may have been already primed for the generation of hydrous LILE-LREE enriched magmas prior to the 2820–2738 Ma period studied here.

5.4.1.2. Paleoproterozoic crust in the Narryer Terrane and the origins of the >3200 Ma zircons in the Youanmi Terrane

The Mount Narryer and Jack Hills metasedimentary belts both contain near-shore fluvial clastic associations with chemical sedimentary rocks and extensive turbiditic sediments (Maas and McCulloch; 1991) and there is a general consensus that the Narryer metasedimentary packages to the west of the Youanmi-Narryer Terrane boundary were deposited in a continental margin setting (see review in Kemp *et al.*, 2019). Surprisingly few geochemical studies have been published on the

granite-gneiss dominated Narryer Terrane and the region between the Youanmi Terrane greenstone belts and the Narryer-Youanmi Terrane boundary, yet if this was a convergent margin, and the northwestern Youanmi greenstone belts represent a back-arc rift as suggested here, then this region may represent the site of the arc itself and chemical data would be of great importance. However, the presence of Paleoproterozoic zircons (c. 12% of samples contain one or more; Wang and Wilde 2018) and metamorphic ages recorded in the Jack Hills metasediments (Spaggiari *et al.*, 2008; Rasmussen *et al.*, 2010) indicate some of these rocks at least were emplaced during the Paleoproterozoic and therefore, the present Narryer-Youanmi terrane boundary was almost certainly modified after the Meso-Neoproterozoic.

Nevertheless, targeted studies of the Paleo-Mesoarchean components could inform chemical and isotopic studies into potential recycled components in the sources to 2820–2738 Ma magmatic rocks.

5.4.2. Subduction zone metamorphism

The validity of Archean arc settings are sometimes questioned based on the absence of blueschists, glaucophane bearing meta-basalts that form at high-pressure and low temperature conditions and are diagnostic of subduction zone metamorphism in the modern geologic record. However, the oldest blueschists are Neoproterozoic in age (0.7 – 0.8 Ga; Palin and White, 2016) and there is broad consensus that subduction has been occurring much earlier than that. Some studies have argued that it is unrealistic to expect the same metamorphic assemblages in Archean subduction related metamorphism because mantle temperatures were hotter and compositions of basaltic crust being generally more magnesian would form greenschists rather than blueschists (Palin and White, 2016).

Greenschist, amphibolite and granulite facies metamorphic rocks are common in the Archean and in most instances likely reflect burial metamorphism at varying crustal depths. In this study area, however, chemical and petrographic evidence from 2820–2738 Ma magmatic rocks indicate widespread refertilisation of the mantle and, at least locally, a sedimentary-mantle mélange component. It is therefore worth considering whether amphibolite-granulite facies rocks adjacent to

the study area, e.g., in the Narryer Terrane and along the terrane margins, reflect subduction zone metamorphism rather than simply burial metamorphism.

Monazite ages in metasediments at Mt Narryer (immediately west of the terrane boundary) show two major peaks; firstly at *c.* 3.3–3.2 Ga, around the time that the Mt Narryer metasediments were deposited (Kinny *et al.*, 1990; Iizuka *et al.*, 2010), and then at 2.7–2.6 Ga, which likely reflects recrystallization during regional metamorphism and ductile deformation associated with the cratonization of the Yilgarn Craton. Based on their REE compositions, the 3.3–3.2 Ga and 2.7–2.6 Ga metamorphic monazites from Mt Narryer grew in equilibrium with garnet, indicating at least two distinct episodes of granulite facies metamorphism (Iizuka *et al.*, 2010 and references within). In contrast, samples from the Jack Hills (60 km NE of Mt Narryer) show negligible metamorphic monazite growth and 3.3–3.2 Ga igneous monazites are preserved, suggesting a lack of high-grade metamorphism in that locality (Iizuka *et al.*, 2010). Hence, there are quite variable grades of metamorphism between the Narryer Terrane metasedimentary belts which suggests that similar aged metasedimentary blocks were either faulted and buried under contrasting P-T conditions, or else potentially the Jack Hills were faulted above the 3.0–2.9 Ga Youanmi crust and were therefore unaffected by the high pressure subduction zone metamorphism expressed at Mt Narryer.

Only one of the Mt Narryer samples convincingly records the 3.3–3.2 Ga metamorphic event, which Iizuka *et al.* (2010) attribute to shielding from metamorphism by garnet; this sample also preserves a smaller peak at 3050 to 2920 Ma, potentially reflecting metamorphism due to continental collision. Except for cryptic evidence such as that sample, however, any diagnostic tectonothermal evidence related to major crust building episodes at *c.* 3050 to 2920 Ma and *c.* 2820 to *c.* 2738 Ma were likely overprinted by widespread high-grade metamorphism and ductile deformation from 2710 to 2600 Ma. Further study of metasedimentary belts along this Terrane boundary, particularly of rocks that contain garnet that may shield the monazite from metamorphic recrystallization, may provide further constraints on older episodes of metamorphism.

Chapter 6: Conclusions

This study has integrated whole rock geochemical, isotopic and petrographic data to evaluate the 2820–2738 Ma magmatic components and geodynamic history of the northwestern Youanmi Terrane, in the western part of the Yilgarn Craton.

Initial attempts to reconcile boninite–low Ti basalt rocks in the Meekatharra Formation with Van Kranendonk *et al.*'s (2013) plume-based tectonostratigraphic model for *c.* 2820–2710 Ma magmatism in the northwestern Youanmi Terrane led to a critical assessment of purported komatiites in the Meekatharra area, which were fundamental to Van Kranendonk *et al.*'s interpretations that magmatism necessitated anomalously high-temperatures of a mantle plume. Chapter 2 (Lowrey *et al.*, 2017) demonstrated that the chemistry and petrography of spinifex textured volcanic rocks in the Meekatharra area are not komatiites, but rather siliceous high-Mg basalts, with platy pyroxene spinifex textures that had been mistakenly identified as olivine spinifex over several generations of field studies, as geologists are commonly taught to distinguish between pyroxene and olivine spinifex textures by their crystal habits. It was shown that these rocks do not necessitate anomalously hot mantle potential temperatures. A subsequent study by Lowrey and Ivanic (2018)(Electronic Appendix 6.1) expanded the distribution of siliceous high-Mg basalts with platy pyroxene spinifex textures beyond this study area to five localities in the Yilgarn Craton and one locality in the Pilbara Craton which had each been previously interpreted as komatiite or komatiitic basalt, demonstrating that this new type of spinifex texture is potentially of great significance to Archean terranes globally. Chapter 3 (Lowrey *et al.*, 2019) showed that purported Al-depleted komatiites lower in the stratigraphy, in the Singleton Formation, are instead high-Mg basalts, picrites and olivine orthocumulates. It was noted that their trace element patterns and incompatible trace element ratios, such as $\text{Al}_2\text{O}_3/\text{TiO}_2$, bear a strong similarity to both Barberton Al-depleted komatiitic rocks and Phanerozoic arc-picrites, and are therefore compatible with melting in the presence of residual garnet (i.e. ≥ 3 GPa) in a mantle plume, or metasomatised mantle source, respectively. However, over the course of this study, every effort was made to investigate all reported komatiite occurrences in the northwestern Youanmi Terrane and

to date no examples have been confirmed. Their absence from the exposed geologic record has clear negative implications for komatiite-hosted nickel sulfide prospectivity and differentiates this study area from komatiite-rich provinces that require very high mantle temperatures, such as the Kalgoorlie Terrane of the eastern Yilgarn Craton. It also raises significant questions about whether a mantle plume is the most appropriate geodynamic model for a stratigraphy where magmatic rocks predominantly have arc-like compositions.

Using a combination of new whole-rock compositions and Sm-Nd isotopic data and existing U-Pb geochronology, a detailed unit by unit magmatic framework has been established consisting of (but not limited to) boninite, LOTI basalt, tholeiitic basalt, hornblende-rich gabbros, high-Mg basalt-andesite-dacite-rhyolite, sanukitoid and hornblende-biotite-rich shoshonitic lamprophyres and granites. Compared to other Archean terranes, the *c.* 2820–2738 Ma northwestern Youanmi Terrane contains perhaps the best preserved and most complete set of rock types that would be considered diagnostic of subduction magmatism in the modern geologic record. The timeline of magmatic events, summarized below is strongly compatible with an arc accretion tectonic setting:

- (1) Th/Yb-Nb/Yb systematics and Nd isotopes suggest LILE±LREE enrichment was a characteristic of *c.* 2820–2738 Ma mantle sources, which evolved in composition over time.
- (2) High-Mg basalts and picrites of the lower Singleton Formation and tholeiitic basalts in the Stockyard Basalt Member erupted with minimal interaction with crust and indicate locally thinned lithosphere and upwelling asthenosphere, consistent with two rifting events at *c.* 2820 Ma and *c.* 2793 Ma.
- (3) Boninite-like rocks and siliceous high-Mg basalts contain magmatic textures, such as varioles, that indicate hydrous melt compositions. The long history of hornblende-rich gabbroic, lamprophyric, andesitic and granitic units in the study area, from *c.* 2815 to 2735 Ma, also indicate widespread hydrous mantle domains.
- (4) Integration of the available geochemical, geochronological and isotopic data implicates two consecutive cycles of depletion and metasomatism at *c.* 2820 and *c.* 2793 Ma mafic magma sources in the northwestern Youanmi Terrane. This requirement cannot be achieved in

sagduction or crustal drip models within the temporal and spatial restrictions imposed by the results of this study. Conversely, two subduction events, *c.* 25 Ma apart, may be attributed to subduction step-back or plate arrangements.

- (5) Following a *c.* 25 Ma hiatus, a second magmatic episode from *c.* 2761–2738 Ma is interpreted to represent a post-orogenic event related to delamination of arc-crust or slab breakoff.
- (6) The mantle sources of mafic rocks in the Singleton Formation and Meekatharra Formation are interpreted to have been metasomatised by fluids derived from hydrated mafic crust whereas the sources to *c.* 2754 Ma shoshonitic rocks are interpreted to have mixed with and been metasomatised by sedimentary components.
- (7) The geodynamic environment is interpreted to have initiated with extension of older Youanmi Terrane crust resulting in oceanic crust, prior to accretionary events confined to the Cue Isotopic Zone.

A number of chemostratigraphic conclusions are also drawn from this study:

- (1) Although broadly of similar ages, there are significant differences in the compositions of supracrustal rocks between greenstone belts.
- (2) Distinctive ‘marker’ units such as boninite like rocks and Al-depleted picrites, which are quite sensitive to contamination, can be traced sporadically for hundreds of kilometres along strike (i.e., between Meekatharra and Mount Singleton in a NNE-SSW orientation), with little variation in composition.
- (3) There is far less compositional continuity in the E-W orientation (i.e., between greenstone belts), than in the N-S orientation (i.e., along strike within greenstone belts), which indicates that there was a N-S control on the emplacement of these rocks originally. Possible explanations include magmatic asymmetry and/or primary belt- or corridor-like nature to the magmatism, but this is likely emphasized by losses of segments the supracrustal sequence, possibly due to E-W shortening and ‘stopping out’ by younger granites (Zibra, 2020).

- (4) The distribution of chemical units indicate a ~300 x 50 km corridor of variably sediment-fluxed mantle wedge-sourced volcanic rocks to the western side of the study area and a ~400 km corridor of back arc-like volcanic rocks to the eastern side of the study area.

References

- Angerer, T., Kerrich, R. and Hagemann, S. G. (2013). Geochemistry of a komatiitic, boninitic, and tholeiitic basalt association in the Mesoarchean Koolyanobbing greenstone belt, Southern Cross Domain, Yilgarn craton: Implications for mantle sources and geodynamic setting of banded iron formation. *Precambrian Research* 224, p. 110–128.
- Armstrong, J. T. (1988). Quantitative analysis of silicate and oxide materials: comparison of Monte Carlo, ZAF, and phi-rho-z procedures. *Microbeam Analysis*, p. 239–246.
- Arndt, N. T. (1977). Thick, layered peridotite–gabbro lava flows in Munro Township, Ontario. *Canadian Journal of Earth Sciences* 14, p. 2620–2637.
- Arndt, N. T. (1982). Proterozoic spinifex-textured basalts of Gilmour Island, Hudson Bay. *Geological Survey of Canada, Paper* 83–1A, p. 137–142.
- Arndt, N. T. (1986). Differentiation of komatiite flows. *Journal of Petrology* 27, p. 279–301.
- Arndt, N. T., Bruzak, G. and Reischmann, T. (2001). The oldest continental and oceanic plateaus: geochemistry of basalts and komatiites of the Pilbara Craton, Australia. *In*: R. E. Ernst and Buchan, K. L. (Eds.) *Mantle plumes: their identification through time*. Geological Society of America, Boulder Colorado. p. 359–387.
- Arndt, N. T. and Fleet, M. E. (1979). Stable and metastable pyroxene crystallization in layered komatiite lava flows. *American Mineralogist* 64, p. 856–864.
- Arndt, N. T., Leshner, C. M., Houlié, M. G., Lewin, E. and Lacaze, Y. (2004). Intrusion and crystallization of a spinifex-textured komatiite sill in Dundonald Township, Ontario. *Journal of Petrology* 45, p. 2555–2571.
- Arndt, N. T., Leshner, C. M. and Barnes, S. J. (2008). *Komatiite*. Cambridge University Press, New York, USA.

Arndt, N. T. and Jenner, G. A. (1986). Crustally contaminated komatiites and basalts from Kambalda, Western Australia. *Chemical Geology* 56, p. 229–255.

Arndt, N. T., Naldrett, A. J. and Pyke, D. R. (1977). Komatiitic and iron-rich tholeiitic lavas of Munro Township, Northeast Ontario. *Journal of Petrology* 18, p. 319–369.

Ayers, L.D. and Thurston, P.C. (1985). Archean supracrustal sequences in the Canadian Shield: an overview. *In: Ayers, L.D., Thurston, P.C., Card, K.D. and Weber, W. (Eds.) Evolution of Archean Crustal Sequences*. The Geological Association of Canada Special Paper 28, p. 343–380.

Ballhaus, C., Fonseca, R.O.C., Münker, C., Kirchenbaur, M., and Zirner, A. (2015). Spheroidal textures in igneous rocks – Textural consequences of H₂O saturation in basaltic melts. *Geochimica et Cosmochimica Acta* 167, p. 241–252.

Baragar, W. R. A. and Scoates, R. F. J. (1987). Volcanic geochemistry of the northern segments of the Circum-Superior Belt of the Canadian Shield. *In: Pharoah, T. C., Beckinsale, R. D., and Rickard, D. (Eds.) Geochemistry and mineralization of Proterozoic volcanic suites: Geological Society, London, Special Publication No 33*. London, UK, p. 113–131.

Barley, M. E., Eisenlohr, B. N., Groves, D. I., Perring, C. S. and Vearncombe, J. R. (1989). Late Archean convergent margin tectonics and gold mineralization: A new look at the Norseman-Wiluna Belt, Western Australia. *Geology* 17, p. 826–829.

Barley, M. E., Kerrich, R., Reudavy, I. and Xie, Q. (2000). Late Archaean Ti-rich, Al-depleted komatiites and komatiitic volcanoclastic rocks from the Murchison Terrane in Western Australia. *Australian Journal of Earth Sciences* 47, p. 873–883.

Barley, M. E., Sylvester, G. C., Groves, D. I., Borley, G. D. and Rogers, N. (1984). Archaean calc-alkaline volcanism in the Pilbara Block, Western Australia. *Precambrian Research* 24, p. 285–319.

Barnes, S.-J. (1985). The petrography and geochemistry of komatiite flows from the Abitibi Greenstone Belt and a model for their formation. *Lithos* 18, p. 241–270.

- Barnes, S. J. (2006). Komatiites: petrology, volcanology, metamorphism and geochemistry. *In*: S. J. Barnes (ed) Nickel deposits of the Yilgarn Craton: geology, geochemistry and geophysics applied to exploration. Society of Economic Geologists. p. 13–49.
- Barnes, S. J. and Roeder, P. L. (2001). The range of spinel compositions in terrestrial mafic and ultramafic rocks. *Journal of Petrology* 42, p. 2279–2302.
- Barnes, S. J. and Van Kranendonk, M. J. (2014). Archean andesites in the east Yilgarn craton, Australia: Products of plume-crust interaction? *Lithosphere* 6, p. 80–92.
- Barnes, S. J., Van Kranendonk, M. J. and Sonntag, I. (2012). Geochemistry and tectonic setting of basalts from the Eastern Goldfields Superterrane. *Australian Journal of Earth Sciences* 59, p. 707–735.
- Barr, J. A., Grove, T. L. and Wilson, A. H. (2009). Hydrous komatiites from Comondale, South Africa: an experimental study. *Earth and Planetary Science Letters* 284, p. 199–207.
- Baziotis, I., Economou-Eliopoulos, M. and Asimow, P.D. (2017). Ultramafic lavas and high-Mg basaltic dykes from the Othris ophiolite complex, Greece. *Lithos* 288, p. 231–247.
- Bédard, J. H. (2006). A catalytic delamination-driven model for coupled genesis of Archaean crust and sub-continental lithospheric mantle. *Geochimica et Cosmochimica Acta* 70, p. 1188–1214.
- Bédard, J. H. (2018). Stagnant lids and mantle overturns: Implications for Archaean tectonics, magmagenesis, crustal growth, mantle evolution, and the start of plate tectonics. *Geoscience Frontiers* 9, p. 19–49.
- Bédard, J. H., Harris, L. B. and Thurston, P. C. (2013). The hunting of the snArc. *Precambrian Research* 229, p. 20–48.
- Bickle, M. J., Arndt, N. T., Nisbet, E. G., Orpen, J. L., Martin, A., Keays, R. R. and Renner, R. (1993). Geochemistry of the igneous rocks of the Belingwe Greenstone Belt: alteration, contamination and petrogenesis. *In*: M. J. Bickle and Nisbet, E. G. (Eds.) *The geology of the Belingwe Greenstone*

Belt, Zimbabwe: A study of the evolution of Archaean continental crust. Geological Society of Zimbabwe. p. 175–213.

Bizimis, M., Salters, V.J.M. and Bonatti, E. (2000). Trace and REE content of clinopyroxenes from supra-subduction zone peridotites. Implications for melting and enrichment processes in island arcs. *Chemical Geology* 165, p. 67–85.

Bleeker, W. (2015). Synorogenic gold mineralization in granite-greenstone terranes: the deep connection between extension, major faults, synorogenic clastic basins, magmatism, thrust inversion, and long-term preservation. *In: Dubé, B. and Mercier-Langevin P. (Eds.) Targeted Geoscience Initiative 4: contributions to the understanding of Precambrian lode gold deposits and implications for exploration.* Geological Survey of Canada, Open File 7852, p. 25–47.

Blewett, R. S., Henson, P. A., Roy, I. G., Champion, D. C. and Cassidy, K. F. (2010). Scale-integrated architecture of a world-class gold mineral system: the Archaean eastern Yilgarn Craton, Western Australia. *Precambrian Research* 183, p. 230–250.

Bloomer, S. H. and Hawkins, J. W. (1987). Petrology and geochemistry of boninite series volcanic rocks from the Mariana Trench. *Contributions to Mineralogy and Petrology* 97, p. 361–377.

Boily, M. and Dion, C. (2002). Geochemistry of boninite-type volcanic rocks in the Frotet-Evans greenstone belt, Opatica subprovince, Quebec: implications for the evolution of Archaean greenstone belts. *Precambrian Research* 115, p. 349–371.

Borg, L. E. and Draper, D. S. (2003). A petrogenetic model for the origin and compositional variation of the martian basaltic meteorites. *Meteoritics and Planetary Science* 38, p. 1713–1731.

Bouquain, S., Arndt, N. T., Hellebrand, E. and Faure, F. (2009). Crystallochemistry and origin of pyroxenes in komatiites. *Contributions to Mineralogy and Petrology* 158, p. 599–617.

Bouvier, A., Vervoort, J. and Patchett, J. P. (2008) The Lu-Hf and Sm-Nd isotopic composition of CHUR: Constraints from unequilibrated chondrites and implications for the bulk composition of terrestrial planets. *Earth and Planetary Science Letters* 272, p. 48–57

- Brown, M. and Johnson, T. (2018). Secular change in metamorphism and the onset of global plate tectonics. *American Mineralogist* 103, p. 181–196.
- Buckley, H. E. (1949). Habit modification in crystals as a result of the introduction of impurities during growth. *Discussions of the Faraday Society* 5, p. 243–254.
- Campbell, I. H. and Arndt, N. T. (1982). Pyroxene accumulation in spinifex-textured rocks. *Geological Magazine* 119, p. 605–610.
- Campbell, I. H. and Hill, R. I. (1988). A two-stage model for the formation of the granite-greenstone terrains of the Kalgoorlie-Norseman area, Western Australia. *Earth and Planetary Science Letters* 90, p. 11–25.
- Champion, D. C. (2013). Neodymium depleted mantle model age map of Australia - explanatory notes and user guide. *Geoscience Australia Record* 2013/44.
- Champion, D. C. and Cassidy, K. F. (2002). Granites of the northern Murchison Province: their distribution, age, geochemistry, petrogenesis, relationships with mineralisation, and implications for tectonic environment. *In*: Whitaker, A., Champion, D., Cassidy, K., Budd, A., Fletcher, I., McNaughton, N., and Hagemann, S. (Eds.) *Characterisation and metallogenic significance of Archaean granitoids of the Yilgarn Craton, Western Australia*. Minerals and Energy Research Institute of Western Australia report 222 and Australian Mineral Industries Research Association project report P482.
- Champion, D. C. and Smithies, R. H. (2007). Geochemistry of Paleoarchean granites of the East Pilbara Terrane, Pilbara Craton, Western Australia: Implications for early Archean crustal growth. *In*: M. J. Van Kranendonk, Smithies, R. H. and Bennett, V. C. (Eds) *Earth's Oldest Rocks*. Elsevier Science.
- Chung, S-L., Liu, D., Jianqing, J., Chu, M-F., Lee, H-Y., Wen, D-J., Lo, C-H., Lee, T-Y., Qian, Q. and Zhang, Q. (2003). Adakites from continental collision zones: melting of thickened lower crust beneath southern Tibet. *Geology*, 31, p. 1021–2024.

Clos, F., Weinberg, R. and Zibra, I. (2018). Building the Archean continental crust: 300 Ma of felsic magmatism in the Yalgoo Dome (Yilgarn Craton). Geological Survey of Western Australia, Report 186.

Coish, R. A. and Taylor, L. A. (1979). The effects of cooling rate on texture and pyroxene chemistry in DSDP Leg 34 basalt: a microprobe study. *Earth and Planetary Science Letters* 42, p. 389–398.

Conceição R.V. and Green D. H. (2004). Derivation of potassic (shoshonitic) magmas by decompression melting of phlogopite + pargasite lherzolite. *Lithos* 72, p. 209–229.

Condie, K. C. (2005a). High field strength element ratios in Archean basalts: a window to evolving sources of mantle plumes? *Lithos* 79, p. 491–504.

Condie, K.C. (2005b). TTGs and adakites: are they both slab melts? *Lithos* 80, p. 33–44.

Cooper, A. F. and Reid, D. L. (1991). Textural evidence for calcite carbonatite magmas, Dicker Willem, southwest Namibia. *Geology* 19, p. 1193.

Corgne, A. and Wood, B. J. (2004). Trace element partitioning between majoritic garnet and silicate melt at 25GPa. *Physics of the Earth and Planetary Interiors* 143–144, p. 407–419.

Crabtree, S. and Lange, R. (2011). Complex phenocryst textures and zoning patterns in andesites and dacites: evidence of degassing-induced rapid crystallization? *Journal of Petrology* 52, p. 3–38.

Crawford, A. J., Falloon, T. J. and Green, D. H. (1989). Classification, petrogenesis and tectonic setting of boninites. *In: A. J. Crawford (Eds) Boninites and related rocks*. p. 1–49.

Dallwitz, W.B., Green, D.H., and Thompson, J.E. (1966). Clinoenstatite in a Volcanic Rock from the Cape Vogel Area, Papua. *Journal of Petrology* 7, p. 375–403.

Danyushevsky, L.V., Sobolev, A.V. and Falloon, T.J. (1995). North Tongan high-Ca boninite petrogenesis: the role of Samoan plume and subduction zone-transform fault transition. *Journal of Geodynamics* 20, p. 219–241.

- Dasgupta, R., Hirschmann, M. M., McDonough, W. F., Spiegelman, M. and Withers, A. C. (2009). Trace element partitioning between garnet lherzolite and carbonatite at 6.6 and 8.6 GPa with applications to the geochemistry of the mantle and of mantle-derived melts. *Chemical Geology* 262, p. 57–77.
- De Laeter, J.R., Fletcher, I.R., Bickle, M.J., Myers, J.S., Libby, W.G. and Williams, I. R. (1985). Rb-Sr, Sm-Nd and Pb-Pb geochronology of ancient gneisses from Mt Narryer, Western Australia. *Australian Journal of Earth Sciences* 32, p. 349–358.
- DePaolo, D.J. (1981). Neodymium isotopes in the Colorado Front Range and crust-mantle evolution in the Proterozoic. *Nature* 291, p. 193–196.
- Deer, W.A., Howie, R.A. and Zussman, J. (2013). *An introduction to the rock forming minerals*. The Mineralogical Society. London, UK.
- Dey, S. (2013). Evolution of Archaean crust in the Dharwar craton: The Nd isotope record. *Precambrian Research* 227, p. 227–246
- Donaldson, C.H. (1976). An experimental investigation of olivine morphology. *Contributions to Mineralogy and Petrology* 57, p. 187–213.
- Donaldson, C.H. (1979). An experimental investigation of the delay in nucleation of olivine in Mafic Magmas. *Contributions to Mineralogy and Petrology* 69, p. 21–32.
- Donovan, J.J., Snyder, D.A. and Rivers, M.L. (1993). An improved interference correction for trace element analysis. *Microbeam Analysis* 2, p. 23–28.
- Donovan, J.J. and Tingle, T.N. (1996). An Improved Mean Atomic Number Correction for Quantitative Microanalysis. *Microscopy and Microanalysis* 2, p. 1–7.
- Duuring, P., Hassan, L., Zelic, M., Gessner, K. (2016) Geochemical and Spectral Footprint of Metamorphosed and Deformed VMS-Style Mineralization in the Quinns District, Yilgarn Craton, Western Australia. *Economic Geology* 111, p. 1411–1438.

Elliott, T. Plank, T. Zindler, A. White, W. and Bourdon, B. (1997). Element transport from slab to volcanic front at the Mariana arc. *Journal of Geophysical Research* 102, p. 14991–15019.

Emeleus, C.H. (1987). The Rhum layered complex, Inner Hebrides, Scotland. *In*: I. Parsons (Eds) *Origins of igneous layering*. Springer. p. 263–286.

Ersoy, E. Y. (2013). PETROMODELER (Petrological Modeler): a Microsoft® Excel© spreadsheet program for modelling melting, mixing, crystallization and assimilation processes in magmatic systems. *Turkish Journal of Earth Sciences* 22, p. 115–125.

Fan, J. and Kerrich, R. (1997). Geochemical characteristics of aluminium depleted and undepleted komatiites and HREE-enriched low-Ti tholeiites, western Abitibi greenstone belt: a heterogeneous mantle plume-convergent margin environment. *Geochimica et Cosmochimica Acta* 61, p. 4723–4744.

Falloon, T.J., Danyushevsky, L.V., Crawford, A.J., Meffre, S., Woodhead, J. D. and Bloomer, S. H. (2008). Boninites and Adakites from the Northern Termination of the Tonga Trench: Implications for Adakite Petrogenesis. *Journal of Petrology* 49, p. 697–715.

Falloon, T.J. and Crawford, A.J. (1991). The petrogenesis of high-calcium boninite lavas dredged from the northern Tonga ridge. *Journal of Petrology*, 102, p. 375–394.

Farina, F., Albert, C. and Lana, C. (2015). The Neoproterozoic transition between medium- and high-K granitoids: Clues from the Southern São Francisco Craton (Brazil). *Precambrian Research* 266, p. 375–394.

Faure, F., Trolliard, G., Nicollet, C. and Montel, J.-M. (2003). A developmental model of olivine morphology as a function of the cooling rate and the degree of undercooling. *Contributions to Mineralogy and Petrology* 145, p. 251–263.

Faure, F., Arndt, N. and Libourel, G. (2006). Formation of spinifex texture in komatiites: an experimental study. *Journal of Petrology* 47, p. 1591–1610.

Fletcher, I.R. and McNaughton, N.J. (2002). Granitoid geochronology: SHRIMP zircon and titanite data, *In*: Cassidy, K, Champion, D, McNaughton, N, Fletcher, I, Whitaker, A, Bastrakova, I and Budd, A 2002, Characterization and metallogenic significance of Archaean granitoids of the Yilgarn Craton, Western Australia: Minerals and Energy Resources Institute of Western Australia, Report 222.

Fowler, A. D., Berger, B., Shore, M., Jones, M. I. and Ropchan, J. (2002). Supercooled rocks: development and significance of varioles, spherulites, dendrites and spinifex in Archaean volcanic rocks, Abitibi Greenstone belt, Canada. *Precambrian Research* 115, p. 311–328

Frei, R., Rosing, M. T., Waight, T. E. and Ulfbeck, D. G. (2002) Hydrothermal-metasomatic and tectono-metamorphic processes in the Isua supracrustal belt (West Greenland): A multi-isotopic investigation of their effects on the Earth's oldest oceanic crustal sequence. *Geochimica et Cosmochimica Acta* 66, p. 467–486

Gao, Y., Hou, Z., Wei, R. and Zhao, R. (2003). Post-collisional adakitic porphyries in Tibet: geochemical and Sr-Nd-Pb isotopic constraints on partial melting of oceanic lithosphere and crust-mantle interaction. *Acta Geologica Sinica*, 77, p. 194–203.

Gee, R.D. (1979). Structure and tectonic style of the Western Australian shield. *Tectonophysics*, v. 58, p. 327–369.

Gee, R.D., Baxter, J.L., Wilde, S.A. and Williams, I.R. (1981). Crustal development in the Yilgarn Block, Western Australia. *Geological Society of Australia Special Publication* 7, p. 43–56.

Geological Survey of Western Australia (2018a). Compilation of geochronology information, 2018: Geological Survey of Western Australia, Digital Data Package.

Geological Survey of Western Australia (2018b). 'WACHEM database', <http://geochem.dmp.wa.gov.au/geochem/> (accessed 1 July 2018).

Geological Survey of Western Australia (2018c). Murchison, 2018: Geological Survey of Western Australia, Geological Information Series.

Geological Survey of Western Australia (2020). Youanmi, 2020: Geological Survey of Western Australia, Geological Information Series.

Geological Survey of Western Australia (2021a). Compilation of geochronology information, 2021: Geological Survey of Western Australia, Digital Data Package.

Geological Survey of Western Australia (2021b). 'WACHEM database', <http://geochem.dmp.wa.gov.au/geochem/> (accessed 1 October 2021).

Goldstein, S. L., O'Nions, R. K. and Hamilton, P. J. (1984). A Sm-Nd isotopic study of atmospheric dusts and particulates from major river systems. *Earth and Planetary Science Letters* 70, p. 221–236.

Golowin, R., Portnyagin, M., Hoernle, K., Hauff, F., Gurenko, A., Garbe-Schonberg, D., Werner, R. and Turner, S. (2017a). Boninite-like intraplate magmas from Manihiki Plateau require ultra-depleted and enriched source components. *Nature Communications* 8, Article 14322.

Golowin, R., Portnyagin, M., Hoernle, K., Sobolev, A., Kuzmin, D. and Werner, R. (2017b). The role and conditions of second-stage mantle melting in the generation of low-Ti tholeiites and boninites: the case of the Manihiki Plateau and the Troodos ophiolite. *Contributions to Mineralogy and Petrology* 172, Article 104.

Grove, T. L. and Bence, A. E. (1977). Experimental study of pyroxene-liquid interaction in quartz-normative basalt 15597. *Proceedings of the Eighth Lunar Science Conference*, p. 1549–1579.

Groves, D.I. and Batt, W.D. (1984). Spatial and temporal variations of Archaean metallogenic associations in terms of evolution of granitoid-greenstone terrains with particular emphasis on the Western Australian shield. *In*: Kroner, A., Manson, G.N. and Goodwin, A.M. (Eds) *Archaean Geochemistry the origin and evolution of the Archaean continental crust*. Berlin, Springer-Verlag, p. p. 73–98.

Guilliamse, J.N. (2014). Assessing the potential for volcanic-associated massive sulfide mineralization at Weld Range, using Golden Grove for comparison. Geological Survey of Western Australia, Report 141, 61p.

- Guo, Z., Wilson, M., and Liu, J. (2007). Post-collisional adakites in south Tibet: products of partial melting of subduction-modified lower crust. *Lithos*, 96, p. 205–224.
- Haase, K. M., Freund, S., Koepke, J., Hauff, F. and Erdmann, M. (2015). Melts of sediments in the mantle wedge of the Oman ophiolite. *Geology* 43, p. 275–278.
- Hallberg, J. A. (2000). Notes to accompany the Hallberg Murchison 1:25 000 geology dataset 1989–1994. Geological Survey of Western Australia. Perth, Australia.
- Hallberg, J. A., Carter, D. N. and West, K. N. (1976). Archaean volcanism and sedimentation near Meekatharra, Western Australia. *Precambrian Research* 3, p. 577–595.
- Hammond, R.L. and Nisbet, B.W. (1992). Towards a structural and tectonic framework for the Norseman-Wiluna Greenstone Belt, Western Australia. *In*: Glover, J.E. and Ho, S.E. (Eds.). *The Archaean: Terrains, Processes and Metallogeny*. University of Western Australia Geology Department and University, Publication 22, p. 39–50.
- Hart, T. R., Gibson, H. L. and Leshner, C. M. (2004). Trace element geochemistry and petrogenesis of felsic volcanic rocks associated with volcanogenic massive Cu-Zn-Pb sulfide deposits. *Economic Geology* 99, p. 1003-1013.
- Hawkesworth, C.J., Turner, S.P., McDermott, F., Peate, D.W. and van Calsteren, P. (1997). U-Th isotopes in arc magmas: implications for element transfer from the subducted crust. *Science* 276, p. 551–555.
- Hayman, P. C., Hull, S. E., Cas, R. a. F., Summerhayes, E., Amelin, Y., Ivanic, T. J. and Price, D. (2015). A new period of volcanogenic massive sulfide formation in the Yilgarn: a volcanological study of the c. 2.76 Ga Hollandaire VMS deposit, Yilgarn Craton, Western Australia. *Australian Journal of Earth Sciences* 62, p. 189–210.
- Hermann, J. and Rubatto, D. (2009). Accessory phase control on the trace element signature of sediment melts in subduction zones. *Chemical Geology* 265, p. 512–526

Herzberg, C., Asimow, P. D., Arndt, N., Niu, Y., Leshner, C. M., Fitton, J. G., Cheadle, M. J. and Saunders, A. D. (2007). Temperatures in ambient mantle and plumes: Constraints from basalts, picrites, and komatiites. *Geochemistry, Geophysics, Geosystems* 8, Q02006.

Herzberg, C., Condie, K. and Korenaga, J. (2010). Thermal history of the Earth and its petrological expression. *Earth and Planetary Science Letters* 292, p. 79–88.

Hickey-Vargas, R., Yogodzinski, G. M., Ishizuka, O., McCarthy, A.; Bizimis, M., Savov, I. P. and Arculus, R. (2018) Origin of depleted basalts during subduction initiation and early development of the Izu-Bonin-Mariana island arc: evidence from IODP expedition 351 site U1438, Amami-Sankaku basin. *Geochimica et Cosmochimica Acta* 229, p. 85–111.

Hildreth, W. and Moorbath, S. (1988). Crustal contributions to arc magmatism in the Andes of Central Chile. *Contributions to Mineralogy and Petrology* 98, p. 455–489.

Hirai, Y., Yoshida, T., Okamura, S., Tamura, Y., Sakamoto, I. and Shinjo, R. (2018). Breakdown of residual zircon in the Izu Arc subducting slab during backarc rifting, *Geology* 46, p. 371–374.

Hoffmann, J. E. and Wilson, A. H. (2017). The origin of highly radiogenic Hf isotope compositions in 3.33 Ga Comondale komatiite lavas (South Africa). *Chemical Geology* 455, p. 6–21.

Hollis, S. P., Yeats, C. J., Wyche, S., Barnes, S. J., Ivanic, T. J., Belford, S. M., Davidson, G. J., Roache, A. J., Wingate, M. T. D. (2015). A review of volcanic-hosted massive sulfide (VHMS) mineralization in the Archaean Yilgarn Craton, Western Australia: Tectonic, stratigraphic and geochemical associations. *Precambrian Research* 260, p113-135.

Howard, H. M., Werner, M., Smithies, R. H., Evins, P. M., Kirkland, C. L., Kelsey, D. E., Hand, M., Collins, A., Pirajno, F., Wingate, M. T. D., Maier, W. D. and Raimondo, T. (2011). The geology of the West Musgrave Province and the Bentley Supergroup - a field guide. Geological Survey of Western Australia. Perth, Australia.

Huppert, H.E. and Sparks, S. J. (1985) Cooling and contamination of mafic and ultramafic magmas during ascent through continental crust. *Earth and Planetary Science Letters* 74, p. 371–386

Iizuka, T., McCulloch, M.T., Komiya, T., Shibuya, T., Ohta, K., Ozawa, H., Sugimura, E. and Collerson, K.D. (2010). Monazite geochronology and geochemistry of meta-sediments in the Narryer Gneiss Complex, Western Australia: constraints on the tectonothermal history and provenance, *Contributions to Mineralogy and Petrology* 160, p. 803–823.

Ingle, S., Mahoney, J. J., Sato, H., Coffin, M. F., Kimura, J.-I., Hirano, N. and Nakanishi, M. (2007). Depleted mantle wedge and sediment fingerprint in unusual basalts from the Manihiki Plateau, central Pacific Ocean. *Geology* 35, p. 595–598.

Ivanic, T. J. (2016). A field guide to the mafic–ultramafic intrusions of the Youanmi Terrane, Yilgarn Craton: Geological Survey of Western Australia, Record 2016/6, 61p.

Ivanic T.J. (2019). Mafic-ultramafic intrusions of the Youanmi Terrane, Yilgarn Craton. Geological Survey of Western Australia, Report 192, 130p.

Ivanic, T. J., Nebel, O., Brett, J. and Murdie, R. E. (2017). The Windimurra Igneous Complex: an Archean Bushveld? *In*: K. Gessner, Blenkinsop, T. G. and Sorjonen-Ward, P. (Eds.) *Characterization of Ore-Forming Systems from Geological, Geochemical and Geophysical Studies*. . The Geological Society of London, London.

Ivanic, T. J., Nebel, O., Jourdan, F., Faure, K., Kirkland, C. L. and Belousova, E. A. (2015). Heterogeneously hydrated mantle beneath the late Archean Yilgarn Craton. *Lithos* 238, p. 76–85.

Ivanic, T. J., Van Kranendonk, M. J., Kirkland, C. L., Wyche, S., Wingate, M. T. D. and Belousova, E. A. (2012). Zircon Lu–Hf isotopes and granite geochemistry of the Murchison Domain of the Yilgarn Craton: Evidence for reworking of Eoarchean crust during Meso-Neoarchean plume-driven magmatism. *Lithos* 148, p. 112–127.

Ivanic, T. J., Wingate, M. T. D., Kirkland, C. L., Van Kranendonk, M. J. and Wyche, S. (2010). Age and significance of voluminous mafic–ultramafic magmatic events in the Murchison Domain, Yilgarn Craton. *Australian Journal of Earth Sciences* 57, p. 597–614.

Jackson, S. (1990). Structural and hostrock controls, wallrock alteration and genesis of gold mineralization in the Phar Lap Deposit, Meekatharra, Western Australia. University of Western Australia. Unpublished.

Jónasson, K., 2005. Magmatic evolution of the Heiðarsporður ridge, NE-Iceland. *Journal of Volcanology and Geothermal Research* 147, p. 109–124.

Joshi, S. S. (2012). Crystal habit modification using habit modifiers. *In*: N. Kolesnikov and Borisenko, E. (Eds.) *Modern aspects of bulk crystal and thin film preparation*. InTech. 618.

Johnson, M.C. and Plank, T. (1999). Dehydration and melting experiments constrain the fate of subducted sediments. *Geochemistry, Geophysics, Geosystems*, 1, 26p. doi:10.1029/1999GC000014

Johnson, T. E., Brown, M. Kaus, B. and Van Tongeren, J. A. (2013). Delamination and recycling of Archaean crust caused by gravitational instabilities. *Nature geoscience* 7, p. 47–52.

Johnson, T.E., Brown, M., Gardiner, N.J., Kirkland, C.L., and Smithies, R.H. (2017). Earth's first stable continents did not form by subduction. *Nature*, 543, p. 239–242, doi: 10.1038/nature21383.

Kanayama, K., Umino, S. and Ishizuka, O. (2012). Eocene volcanism during the incipient stage of Izu-Ogasawara arc: Geology and petrology of the Mukojima Island Group, the Ogasawara Islands. *Island Arc* 21, p. 288–316.

Kareem, K. (2005). Komatiites of the Weltevreden Formation, Barberton Greenstone Belt, South Africa: implications for the chemistry and temperature of the Archean mantle (Unpublished PhD Thesis). Department of Geology and Geophysics, Tulane University. Louisiana, USA.

Kareem, K. M. and Bryerly, G. R. (2003). Petrology and geochemistry of 3.3 Ga komatiites – Weltevreden Formation, Barberton Greenstone Belt (abstract). 34th Lunar and Planetary Science Convention, Lunar and Planetary Institute.

Kelemen, P. B., Hanghøj, K. and Greene, A. R. (2007). One view of the geochemistry of subduction-related magmatic arcs, with an emphasis on primitive andesite and lower crust. *In*: Holland, H. D. and K. K. Turekian (Eds.) *Treatise on Geochemistry*. Pergamon, Oxford. p. 1–70.

Kemp, A.I.S., Wilde, S.A. and Spaggiari, C. (2019). The Narryer Terrane, Yilgarn Craton, Western Australia: review and recent developments *In*: Van Kranendonk, M.J., Bennett, V.C., and Hoffman, J.E. (Eds.) *Earth's Oldest Rocks* (Second Edition), Elsevier, p. 401–433.

Kerr, A. C., Marriner, G. F., Arndt, N. T., Tamey, J., Nivia, A., Saunders, A. D. and Duncan, R. A. (1996). The Petrogenesis of Gorgona komatiites, picrites and basalts - new field, petrographic and geochemical constraints. *Lithos* 37, p. 245–260.

Kerrick, R., Wyman, D., Fan, J. and Bleeker, W. (1998). Boninite series: low Ti-tholeiite associations from the 2.7 Ga Abitibi greenstone belt. *Earth and Planetary Science Letters* 164, p. 303–316.

Kinny, P.D., Wijbrans, J.R., Froude, D.O., Williams, I.S., and Compston, W. (1990). Age constraints on the geological evolution of the Narryer Gneiss Complex, Western Australia. *Australian Journal of Earth Sciences*, 37, p. 51–69.

Komatsu, M. (1980). Clinoenstatite in volcanic rocks from the Bonin Islands. *Contributions to Mineralogy and Petrology* 74, p. 329–338.

König, S., Münker, C., Schuth, S. and Garbe-Schönberg, D. (2008). Mobility of tungsten in subduction zones. *Earth and Planetary Science Letters* 274, p. 82–92.

König, S., Münker, C., Schuth, S., Luguet, A., Hoffmann, J. E. and Kuduon, J. (2010). Boninites as windows into trace element mobility in subduction zones. *Geochimica et Cosmochimica Acta* 74, p. 684–704.

Korenaga, J. (2008). Urey ratio and the structure and evolution of Earth's mantle. *Reviews of Geophysics* 46.

Laflèche, M.R., Dupuy, C., and Dostal, J. (1992). Tholeiitic volcanic rocks of the late Archean Blake River Group, southern Abitibi greenstone belt: origin and geodynamic implications. *Canadian Journal of Earth Sciences*, 29, p. 1448–1458.

Lahaye, Y., Arndt N., Byerly, G. Chauvel, C. Fourcade, S. and Gruau, G. (1995). The influence of alteration on the trace-element and Nd isotopic compositions of komatiites. *Chemical Geology* 126, p. 43–64.

Le Bas, M. J. (2000). IUGS Reclassification of the High-Mg and Picritic Volcanic Rocks. *Journal of Petrology* 41, p. 1467–1470.

Le Maitre, R.W., Streckeisen, A., Zanettin, B., Le Bas, M. J., Bonin, B., Bateman, P., Bellieni, G., Dudek, A., Efremova, S., Keller, J., Lameyre, J., Sabine, P. A., Schmid, R., Sørensen, H. and Woolley, A. R. (2002). *A Classification and Glossary of Terms: recommendations of the International Union of Geological Sciences Subcommittee on the Systematics of Igneous Rocks, 2nd ed.* Cambridge University Press, 236p.

Lofgren, G. E., Donaldson, C. H. and Usselman, T. M. (1975). Geology, petrology and crystallization of Apollo 15 quartz-normative basalts. *Proceedings of the Sixth Lunar Science Conference*, p. 79–99.

Lowrey, J.R. and Ivanic, T.J. (2018). Platy pyroxene spinifex: re-evaluating the distribution of komatiite across Western Australia's Archean cratons. *Australian Journal of Mineralogy*, 19, p. 39–42.

Lowrey, J.R., Ivanic, T.J., Wyman, D.A. and Roberts, M.P. (2017). Platy Pyroxene: New Insights into Spinifex Texture. *Journal of Petrology* 58, p. 1671–1700.

Lowrey, J. R., Wyman, D., Ivanic, T. J., Smithies, R. H. and Maas, R. (2019). Archean boninite-like rocks of the northwestern Youanmi Terrane, Yilgarn Craton: geochemistry and genesis. *Journal of Petrology*.

Lu, Y-J, Campbell McCuaig, T, Li, Z-X, Jourdan, F, Hart, CJ., Hou, Z-Q, and Tang, S-H, 2015, 'Paleogene post-collisional lamprophyres in western Yunnan, western Yangtze Craton: Mantle source and tectonic implications', *Lithos*, vol. 233, p. 139–161.

Lu, Y, Wingate, MTD, Champion, DC, Smithies, RH, Johnson, SP, Mole, DR, Poujol, M, Zhao, J, Maas, R and Creaser RA 2021, Samarium–neodymium isotope map of Western Australia: Geological Survey of Western Australia, digital data layer, <<https://www.dmirs.wa.gov.au/geoview>>.

Maas, R., Grew, E. S. and Carson, C. J. (2015) Isotopic constraints (Pb, Rb-Sr, Sm-Nd) on the sources of Early Cambrian pegmatites with boron and beryllium minerals in the Larseman Hills, Prydz Bay, Antarctica. *The Canadian Mineralogist* 53, p. 249–272

Maas, R. and McCulloch, M.T. (1991). The provenance of Archean clastic metasediments in the Narryer Gneiss Complex, Western Australia: Trace element geochemistry, Nd isotopes, and U-Pb ages for detrital zircons. *Geochimica et Cosmochimica Acta*, 55, p. 1915–1932.

Macpherson, C. G. and Hall, R. (2001). Tectonic setting of Eocene boninite magmatism in the Izu–Bonin–Mariana forearc. *Earth and Planetary Science Letters* 186, p. 215–230.

Manikyamba, C., Naqvi, S. M., Subba Rao, D. V., Ram Mohan, M., Khanna, T. C., Rao, T. G. and Reddy, G. L. N. (2005). Boninites from the Neoarchaeon Gadwal greenstone belt, Eastern Dharwar Craton, India: implications for Archaeon subduction processes. *Earth and Planetary Science Letters* 230, p. 65–83.

Martin, H., Smithies, R. H., Rapp, R., Moyen, J. F. and Champion, D. (2005). An overview of adakite, tonalite–trondhjemite–granodiorite (TTG), and sanukitoid: relationships and some implications for crustal evolution. *Lithos* 79, p. 1–24.

Matzen, A.K., Baker, M. B., Beckett, J. R. and Stolper, E.M. (2011). Fe-Mg partitioning between olivine and high-magnesian melts and the nature of Hawaiian parental liquids. *Journal of Petrology* 52, p. 1243–1263.

Meffre, S., Aitchison, J.C. and Crawford, A.J. (1996). Geochemical evolution and tectonic significance of boninites and tholeiites from the Koh ophiolite, New Caledonia. *Tectonics* 15, p. 67–83.

Middlemost, E.A.K. (1994). Naming materials in the magma/igneous rock system. *Earth Science Reviews*, 37, p. 215–224.

Mole, D.R., Barnes, S. J., Yao, Z., White, A. J. R., Maas, R. and Kirkland, C. L. (2018) The Archean Fortescue large igneous province: A result of komatiite contamination by a distinct Eo-Paleoarchean crust. *Precambrian Research* 310, p. 365–390

Mole, D., Thurston, P., Marsh, J., Stern, R., Ayer, J., Martin, L.A., and Lu, Y. (2021). The formation of Neoarchean continental crust in the south-east Superior Craton by two distinct geodynamic processes, *Precambrian Research*, 356, p.106104. doi: 10.1016/j.precamres.2021.106104.

Morimoto, N., Fabries, J., Ferguson, A. K., Ginzburg, I. V., Ross, M., Seifert, F. A., Zussman, J., Aoki, K. and Gottardi, G. (1988). Nomenclature of pyroxenes. *American Mineralogist* 73, p. 1123–1133.

Moyen, J. F., Martin, H., Jayananda, M. and Auvray, B. (2003). Late Archaean granites: a typology based on the Dharwar Craton (India). *Precambrian Research* 127, p. 103–123.

Mueller, A.G., Campbell, I.H., Schiøtte, L., Sevigny, J.F. and Layer, P.W. (1996). Constraints on the age of granitoid emplacement, metamorphism, gold mineralization, and subsequent cooling of the Archean greenstone terrane at Big Bell, Western Australia. *Economic Geology*, 91, p. 896–915.

Myers, J.S. (1990). Precambrian tectonic evolution of part of Gondwana, southwestern Australia. *Geology*, 18, p. 537–540.

Myers, J.S. (1995). The generation and assembly of an Archaean supercontinent: evidence from the Yilgarn craton, Western Australia. *In*: Coward, M.P., and Ries, A.C. (Eds.) *Early Precambrian processes*. Geological Society Special Publication No 95, p. 143–154.

Natland, J. H. (1982). Crystal morphologies and pyroxene compositions in boninites and tholeiitic basalts from deep sea drilling project holes 458 and 459B in the Mariana fore-arc region. *Initial reports of the Deep Sea Drilling Project* 60, p. 681–707.

Nebel, O., Arculus, R.J., Ivanic, T.J., Nebel-Jacobsen, Y.J., (2013) Lu–Hf isotopic memory of plume–lithosphere interaction in the source of layered mafic intrusions, Windimurra Igneous Complex, Yilgarn Craton, Australia. *Earth and Planetary Science Letters* 380, p. 151–161.

Nebel, O., Capitanio, F.A., Moyen, J.-F., Weinberg, R. F., Clos, F., Nebel-Jacobsen, Y. J. and Cawood, P.A. (2018). When crust comes of age: on the chemical evolution of Archaean, felsic continental crust by crustal drip tectonics. *Philosophical Transactions*. 376. 21p

Nesbitt, R. W. (1971). Skeletal crystal forms in the ultramafic rocks of the Yilgarn Block, Western Australia: evidence for an Archaean ultramafic liquid. *Geological Society of Australia Special Publication No.* 3331–347.

Nisbet, E. G., Arndt, N. T. and Bickle, M. J. (1987). Uniquely fresh 2.7 Ga komatiites from the Belingwe greenstone belt, Zimbabwe. *Geology* 15, p. 1147–1150.

Nutman, A. P., Bennett, V. C., Kinny, P. D. and Price, R. (1993). Large-scale crustal structure of the north-western Yilgarn Craton, Western Australia: Evidence from Nd isotopic data and zircon geochronology. *Tectonics* 12, p. 971–981.

Nutman, A.P., Kinny, P.D., Compston, W. and Williams, I.S. (1991). SHRIMP U-Pb zircon geochronology of the Narryer Gneiss Complex, Western Australia. *Precambrian Research*, 52, p. 275–300.

Ohnenstetter, D. and Brown, W. L. (1992). Overgrowth textures, disequilibrium zoning, and cooling history of a glassy four-pyroxene boninite dyke from New Caledonia. *Journal of Petrology* 33, p. 231–271.

O'Reilly, S. Y. & Zhang, M. (1995). Geochemical characteristics of lava-field basalts from eastern Australia and inferred sources: Connections with the subcontinental lithospheric mantle? *Contributions to Mineralogy and Petrology* 121, p. 148–170.

Orpen, J. L., Martin, A., Bickle, M. J. and Nisbet, E. G. (1993). The Mtshingwe Group in the west: andesites, basalts, komatiites and sediments of the Hokonui, Bend and Koodoovale Formations. *In: M. J. Bickle and Nisbet, E. G. (Eds.) The geology of the Belingwe Greenstone Belt, Zimbabwe: A study of the evolution of Archaean continental crust.* Geological Society of Zimbabwe. p. 69–86.

Osozawa, S., Shinjo, R., Lo, C. H., Jahn, B. M., Hoang, N., Sasaki, M., Ishikawa, K., Kano, H., Hoshi, H., Xenophontos, C. and Wakabayashi, J. (2012). Geochemistry and geochronology of the

Troodos ophiolite: An SSZ ophiolite generated by subduction initiation and an extended episode of ridge subduction? *Lithosphere* 4, p. 497–510.

Palin, R.M. and White, R.W. (2015). Emergence of blueschists on Earth linked to secular changes in oceanic crust composition. *Nature Geoscience*, 9, p. 60–64.

Patriat, M., Falloon, T., Danyushevsky, L., Collot, J., Jean, M.M., Hoernle, K., Hauff, F., Maas, R., Woodhead, J.D. and Feig, S.T. (2019). Subduction initiation terranes exposed at the front of a 2 Ma volcanically-active subduction zone. *Earth and Planetary Science Letters* 508, p. 30–40.

Pearce, J. A. (2008). Geochemical fingerprinting of oceanic basalts with applications to ophiolite classification and the search for Archean oceanic crust. *Lithos* 100, p. 14–48.

Pearce, J. A., Kempton, P. D., Nowell, G. M. and Noble, S. R. (1999). Hf-Nd Element and Isotope Perspective on the Nature and Provenance of Mantle and Subduction Components in Western Pacific Arc-Basin Systems. *Journal of Petrology* 40, p. 1579–1611.

Pearce, J. A. and Reagan, M. K. (2018). Identification, classification and interpretation of boninites from the Recent-Eoarchean geologic record using Si-Mg-Ti systematics. *Geosphere*.

Pearce, J. A. and Stern, R. J. (2006). Origin of Back-Arc Basin Magmas: Trace Element and Isotope Perspectives (Eds.) *Back-Arc Spreading Systems: Geological, Biological, Chemical, and Physical Interactions*. American Geophysical Union. p. 63–86.

Peccerillo, A. and Taylor, S.R. (1976). Geochemistry of Eocene calc-alkaline volcanic rocks from the Kastamonu area, Northern Turkey. *Contributions to Mineralogy and Petrology*, 58, p. 63–81.

Perchuk, A.L., Zakharov, V.S., Gerya, T.V. and Brown, M. (2019). Hotter mantle but colder subduction in the Precambrian: what are the implications? *Precambrian Research* 330, p. 20–34.

Pidgeon, R.T. and Wilde, S.A. (1990). The distribution of 3.0 Ga and 2.7 Ga volcanic episodes in the Yilgarn Craton of Western Australia. *Precambrian Research*, 48, p. 309–325.

Pidgeon, R. T. and Hallberg, J. A. (2000). Age relationships in supracrustal sequences of the northern part of the Murchison Terrane, Archaean Yilgarn Craton, Western Australia: a combined field and zircon U–Pb study. *Australian Journal of Earth Sciences* 47, p. 153–165.

Pin, C. and Santos Zalduegui, J. F. (1997) Sequential separation of light rare-earth elements, thorium and uranium by miniaturized extraction chromatography: application to isotopic analyses of silicate rocks. *Analytica Chimica Acta* 339, p. 79–89

Polat, A., Kerrich, R., 2002. Nd-isotope systematics of (2.7 Ga adakites, magnesian andesites, and arc basalts, Superior Province, Canada: evidence for shallow crustal recycling at Archean subduction zones. *Earth Planet. Sci. Lett.* 202, p. 345–360.

Polat, A., Hoffmann, J. E. and Rosing, M. T. (2002). Boninite-like volcanic rocks in the 3.7–3.8 Ga Isua greenstone belt, West Greenland: geochemical evidence for intra-oceanic subduction zone processes in the early Earth. *Chemical Geology* 184, p. 231–254.

Portnyagin, M. V., Danyushevsky, L. V. and Kamenetsky, V. S. (1997). Coexistence of two distinct mantle sources during formation of ophiolites: a case study of primitive pillow-lavas from the lowest part of the volcanic section of the Troodos Ophiolite, Cyprus. *Contributions to Mineralogy and Petrology* 128, p. 287–301.

Puchtel, I. S., Blichert-Toft, J., Touboul, M., Walker, R. J., Byerly, G. R., Nisbet, E. G. and Anhaeusser, C. R. (2013). Insights into early Earth from Barberton komatiites: Evidence from lithophile isotope and trace element systematics. *Geochimica et Cosmochimica Acta* 108, p. 63–90.

Puchtel, I. S., Hofmann, A. W., Mezger, K., Shchipansky, A. A., Kulikov, V. S. and Kulikova, V. V. (1996). Petrology of a 2.41 Ga remarkably fresh komatiitic basalt lava lake in Lion Hills, central Vetreny Belt, Baltic Shield. *Contributions to Mineralogy and Petrology* 124, p. 273–290.

Puchtel, I. S., Walker, R. J., Brandon, A. D. and Nisbet, E. G. (2009). Pt–Re–Os and Sm–Nd isotope and HSE and REE systematics of the 2.7Ga Belingwe and Abitibi komatiites. *Geochimica et Cosmochimica Acta* 73, p. 6367–6389.

Pyke, D. R., Naldrett, A. J. and Eckstrand, O. R. (1973). Archean ultramafic flows in Munro Township, Ontario. *Geological Society of America Bulletin* 84, 955.

Rapp R.P., Shimizu N., Norman M.D., Applegate G.S. (1999). Reaction between slab-derived melts and peridotite in the mantle wedge: experimental constraints at 3.8 GPa. *Chemical Geology*, 160, p. 335–356.

Rasmussen, B., Fletcher, I.R., Muhling, J.R. and Wilde, S.A. (2010). In situ U–Th–Pb geochronology of monazite and xenotime from the Jack Hills belt: Implications for the age of deposition and metamorphism of Hadean zircons. *Precambrian Research*, 180, p. 26–46.

Renner, R., Nisbet, E. G., Cheadle, M. J., Arndt, N., Bickle, M. J. and Cameron, W. E. (1994). Komatiite Flows from the Reliance Formation, Belingwe Belt, Zimbabwe: I. Petrography and Mineralogy. *Journal of Petrology* 35, p. 361–400.

Reudavey, I. (1990). The nature, petrogenesis and deformation style of the Gabanintha ultramafic sequence and its bearing on gold mineralization at Gabanintha, Murchison Province, Western Australia. Department of Geology. Perth, Western Australia, University of Western Australia. Bachelor of Science (Honours).

Robin-Popieul, C. C. M., Arndt, N. T., Chauvel, C., Byerly, G. R., Sobolev, A. V. and Wilson, A. (2012). A New Model for Barberton Komatiites: Deep Critical Melting with High Melt Retention. *Journal of Petrology*.

Roeder, P. L. and Emslie, R. F. (1970). Olivine-liquid equilibrium. *Contributions to Mineralogy and Petrology* 29, p. 275–289.

Rollinson, H. (2007). *Early Earth systems: a geochemical approach*. John Wiley and Sons Inc.

Romano, S. S. (2018). Gabanintha, WA Sheet 2644: Geological Survey of Western Australia, 1:100 000 Geological Series.

Said, N. and Kerrich, R. (2010). Elemental and Nd-isotope systematics of the Upper Basalt Unit, 2.7 Ga Kambalda Sequence: quantitative modelling of progressive crustal contamination of plume asthenosphere. *Chemical Geology* 273, p. 193–211.

Salters, V. J. M. and Stracke, A. (2004). Composition of the depleted mantle. *Geochemistry, Geophysics, Geosystems* 5, 27p.

Quentin de Gromard, R., Ivanic, T.J. and Zibra, I., 2021, Pre-Mesozoic interpreted bedrock geology of the southwest Yilgarn, 2021, in Accelerated Geoscience Program extended abstracts: Geological Survey of Western Australia, Record 2021/4, p. 122–144.

Schiøtte, L and Campbell, IH 1996, Chronology of the Mount Magnet granite-greenstone terrain, Yilgarn Craton, Western Australia: implications for field based predictions of the relative timing of granitoid emplacement: *Precambrian Research*, v. 78, p. 237–260.

Sharpe, R. & Gemmell, J.B. (2002). The Archean Cu-Zn magnetite-rich Gossan Hill volcanic-hosted massive sulfide deposit, Western Australia; genesis of a multistage hydrothermal system. *Economic Geology and the Bulletin of the Society of Economic Geologists*, 97, p. 517–539.

Shimizu, K., Nakamura, E. and Maruyama, S. (2005). The geochemistry of ultramafic to mafic volcanics from the Belingwe Greenstone Belt, Zimbabwe: magmatism in an Archean continental large igneous province. *Journal of Petrology* 46, p. 2367–2394.

Shimizu, K. Nakamura, E., Kobayashi, K. and Maruyama, S. (2004). Discovery of Archean continental and mantle fragments inferred from xenocrysts in komatiites, the Belingwe greenstone belt, Zimbabwe. *Geology* 32, p. 285–288.

Shiraki, K., Kuroda, N., Urano, H. and Maruyama, S. (1980). Clinoenstatite in boninites from the Bonin Islands, Japan. *Nature* 285, p. 31–32.

Shirey, S. B. and Hanson, G. N. (1984). Mantle-derived Archaean monzodiorites and trachyandesites. *Nature* 310.

Smithies, R. H. (2000). The Archaean tonalite-trondhjemite-granodiorite (TTG) series is not an analogue of Cenozoic adakite, *Earth and Planetary Science Letters*, 182, p. 115–125.

Smithies, R. H. (2002). Archean boninite-like rocks in an intracratonic setting. *Earth and Planetary Science Letters* 197, p. 19–34.

Smithies, R.H., Lowrey, J.R., Sapkota, J., De Paoli, M., Hayman, P., Masurel, Q., Thébaud, N. and Grech L.L. (in review). Geochemical characterisation of the magmatic stratigraphy of the Kalgoorlie and Black Flag Groups - Ora Banda to Kambalda region. Geological Survey of Western Australia, Report.

Smithies, R.H., Lu, Y., Kirkland, C.L., Johnson, T.E., Mole, D.R., Champion, D.C., Martin, L., Jeon, H., Wingate, M.T.D., and Johnson, S.P. (2021). Oxygen isotopes trace the origins of Earth's earliest continental crust. *Nature*, 592, p. 70–75.

Smithies, R.H., Lu, Y., Johnson, T.E., Kirkland, C.L., Cassidy, K.F., Champion, D.C., Mole, D.R., Zibra, I., Gessner, K., Sapkota, J., De Paoli, M.C., and Poujol, M. (2019). No evidence for high-pressure melting of Earth's crust in the Archean. *Nature Communications*, 10, 5559–12, doi: 10.1038/s41467-019-13547-x.

Smithies, R. H., Champion, D. C. and Sun, S.-S. (2004). The case for Archaean boninites. *Contributions to Mineral Petrology* 147, p. 705–721.

Smithies, R. H., Champion, D. C., Van Kranendonk, M. J., Howard, H. M. and Hickman, A. H. (2005). Modern-style subduction processes in the Mesoarchaeon: Geochemical evidence from the 3.12 Ga Whundo intra-oceanic arc. *Earth and Planetary Science Letters* 231, p. 221–237.

Smithies, R. H., Ivanic, T. J., Lowrey, J. R., Morris, P. A., Barnes, S. J., Wyche, S. and Lu, Y.-J. (2018). Two distinct origins for Archean greenstone belts. *Earth and Planetary Science Letters* 487, p. 106–116.

Spaggiari, C.V., Wartho, J-A., and Wilde, S.A. (2008). Proterozoic deformation in the northwest of the Archean Yilgarn Craton, Western Australia. *Precambrian Research*, 162, p. 354–384.

Stern, R., J. and Bloomer, S. H. (1992). Subduction zone infancy: examples from the Eocene Izu-Bonin-Mariana and Jurassic California arcs. *Geological Society of America Bulletin* 104, p. 1621–1636.

Stiegler, M. T., Cooper, M., Byerly, G. R. and Lowe, D. R. (2012). Geochemistry and petrology of komatiites of the Pioneer Ultramafic Complex of the 3.3 Ga Weltevreden Formation, Barberton Greenstone Belt, South Africa. *Precambrian Research* 212–213, p. 1–12.

Sun, S.-S., Nesbitt, R. W. and Mcculloch, M. T. (1989). Geochemistry and petrogenesis of Archaean and early Proterozoic siliceous high-magnesian basalts. *In: A. J. Crawford (ed) Boninites*. p. 148–173.

Sun, S. S. and McDonough, W. F. (1989). Chemical and isotopic systematics of oceanic basalts: implications for mantle composition and processes. *Geological Society, London, Special Publications* 42, p. 313–345.

Swager, C.P. (1997). Tectono-stratigraphy of late Archaean greenstone terranes in the southern Eastern Goldfields, Western Australia. *Precambrian Research*, 83, p. 11–42.

Tatsumi, Y. (2005). The Petrology and Geochemistry of Oto-Zan Composite Lava Flow on Shodo-Shima Island, SW Japan: Remelting of a Solidified High-Mg Andesite Magma. *Journal of Petrology* 47, p. 595–629.

Tatsumi, Y. (2006). High-Mg andesites in the Setouchi volcanic belt, Southwestern Japan: Analogy to Archean Magmatism and Continental Crust Formation? *Annual Review of Earth and Planetary Sciences* 34, p. 467–499.

Taylor, R. N., Nesbitt, R. W., Vidal, P., Harmon, R. S., Auvray, B. and Croudace, I. W. (1994). Mineralogy, Chemistry, and Genesis of the Boninite Series Volcanics, Chichijima, Bonin Islands, Japan. *Journal of Petrology* 35, p. 577–617.

Taylor, S. R. and McLennan, S. M. (1995). The geochemical evolution of the continental crust. *Review of Geophysics* 33, p. 241–265.

Thorkelson, D.J. and Breitsprecher, K. (2005). Partial melting of slab window margins: genesis of adakitic and non-adakitic magmas. *Lithos*, 79, p. 25–41.

Timm, C., Hoernle, K., Werner, R., Hauff, F., Den Bogaard, P. V., Michael, P., Coffin, M. F. and Koppers, A. (2011). Age and geochemistry of the oceanic Manihiki Plateau, SW Pacific: New evidence for a plume origin. *Earth and Planetary Science Letters* 304, p. 135–146.

Tollstrup, D.L., Gill, J., Kent, A.J.R., Prinkey, D., Williams, R., Tamura, Y., and Ishizuka, O., 2010, Across-arc geochemical trends in the Izu-Bonin arc: Contributions from the subducting slab, revisited: *Geochemistry Geophysics Geosystems*, 11, 1019, <https://doi.org/10.1029/2009GC002847>.

Turner, S. Rushmer, T., Reagan, M., Moyen, J-F. (2014) Heading down early on? Start of subduction on Earth. *Geology* 42, p. 139–142.

Umino, S., Kanayama, K., Kitamura, K., Tamura, A., Ishizuka, O., Senda, R. and Arai, S. (2017). Did boninite originate from the heterogeneous mantle with recycled ancient slab? *Island Arc* 27, 16.

Van Kranendonk, MJ 2010, Cue, WA Sheet 2443, Geological Survey of Western Australia, 1:100 000 Geological Series.

Van Kranendonk, M. J. and Ivanic, T. J. (2009). A new lithostratigraphic scheme for the northeastern Murchison Domain, Yilgarn Craton: p. 34–53.

Van Kranendonk, M. J., Ivanic, T. J., Wingate, M. T. D., Kirkland, C. L. and Wyche, S. (2013). Long-lived, autochthonous development of the Archean Murchison Domain, and implications for Yilgarn Craton tectonics. *Precambrian Research* 229, p. 49–92.

Vance, D. and Thirlwall, M. F. (2002) An assessment of mass discrimination in MC-ICPMS using Nd isotopes. *Chemical Geology* 185, p. 227–240

Viljoen, M. J. and Viljoen, R. P. (1969). Evidence for the existence of a mobile extrusive peridotitic magma from the Komati Formation of the Onverwacht Group. Geological Society of South Africa, Special Publication No 2.

Walker, D. A. and Cameron, W. E. (1983). Boninite primary magmas: evidence from the cape vogel peninsula, PNG. *Contributions to Mineralogy and Petrology* 83, p. 150–158.

Wang L.G., McNaughton, N.J. and Groves, D.I. (1993). An overview of the relationship between granitoid intrusions and gold mineralization in the Archaean Murchison Province, Western Australia. *Mineralium Deposita*, 28, p. 428–494.

Wang L.G., McNaughton, N.J. and Groves, D.I. (1995). New geochronological data for granitoid intrusions in the Reedy's area, Murchison Province, Western Australia: constraints on genesis of gold mineralization.

Wang, Q. (1998). Geochronology of the Granite-Greenstone Terranes in the Murchison and Southern Cross Provinces of the Yilgarn Craton, Western Australia.

Wang, Q., Schiøtte, L. and Campbell, I. H. (1998). Geochronology of supracrustal rocks from the Golden Grove area, Murchison Province, Yilgarn Craton, Western Australia*. *Australian Journal of Earth Sciences* 45, p. 571–577.

Wang, Q. and Wilde, S.A. (2018). New constraints on the Hadean to Proterozoic history of the Jack Hills belt, Western Australia. *Gondwana Research*, vol. 55, p. 74–91.

Wang, Q., Wyman, D.A., Xu, J-F., Dong, Y., Vasconcelos, P.M.P., Pearson, N.J., Wan, Y., Dong, H., Li, C-F., Yu, Y., Zhu, T., Feng, X., Zhang, Q., Zi, F. and Chu, Z. (2008). Eocene melting of subducting continental crust and early uplifting of central Tibet: evidence from central-western Qiangtang high-K calc-alkaline andesites, dacites and rhyolites. *Earth and Planetary Science Letters*, 272, p. 158–171.

Wasserburg, G. J., Jacobsen, S. B., DePaolo, D. J., McCulloch, M. T. and Wen, T. (1981) Precise determination of Sm/Nd ratios, Sm and Nd isotopic abundances in standard solutions. *Geochimica et Cosmochimica Acta* 45, p. 2311–2321

Watkins, K. P. and Hickman, A. H. (1990). Geological evolution and mineralization of the Murchison Province, Western Australia. Geological Survey of Western Australia. Perth. Australia.

- Welsch, B., Faure, F., Famin, V., Baronnet, A. and Bachelery, P. (2013). Dendritic Crystallization: A Single Process for all the Textures of Olivine in Basalts? *Journal of Petrology* 54, p. 539–574.
- Wiedenbeck, M. and Watkins, K.P. (1993). A time scale for granitoid emplacement in the Archean Murchison Province, Western Australia, by single zircon geochronology. *Precambrian Research*, 61, p. 1–26.
- Wilde, S.A., Middleton, M.F. and Evans, B. J. (1996). Terrane accretion in the southwestern Yilgarn Craton: Evidence from a deep seismic crustal profile. *Precambrian Research*, 78, p. 179–196.
- Wilson, A. H. (2003a). Archaean ultra-depleted komatiites formed by hydrous melting of cratonic mantle. *Nature* 423, p. 858–861.
- Wilson, A. H. (2003b). A new class of silica enriched, highly depleted komatiites in the southern Kaapvaal Craton, South Africa. *Precambrian Research* 127, p. 125–141.
- Wilson, A. H. and Versfeld, J. A. (1994). The early Archaean Nondweni Greenstone Belt, southern Kaapvaal Craton, South Africa, Part II. Characteristics of the volcanic rocks and constraints on magma genesis. *Precambrian Research* 67, p. 277–320.
- Wingate, M. T. D., Bodorkos, S. and Kirkland, C. L. (2008). 183921: felsic volcanoclastic rock, Lordy Bore; Geochronology Record 733. *In: Compilation of geochronology data. Geological Survey of Western Australia.*
- Wingate, M. T. D., Kirkland, C. L. and Forbes, C. J. (2011). 178142: metarhyolite, Cullculli Hill; Geochronology Record 967. *Geological Survey of Western Australia*, 4p.
- Witt, W.K., Geology and mineral resources of the Ravensthorpe and Cocaranup 1:100 000 sheets. *Western Australia Geological Survey, Report 54*, 152p.
- Woelki, D., Regelous, M. Haase, K. M. and Beier, C. (2018). Geochemical mapping of a paleo-subduction zone beneath the Troodos Ophiolite. *Chemical Geology* 523, p. 1–8.
- Wood, C. P. (1980). Boninite at a continental margin. *Nature* 288, 692–694.

Woodhead, J., Hergt, J., Greig, A. and Edwards, L. (2011). Subduction zone Hf-anomalies: Mantle messenger, melting artefact or crustal process? *Earth and Planetary Science Letters* 304, p. 231–239.

Workman, R. K. and Hart, S. R. (2005). Major and trace element composition of the depleted MORB mantle (DMM). *Earth and Planetary Science Letters* 231, p. 53–72.

Wyche, S., Spaggiari, C. V., Forbes, C. J., Bunting, J. A., Thebaud, N., Hollingsworth, D., Culpan, N. and Vearncome, J. (2007). A geological traverse across the northern Yilgarn Craton - a field guide. Geological Survey of Western Australia. Perth, Australia.

Wyche, S., Kirkland, C. L., Riganti, A., Pawley, M. J., Belousova, E. and Wingate, M. T. D. (2012). Isotopic constraints on stratigraphy in the central and eastern Yilgarn Craton, Western Australia. *Australian Journal of Earth Sciences* 59, p. 657–670.

Wyman, D. A. (2003). Upper mantle processes beneath the 2.7 Ga Abitibi belt, Canada: a trace element perspective. *Precambrian Research* 127, p. 143–165.

Wyman, D., Kerrich, R., and Polat, A. (2002). Assembly of Archean cratonic mantle lithosphere and crust: plume–arc interaction in the Abitibi–Wawa subduction–accretion complex. *Precambrian Research*, 115, p. 37–62.

Wyman, D. A. (2013). A critical assessment of Neoarchean “plume only” geodynamics: Evidence from the Superior Province. *Precambrian Research* 229, p. 3–19.

Wyman, D. A. (2019). 2.8 Ga subduction-related magmatism in the Youanmi Terrane and a revised geodynamic model for the Yilgarn Craton. *Precambrian Research* 327, p. 14–33.

Wyman, D. A., Bleeker, W. and Kerrich, R. (1999). A 2.7 Ga komatiite, low Ti tholeiite, arc tholeiite transition and inferred proto-arc geodynamic setting of the Kidd Creek deposit: evidence from precise trace element data. *Economic Geology Monograph* 10, p. 311–328.

Wyman, D. A. and Kerrich, R. (2012). Geochemical and isotopic characteristics of Youanmi terrane volcanism: the role of mantle plumes and subduction tectonics in the western Yilgarn Craton. *Australian Journal of Earth Sciences* 59, p. 671–694.

Yang, Z.-M., Lu, Y.-J., Hou, Z.-Q., Chang, Z.-S., 2015. High-Mg Diorite from Qulong in Southern Tibet: Implications for the Genesis of Adakite-like Intrusions and Associated Porphyry Cu Deposits in Collisional Orogens. *Journal of Petrology* 56, p. 227–254.

Yeats, C. J., McNaughton, N. J. and Groves, D. I. (1996). SHRIMP U-Pb Geochronological Constraints on Archean Volcanic-Hosted Massive Sulfide and Lode Gold Mineralization at Mount Gibson, Yilgarn Craton, Western Australia. *Economic Geology* 91, p. 1354–1371.

Zhao, S.-R., Liu, R., Wang, Q.-Y., Xu, H.-J. and Fang, M. (2011). Skeletal morphologies and crystallographic orientations of olivine, diopside and plagioclase. *Journal of Crystal Growth* 318, p. 135–140.

Zhou, M.-F., Zhao, T.-P., Malpas, J. and Sun, M. (2000). Crustal-contaminated komatiitic basalts in Southern China: products of a Proterozoic mantle plume beneath the Yangtze Block. *Precambrian Research* 103, p. 175–189.

Zibra, I., 2020. Neoarchean structural evolution of the Murchison Domain (Yilgarn Craton). *Precambrian Research* 343, Article 105719, doi: 10.1016/j.precamres.2020.105719.

REPORT 259

PETROGENESIS OF C. 2820–2738 MA MAGMATISM IN THE NORTHWESTERN YOUANMI TERRANE, YILGARN CRATON

JR Lowrey

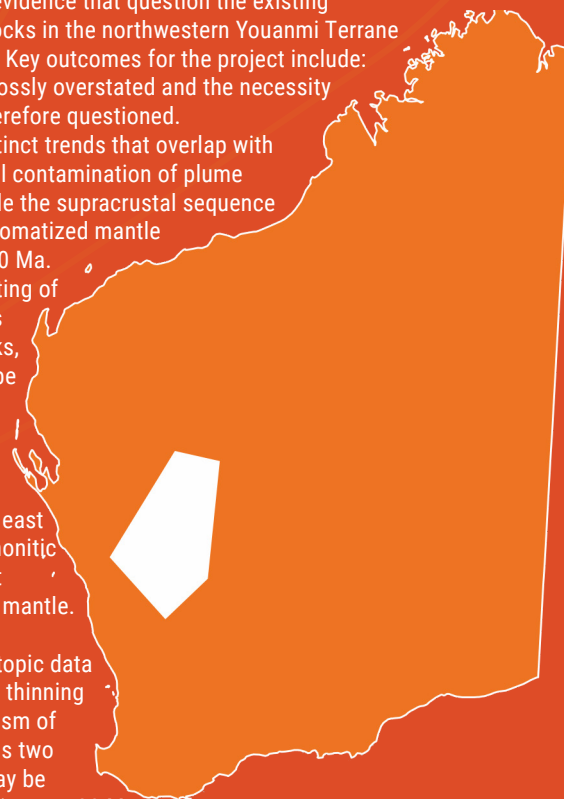
The Yilgarn Craton is one of the largest remaining fragments of Earth's Archean crust and is critical to understanding geodynamic processes that operated on early Earth. Using new petrographic, geochemical and Sm-Nd isotopic data and existing geochronological data, this study follows several lines of evidence that question the existing plume-based geodynamic model for c. 2820–2735 Ma magmatic rocks in the northwestern Youanmi Terrane (NW Yilgarn Craton) and instead suggests an arc-accretion setting. Key outcomes for the project include:

(1) The distribution of komatiites reported in previous studies is grossly overstated and the necessity for anomalously high mantle temperatures of a mantle plume is therefore questioned.

(2) Th/Yb–Nb/Yb systematics for volcanic rocks define several distinct trends that overlap with trends from modern subduction settings and do not suggest crustal contamination of plume magmas. (3) Coeval mafic–ultramafic and granitic rocks that intrude the supracrustal sequence are locally hornblende-rich and indicate widespread hydrous metasomatized mantle sources throughout the northwestern Youanmi Terrane from c. 2810 Ma.

(4) A detailed chemostratigraphic framework is established consisting of 16 units that include boninite-like rocks, tholeiitic basalts, siliceous high-Mg basalts and high-Mg calc-alkaline intermediate–felsic rocks, locally with shoshonitic compositions that would almost certainly be considered diagnostic of subduction setting if documented in the modern geologic record. (5) Sm-Nd isotope and trace element systematics of magmatic rocks implicate increasing degrees of mantle metasomatism from c. 2820 to 2738 Ma and variable recycling of ≥ 3050 –2920 Ma crustal components, increasing from east to west and upwards through the stratigraphic sequence. (6) Shoshonitic rocks on the western side of the study area have compositions that implicate recycling of ancient, chemically evolved material into the mantle.

Integration of the available geochemical, geochronological and isotopic data implicates two consecutive magmatic events involving lithospheric thinning and upwelling asthenosphere, as well as depletion and metasomatism of mafic magma sources at c. 2820 and c. 2793 Ma interpreted here as two subduction events with associated rifting, c. 25 Ma apart, which may be attributed to subduction step-back or plate rearrangements. Following a c. 20 Ma hiatus, a second magmatic episode from c. 2761–2738 Ma that included crustal-derived transitional TTGs and mantle-derived shoshonitic and sanukitoid rocks is interpreted to represent a post-orogenic event related to delamination of arc-crust or slab breakoff.



Further details of geoscience products are available from:

First Floor Counter

Department of Energy, Mines, Industry Regulation and Safety

100 Plain Street

EAST PERTH WESTERN AUSTRALIA 6004

Phone: +61 8 9222 3626 Email: publications@demirs.wa.gov.au

www.demirs.wa.gov.au/GSWApublications